3-Tissue Constrained Spherical Deconvolution as a novel means of assessing free water and cellular microstructure across the brain and lifespan

Benjamin F. McGartland Newman

MSc. (Res) Psychology, University of St Andrews 2018

A Dissertation presented to the Graduate Faculty
of the University of Virginia in Candidacy for the Degree of
Doctor of Philosophy

University of Virginia
Spring, 2022

Table of Contents

Abstract and Specific Aims

Diffusion MRI (dMRI) is a rapidly expanding technique for non-invasively tracking the movement of water molecules throughout the brain. Within the microarchitectural environment of the brain, the free movement of water molecules is restricted by various cellular components, particularly the lipid bilayers that make up cell membranes and the myelin sheaths that wrap axons. As a consequence of the Brownian motion of water molecules[1], there is a constant degree of movement within the brain that is directed and shaped by these cellular components. These patterns of diffusion are extremely complex and require mathematical models to interpret, the earliest and most widespread being diffusion tensor imaging (DTI) which provides a geometric representation of diffusion on a voxel-wise scale[2,3]. The geometric information available from DTI led to the development of diffusion tractography, a means to describe axonal connections between brain regions[4,5]. With tractography came a focus on isolating the white matter (WM) axonal diffusion signal from 'noise' generated by other tissue compartments within the brain, such as grey matter (GM), and cerebrospinal fluid (CSF). However the diffusion signal from these tissue compartments might be a useful biomarker for a number of conditions[6–8] as well as across the lifespan in development and aging.

This project aims to use an advanced mathematical representation of diffusion to generate voxel-wise quantitative estimates of brain cellular microstructure, and then demonstrate the utility of these estimates in a range of subjects across the lifespan. Rather than relying on DTI, which has only 6 free terms to describe the diffusion signal, estimates of cellular microstructure will be derived from constrained spherical deconvolution (CSD). CSD is a more recently developed method that uses spherical harmonics with a theoretically unlimited number of terms available for describing the diffusion signal[9–11]. CSD will allow for more advanced and anatomically accurate estimates of 3 underlying tissue components, each of which predominates in specific brain areas: intracellular anisotropic signal (ICA) which is primarily located in myelinated axonal areas, intracellular isotropic signal (ICI) which is highest in GM areas such as the cortex, and extracellular isotropic signal (ECI) which predominates outside brain tissue but also represents freely diffusing water within the brain. Changes in these tissue compartments may be important

biomarkers for various disorders or may occur throughout the lifespan as a component of healthy development and aging.

Aim 1: Assess the reliably and reproducibly of 3T-CSD measurements of ICA, ICI, and ECI signal fractions as a means of quantifiably assessing brain cellular microstructure from diffusion MRI. It will be determined if 3T-CSD measurements are affected by image quality and scanning location, if measurements are biased by CSD algorithm selection, and if the underlying CSD model can be used to register images to stereotaxic space.

To achieve this aim a widely used CSD analysis implemented in the open-source dMRI processing software MRtrix[12] will be adapted in order to derive quantitative information on a voxel-wise level about ICA, ICI, and ECI tissue compartments in the human brain. This will improve on existing quantitative dMRI models by capturing 3 easily interpretable tissue compartments from even single-shell data using a state-of-the-art spherical harmonic representation to capture the most complex microstructure arrangements. This technical development will encompass diffusion acquisition selection, CSD algorithm selection, novel image registration methods, and tests of reliability and reproducibility both longitudinally between timepoints and between MRI scanners.

Aim 2a: To generate trajectories of 3T-CSD measurements of ICA, ICI, and ECI signal fractions across the lifespan and during a variety of developmental and degenerative processes similar to existing structural MRI modalities.

The basic cellular processes that occur in the brain during human development, aging, and decline, are still poorly understood. Volumetric MRI studies have established that the volumes of brain white matter and gray matter change dramatically across the lifespan[13,14]. However since 3T-CSD is potentially more sensitive to cellular changes at the sub-voxel level it may be able to detect changes in brain microstructure before they manifest as changes in brain volume[15]. It is also necessary to explore the cellular microstructure that underlies volumetric change with detailed analysis of specific regions of the brain at multiple scales and between hemispheres. The goal of this study is to analyze a large number of subjects from a publicly available population cohort in

order to provide a lifespan trajectory for 3T-CSD measurements of cellular microstructure from multiple areas of the brain. Establishing the relationship between chronological age and microstructural metrics will establish normal reference ranges and trajectories that are essential before investigating abnormal populations.

Aim 2b: Determine if 3T-CSD microstructure measurements are altered by pubertal development during the critical period of early adolescence.

Adolescence is a time of rapid physiological and neurological change that is primarily driven by the surge in production of sex-specific hormones. Identifying microstructural changes that occur naturally during this time period will allow for further evaluation into life events that alter brain cellular microstructure. Understanding the relationship between the cells of the brain and maturation is an important component of adolescent health and well-being throughout the remainder of the lifespan.

Aim 2c: Determine if the epigeneticly derived risk score 'GrimAge' is an effective peripheral blood biomarker of small vessel disease driven damage to brain microstructure in a 'healthy' aging cohort.

Though macro-level changes in the aging brain are well described, the microstructural cellular alterations underlying these changes are relatively unknown. We would expect microstructural alterations to be more sensitive to physiological change or pathological development before they accumulated into macro-level changes in brain structure. The age-adjusted version of GrimAge presents a powerful means for studying the effects of cardiovascular health on the brain and has been shown to be predictive of the presence and size of white matter hyperintensities (WMH)[16]. A specific focus will be made on white matter hyperintensities, a visible neurological manifestation of small vessel disease, and the microstructural composition of the axonal pathways throughout each individual's brain affected by their unique white matter hyperintensity location and volume.

Introduction and Background

Diffusion weighted magnetic resonance imaging (dMRI) is a widely used, noninvasive, tool for measuring the movement of water molecules in the brain. Within the microarchitectural environment of the brain, the free movement of water molecules is restricted by various cellular components, particularly the lipid bilayers that make up cell membranes and the myelin sheaths that wrap axons. As a consequence of the Brownian motion of water molecules[1], there is a constant degree of movement within the brain that is directed and shaped by these cellular components. Measuring diffusion using magnetic resonance has been performed by scientists for over a half century[17], and has grown far beyond merely measuring the Einstein's diffusion coefficient[18] in various tissues.

Two advances that greatly influenced the analysis of dMRI, as well as the general neuroimaging community, are the development of diffusion tensor imaging (DTI)[19], which began to provide a geometric representation of diffusion on the voxel-wise scale, and diffusion tractography[4,5], which used the geometric information from DTI to describe axonal connections between brain regions. With this came a focus on isolating the white matter (WM) axonal diffusion signal from 'noise' generated by other tissue compartments within the brain, such as grey matter (GM), and cerebrospinal fluid (CSF). A great deal of research in the following decade created various tensor-based models of varying complexity to describe the diffusion signal[20–23].

One of these tensor-based models, termed Free Water Elimination, included an isotropic tensor representing freely diffusing water, which was designed to be removed from an image to improve the accuracy of WM tractography[24]. However, it was quickly realized that the eliminated tensor, representing the proportion of each voxel composed of water and termed the Free Water Volume Fraction, could be a useful biomarker for a number of conditions[6,8,25]. Tensor-based models suffer from a number of different flaws[26,27] and to resolve these issues, different models of diffusion became necessary. This line of thought led to the creation of

constrained spherical deconvolution, a model-free method of representing the diffusion signal using spherical harmonics[9], and created by Tournier et al.,[11]. Constrained spherical deconvolution was extended to include multiple tissue types a few years later[10]. This extension allowed for signal from all three tissue compartments, WM, GM, and CSF, to be detected and described without the use of tensors.

Mirroring the original use of Free Water Elimination, the GM and CSF compartments were discarded to improve the signal from WM[10,28]. While this led to improved resolution of WM fiber density and directionality for use in tractography, the discarded signal from the GM and CSF tissue compartments may also hold important microstructural information about the composition of brain tissue. This review will cover the historical and theoretical background of dMRI in general, as well as the specific effects this background has had on the development of microstructural models of diffusion, and finally, on the potential significance and applications of 3-tissue constrained spherical deconvolution (3T-CSD).

Historical Development and Grounding in Physics

The experiments of Stejskal & Tanner,[17] built on the spin-echo work of Hahn,[29] and demonstrated that magnetic resonance could be successfully used to determine the self-diffusion coefficient of molecules in a liquid state. This provided evidence that the diffusion coefficient (D) behaved as initially described by Einstein[18]:

(1) $$D = \frac{RT}{6\pi kN}$$

Where R is the universal gas constant, T is the temperature, k is the viscosity of fluid, and N is Avogadro's number. Stejskal & Tanner's diffusion sequence was composed of two identical radiofrequency gradients, followed by an acquisition based on the resulting spin echo. The first radiofrequency gradient 'tagged' the molecules in a spatial position. After a brief period of time, the second identical radiofrequency gradient then refocuses the proton spins. This has the effect of generating an echo of magnitude proportional to the distance moved across the gradient[17].

Early research using the Stejskal & Tanner's spin-echo technique focused on determining the diffusion coefficient of a particular tissue or sample, with many applications initially in physical chemistry[30–32]. It was rapidly discovered that diffusion was not consistent when the magnetic field gradient was applied in different orientations across a sample (Figure 1). The reason for this difference was inferred to be barriers that restricted the movement of water relative to its unrestricted self-diffusion coefficient[17,33,34]. This developed the idea of the Apparent Diffusion Coefficient (ADC) which made clear that the pattern of diffusion observed in tissue did not match the unrestricted movement assumed from Einstein's isotropic diffusion coefficient despite it being treated as such for the purpose of calculation[17,35].

It is important to remember that many of these developments occurred prior to the implementation of magnetic resonance imaging and instead were conducted under the auspices of nuclear magnetic resonance experiments, with a single diffusion coefficient as the measured variable. Despite this, many basic features of modern diffusion experiments were present such as early precursors to modern b-values. These were framed in regards to time intervals between, as well as the duration of, the two diffusion gradients. Early physiological experiments varied the gradient duration in order to capture longer diffusion times in tissues with more sparse cellular boundaries, also demonstrating how alteration of gradient duration provides differential signal from different tissue types (Figure 2). This b-value equation was first described by Stejskal & Tanner [17], and has become a descriptor for all modern diffusion acquisition schemes:

$$b = \gamma^2 G^2 \delta^2 (\Delta - \delta/3) \quad (2)$$

Where γ is the gyromagnetic ratio (~42.577 MHz/T), G is the gradient strength (T/m), δ is the duration for which the diffusion gradients are applied, and Δ is the time interval between gradient applications.

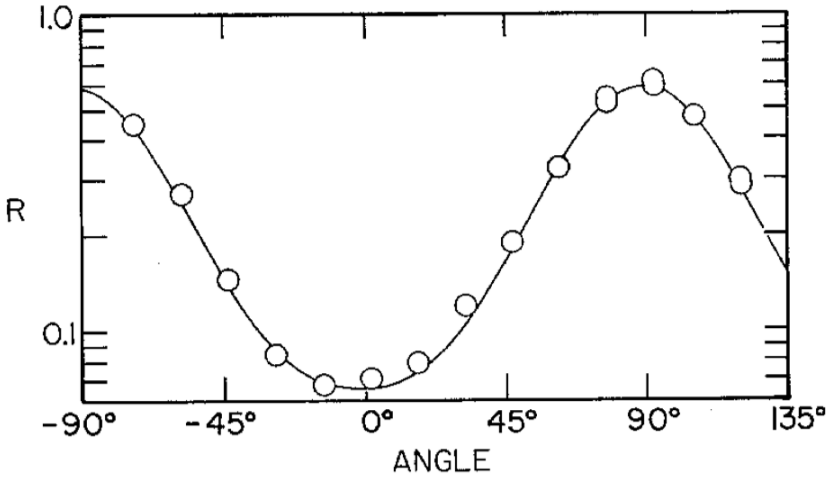

Figure 1: Example of anisotropic diffusion observed from an early diffusion experiment using the Stejskal & Tanner spin echo technique on the mineral biotite vermiculite swollen in a capsule of water. The variable R is analogous to the observed diffusion signal measured as the sample was rotated relative to the applied radiofrequency gradient. The molecular structure of vermiculite forms sheets, and 0° is perpendicular to the sheet direction. Figure appears in Boss & Stejskal (1968)[36].

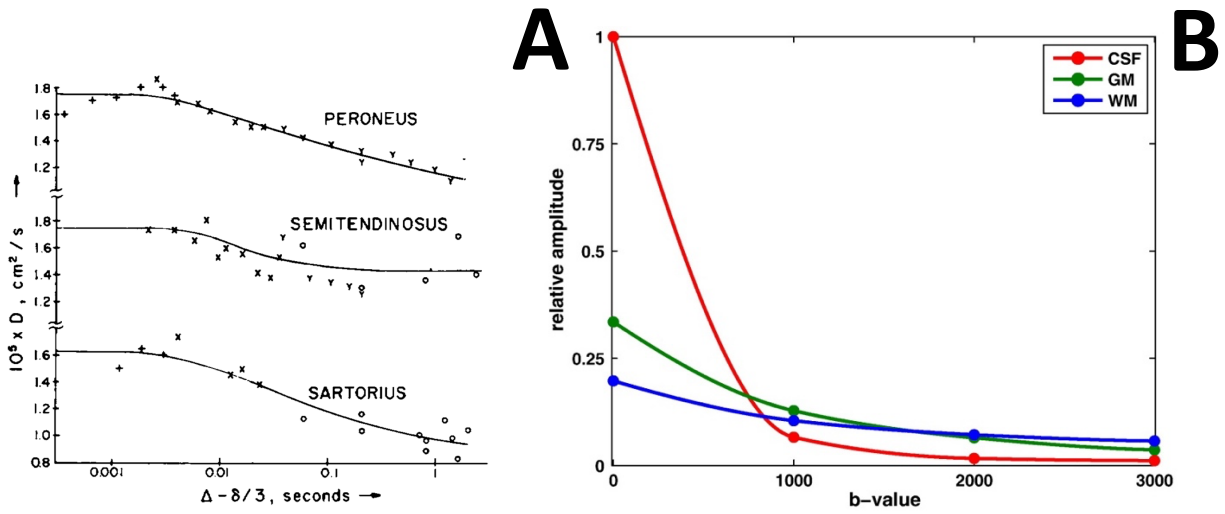

Figure 2: (A) Diffusion coefficient vs. time interval between gradient application (Δ) and gradient duration (δ), the variables typically varied in modern b-values (as displayed is Eq. 2). Each graph shows a different diffusion coefficient response with increasing 'b-value' in three muscles of Rana pipiens. Symbols refer to different samples and diffusion sequences, "smooth curves were drawn by eye". Figure adapted from Tanner[37]. (B) Chart describing the relationship between signal amplitude and gradient b-value from a modern diffusion experiment. This shows how multiple b-value shells can be useful for discriminating signal from different tissue types in the brain. CSF signal will be brightest on b0 images but at higher b-values signal will primarily be obtained from WM. Figure adapted from Jeurissen et al.,[10].

Many of the early experiments calculating the diffusion coefficient followed along the idea that the object under study could be rotated within the magnetic field to determine which angle was the direction of primary diffusion, as in the experiment referenced in Figure 1[17,36,37]. In liquid or mineral samples with simplistic underlying geometry this was acceptable, but in brain tissue and skeletal muscle the microgeometry is extremely complex and spatially heterogenous, with many different cell types and structures present especially throughout the brain. In brain white matter in particular, the myelin sheaths surrounding axons restrict diffusion along a narrow angular direction, imposing anisotropic movement, as opposed to the isotropic diffusion (i.e. lacking a specific summation vector and occurring relatively equally in all directions), that occurs in pure fluid[38,39]. Diffusion coefficient measurements along a single direction are not sufficient to spatially resolve these complexities[38].

Portraying Diffusion in 3D: The development of the diffusion tensor model

A crucial advance in relating the magnitude of diffusion to the underlying tissue environment came with the application of the tensor[19]. This allowed for an objective, orthotropic description of diffusion on a voxel-wise basis, and due to the relative ease of computation and the variety of derivative measures has rapidly become one of the primary mathematical models for analyzing diffusion MR in the neuroimaging community.

Tensors in diffusion imaging are defined as geometric objects composed of three primary vectors and their orientations, referred to as eigenvalues and eigenvectors, respectively[19]. These compose a matrix of directionality and magnitude displayed in Eq. 3:

$$D = [\varepsilon_1 \mid \varepsilon_2 \mid \varepsilon_3] \begin{bmatrix} \lambda_1 & 0 & 0 \\ 0 & \lambda_2 & 0 \\ 0 & 0 & \lambda_3 \end{bmatrix} \quad (3)$$

Where λ represents each of the primary ADC magnitude eigenvalues and ε represents each orthonormal eigenvector, orienting the tensor so that λ_1 is maximized. This allows the principal

eigenvector (λ_1), which has the greatest diffusivity, to define diffusion along the principal direction, or axis, of a fiber tract. This is occasionally referred to as the axial diffusivity. The next two largest eigenvectors define diffusion along the two remaining orthotropic axes, and when averaged together are referred to as radial diffusivity[2,40]. Eq. 3 includes six independent elements and thus requires at least six non-colinear gradient directions in order to fully reconstruct each tensor[19] and the model can be expanded to combine information from multiple different b-values[41].

One of the most straightforward examples of the utility in using radial and axial diffusivity appears in studies of multiple sclerosis (MS). MS involves an immune response that damages the integrity of myelin that surrounds WM axonal tracts in the brain[42]. When this occurs, the previously highly impermeable myelin barrier allows water molecules to move with greater freedom perpendicular to the direction of principal diffusivity, increasing the radial diffusivity without decreasing the axial diffusivity[43,44].

Axial and radial diffusivity can be accounted for in a single relative measurement describing the degree of anisotropy for the tensor by calculating the Fractional Anisotropy (FA) proposed by van Gelderen et al.,[45]. This formula (Eq. 4), is the standard deviation of the three ADC eigenvalues divided by the average ADC:

$$FA = \frac{\sqrt{3((\lambda_1 - \sum[\lambda])^2 + (\lambda_2 - \sum[\lambda])^2 + (\lambda_3 - \sum[\lambda])^2)}}{\sqrt{2(\lambda_1^2 + \lambda_2^2 + \lambda_3^2)}} \quad (4)$$

This creates a single scalar measurement to describe the overall diffusion pattern within a voxel. FA scales from 0-1, with 0 being perfectly isotropic and 1 being perfectly anisotropic, making interpretation relatively simple. Mean Diffusivity is another commonly cited diffusion tensor derived metric. It can simply be calculated as the average magnitude of the eigenvalues (for a full review of simple tensor-based measurements see Soares et al.,[46]).

The orientation or directionality of WM fibers has become commonly visualized via the tensors themselves, or by tractography. Tractography of tensor-based diffusion models typically

involves the drawing of paths along the primary eigenvector direction in a step-wise function[4]. Visualizing this directionality has generally become standardized along an R-G-B color channel setup where each color channel represents directionality in the X-Y-Z plane. Bihan[47] attributed this visualization scheme to have originated with Nakada et al.[48], and it was formalized by Pajevic & Pierpaoli,[49]. It has become widely adopted in the diffusion community that red represents left-right directionality, green represents anterior-posterior directionality, and blue represents superior-inferior directionality.

Criticisms of Tensors for Evaluating dMRI Data

One of the fundamental flaws with the basic tensor model of diffusion representation is that a single ellipsoid, while elegant, cannot describe the complex patterns of diffusion created by brain structure. Diffusion along neuronal axons is, by nature, anisotropic with the primary direction of diffusion following the direction of the fiber and myelin and cellular boundaries preventing water molecules from moving as easily in a radial direction. This model works well when there is a homogeneous sub-voxel orientation of WM fibers. However, when isotropic signals arising from GM or CSF tissue is present in the same voxel the tensor must still represent these mixed signal forms with a single ellipsoid. Even more damaging to tensor models is the effect that occurs when multiple directions of WM fibers are present in a single voxel. This is commonly referred to as the issue of 'crossing fibers' and can eliminate nearly all directional information by compacting the tensor into a flat disc[50]. This is essentially a failure of the model, as the typical diffusion tensor measurements such as FA are unable to provide meaningful values. This can be seen in an example of Wallerian degeneration, where a loss of WM fibers appears less serious in different brain regions due to the underlying directional pattern (Figure 3) and not due to the actual change in underlying tissue[51].

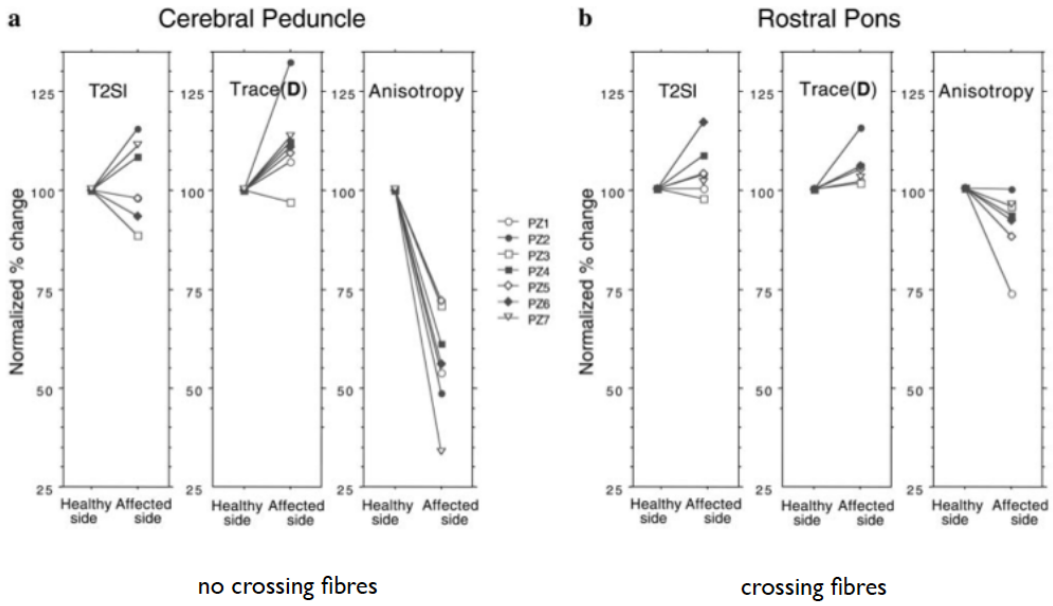

Figure 3: Example of changes in diffusion measurements in patients following infarction showing how the Wallerian degeneration appears different and is dependent on the pre-injury directionality of WM in an ROI. The greatest change is in FA, when in the cerebral peduncle the affected side of the brain shows a significant decrease in FA, but in the rostral pons there is no significant drop even though both areas have experienced loss of neurons from the primary motor pathway. Figure adapted from Pierpaoli et al.,[51].

The directionality of WM fiber representations can also suffer when the underlying fiber distribution is not uniform due to curved fibers that are not linearly oriented within a voxel, such as in the ucinate fasciculus or in pyramidal projections[27,52]. Because of the construction of tensors as three vectors tied to a central point, the only way the model is capable of portraying these inhomogeneities is by widening the second or third eigenvalue. These crossing or multiple fibers are extremely common in the brain, and it has been estimated that up to 63-90% of WM voxels in the brain have more than one WM fiber orientation[53]. This indicates that the physical problem is widespread, but the underlying mathematical model is also the source of error. Further mathematical issues have been comprehensively described by Wheeler-Kingshott & Cercignani[26], where theoretical tensor matrices can be easily manipulated and the effect of simple ratio changes between the three eigenvalues in opposite dimensions can have identical effects on the summary FA and mean diffusivity values.

<u>Modeling Brain Microstructure Using dMRI</u>

The shortcomings of diffusion tensor analysis have led to the creation of a number of other models that have attempted to either correct a particular problem inherent to the original single tensor model or take advantage of new developments in sequence design and acquisition. As more powerful scanners and computational resources became available, it was proposed that increasing the angular resolution by adding more gradient directions would provide a clearer spatial description of tissue structure in the brain[54]. This eventually became known as high angular resolution diffusion imaging (HARDI) and with the enhanced resolution of crossing fibers was able to demonstrate that fiber orientation was frequently heterogenous within certain WM regions such as the forceps minor, fascicle base of the frontal gyri, and where the callosal striations crossed the projections of the superior frontal gyrus[55]. With the idea of crossing fibers becoming particularly acute, the field attempted to move into more complex models of diffusion that took the microstructure of the brain into account in interpreting the diffusion signal. This led to the creation of several models such as multiple tensor[56,57], models that define specific shapes for the tensors to represent specific tissues of interest, such as ball and stick[23], or Free Water Elimination[24]. Some models use the idea of intra- and extra-cellular compartments based on if the distance of diffusion is hindered or totally restricted such as CHARMED[21]. Neurite Orientation Dispersion and Density Imaging (NODDI) represents neurites and dendrites as sticks and uses the non-Gaussian signal response at high b-values to estimate neurite density[58]. Other methods attempted to fit probabilistic tracts to the tensors in order to re-create the heterogenous directions without a new model[59]. For a review in detail of many of these models see Seunarine & Alexander,[60]. Though there is a wealth of models currently proliferating in the field, the remainder of this review will focus on two models in particular that have become widely used in the field of diffusion microstructural imaging, and that add a key component beyond WM modeling. This is the free diffusion of water, and importantly, the ability to determine the fraction of freely diffusing water from the diffusion signal at the voxel level.

Free Water Imaging

As discussed previously, isotropic CSF signal can be thought of as ‘contaminating’ the anisotropic signal from single axonal fibers. This effect reduces FA and makes the true

directionality of the underlying WM fibers more difficult to discern. In an attempt to reduce this effect, Paskternak et al.,[24] designed a bi-tensor model of diffusion (Eq. 5) including two compartments (C), a tissue compartment composed of a variably shaped tensor (C_{tissue}), and a free water compartment composed of an isotropic tensor of fixed diameter (C_{water}):

$$(5)\ A_{bi-tensor}(D,f) = C_{tissue} + C_{water} = fA_{tissue}(D) + (1-f)A_{water}$$

Where the attenuated diffusion signal A , composed of the signal from brain tissue and free water, is described by the tissue tensor D modulated by the tissue volume fraction f[24].This equation is then solved for the tensor D and tissue volume fraction f that minimizes the difference from the observed signal using a linear least squares metric. This outcome of implementing this model was both an improvement to WM fiber tracking by increasing the FA of tissue voxels (demonstrated via tracking the connection between the hippocampus and fornix), and the successful delineation of edema from the solid tissue components of a malignant meningioma[24].

While this method was initially termed Free Water Elimination, relating to the improvement of WM tractography once the contaminating free water signal was detected and eliminated (Figure 4), it was quickly realized that the volume fraction of free water itself could serve as a useful biomarker for brain tissue integrity. This model assumes that altered fractions of freely diffusing water present in areas of brain tissue results from a change in the cohesiveness of brain tissue, allowing CSF to infiltrate into spatial areas previously occupied by cellular boundaries. If the cellular membranes are removed, either through cell death or a non-specified increase in permeability, the volume of water molecules present will present a signal profile more alike to unrestricted diffusion[61].

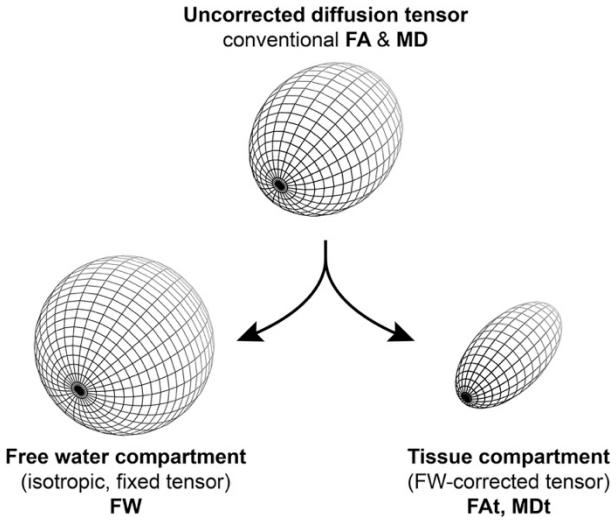

Figure 4: Visual demonstration of the application of the Pasternak (2009) bi-tensor Free Water Elimination model to an acquired uncorrected diffusion signal. This free water-corrected, tissue compartment tensor, has an increased fractional anisotropy (FA) and a decreased mean diffusivity (MD) compared to the original, uncorrected signal. Figure adapted from Duering et al.,[62].

Free water volume fraction was examined in the context of Parkinsonism as a potential non-invasive biomarker for disease progression[7,25,63,64]These studies specifically examined the free water content in the posterior substantia nigra, a region containing dopaminergic neurons known to degenerate severely in Parkinson's disease[65,66]. By making use of the publicly available Parkinson's Progression Marker Initiative longitudinal cohort[67] as well as data from a local population, Ofori et al.[25] found that free water was significantly increased in the posterior substantia nigra in patients with Parkinson's disease compared to controls. The level of free water in the posterior substantia nigra was then found to increase in patients with Parkinson's disease when followed longitudinally over one to four years while controls showed no significant change[7,63]. Additionally, the initial level of free water, and subsequent increase in the amount of free water, correlated with several symptom severity measures such as the Montreal Cognitive Assessment[7,68], and the Hoehn & Yahr movement scale[63,69].

It should also be noted that a study using the same publicly available cohort to analyze the substantia nigra using traditional FA measures, mean diffusivity, and radial diffusivity, and was unable to find a difference between subjects diagnosed with Parkinson's and healthy

controls[70], demonstrating the potential value of free water infiltration. The importance of free water infiltration was additionally demonstrated by Duering et al.,[62] who found that changes in FA and mean diffusivity found in the WM of patients with small vessel disease were driven by changes in FW volume fraction and not by changes in the WM itself.

A number of publications have also examined free water volume fraction and found altered volume fraction, or altered WM measures following free water elimination; in the context of schizophrenia[71–76] depression[77], bipolar disorder[78], and mild traumatic brain injury[79].

Criticism of Tensor-derived Free Water Imaging

The method described by Pasternak et al,[24] has been valuable for demonstrating the usefulness of freely diffusing water in a neurobiological context, however beyond the shortcomings inherent to tensor-based methods that have been discussed earlier in this review, the method by which freely diffusing water is modeled is not valid in all cases. Additionally, the construction of the bi-tensor model of brain tissue can suffer from misidentification of tissue compartment due to an overly stringent classification of freely diffusing water. This misidentification results in the assigned compartments' flipping classification, and the freely varying tissue tensor instead describing the signal from CSF. This leads to an obviously visible artifact in areas of high free water volume fraction (Figure 5) and is likely a major contributor to the finding that the accuracy of free water measurements can vary considerably (reproducibility error ranged from 5.2% (±3.6%, S.D.) - 18.2% (±11.6%, S.D.) across ROIs in a test-retest cohort) with the highest degrees of variability found in the superior fronto-occipital fasciculus and the uncinate fasciculus[80]. High variablility was also found in larger regions like the middle cerebellar peduncle (5.5% (±5.1%, S.D.). The heterogenous WM geometry of these regions may be playing a role in this variability (they have many fanning and curved WM tracts, respectively[81]), but for a measure that purports to quantify a directionless, isotropic phenomena it is concerning.

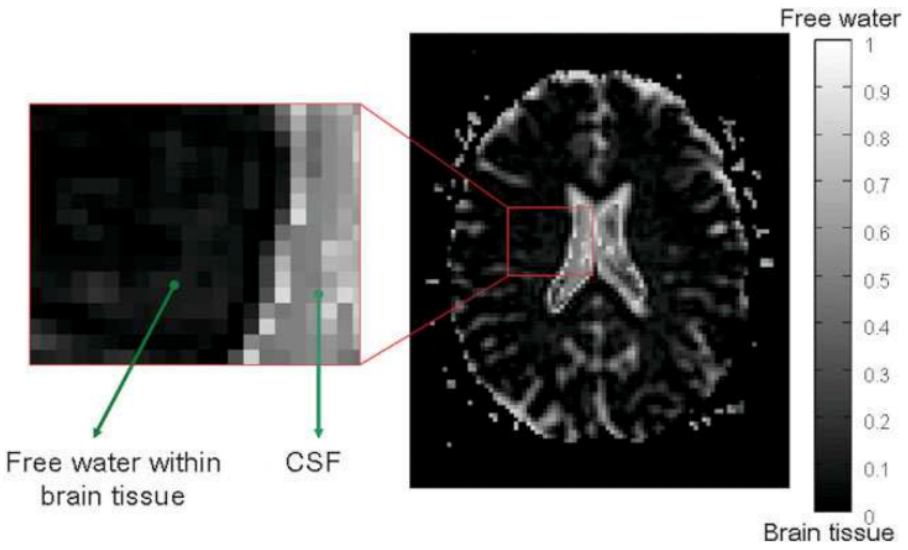

Figure 5: Image demonstrating the variability in free water volume fraction, particularly in the ventricles. The high voxel to voxel variation suggests that the CSF present is not meeting the exact classification of free water used in the algorithm, rather than there being pockets of tissue present within the ventricles of a healthy control subject. Figure adapted from Pasternak et al.,[24].

The primary reason for this occurrence likely results from the overly stringent definition of freely diffusing water hard coded into the free water elimination algorithm. Pasternak et al.,[24] states that the attenuated diffusion signal for tissue ($A_{tissue}(D)$, Eq. 5) should be equal to the definition of a tensor (Eq. 6) taken from Pierpaoli & Basser[3]:

$$[A_{tissue}(D)]_k = \exp(-b\, q_k^T\, D\, q_k) \quad (6)$$

Where k represents the k'th gradient direction, b represents the b-value, q^T represents the obtained orientation matrix and q represents the identity matrix used to reorient the tensor to align the maximum eigenvalue. Based on this equation, Pasternak et al.,[24] modified the A_{water} representation to evaluate isotopically diffusing water, since the magnitude of unrestricted freely diffusing water molecules should, on average, be equal in all directions. This allows for the removal of the eigenvector terms and for the holding of each eigenvalue equal ($\lambda_1 = \lambda_2 = \lambda_3$) (Eq.7) resulting in a much more computationally simple equation:

$$[A_{water}]_k = \exp(-b\, d) \quad (7)$$

Where b is the b-value and d represents a single, isotropic diffusion coefficient. Pasternak et al.,[24] sets the diffusion coefficient to 3 x 10^{-3} mm^2/s, which is the diffusion self-coefficient of water at 37^0 C. This was the division between CSF water and tissue proposed in bi-tensor model that briefly appeared in an abstract written by Pierpaoli & Jones[82]. That model had two independently varying tensors, one to capture CSF contamination and one to capture tissue, with the division between the information represented by the tensors being the fixed magnitude.

This simple, fixed diffusion coefficient follows Einstein's[18] equation (Eq. 1) which, when mathematical constants are removed, only has two variables that contribute toward variation in diffusion coefficient: temperature and viscosity. Viscosity itself, is dependent on pressure and temperature (Figure 5) as shown by classical physics experiments[83]. It has also been found that intracranial pressure varies in different parts of the brain (Figure 6) by insertion of a catheter into a patient[84]. This experiment showed that pressure can vary between a maximum of 190 mm. water to a minimum of -15 mm. water relative to atmospheric pressure across different microenvironments of the brain (Figure 6b). This is relatively mild compared to the full measured curves of possible viscosity, but this may drive the diffusion coefficient of water in the brain away from the stringent 3 x 10^{-3} mm^2/s fixed isotropic water tensor.

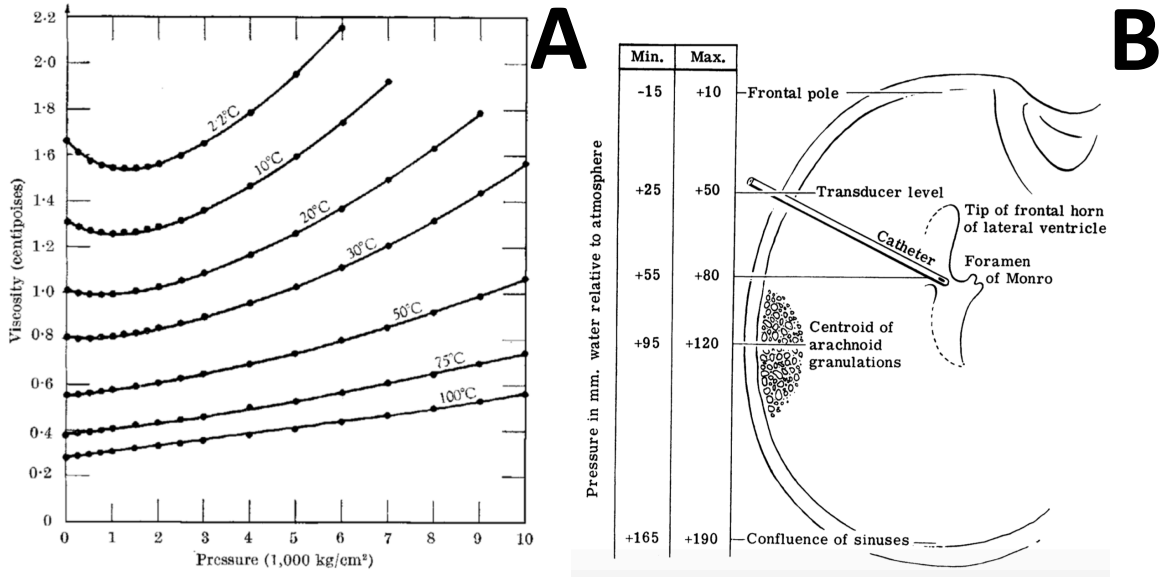

Figure 6: (A) Plot demonstrating the relationship between temperature, pressure and viscosity for water. Note that the intracranial pressure due to CSF sits at around 1,000 kg/cm² [84]. Figure adapted from Bett & Cappi[83]. (B) Diagram showing the pressure as mm. of water relative to atmosphere determined by catheter insertion into in-vivo human brain. Figure adapted from Bradley[84]. To relate the deviation from atmosphere in panel B to the chart in panel A, 100 mm. water is equivalent to 0.01 kg/cm², while 1 atm is equivalent to ~1033 kg/cm².

The other component of Einstein's self-diffusion equation (Eq. 1) that varies enough to affect the output is the temperature. Pasternak et al.,[24] assume the self-diffusion coefficient to be the assigned value at the standard human body temperature of 37°. This has been found to be both fairly variable (34.9°C to 37.1°C (median 36.5°C)) between individuals using in-vivo MR thermometry measurements of the brain[85]. These variations in temperature add variation to the actual self-diffusion coefficient of water that is attempted to be fit by the model. These variations have been known for some time, with CSF diffusion coefficient measured in-vivo in one experiment to be 2.5 x 10^{-3} mm^2/s in a healthy control and was then measured to be 3.5 x 10^{-3} mm^2/s in a patient with hypertension[86].

Given these variations, the free water elimination model remains relatively robust because the tissue signal in WM tends to be sufficiently anisotropic that the linear least squares equation that solves for f (Eq. 5) will settle on a best fit that approximates the direction of tissue. However, the greatest issue for the model comes when the isotropic free water volume fraction approaches a majority of the voxel. If the free water self-diffusion coefficient is not close enough to a magnitude of 3 x 10^{-3} mm^2/s then the best fit is to use the variable tissue tensor to fit the freely diffusing water as is visible in Figure 5. The issue is not necessarily in fitting a single value to every water diffusivity, it is that if it is not exactly fitted, the freely varying tensor may incorporate this less than ideal free water diffusion signal to minimize the overall linear least squares equation. It is also important that the f term is used to account for both tissue and water volume fractions, this results in a model that potentially encourages pushing the f term closer to 1 if the difference between actual free water self-diffusion and the fixed isotropic tensor contributes more error than can be made up by warping the tissue tensor.

These issues collectively cause a large degree of test-retest error. The single reliability study published, Albi et al.,[80] looked specifically at WM tracts, which theoretically, where a model like free water elimination should be free from interference by isotropic GM signal.

However as mentioned previously, this still did not lead to good reproducibility in free water volume fraction. This suggests that there is room to develop a new method of quantifying brain structure from diffusion imaging that is more reliable, more adaptable to heterogeneous tissue signal profiles, and can separate the isotropic CSF and GM tissues.

Constrained Spherical Deconvolution

First developed as a model-free way to describe the direction and degree of diffusion across a sphere using spherical harmonics[9], Constrained Spherial Deconvolution (CSD) has seen success in providing detailed quantitative information regarding the signal from diffusing water obtained from HARDI protocols[11,87]. CSD uses a theoretically infinite number of spherical harmonics to describe the observed signal, allowing for detailed representation of the observed diffusion signal far beyond what is achievable with traditional tensor-based methods (Figure 7). The spherical harmonic series that describes the observed signal has an order directly related to the number of non-collinear gradient directions collected from the scanner sequence[10]. In order to relate this signal representation to the underlying tissue microarchitecture, we can posit the observed signal as the convolution of a response function, a unique prototypical diffusion profile from a category of tissue, and the fiber orientation distribution (FOD), how the set of response functions are oriented to compose the observed signal. The FOD is crucial for the determination of white matter fiber tract orientation, in which myelin sheaths impermeable to water impose a directionality on molecular diffusion within the axon. The orientation of the response function is not obviously not required for tissues with isotropically diffusing profiles, however the amplitude of the observed isotropic signal varies across b-value shells due to the inherent properties of the tissue[10]. This both aids in discrimination between the sources of isotropic signal as well as reduces the isotropic signal compartments to a scalar signal fraction.

Dhollander et al.,[88] developed a means of selecting response functions from three different tissue compartments in the brain defined by the varying pattern of diffusion which appear to reflect commonly assumed divides in brain tissue: white matter (WM), grey matter (GM), and cerebrospinal fluid (CSF). By relying on exclusively the signal gained from the diffusion images, this algorithm involves calculating a signal decay metric (SDM), which

calculates the degree of signal intensity change between b-value shells in each voxel, Eq. (7)[89]. The SDM is additionally weighted toward shells containing more images in multi-shell data[88].

$$SDM = \ln\left(\frac{[\overline{b=0}]}{[\overline{DWI}]}\right) \tag{7}$$

This intensity decline is largest in voxels containing CSF, allowing for a quantitative means to identify voxels entirely or close-to-entirely composed of CSF, and thus obtain a CSF response function[88]. For WM, fractional anisotropy (FA) values were calculated across each voxel. CSD requires a single fiber response function in order to determine the contribution of WM to the observed signal. Thus, knowing voxels with a high degree of FA are likely composed of a single, identically oriented fiber population, the 0.5% of voxels with the highest FA values were selected to compose the WM response function. The GM response function was calculated by first separating out all voxels likely composed of WM via an FA threshold (0.2). The remaining voxels are additionally separated from CSF via the earlier described signal decay metric[88] at a point determined by an optimal thresholding algorithm that compares intensity values between shells[89]. Exemplar GM voxels are selected as the 2% of remaining voxels closest to the median SDM value.

These response functions are then used in multi-shell, multi-tissue, constrained spherical deconvolution (MSMT-CSD) as described in Jeurissen et al.,[10]. MSMT-CSD expands upon the linear least squares CSD equation to include matrix terms for each included tissue type and each b-value shell at each voxel as well as imposing a non-negativity constraint as a soft regularizer to relate the relationship between the spherical harmonic representation and signal amplitude[10,11,87]. Eq. (8) displays this function for the FOD coefficients f in n tissue types, across i shells related to the observed signal m.

$$\begin{bmatrix} \hat{f}_1 \\ \vdots \\ \hat{f}_n \end{bmatrix} = \min_{\begin{bmatrix} f_1 \\ \vdots \\ f_n \end{bmatrix}} \left\| \begin{bmatrix} H_{1,1} & \cdots & H_{1,n} \\ \vdots & \ddots & \vdots \\ H_{i,1} & \cdots & H_{i,n} \end{bmatrix} \begin{bmatrix} f_1 \\ \vdots \\ f_n \end{bmatrix} - \begin{bmatrix} m_1 \\ \vdots \\ m_i \end{bmatrix} \right\|^2 + \lambda \left\| \begin{bmatrix} A_1 & 0 & 0 \\ 0 & \ddots & 0 \\ 0 & 0 & A_n \end{bmatrix} \begin{bmatrix} f_1 \\ \vdots \\ f_n \end{bmatrix} \right\|^2_{-} \tag{8}$$

The presence of a term to relate the amplitude of the observed signal A to the coefficients generally provides for positive FOD coefficients. However, this imposes a limitation on the algorithm used to solve the CSD equation: if there are less than 2 non-zero b-value shells present in the diffusion data, the cost function inherent to the algorithm will assign a value close to 0 to the GM compartment. This has recently been overcome using an iterative approach developed by Dhollander & Connelly,[90] where MSMT-CSD is applied on 2 tissue types at a time, utilizing a specialized optimizer to alternate between estimations of WM-GM and GM-CSF with the third tissue compartment successively acting as a constraint. This method has been termed Single-Shell 3-Tissue (SS3T) and has been demonstrated to improve the analysis of single-shell diffusion data to a level comparable to that of multi-shell data when the highest shell b-value is equivalent[90,91].

3-Tissue Constrained Spherical Deconvolution

Solving the above equation (Eq. 8) for a single set of response functions provides a coefficient matrix $[f_1]$ - $[f_n]$ which, following summing all present tissue coefficients to 1, can be understood as the fraction of the total signal observed in each voxel arising from either the WM-, GM-, or CSF-like compartments (Figure 7).These signal fractions are potentially of great biological interest, as the fraction of signal arising from each tissue compartment could be used to infer differences in the underlying microarchitectural arrangement of brain tissue[92]. This has been utilized to examine tissue changes in WM in patients diagnosed with Alzheimer's disease and presenting with WM hyperintensities, finding that the tissue signal fraction from CSF was significantly elevated in periventricular WM hyperintensities compared with healthy WM. Additionally, it was found that within WM hyperintensities that appeared homogenous on MR images obtained with a FLAIR sequence displayed a heterogenous distribution of tissue types within them[91]. This illustrates a particular strength of the scalar signal fractions derived from MSMT-CSD: because the measure is calculated on a voxel-wise basis it can be used to evaluate tissue properties in a quantifiable manner between or within ROIs[91,92].

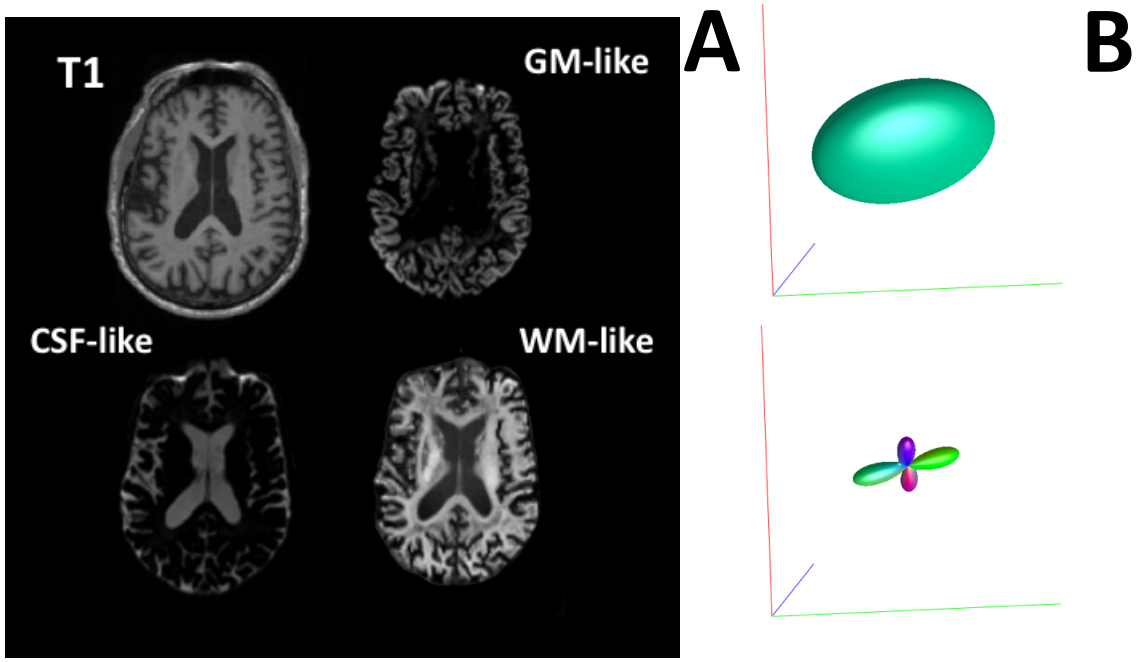

Figure 7: (A) Representative axial images of a T1-weighted MPRAGE and the GM-, CSF-, and WM-like tissue compartments derived from the diffusion weighted images of a single subject using 3-tissue constrained spherical deconvolution. This represents an improvement over discriminate assignment of T1-weighted voxels to a single tissue type based on gross intensity[93] because the sub-voxel contributions of each tissue type are represented in each voxel. (B) Example difference between a tensor representation (top) and a spherical harmonic FOD from 3T-CSD (bottom) taken from the same voxel in the frontal lobe of a healthy control subject (unpublished data). Note the additional direction present in the FOD that is not present in the tensor indicating the presence of a crossing WM fiber.

CSD-derived 3-tissue compartments are a promising, noninvasive method for exploring tissue composition in the brain. The utilization of state-of-the-art CSD approaches toward analyzing tissue composition should hold advantages over tensor-based methods such as Free Water Elimination[24] which suffers from unreliable estimates (reproducibility error ranged from 5.2-18.2% across ROIs in a test-retest cohort) for the free water volume fraction equivalent of the CSF compartment[80]. Additionally, MSMT-CSD is able to evaluate signal contribution from 3 tissue compartments, providing more depth and detail for evaluating brain tissue microarchitecture. With the advances provided in SS3T, it is also able to provide signal contribution from the full 3 tissue compartments using data with only one non b0-shell, allowing for a broader range of input data compared to other 3 tissue compartment models such as NODDI[58]. In a recent review of microstructural diffusion imaging applied to psychiatric

disorders, Pasternak et al.,[8] illustrated the acquisition sequence complexity compared to the number of microstructure compartments evaluated for several common dMRI analysis techniques. Addition of SS3T and MSMT-CSD clearly demonstrate the wide range of applicable data suitable for analysis as well as the full range of compartmental information available as output compared to other techniques (Figure 8).

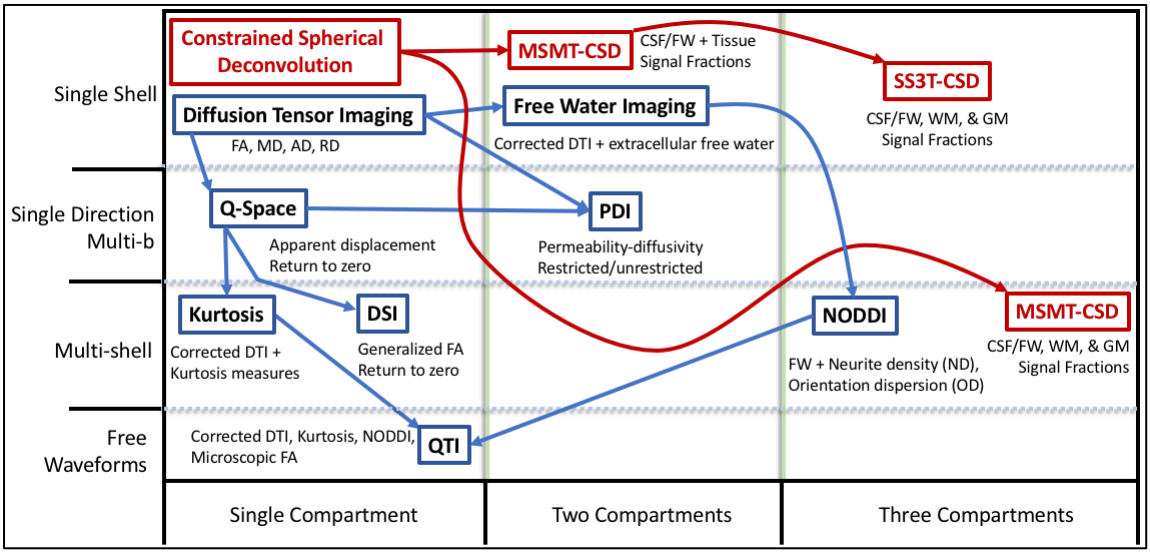

Figure 8: Chart adapted from Pasternak et al.,[8]; comparison of common DTI metrics to CSD derived quantitative signal fraction by complexity of acquisition (y-axis, acquisitions become more complex as they descend) and number of output compartments analyzed (x-axis, more compartments are analyzed toward the right). Methods derived from DTI follow blue lines, while methods derived from CSD have been added to the original image in red. MSMT-CSD is suitable with either single or multi-shell diffusion data for obtaining 2 or 3 tissue compartments, respectively[10]. When performed iteratively as part of SS3T-CSD, all 3 tissue compartments can be obtained using single shell data[90]. This demonstrates the potential utility of CSD derived methods to quantitatively measure data from multiple tissue compartments in commonly available diffusion sequences.

For each subject, the FOD were intensity normalized in the log-domain so that the summed density of the three compartments averaged $\sqrt{1/(4\pi)}$. This had the additional benefit of removing residual bias field effects[94]. Each subject's three FOD compartments were then summed to equal 1 in order to generate the final tissue signal fraction maps. For any averages of the CSF-like compartment our lab first sums in native subject space the tissue compartments from GM- and WM-like tissue in order to generate a tissue signal fraction. We then threshold

that tissue signal fraction at 50% in analyze the CSF-like signal in the voxels that remain. This is performed in order to remove global effects from the size of the ventricles and subarachnoid space, and to specifically examine the CSF-like tissue compartment that has infiltrated the tissue of the brain.

Criticism of CSD

The primary criticisms of CSD-based analysis in regards to accuracy (there has also been considerable criticism of analysis time, especially early after CSD was introduced, but these criticisms have been greatly reduced with the proliferation of faster computing) is that CSD can be overly sensitive to directional noise. One particular area of concern has been noted as the generation of 'false-fibers' on tracking algorithms due to spurious fODF peaks[95–97]. While some studies using recent methodological improvements in both CSD, as well as validation using simulations or histology, have suggested that the prevalence of false-fibers in CSD is oversold compared to other methods[98,99]. In our lab's reliability study 3T-CSD demonstrated excellent reliability across all compartments, suggesting that if false-fibers are present, they are not a large enough component of the overall signal in each voxel to introduce significant amounts of noise[100]. Additionally, by evaluating each compartment as a simple scalar value, errors in directional fiber orientation are negated.

Additional criticisms have focused on the use of a single response function to represent entire classes of tissue that may be quite heterogeneous in structure. Though similar to criticisms of the free water elimination method already discussed, CSD allows for variation in the magnitude of signal from each compartment, as well as changing magnitudes across b-value shells for better identification and matching of signal patterns. The lack of a spatially variable compartment ensures that all signal is assigned into the compartment that best matches the pattern established by the response function. As demonstrated by Pietsch et al.,[101] additional subtypes of response function can be utilized to discriminate between heterogeneous tissue sub-types, for instance two classes of WM in that example. The use of the selection algorithm from Dhollander et al.,[88] allows the response functions to be obtained directly from the diffusion image being analyzed, allowing for flexibility with different subject populations or acquisition

parameters. These advances allow 3T-CSD to be flexible to different datasets and applications while maintaining robust and reproducible analysis[100].

Preprocessing of Images

The following preprocessing steps have been implemented in our lab's pipeline for performing 3-tissue CSD. These correct for both common sources of error present in all MR imaging modalities (such as subject motion and susceptibility distortions) as well as sources of error with unique properties regarding diffusion imaging (such as the relationship between non-colinear gradient directions and eddy currents). These preprocessing steps are largely similar with those in other recently published works[101,102] and all of these algorithms are implemented using the software packages MRtrix[103] and FSL[104,105], both of which are free to use and installable on any Unix capable computer.

Denoising

Due to the relatively long gradient application time inherent in diffusion imaging sequences[17], images suffer from loss of signal due to intrinsic factors such as T2 decay and thermal fluctuations. This results in a low signal to noise ratio, making noise correction essential[106]. Due to the intrinsic nature of the noise being largely built into the sequence itself, it becomes necessary to perform a denoising step post-acquisition. Images were denoised using a Marchenko-Pastur distribution based principal component analysis technique that suppresses the effect of signal fluctuations[107].

Gibbs Ring Removal

Diffusion imaging, like most MR imaging modalities, is reconstructed from a spatial frequency domain referred to as k-space. This space is sampled in a regulated way during signal acquisition and is then reconstructed using a Fourier transform[108]. There is an inherent conflict between the sinc-function that composes the Fourier transform and the step-wise magnetic field gradients applied in diffusion imaging[17]. The oscillation pattern of the function can over- or

under- shoot the edges of the stepwise function, depending on the truncation of k-space[109]. Gibbs rings can be removed by reinterpolating the image to sample at different, zero-crossing points, of the intersection between the oscillating sinc-function performed by the Fourier transform and the stepwise function[109].

Susceptibility Distortion, Eddy Currents, and Subject Motion

These three separate sources of error are corrected in a single preprocessing function implemented by Andersson & Sotiropoulos[110] as the interplay between two components of FSL. Susceptibility distortions occur due to the presence of the subject within the magnetic field. Organic matter is non-ferrous in nature but can still interact with, and distort, the magnetic field by virtue of its own electromagnetic properties. These properties can differ between types of tissue, or at the boundaries between tissue and liquid or air-filled space[111]. These distortions can be significant enough to significantly alter image quality, including resulting tractography[112]. Eddy currents are caused by application of magnetic field gradients. Diffusion imaging applies magnetic field gradient pulses in larger magnitude and for a greater duration than other MR imaging modalities, making it particularly susceptible to eddy current induced image distortions[113].

Gross subject motion is a problem in every MR imaging technique, and dMRI is especially sensitive given that diffusion imaging is specifically designed to measure motion on the molecular scale. If motion does occur between gradient applications, the subject's head will need to be self-registered to the same spatial location between each gradient application. However, if the subject moves while the gradient is being applied, the resulting signal frequency will move outside the k-space frequency sampling range and no signal will be recorded[114]. This is referred to as signal dropout, and the best attempt should be made to re-run the sequence on the subject if severe information loss is observed during the scanning session. It is not uncommon though, to have a small number of gradient directions affected by movement, especially in certain subject populations such as young children or individuals with motion disorders.

Two FSL program commands, termed topup and eddy, together perform the necessary corrections for susceptibility distortion, eddy currents, and subject motion[104]. Topup reconstructs the off-resonance field by warping the non-colinear gradient directions to minimize differences via a sum-of-squares equation[115]. This information is used by eddy to correct for susceptibility distortions. Eddy however is also involved in the correction of eddy currents and subject movement, conveniently performing all of these actions within a single, simplified package[110]. At the heart of this tool is a Gaussian Process that models the diffusion signal according to the assumptions:

a. The signal from each direction should equal the signal from the inverse direction (i.e. the opposite phase-encoding direction).
b. Gradient directions along two vectors that have a small angle between them result in acquisitions that are more similar than vectors with a large angle between them.

This is used to create a predicted signal intensity at each voxel for each b-value shell acquired[110]. This predicted diffusion signal can then be used to replace erroneous voxels such as those affected by motion-induced signal dropout. Voxels that have suffered from total signal dropout due to motion can be detected by a simple test of signal intensity being below a set number of standard deviations from the mean [116].

Upsampling

The final preprocessing step prior to CSD-related analysis involves upsampling the diffusion images to a 'super-resolution' for higher image contrast and quality. In our lab we upsample all diffusion images to 1.3mm isotropic voxels as this has been recommended by the MRtrix team and performed by other research groups [102,117,118]. Brain masks were obtained for all subjects in the upsampled space by first converting the images for use in FSL and performing a recursive application of the Brain Extraction Tool [119,120]. This allowed for faster processing time and a restriction of all analysis to the brain tissue.

<u>Applications of 3-tissue CSD</u>

One of the first applications of 3T-CSD was performed by Dhollander et al.,[92] demonstrating the detection of white matter hyperintensities in Alzheimer's disease patients. This was work was expanded by Mito et al.,[121] which found that the white matter hyperintensities displayed different profiles of tissue depending on location. White mater hyperintensities proximal to the ventricles showed a higher level of freely diffusing water (CSF-like signal fraction) than white matter hyperintensities located in the deep white matter. In this context, 3T-CSD was able to both locate and characterize the hyperintense lesions in WM. Mito et al.,[91] went further to show that this same pattern held in healthy controls with white matter hyperintensities and that 3T-CSD could be used to show that the CSF-signal fraction increased in a distance dependent manner with distance from the ventricles.

Other areas of research performed by other groups include using 3T-CSD in developing newborns, to measure the progression of WM maturation in these neonates and to examine the change in CSF-like signal fraction throughout early adolescence[122]. Publications have also examined results from 3T-CSD in delineating tissue types in tumors. This is a particularly well-suited application as the output from 3T-CSD can be used to examine the extent of edema for example, and the areas of the brain affected, but also the spherical harmonic FODs generated can be used for tractography and thus surgical planning. 3T-CSD was able to perform this analysis even inside infiltrating gliomas[123].

Our lab has first focused on studying the reliability and stability of 3T-CSD to ensure that measurements derived from the signal fraction analysis are reliable enough to be useful in longitudinal studies as a quantitative biomarker and will not bias results when used in patient populations. This was evaluated using a test-retest design, and study measures in this work were evaluated over three separate cohorts of healthy control subjects. Two of these cohorts were collected by our lab as part of separate studies and one cohort was collected as a test-retest sample from a publicly available dataset: the enhanced Nathanial Kline Institude (eNKI), Rockland community study, part of the 1000 Functional Connectomes Project[124]. These cohorts differed in image quality (for example, the first two cohorts were multi-shell data, whereas the eNKI study was single shell), in time scale between baseline test and retest scan, and in subject

composition (i.e. one cohort included individuals with prior diagnoses that are known to cause changes in brain structure[125,126]). This gave the study a wide range of factors to test if reliability would be affected by common sources of variation in typical control cohorts. The wide range of timescales, from the same scanning session to a full 3 months between baseline and rescan, allowed for the evaluation of the stability of 3T-CSD derived measurements, a crucial component for long-term tracking of longitudinal cohorts. The results from our study are presented in Table 1:

Dataset	Tissue	Subjects	ICC	Pearson's Rho	p-value
Immediate rescan	CSF	59	0.9731	0.9636	<0.001
	WM	59	0.9868	0.9748	<0.001
	GM	59	0.9929	0.9868	<0.001
	LH	59	0.9578	0.9181	<0.001
	RH	59	0.9376	0.8915	<0.001
Short timescale (7-60 days)	CSF	20	0.9546	0.9281	<0.001
	WM	20	0.9692	0.9423	<0.001
	GM	20	0.9852	0.9700	<0.001
Long timescale (90 days)	CSF	52	0.9564	0.9364	<0.001
	WM	52	0.8157	0.7200	<0.001
	GM	52	0.8746	0.8024	<0.001

Table 1: Statistical analysis of the 3 test-retest cohorts in the experiment; p-values are calculated based on the Pearson's correlation. For the immediate rescan cohort the left hippocampus (LH) and right hippocampus (RH) were selected as ROIs and the CSF signal-fraction was measured to examine the reliability of 3-tissue CSD in subcortical structures as well as on the whole brain level. CSF levels within the ROI are analogous to Free Water volume fraction measurements that have been previously published to examine specific ROIs in pathological conditions[24,25]. This table was adapted from Newman et al.,[100].

Each of the measures showed excellent reliability as measured by intraclass correlation coefficients (ICC) and Pearson's correlation[100]. This was especially reliable in the immediate

rescan and short timescale cohorts as well as showing good reliability in the long timescale cohort. There was also excellent reliability in the CSF-like compartment within the bilateral hippocampus ROI while the measured average of CSF-like signal fraction showed an effect of laterality. When averaged across the entire cohort, the average left hippocampus had an average CSF-like signal fraction of 3.2% while the right had an average of 4.0%, (ANOVA, $F_{1,232}$=120.2, $p<0.001$). This demonstrates the potential of 3T-CSD to be sensitive enough to detect biologically relevant differences in brain tissue, while still being stable and reliable enough to confidently obtain measurements.

Future Directions

The formulation and development of the existing 3T-CSD pipeline has created a number of opportunities for evaluating free water from the CSF-like compartment, as well as the GM- and WM-like tissue signal fractions, in a number of contexts. A previous student has focused their research on performing grey matter density measurements on a number of ROIs in the brains of patients diagnosed with Parkinson's disease. This has attempted to find a radiological marker corresponding to the ascending spread hypothesis proposed by Braak et al.,[65]. We believe that 3T-CSD may be more sensitive to changes in brain microstructure than grey matter density due to our recent work comparing the two in a correlation with age related change[15]. We are currently investigating both a longitudinal and cross-sectional database of Parkinson's disease patients in order to investigate the feasibility of the CSF-like signal fraction as a biomarker for diagnosis and progression.

Additionally, corresponding to the work performed by Mito et al.,[91] our lab wishes to further pursue changes in undiagnosed 'healthy' aging and lifespan measures derived from 3T-CSD. We have begun investigating a subset of the Virginia Cognitive Aging Project, a diagnostically healthy aging cohort collected here at UVA. We have observed significant age-related changes in 3T-CSD signal fractions as well as correlations between CSF-like signal fraction across the whole brain and the cognitive trail marking task, a cognitive task known to correlate with neuronal degeneration[127]. Examining which ROIs signal fraction measurements

contribute most to performance on the cognitive tasks could identify areas of the brain either susceptible to CSF infiltration in aging or identify particularly vulnerable areas.

Our lab is also interested in the use of extremely large cohorts to examine the effect of mild traumatic brain injury (mTBI) on the developing brain. The Adolescent Brain Cognitive Development study (ABCD) represents the largest dataset of developing adolescents collected in North America[128]. This size, combined with the narrow age range and longitudinal follow up, provide a unique opportunity to apply novel methods such as 3T-CSD to investigate microstructural changes resulting from traditionally difficult to detect events, such as mTBI. We would predict that the CSF-like signal fraction would be altered in the presence of neuroinflammation or injury, potentially giving insight into the previously unknown effect of mTBI on developing adolescent brain microstructure.

A fourth direction concerns the investigation of microstructural changes in focus ultrasound (FUS) ablation of the thalamus to treat essential tremor[129]. This treatment technique has recently been adopted as a means to perform non-invasive surgical intervention on over-active thalamic neurons implicated in essential tremor. However, the surgery is not always completely successful and difficult targeting and evaluation challenges remain. It has been demonstrated that dMRI can be useful in determining if the FUS ablation damaged targeted WM tracts[130]. But a full microstructural characterization in humans of the cellular process underlying the surgery and lesion resolution has not occurred. 3T-CSD analysis could potentially track changes in the microstructure and determine why some surgical interventions do not permanently treat the condition, and potentially provide detailed information for prospective surgical planning.

Chapter 1

Development of 3-Tissue Constrained Spherical Deconvolution

Aim 1: Assess the reliably and reproducibly of 3T-CSD measurements of ICA, ICI, and ECI signal fractions as a means of quantifiably assessing brain cellular microstructure from diffusion MRI. It will be determined if 3T-CSD measurements are affected by image quality and scanning location, if measurements are biased by CSD algorithm selection, and if the underlying CSD model can be used to register images to stereotaxic space.

Rationale: Development of a novel dMRI method necessitates testing in a wide variety of cohorts and acquisitions to ensure observed effects are reliable, repeatable, and accurate. As there is no standard acquisition protocol for dMRI even within research or clinical domains it is important to evaluate the effects of acquisition parameters on 3T-CSD metrics and to optimize a protocol for future studies. Particularly crucial is the comparison between MSMT-CSD and SS3T-CSD for analyzing either multi-shell or single-shell data. As all dMRI acquisitions by definition must have at least one non-b=0 shell SS3T-CSD is always an available option for modeling. However there may be an advantage to including multiple non-b=0 shells to gain contrast between tissue types. Finally, as much of this work will involve comparisons between large cohorts, adequate cross-subject registration will be essential for brain parcellation and metric comparison. Both CSD methods generate extremely detailed fiber orientation distribution maps that may be superior for registration compared to intensity-based techniques.

Experimental Procedures: To meet this aim, several studies will be performed to assess various technical components of 3T-CSD analysis. These studies will establish which dMRI acquisition factors most influence 3T-CSD metrics, which CSD algorithm is optimal for distinguishing between anatomically variable regions, within-site reliability and longitudinal stability, between-site reliability, and assessment of a novel registration method to warp 3T-CSD maps to stereotaxic space:

Study 1a: The first step in any neuroimaging analysis is acquisition of the images. There is currently no established standard for parameters such as image resolution, b-value shell number, value of outer b-value shell, number of gradient directions, or voxel size/shape and it is unknown if the effect from different acquisition parameters present in the imaging sequence will be greater on 3T-CSD metrics than subject-specific demographic characteristics. This work will be useful both for clinical data collected without standardization, and for harmonization of data between imaging sites.

For this study we will utilize a large dataset collected from clinical sources Clinical diffusion MRI data were collected from 100 patients with medication-refractory symptoms of Parkinson's disease (PD) at the University of Virginia Hospital prior to the implantation of a deep brain stimulator electrode. These images were obtained with one of 27 different combinations of 8 separate acquisition parameters, however all datasets had a single non b=0 valued shell of b=1000s/mm. All subjects have documented demographic information including age, time since initial PD diagnosis, Total Movement Disorders Society, Unified Parkinson's Disease Rating Scale (MDS-UPDRS) scores, and Montreal Cognitive Assessment (MoCA) scores. Statistical analysis will be performed for the weighted average free water signal fractions in each ROI by creating linear models with each subject's acquisition parameters and demographic factors as predictor variables. Stepwise model selection by Akaike Information Criterion will be performed to create final models with predictors.

Study 1b: Investigate the utility of SS3T-CSD compared to MSMT-CSD for generating 3T-CSD results. SS3T-CSD is more flexible and can be applied to any dMRI dataset because it requires only a single non-b=0 shell. For a variety of reasons, both historical and clinical, many dMRI datasets have not been collected with multiple non-b=0 shells. To date though there has not been a comprehensive investigation into differences between the signal fractions obtained from either method. Because diffusion MRI data suitable for MSMT-CSD is also able to be analyzed by SS3T-CSD, it is possible to compare outputs of both methods from the same dataset (if it is multi-shell). In this work, we evaluate the ability of 3-tissue signal fractions from MSMT-CSD and SS3T-CSD in 7 hippocampal subregions to generate contrast between anatomically distinct brain areas. For reasons unique to each algorithmic approach, namely that MSMT-CSD weighs

each shell and tissue equally (Equation 2), it is expected that SS3T-CSD will generate better contrast between hippocampal subregions and be able to distinguish a unique microstructural profile from each while MSMT-CSD will be less successful.

Study 1c: Any robust and widely applicable neuroimaging metric must be reliable and ideally provides consistent measurements. Equally, if a longitudinal study is being performed comparing healthy cohorts to injured or developmentally distinct groups, then any healthy control group would ideally provide stable and consistent measurements. The reliability and long-term stability of 3T-CSD metrics have not yet been evaluated. This study will examine estimates of whole-brain microstructure for the three tissue compartments derived from 3T-CSD (ICA, ICI, and ECI), in three separate test-retest cohorts. Each cohort had different lengths of time between baseline and retest, ranging from within the same scanning session in the shortest interval to 3 months in the longest interval. Each cohort was also collected with different acquisition parameters. By comparing output 3T-CSD measurements using intraclass correlation coefficients, Pearson's correlations, and mean squared difference between images, we will be able to determine if the development pipeline and 3T-CSD are reliable and stable analysis tools appropriate for use in experimental cohorts.

Study 1d: In recent years a number of large neuroimaging studies have embraced a big data approach to allow the investigation of more nuanced factors influencing the brain. Studies such as the Adolescent Brain Cognitive Development (ABCD) study[128], Human Connectome Project[131], and UK Biobank[132] contain MRI data collected from thousands of subjects across multiple locations. Each study has attempted to harmonize acquisition sequences and data collection across sites, but differences in scanner setup and sometimes even manufacturer remain[133]. It is currently unknown how data from 3T-CSD signal fractions might vary from site specific factors. While Study 1c will establish same-site reliability if 3T-CSD is to be applied to data from large multi-site studies it is necessary to test inter-site reliability and compare it to same-site reliability. Fortunately, Tong et al.,[134] have created a publicly available dataset that will allow this study to be performed. Three subjects were scanned at 10 different sites, each equipped with the same scanner hardware and using the same sequence. The 3 subjects were then scanned in triplicate at the final site, creating 12 images per subject to test reliability between

locations[134]. This study will involve parcellation of the brain into 212 ROIs for detailed analysis of reliability across the brain and give insight for studies involving data collected from multiple locations.

Study 1e: One of the final processing steps in neuroimaging analysis involves parcellating the brain into regions of interest. Automated parcellation techniques are required for large-scale studies which potentially can involve thousands of subjects. Parcellation can be readily achieved through the registration of neuroimaging subjects to a common stereotaxic space. Images aligned with the stereotaxic space allows for comparisons between timepoints, subjects, or with reference atlases of regions of interest. Typically, this has been performed by computing a similarity metric between the voxel-wise intensity values in the subject image, and a reference image. Computing the FODs from either CSD method provides far more detailed voxel-wise information than a simple scalar intensity value. This allows for the potential to use this additional information to perform registration with added within-tissue contrast. In this study, I will adapt the NTU-DSI-122 diffusion spectrum template into a flexible platform for the registration of subject images into stereotaxic space from a number of other studies and cohorts [135]. The reliability and accuracy of this FOD-based registration method will be compared to a leading intensity-based registration method by registering 3T-CSD cellular microstructure maps from two separate cohorts to the NTU-DSI-122 template. Using Sorensen-Dice coefficients at multiple thresholds will measure the precise accuracy of the FOD-based registration method.

The studies performed In Chapter 1 will satisfy the goals of Specific Aim 1 and will establish a reproducible, reliable, and accurate 3T-CSD pipeline for use in future exploratory studies.

Study 1a

Title: Investigating the effect of diffusion MRI acquisition parameters on free water signal fraction estimates from 3-tissue CSD techniques

Synopsis: The CSF-like free water signal fraction is an advanced diffusion MRI metric representing the freely diffusing water in brain tissue. Different methods to calculate the free water signal fraction using constrained spherical deconvolution exist but it is still unknown how variation in data quality and acquisition affect measurements. Using a large clinical dataset with highly variable acquisition schemes, this study shows that the various acquisition parameters significantly affect outcome free water signal fraction, though the multi-shell analysis method is more susceptible than the single-shell method. This highlights the importance of harmonization and quality clinical imaging.

Main Findings

Free water signal fraction can be heavily affected by inconsistent imaging acquisition parameters. Examining the performance of two diffusion analysis algorithms suggests one may be more robust, but acquisition harmonization is essential.

Introduction

Free water signal fraction is an advanced diffusion MRI-derived measure of brain microstructure that can reliably measure the infiltration of freely diffusing water into brain tissue[100]. It is possible to obtain the free water signal fraction from either single-shell (SS3T-CSD)[90] or multi-shell (MSMT-CSD)[10] constrained spherical deconvolution methods. Data harmonization in diffusion MRI has been recently emphasized as a means to improve reliability and to minimize site and scanner effects[136–139]. Many clinical datasets however, are not collected using standardized protocols. It is necessary to assess the influence of changing acquisition parameters, especially on advanced diffusion analysis techniques, if there is a goal of eventual application in a clinical setting. Additionally, there are frequently unique clinical populations that are difficult to collect in a research setting. If retrospective analysis is to be performed on these

subjects the effect of different acquisitions must be determined. In this context the comparative robustness of different diffusion analysis techniques is important to consider. If the outcome of one technique is less dependent on input acquisition parameters, signal from an underlying pathology of interest may be easier to observe. In this work, we evaluate the dependence of MSMT-CSD and SS3T-CSD derived free water fractions on acquisition parameters.

Methods

Clinical diffusion MRI data were collected from 100 patients with medication-refractory symptoms of Parkinson's disease (PD) at the University of Virginia Hospital prior to the implantation of a deep brain stimulator electrode. These images were obtained with one of 27 different combinations of 8 separate acquisition parameters, however all datasets had a single non b=0 valued shell of b=1000s/mm^2. All subjects had documented demographic information including age, time since initial PD diagnosis, Total Movement Disorders Society, Unified Parkinson's Disease Rating Scale (MDS-UPDRS) scores, and Montreal Cognitive Assessment (MoCA) scores. The full list of acquisition parameters and ranges for all imaging and demographic factors are presented in Figure 1.

Predictor Variable	Range of Values (mean)	Factor Category
Voxel Height	3.0 – 6.0mm (4.85)	Acquisition
Voxel Volume	2.4 –19.8mm^3 (14.5)	Acquisition
Isometric Ratio of Voxel (1 is perfect cube)	0.57 – 0.91 (0.67)	Acquisition
In-plane Resolution	0.8 –3.8mm^2 (2.9)	Acquisition
Number of B0 Acquisitions	1 – 12 (3.5)	Acquisition
Number of Gradient Directions	38 – 120 (71.1)	Acquisition
Echo Time of Sequence (TE)	0.07 – 0.11ms (0.09)	Acquisition
Total Readout Time	0.04 – 0.11ms (0.06)	Acquisition
Subject Age	41.4 – 84.0 years (64.3)	Demographic
Subject Time Since PD Diagnosis	1.2 – 36.1 years (9.1)	Demographic
Subject Total MDS UPDRS Score	9.00 – 68.00 (34.98)	Demographic
Subject MoCA Score	11.00 – 30.00 (24.50)	Demographic

Figure 1: Table detailing the full list of imaging acquisition parameters and patient demographic factors, as well as the range of values and mean. Of the imaging acquisition

factors, there were 27 unique combinations of parameters from 100 patients with complete demographic data.

The diffusion data were analyzed using MSMT-CSD[10] in Mrtrix3[12] and SS3T-CSD[90] available in Mrtrix3Tissue (https://3tissue.github.io/), a fork of Mrtrix3. It should be noted that MSMT-CSD outputs only two compartments for these single-shell data: a white matter (WM) and a CSF compartment, the latter of which was used to calculate free water. Several preprocessing steps utilized FSL[105]. Diffusion images were denoised[107], corrected for Gibbs ringing[109], susceptibility distortions[104], motion[116], and eddy currents[110]. All images were then resampled to a voxel size of 1.3x1.3x1.3mm^3. Average response functions were generated for WM, grey matter (GM), and CSF from the images[88] and the fiber orientation distribution (FOD) calculated for each voxel[10,90]. Tissue signal fractions were calculated from the FODs in each cohort and the CSF-like tissue compartment was restricted to voxels where the majority of signal fraction was from a combination of the WM-like and GM-like compartments as a measurement of free water. All free water maps were transformed to MNI space via WM-FOD based registration of each subject's diffusion data to the diffusion template created by Hsu et al.[135]. In MNI space a weighted average was calculated for 27 ROIs from bilateral probabilistic cytoarchitectonic maps[140–142], free water signal fraction was additionally calculated across the whole brain parenchyma.

Statistical analysis was performed for the weighted average free water signal fractions in each ROI by creating linear models with each subject's acquisition parameters and demographic factors as predictor variables. Stepwise model selection by Akaike Information Criterion[143] was performed to create final models with predictors.

Results

A significantly predictive model was able to be constructed for the free water signal fraction in each ROI across all subjects. Adjusted R^2 ranged from 0.159 to 0.899 in the MSMT-CSD results (Figure 2) and from 0.122 to 0.891 in the SS3T-CSD results (Figure 3).

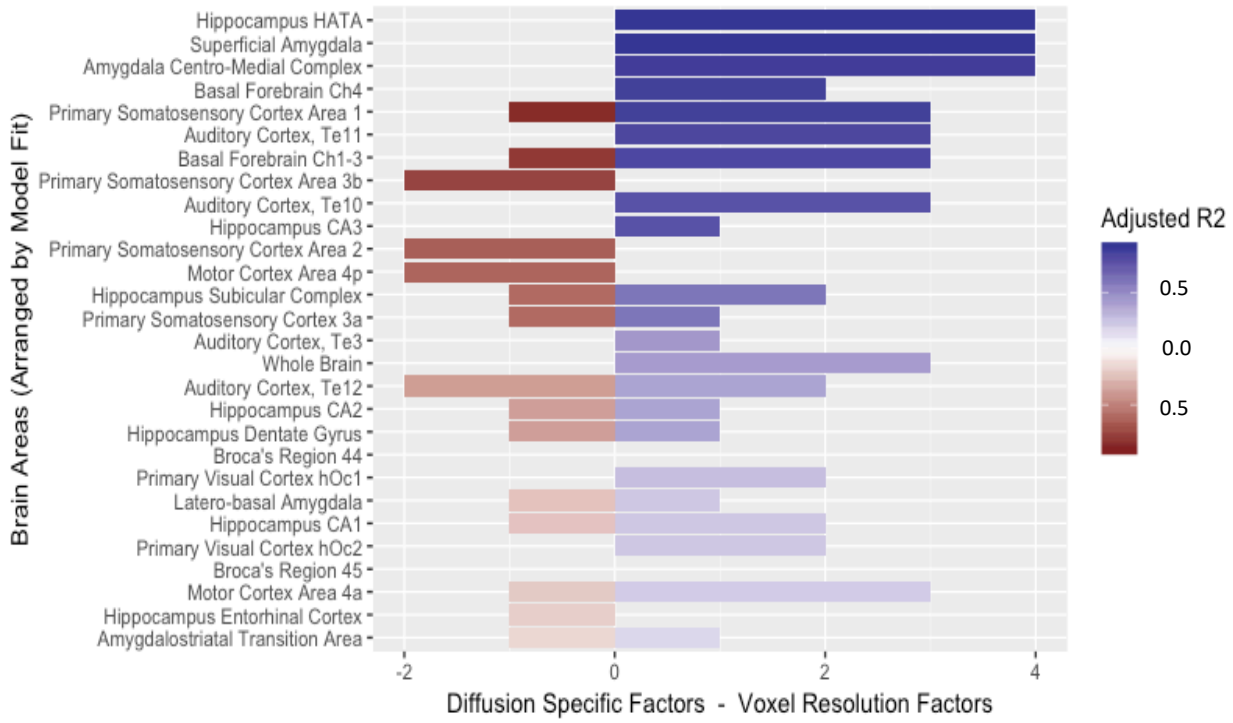

Figure 2: Illustrating the number of predictive factors from each category that was significant in the final linear model for each ROI derived from MSMT-CSD. ROIs are ordered by overall adjusted R^2 with best to worst fit proceeding top to bottom. Significant predictors that were directly related to the diffusion sequence are colored in red and predictors that are directly related to the voxel resolution are colored in blue.

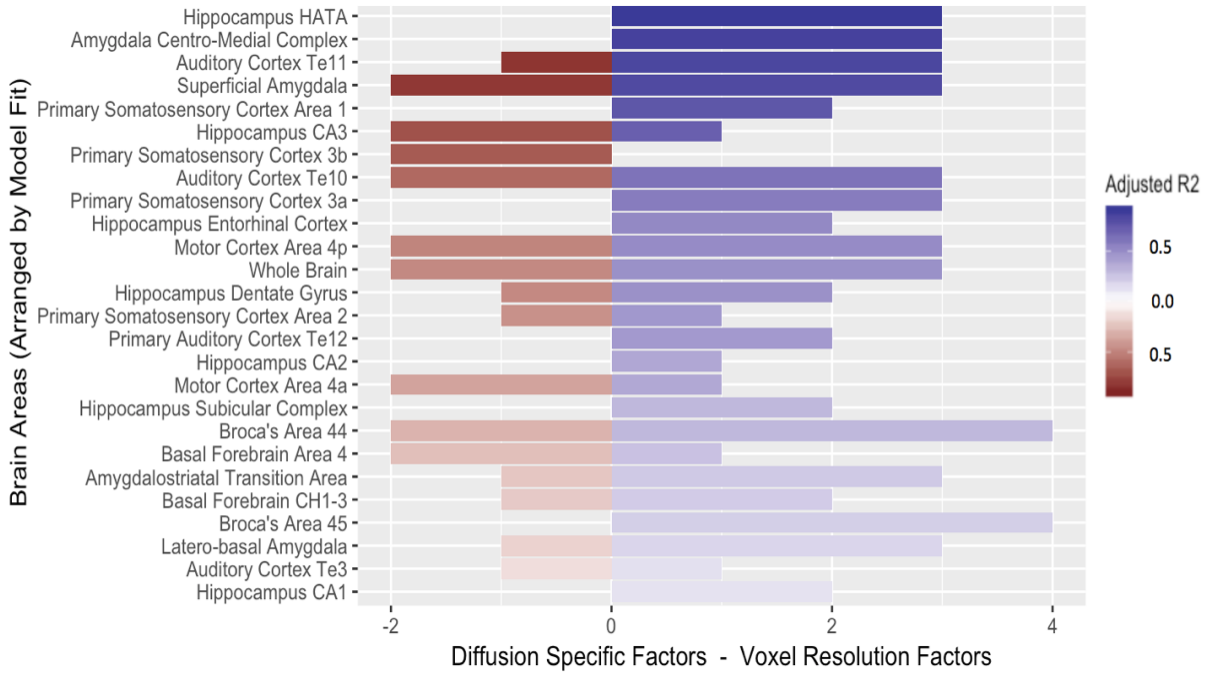

Figure 3: Illustrating the number of predictive factors from each category that was significant in the final linear model for each ROI derived from SS3T-CSD. ROIs are ordered by overall adjusted R^2 with best to worst fit proceeding top to bottom. Significant predictors that were directly related to the diffusion sequence are colored in red and predictors that are directly related to the voxel resolution are colored in blue.

There was a significant difference in average model fit, with the acquisition parameter and demographic models significantly less able to predict free water signal fraction derived from SS3T-CSD (mean adj-R^2 = 0.448) than MSMT-CSD (mean adj-R^2 = 0.530; ANOVA $F_{1,25}$ = 25.89, $p<0.001$). The most common significant predictor in the MSMT-CSD derived-measures was age but PD symptomatic scores did not significantly predict free water signal fraction. The in-plane resolution, number of b=0 images, isometric ratio of voxel size, and voxel volume significantly predicted the outcome measurement for all but three ROIs. In the SS3T-CSD models, the in-plane resolution was the most common significant predictor, followed by age, the isometric ratio, number of b0s, voxel volume, and number of gradient directions (Figure 4). There was a significant negative correlation between model goodness-of-fit and the size of the ROI from MSMT-CSD but this was not significant in SS3T-CSD (Figure 5), suggesting that free water in smaller ROIs were more dependent on different acquisition parameters.

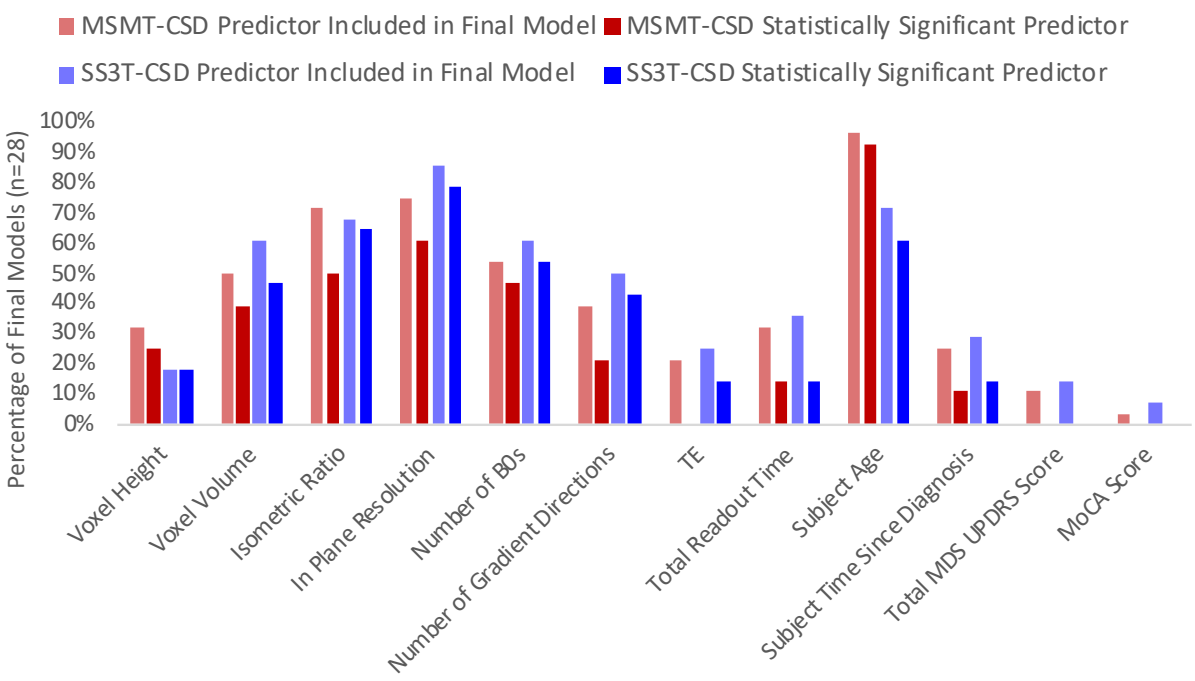

Figure 4: Illustration of the percent of final ROI models that included a specific predictor after stepwise AIC (light red for MSMT-CSD and light blue for SS3T-CSD) and the percent where that predictor was significantly predictive of free water signal fraction (dark red for MSMT-CSD and dark blue for SS3T-CSD).

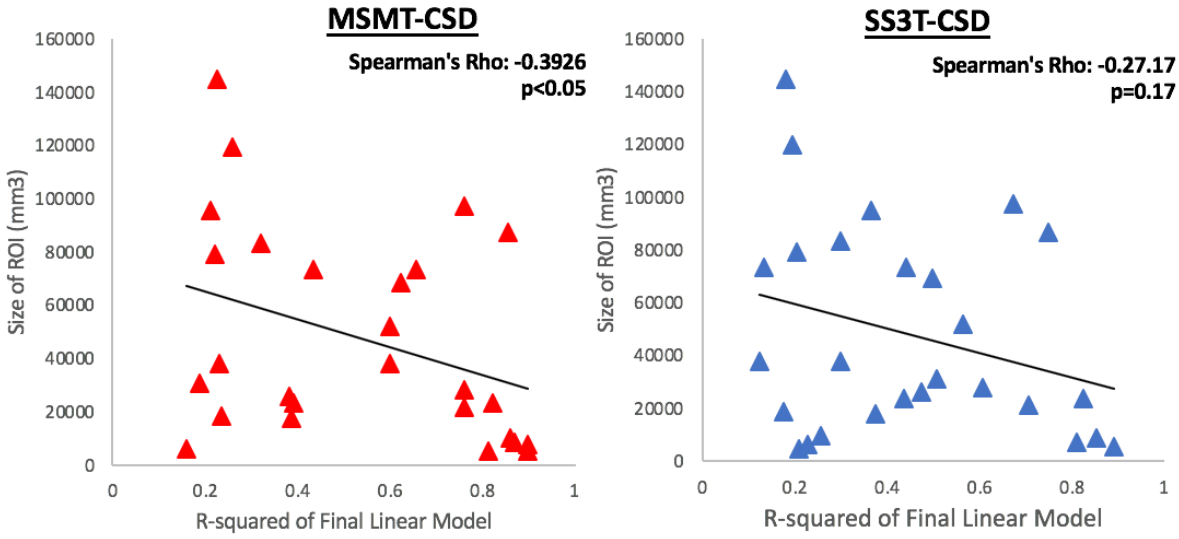

Figure 5: Correlation between R^2 of final linear model and the size of the ROI (as calculated by volume of unthresholded probabilistic map). There was a significant correlation between ROI size and goodness-of-fit in models of free water signal fraction calculated by MSMT-CSD, with smaller ROIs being more likely to have a better predicted model fit. This trend was present in the

free water signal fractions derived from SS3T-CSD but was less well correlated and not significant.

Conclusion

Free water signal fractions derived from MSMT-CSD and SS3T-CSD were both dependent on acquisition factors related to the selection of common imaging parameters. Further analysis suggests that SS3T-CSD is overall more robust and less affected. However, when employing these algorithms or collecting data, harmonization of imaging acquisition parameters is paramount in any case.

Study 1b

Title: Single-shell derived tissue signal fraction maps show increased contrast between hippocampal subfields compared to multi-shell analysis.

Synopsis: Recent advances in the analysis of diffusion MRI have allowed for the estimation of 3 tissue compartments in the brain from data with only a single non b=0 shell. There is currently no published quantitative comparison between signal fractions derived from either single- or multi-shell methods. Applying both single-shell analysis and multi-shell analysis to the same dataset shows high b-value single-shell analysis may increase contrast between different hippocampal subfields. While this effect may occur due to differences in microstructure between ROIs it should be a noted factor when applying either model and deserving of further study.

Main Findings

Single-shell and multi-shell derived signal fraction maps have significantly different results between hippocampal subregions. High b-value single-shell methods are significantly better able to discriminate between subregions by generating increased contrast.

Introduction

Quantitative 3-tissue signal fractions derived from constrained spherical deconvolution (CSD) based analysis of diffusion MRI are a recently developed means to assess tissue microstructure in the brain[90,91,100]. By measuring the relative contribution of white matter (WM), grey matter (GM), and CSF-like diffusion signals in each voxel, it is possible to both assess underlying tissue composition and improve WM tractography[91,123]. 3-tissue CSD was first performed using Multi-Shell, Multi-Tissue CSD (MSMT-CSD)[10], which requires a multi-shell diffusion acquisition scheme to successfully tease apart contributions from three tissue compartments[90]. However, a range of studies, for reasons both historical and clinical do not collect multi-shell diffusion data, and instead only acquire single-shell data.

To obtain the full benefits of 3-tissue CSD from single-shell data, an iterative CSD approach termed Single-Shell 3-Tissue CSD (SS3T-CSD)[90] was proposed. Both MSMT-CSD

and SS3T-CSD deconvolve 3 tissue response functions from the data, and both calculate a WM fiber orientation distribution (FOD) for use in either tractography or as part of 3-tissue signal fractions. To date though there has not been a comprehensive investigation into differences between the signal fractions obtained from either method. Because diffusion MRI data suitable for MSMT-CSD is also able to be analyzed by SS3T-CSD, it is possible to compare outputs of both methods from the same dataset (if it is mult-shell). In this work, we evaluate the ability of 3-tissue signal fractions from MSMT-CSD and SS3T-CSD in 7 hippocampal subregions to generate contrast between anatomically distinct brain areas.

Methods

MRI images were collected as part of a separate study[100] at the University of Virginia. 118 total diffusion images from healthy controls were acquired using a Siemens Prisma 3T scanner with an isotropic voxel size of $1.7\times1.7\times1.7mm^3$, TE=70ms and TR=2900ms; using a multi-shell protocol, 10 b=0 images and 64 gradient directions at both $b=1500s/mm^2$ and $b=3000s/mm^2$ were acquired. This multi-shell dataset was split into two single-shell subsets by retaining the b=0 images and extracting all diffusion images at either $b=1500s/mm^2$ or $b=3000s/mm^2$.

The multi-shell dataset was analyzed using MSMT-CSD[10] implemented in the open source software MRtrix[12]and the two single-shell datasets were analyzed using (SS3T-CSD)[90] as available in MRtrix3Tissue (https://3tissue.github.io/), a fork of MRtrix3. Several preprocessing steps utilized FSL[105]. Diffusion images were denoised[107], corrected for Gibbs ringing[109], susceptibility distortions[104], motion[116], and eddy currents[110]. Average response functions were generated for white matter (WM), grey matter (GM), and CSF from the images in each of the 3 image sets[88] and the fiber orientation distribution (FOD) calculated for each voxel[10,90]. 3-tissue signal fractions were calculated from the FODs[91].

In order to compare images across all datasets and subjects, a group average population template was constructed by non-linear, affine transformation and reorientation of the WM FODs generated by MSMT-CSD. The identical warps that transformed the subject images from native space to template space were then applied to each signal fraction map output from MSMT-CSD and SS3T-CSD, ensuring that each voxel moved identically with its partner from

each analysis group. A diffusion template generated to match MNI space[135] was then registered to the population template and cytoarchitectonic maps of 7 hippocampal subdivisions[140] (CA1, CA2, CA3, Dentate Gyrus, Entorhinal Cortex, and the Hippocampal-Amygdala Transition Area; all thresholded at 50% probability) were applied to calculate average signal fractions for each ROI.

Given that the higher b-value shell would be more likely be utilized in analysis, Kolmogorov–Smirnov tests with Bonferroni corrections were performed between MSMT-CSD and SS3T-CSD at b=3000s/mm^2 results from each hippocampal area from each tissue compartment. This calculation examined the discriminability between areas, if the signal fractions were sufficiently different to be drawn from a separate distribution it would indicate that the signal fraction analysis method would have sufficient contrast to discriminate between hippocampal subfields.

Results

There was a significant difference between each of the measured signal fractions across all subregions of the hippocampus depending on method (Figure 1 & 2), with the exception of the CSF signal fraction derived from MSMT-CSD and SS3T-CSD at b=1500s/mm^2 (T-test; p = 0.794).

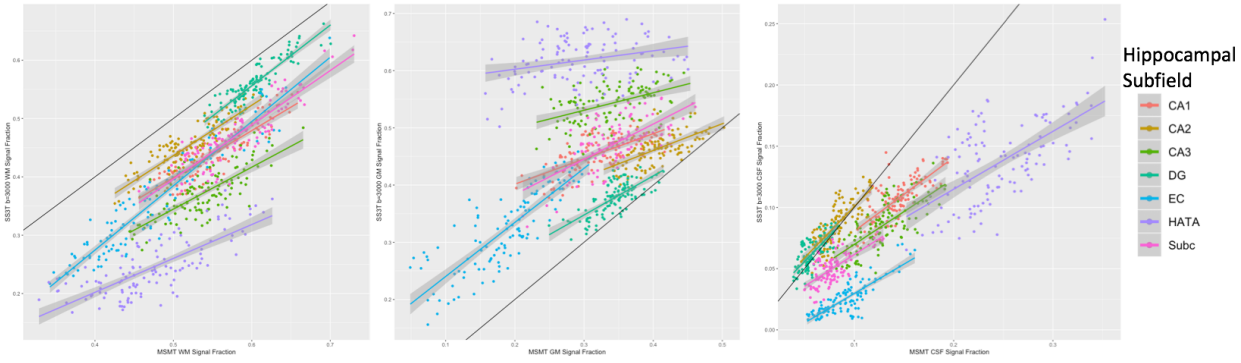

Figure 1: Comparison of signal fraction results derived from SS3T-CSD performed on only the B=3000s/mm^2 shell, with MSMT-CSD from the full multi-shell dataset. Tissue compartments are WM-like signal fraction, GM-like signal fraction, and CSF-like signal fraction from left to right. Gray areas are standard error.

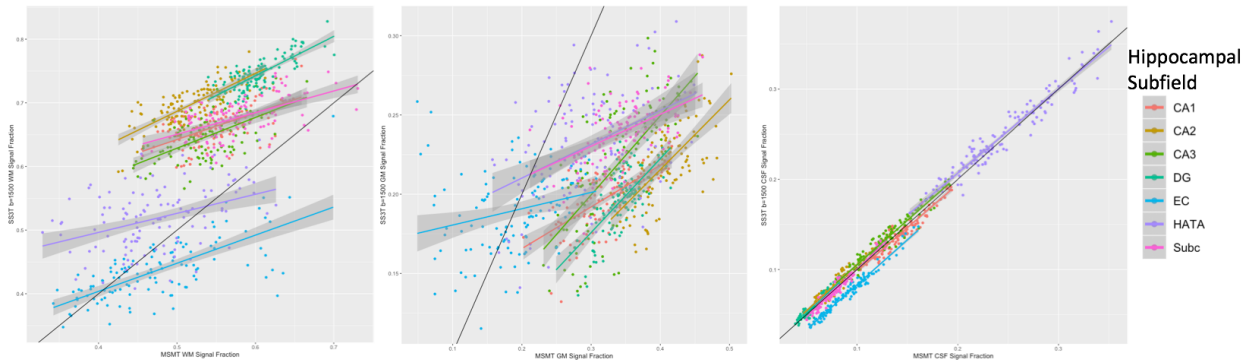

Figure 2: Comparison of signal fraction results derived from SS3T-CSD performed on only the B=1500s/mm² shell, with MSMT-CSD from the full multi-shell dataset. Tissue compartments are WM-like signal fraction, GM-like signal fraction, and CSF-like signal fraction from left to right. Gray areas are standard error.

In each of the signal fractions calculated from the diffusion MRI data, SS3T-CSD at b=3000s/mm² was able to successfully discriminate an individual distribution from 5 of the 7 hippocampal subareas examined. MSMT-CSD in contrast, was not able to discriminate an individual distribution from any of the WM-like signal fraction areas; 3 of the 7 GM-like subareas; and 5 of the 7 CSF-like signal fraction areas (Figure 3&4).

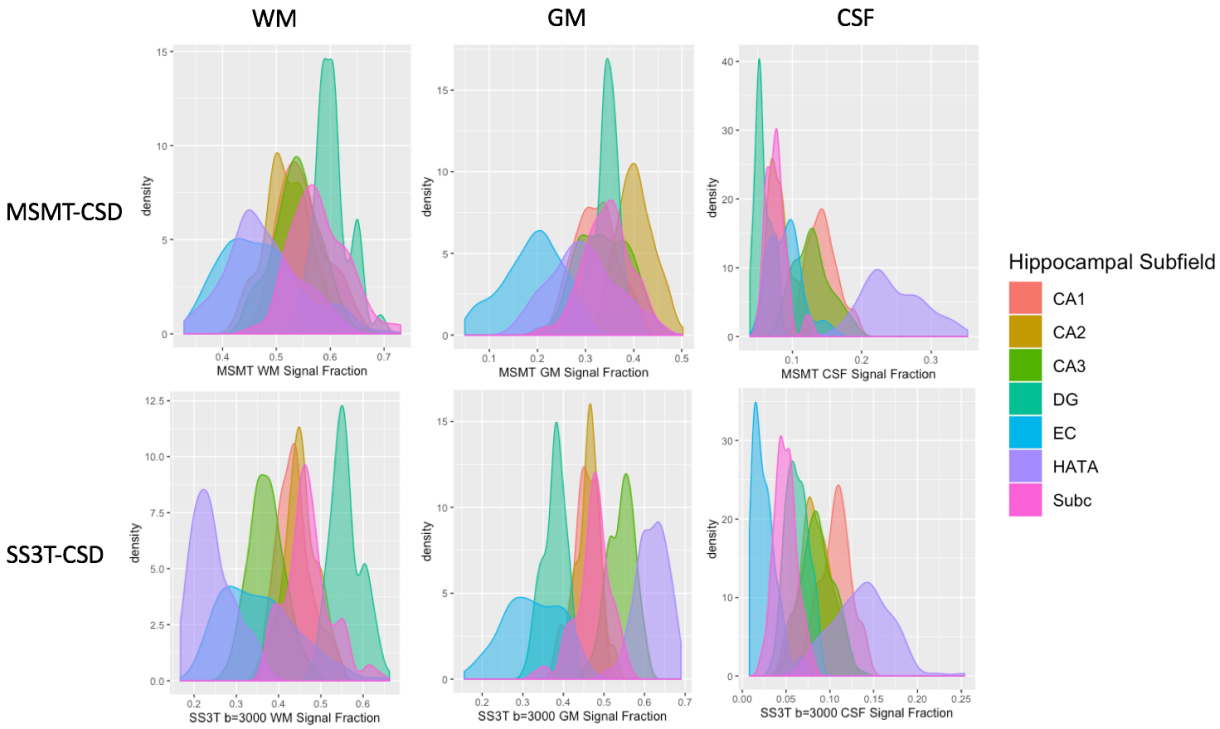

Figure 3: Density plots of signal fraction results from the three tissue compartments as calculated by MSMT-CSD (top row) and SS3T-CSD at b=3000s/mm² (bottom row).

Hippocampal ROI		MSMT-CSD			SS3T-CSD		
ROI Comparisons:		WM	GM	CSF	WM	GM	CSF
CA1	CA2	<0.01	<0.001	<0.001	<0.05	1.00	<0.001
CA1	CA3	1.00	0.137	<0.001	<0.001	<0.001	<0.001
CA1	Dentate Gyrus	<0.001	<0.001	<0.001	<0.001	<0.001	<0.001
CA1	Entorhinal Cortex	<0.001	<0.001	<0.001	<0.001	<0.001	<0.001
CA1	HATA	<0.001	<0.01	<0.001	<0.001	<0.001	<0.001
CA1	Subiculum	<0.01	<0.01	<0.001	<0.001	<0.05	<0.001
CA2	CA3	0.055	<0.001	<0.001	<0.001	<0.001	1.00
CA2	Dentate Gyrus	<0.001	<0.001	<0.001	<0.001	<0.001	<0.001
CA2	Entorhinal Cortex	<0.001	<0.001	<0.01	<0.001	<0.001	<0.001
CA2	HATA	<0.001	<0.001	<0.001	<0.001	<0.001	<0.001
CA2	Subiculum	<0.001	<0.001	0.475	0.319	<0.05	<0.001
CA3	Dentate Gyrus	<0.001	<0.05	<0.001	<0.001	<0.001	<0.001
CA3	Entorhinal Cortex	<0.001	<0.001	<0.001	<0.001	<0.001	<0.001
CA3	HATA	<0.001	<0.001	<0.001	<0.001	<0.001	<0.001
CA3	Subiculum	<0.001	1.00	<0.001	<0.001	<0.001	<0.001
Dentate Gyrus	Entorhinal Cortex	<0.001	<0.001	<0.001	<0.001	<0.001	<0.001
Dentate Gyrus	HATA	<0.001	<0.001	<0.001	<0.001	<0.001	<0.001
Dentate Gyrus	Subiculum	<0.001	1.00	<0.001	<0.001	<0.001	<0.001
Entorhinal Cortex	HATA	1.00	<0.001	<0.001	<0.001	<0.001	<0.001
Entorhinal Cortex	Subiculum	<0.001	<0.001	<0.001	<0.001	<0.001	<0.001
HATA	Subiculum	<0.001	<0.001	<0.001	<0.001	<0.001	<0.001

Figure 4: Table displaying the p-value results of Kolmogorov–Smirnov tests with Bonferroni corrections on distributions from each of the tissue compartments in each hippocampal subfield. Tests that did not find a significant difference between distributions are highlighted in red (indicating the contrast was not sufficient to discriminate between the two regions). MSMT-CSD had more overlapping distributions than SS3T-CSD at b=3000s/mm².

Conclusion

We found that SS3T-CSD reveals greater contrast between hippocampal subareas compared to MSMT-CSD, by relying on high b-value single-shell data. While this initially appears counterintuitive, that SS3T-CSD could generate better contrast while using *less* data than MSMT-CSD, there are two plausible overlapping reasons this may be the case. Most importantly, the middle shell may not contribute much unique signal to the deconvolution algorithm, and may actually be a substantial source of noise when weighed equally to signal from the higher b-value. Secondly, SS3T-CSD operates iteratively, and is thus able to perform several attempts at fitting WM response functions and separating CSF from GM response functions, each iteration clear of signal that has already been fit, and thus improving the overall ability to clearly separate tissue proportions in each different subarea.

Study 1c

Title**:** Test-retest reliability and long-term stability of 3-tissue constrained spherical deconvolution methods for analyzing diffusion MRI data

Abstract

Purpose: Several recent studies have utilized a 3-tissue constrained spherical deconvolution pipeline to obtain quantitative metrics of brain tissue microstructure from diffusion-weighted MRI data. The three tissue compartments, comprising white matter-, grey matter-, and CSF-like (free water) signals, are potentially useful in the evaluation of brain microstructure in a range of pathologies. However, the reliability and long-term stability of these metrics has not yet been evaluated.

Methods: This study examined estimates of whole brain microstructure for the three tissue compartments, in three separate test-retest cohorts. Each cohort has different lengths of time between baseline and retest, ranging from within the same scanning session in the shortest interval to three months in the longest interval. Each cohort was also collected with different acquisition parameters.

Results: The CSF-like compartment displayed the greatest reliability across all cohorts, with intraclass correlation coefficient (ICC) values being above 0.95 in each cohort. White matter-like and grey matter-like compartments both demonstrated very high reliability in the immediate cohort (both ICC>0.90), however this declined in the 3-month interval cohort to both compartments having ICC>0.80. Regional CSF-like signal fraction was examined in bilateral hippocampus and had an ICC>0.80 in each cohort.

Conclusion: The 3-tissue CSD techniques provide reliable and stable estimates of tissue microstructure composition, up to 3 months longitudinally in a control population. This forms an important basis for further investigations utilizing 3-tissue CSD techniques to track changes in microstructure across a variety of brain pathologies.

Introduction

Diffusion-weighted Magnetic Resonance Imaging (dMRI) is a widely used, noninvasive, method for measuring the diffusion of water molecules in the brain. Within the microarchitectural environment of the brain, diffusion of water molecules is hindered by various cellular components, particularly the lipid bilayers that make up cell membranes. This principle has been applied to study white matter fiber bundles ("tracts"), as the myelin sheaths surrounding neuronal axons result in anisotropic diffusion[3,19,144]. dMRI has seen widespread use in studies of brain connectivity as well as in clinical populations and neurosurgery[145–148].

Initially, anisotropic diffusion was typically modelled using a tensor, which sought to quantify both the average orientation, anisotropy, and magnitude of diffusion within each voxel of the brain; this approach is known as Diffusion Tensor Imaging (DTI)[19]. More recently, the dMRI modelling domain has seen a proliferation in novel, more advanced, mathematical methods for analyzing the diffusion-weighted signal. These methods aim to overcome several shortcomings of applying the relatively simplistic DTI model to the complex diffusion-weighted signals observed in the brain. This complexity primarily arises from two physiological qualities of the brain itself: the first being crossing fibers, where white matter (WM) tracts occupying the same voxel are oriented differently in space[149,150]; and the second being the presence of other fluids and tissues, including cerebrospinal fluid (CSF) and grey matter (GM) and other cell bodies which "contaminate" the directional signal[38,151–154]. These are major issues as it has been estimated that up to 90% of WM tissue voxels contain more than one WM fiber tract orientation[53], and partial voluming effects alone ensure that a substantial number of voxels contain proportions of multiple tissue and/or fluid compartments[152,153,155].

To address these issues, and with the advent of high angular resolution diffusion imaging (HARDI) acquisition protocols, more advanced methods for describing the observed dMRI data have been proposed by a number of researchers[22,27,87]. One such method, Constrained Spherical Deconvolution (CSD), allows for the presence of multiple fibers along different orientations[11]. CSD resolves these orientations by deconvolving the signal profile corresponding to a prototypical single fiber-like voxel (termed a response function) from the observed signal in each and every other voxel, resulting in the orientation of fibers as a continuous angular function termed the Fiber Orientation Distribution (FOD). Quantitative information can also be obtained from the FOD, as a measure of "Apparent Fiber Density" (AFD) for each fiber population[156].

The original ("single-tissue") CSD has been expanded into Multi-Shell Multi-Tissue CSD (MSMT-CSD) by performing a similar deconvolution with 3 separate WM, GM, and CSF-like tissue response functions. The approach was initially aimed at separating signal originating from GM and CSF-like tissue compartments, in order to improve the accuracy of the WM FOD itself, which otherwise appears very noisy (with many false positive "peaks" or lobes) when using single-tissue CSD in areas of partial voluming with other tissues and fluids[10,152,153]. This subsequently benefits several other analysis and processing steps, such as streamline tractography, which heavily rely on a "clean" and accurate WM FOD. MSMT-CSD thus attempted to address the main shortcomings of the DTI model as well as additional remaining shortcomings of single-tissue CSD.

As its name hints at, MSMT-CSD requires a multi-shell diffusion acquisition scheme in order to successfully tease apart contributions from the 3 WM-, GM- and CSF-like compartments at once. However, to obtain the same benefits offered by MSMT-CSD, yet using only single-shell data, Dhollander & Connelly[90], have proposed a novel approach named Single-Shell 3-Tissue CSD (SS3T-CSD) that can resolve the WM-, GM- and CSF-like compartments as well. By relying only on single-shell data, it allows for shorter acquisition times and is compatible with a wider range of data, both historical as well as clinical.

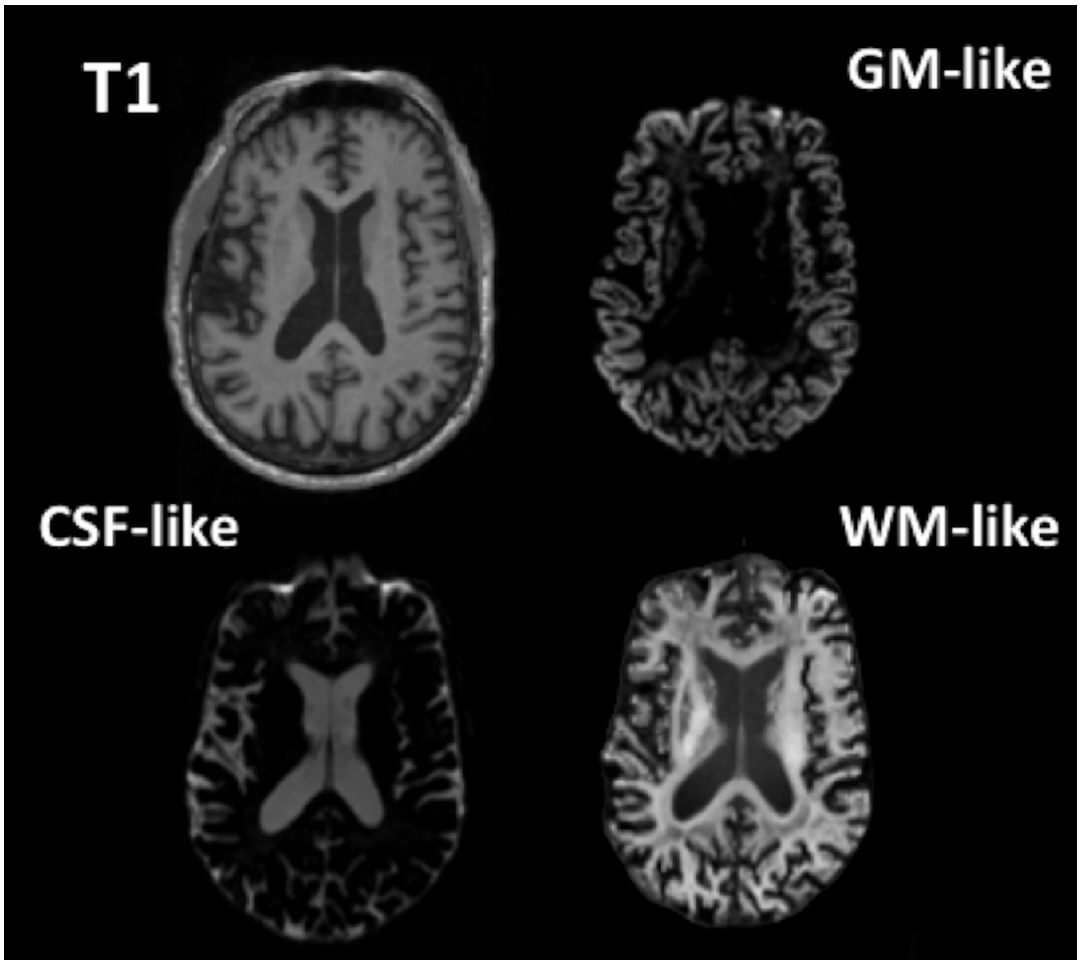

Figure 1: Axial slices showing a T1-weighted MPRAGE and the GM-, CSF-, and WM-like tissue compartments derived from the dMRI data using 3-tissue CSD.

Resolving these different compartments using either 3-tissue CSD method (i.e., MSMT-CSD or SS3T-CSD) holds value beyond improving WM tractography: it can also serve as a proxy for the evaluation of brain microstructure and tissue composition[91,92,157]. By interrogating brain voxels for diffusion signal patterns that look 'like' compositions of the diffusion signals represented by the WM/GM/CSF response functions, it might be possible to gain quantifiable information about microstructure (Figure 1). Using these basic compartments as a diffusion signal model focuses more on coarse properties of brain tissue microstructure rather than separating similar cell types (e.g. different populations of glial cells), or separating different types of pathology (e.g. edema, CSF-infiltration in neurodegeneration, and damage from ischemic stroke). Although, provided with a known context, reasonable inferences of such pathology might be possible to make nonetheless. Even for WM tractography in cases of infiltration by pathological

tissues, the 3-tissue CSD approach can provide direct benefits in terms of recovering healthy WM structures, e.g. in infiltrating tumors[123].

3-tissue CSD derived compartments are a promising, non-invasive method for exploring tissue composition in the brain. The utilization of this approach toward analyzing tissue composition might hold advantages over tensor-based models such as Free Water Elimination (FWE)[24]. The free water estimate from the FWE technique was shown to have limited reproducibility: errors ranged from 5.2-18.2% across ROIs in a test-retest cohort[80]. The CSF-like compartment from 3-tissue CSD techniques might provide an alternative way to recover free water contribution to the signal, using a WM model that does take into account crossing fibres (as opposed to a tensor method). With the advances provided in SS3T-CSD, it is also able to provide signal contribution from the full 3 tissue compartments using single-shell data (i.e. equivalent to acquisition requirements for the FWE technique), allowing for a broader range of input data compared to other 3-tissue compartment models such as NODDI [58]. In a recent review of microstructural diffusion imaging applied to psychiatric disorders, Pasternak et al.[8], illustrated the acquisition sequence complexity compared to the number of microstructure compartments evaluated for several common dMRI analysis techniques. Addition of MSMT-CSD and SS3T-CSD illustrate the range of data required for input to a range of models and the capabilities of resolving compartments compared to other techniques (Figure 2).

To date, there has not been a quantitative test-retest study examining the reliability and long-term stability of 3-tissue CSD techniques. The purpose of this study is to provide evidence that 3-tissue CSD techniques are a reliable and stable approach for assessing brain microarchitecture, via analysis of the 3 resulting tissue signal fractions.

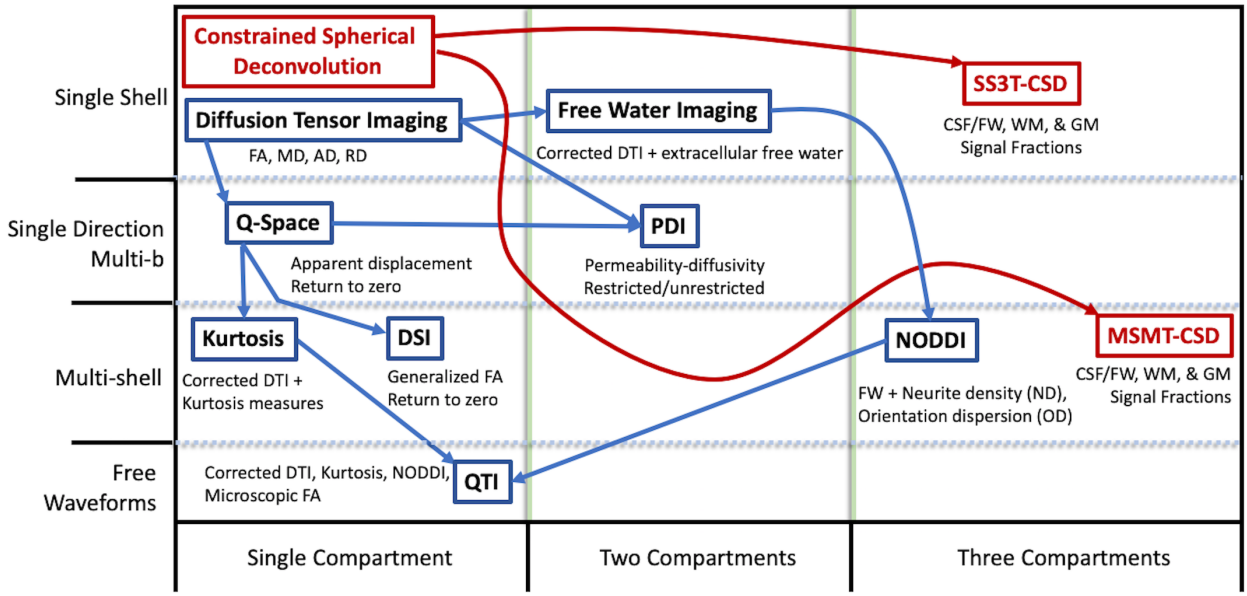

Figure 2: Chart adapted from Pasternak et al.[8]; comparison of common DTI and other model metrics to CSD derived tissue signal fractions by requirements of acquisition (rows) and number of output compartments (columns). Methods derived from CSD have been added in red.

Methods

Cohorts

Three test-retest cohorts were retrospectively evaluated in this study: two local datasets collected at the University of Virginia from ongoing research projects, and one publicly available dataset obtained from the Nathanial Kline Institute for Psychiatric Research: enhanced test-retest (eNKI-TRT) as part of the 1000 Functional Connectomes Project[124,158]. Both studies collected at the University of Virginia received ethical approval from the University of Virginia Institutional Review Board for Health Sciences Research. Each cohort has different time intervals between baseline and retest scans, and was collected with different acquisition parameters. This approach allows reliability to be measured under conditions that represent a variety of different diffusion imaging parameters. Examining stability across different time periods allows for insight into the potential for longitudinal studies tracking changes in 3-tissue signal fractions in individuals or between groups over time.

The first cohort ("immediate rescan" cohort) examined immediate test-retest reliability by performing identical dMRI acquisitions sequentially without table repositioning. This cohort consisted of individuals participating in a separate study at the University of Virginia that included multiple scanning sessions. The cohort consisted of 20 healthy control participants (all male, age at baseline 22.8±3.0 SD). Each participant was scanned twice at each of 3 visits (with the exception of one participant who only attended 2 scans) for a total of 59 baseline-rescan pairs collected for analysis.

The second cohort ("short timescale" cohort) is representative of the quality of diffusion imaging found in large-scale, open science cohorts. Subjects were selected from the original NKI Rockland community study, a group intentionally recruited for similarity to the demographics of the broader United States as a whole[158]. 20 subjects (5 female, age at baseline: 34.4±12.9 SD) had diffusion MRI data available at both baseline and rescan. All participants were rescanned within a range of 7-60 days after baseline. Subjects were not excluded for any history of illness, and 2 participants had a diagnosed history of prior alcohol abuse while 2 other participants had a diagnosed history of a major depressive disorder. Both of these diagnoses are known to affect brain function and structure[125,126]; but the nature of the within-subjects design did not necessitate removing any individuals from the study.

The third cohort ("long timescale" cohort) was collected as a healthy control group for a previously published study conducted at the University of Virginia examining college athletes[159]. 52 participants (all male, age at baseline: 21.9±3.3 SD) were re-scanned 3-4 months after baseline (mean days between scans: 107.9±7.1 SD) and were screened for a history of neurologic disease or concussion.

Image Acquisition

As discussed previously, data from the three cohorts were acquired using different protocols.

The immediate rescan cohort was scanned using a Siemens Prisma 3T scanner with an isotropic voxel size of $1.7\times1.7\times1.7mm^3$, TE=70ms and TR=2900ms; using a multi-shell protocol, 10 b=0 images and 64 gradient directions at both $b=1500s/mm^2$ and $b=3000s/mm^2$ were acquired. This protocol was applied twice with one immediately following the other without actively repositioning the participant in the scanner.

The short timescale cohort was acquired externally and obtained through the Neuroimaging Tools and Resources Collaboratory at www.nitrc.org. Imaging data was collected using a Siemens Trio Tim with an isotropic voxel size of $2\times2\times2mm^3$, TE=85ms and TR=2400ms. Using a single-shell protocol, 9 b=0 images and 127 gradient directions at $b=1500s/mm^2$ were acquired.

The long timescale cohort was scanned using the same Siemens Prisma 3T scanner as the first (immediate rescan) cohort using a different protocol with an isotropic voxel size of $2.7\times2.7\times2.7mm^3$, TE=100ms. Using a multi-shell protocol, 1 b=0 image and 30 gradient directions at both $b=1000s/mm^2$ and $b=2000s/mm^2$ were acquired.

Analysis

Data preprocessing was largely identical across all images in all cohorts in the study. Images were first denoised via use of the "dwidenoise" command in Mrtrix3[107]. Gibbs ringing was then corrected, also using MRtrix3[109]. This was followed by utilizing the FSL package ("topup" and "eddy") to correct for susceptibility induced (EPI) distortions, eddy currents, and subject motion including the –repol flag to perform a Gaussian replacement of outliers [104,110,115,116]. Finally, using MRtrix3 we upsampled the preprocessed data to $1.3\times1.3\times1.3mm^3$ isotropic voxels[102,117,118]. These preprocessing steps are largely similar to those used in other recently published works[91,101,102,123]. A description of a basic single subject pipeline for performing SS3T-CSD, including these preprocessing steps, is available at https://3tissue.github.io/doc/single-subject.html. Brain masks were obtained for all subjects by performing a recursive application of the Brain Extraction Tool[120].

For 3-tissue CSD processing, the 3-tissue response functions were obtained from the data themselves using an unsupervised method[88], resulting in the single-fiber WM response function as well as isotropic GM and CSF response functions for each subject. For each tissue type (WM, GM, CSF), the response function was averaged across all individuals in each cohort to obtain a single unique set of 3-tissue response functions per cohort. For the multi-shell data in the immediate rescan and long timescale cohorts, MSMT-CSD was performed[10]. For the single-shell data in the short timescale cohort, SS3T-CSD was performed[90]. For all subjects in all cohorts, this resulted in their WM-like compartment (represented by a complete WM FOD) as well as GM-like and CSF-like compartments. The CSF-like compartment can in this context also be interpreted as a free-water (FW) compartment[92]. Finally, each subject's three tissue compartments were then normalised to sum to 1 on a voxel-wise basis, resulting in the final 3-tissue signal fraction maps[91]; the metrics for which we performed the test-retest analyses in this work.

To measure the mean squared difference between baseline and rescan for each of the three tissue compartments, a cohort-specific template was first produced. This was achieved using an affine, followed by a non-linear registration guided by the WM FODs themselves in an unbiased manner [160]. The warp that registered each subject's WM FODs to the template was then also applied to the WM-like, GM-like, and CSF-like maps, allowing all three tissue maps to be registered to the same template space and the mean squared difference between baseline and rescan to be calculated. CSF-like (free water) signal fraction in the hippocampus of each subject was measured in each subject relying on these same cohort-specific templates. A whole brain WM image from the LONI atlas[161] was registered along with each hippocampus map to the template using the ANTs image registration toolbox 'SyN' algorithm[162] and then subsequently warped to each individual scan using the reverse transform from template creation. In native space an average was computed of the CSF-like (free water) signal fractions in the ROI, using only voxels with a CSF-like signal fraction smaller than 0.5, to mimic free water analysis (i.e., to avoid accidentally including voxels outside of the brain parenchyma, which might be entirely CSF-filled spaces).

All processing was performed using a combination of different software packages: MRtrix3[12], MRtrix3Tissue (https://3Tissue.github.io , a fork of MRtrix3), FSL[105], ANTs[162].

Results

The CSF-like (free water) tissue signal fraction map was restricted to voxels where the corresponding WM and GM signal maps summed to greater than 50%. This allowed for analysis of the CSF-like signal fraction in tissue without including the ventricles or subarachnoid space, the bulk size of which would otherwise bias a proper whole-brain free water measurement. Additionally, the CSF-like infiltration into brain tissue is a potentially more interesting measurement in the context of healthy functioning or pathology; and is indeed designed to be comparable to measurements of free water encountered in the literature[24]. For all cohorts, results from the 3-tissue signal fractions were averaged across the brain parenchyma. Averages for baseline and retest values were compared by calculating the intraclass correlation coefficient (ICC) and Pearson's correlations. The results for both of these measures are summarized in Table 1.

Data set	Tissue	Subjects	ICC	Pearson's Rho	*P* value
Immediate rescan	CSF-like	59	0.9731	0.9636	<.001
	WM-like	59	0.9929	0.9868	<.001
	GM-like	59	0.9868	0.9748	<.001
	LH CSF-like	59	0.9578	0.9181	<.001
	RH CSF-like	59	0.9376	0.8915	<.001
Short timescale (7-60 days)	CSF-like	20	0.9546	0.9281	<.001
	WM-like	20	0.9692	0.9423	<.001
	GM-like	20	0.9852	0.9700	<.001
	LH CSF-like	20	0.9332	0.9169	<.001
	RH CSF-like	20	0.9094	0.8469	<.001
Long timescale (3-4 months)	CSF-like	52	0.9564	0.9364	<.001
	WM-like	52	0.8157	0.7200	<.001
	GM-like	52	0.8746	0.8024	<.001
	LH CSF-like	52	0.8516	0.7421	<.001
	RH CSF-like	52	0.8217	0.7118	<.001

Table 1: Statistical analysis of the 3 test-retest cohorts in the experiment; p-values are calculated based on the Pearson's correlation. For each cohort the left hippocampus (LH) and right hippocampus (RH) were selected as ROIs and the CSF-like (free water) signal-fraction was measured to examine the reliability of 3-tissue CSD derived free water estimates in subcortical structures specifically as well.

Specific test-retest correlations for each of the three tissue types derived from the 3-tissue CSD techniques are presented in Figures 3-5. All correlations between baseline and retest were significant in all cohorts; the highest whole brain ICC values were obtained from the immediate rescan cohort (Figure 3). In the short timescale cohort, similar to the immediate rescan cohort, all compartments had an ICC value above 0.95 and Pearson's Rho above 0.90 (Figure 4). The long timescale cohort had slightly declined performance, yet with the ICC value for all compartments still being larger than 0.80 (Figure 5). To test the potential significance of this decline, bootstrapping of ICC values from each tissue type and cohort was performed to generate 95% confidence intervals after 100,000 bootstrap iterations. The 95% confidence interval generated from the long-timescale GM-like and WM-like signal fractions did not overlap with the

confidence interval from both the immediate-rescan and short-timescale GM-like and WM-like signal fraction ICCs. The 95% confidence intervals from the CSF-like signal fraction ICCs from each cohort did overlap (Figure 6).

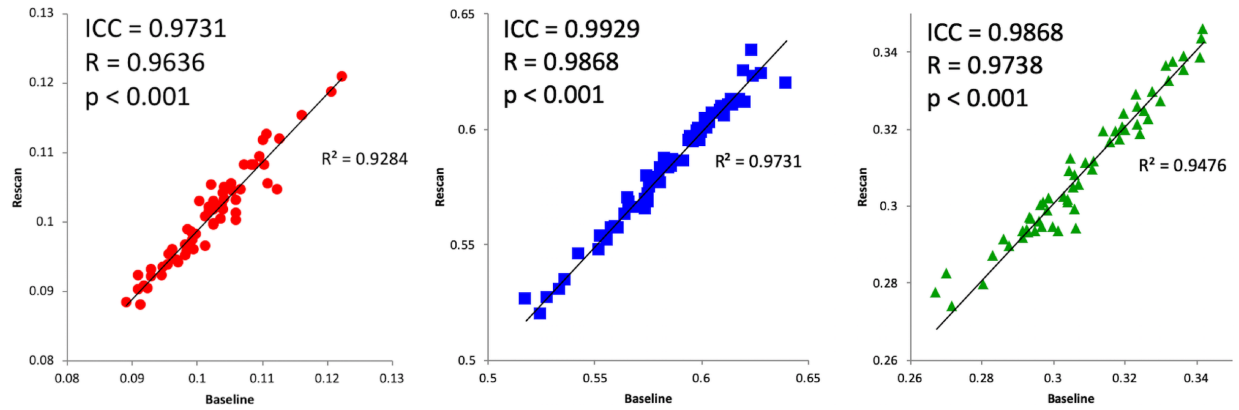

Figure 3: Immediate rescan baseline and re-scan values for CSF- (left), WM- (center), and GM-like (right) signal fractions obtained from a cohort scanned with a duplicate sequence immediately following baseline. Includes ICC and Pearson's correlation values.

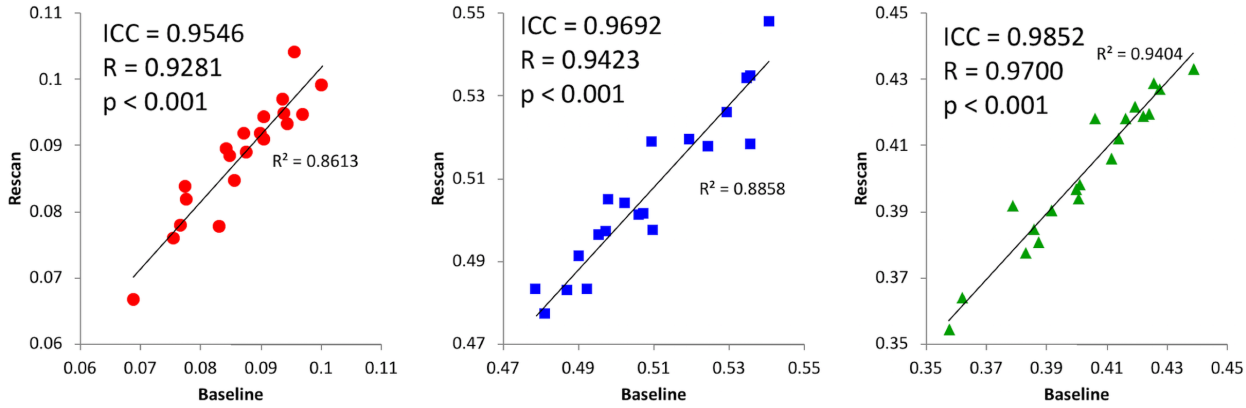

Figure 4: Short timescale baseline and re-scan values from CSF- (left), WM- (center), and GM-like (right) signal fractions obtained from a cohort with 7-60 days between baseline and re-scan. Subjects were taken from the eNKI group and their single-shell dMRI data analyzed with SS3T-CSD. Includes ICC and Pearson's correlation values.

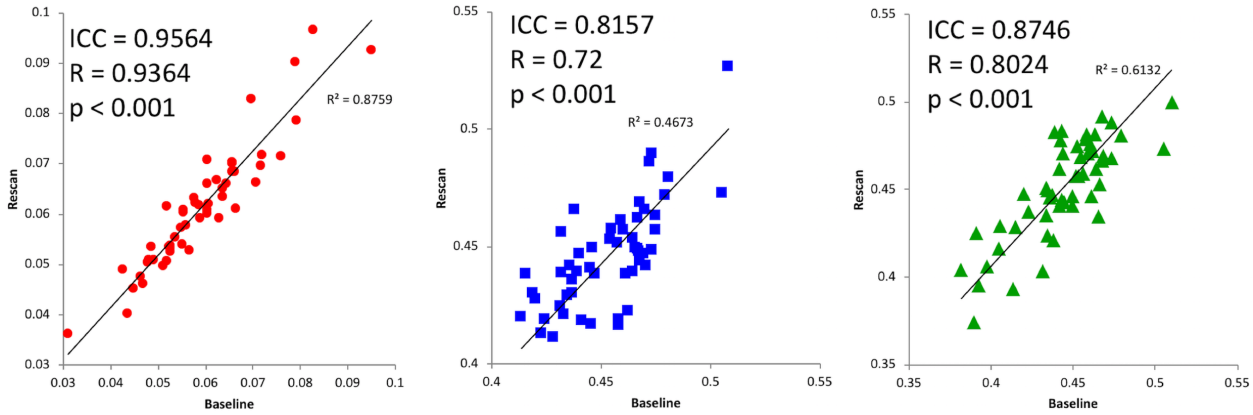

Figure 5: Long timescale baseline and re-scan values from CSF- (left), WM- (center), and GM-like (right) signal fractions obtained from a cohort with 3 months between baseline and re-scan. Includes ICC and Pearson's correlation values.

Additionally the mean squared difference was calculated for each tissue signal fraction map between each subject's baseline and rescan. This showed results largely consistent with overall whole brain averages of the signal fraction maps: each signal fraction map showed good reliability, with the CSF-like map having a mean squared difference less than 0.01 in each cohort, the GM-like map having a mean squared difference less than 0.025 in each cohort, and the WM-like map having a mean squared difference less than 0.035 in each cohort (Figure 7).

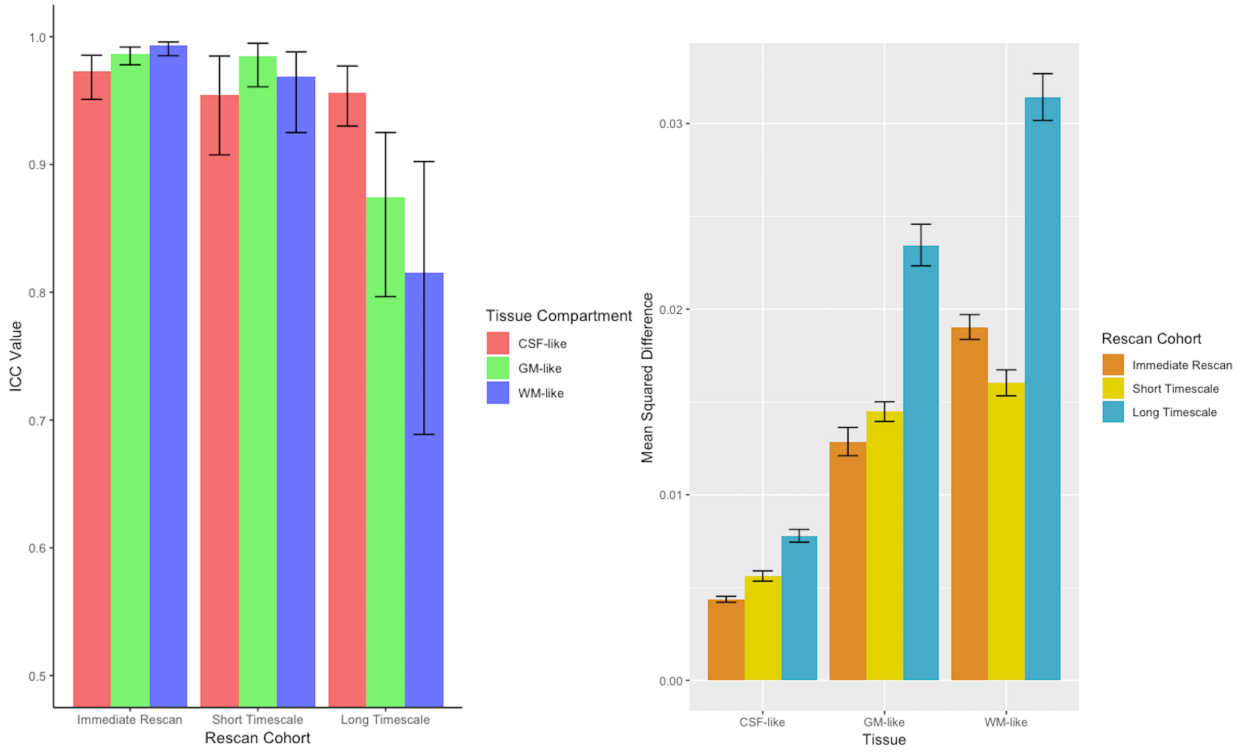

Figure 6 (Left): Results from parametric ICC bootstrapping with ICC calculated from subject data (Table 1) and 95% confidence intervals displayed. There was overlap between the 95% confidence intervals from each cohort's CSF-like ICC but in the long-timescale group the WM-like and GM-like signal fraction ICC did not overlap with either other cohort.

Figure 7 (Right): Bar plot (±SE) displaying the mean squared difference between scan and rescan, averaged across individuals for each tissue map and in each cohort. Comparison between different tissues' mean squared differences is discouraged however, as the average absolute value of each voxel and the distribution of values across the brain is highly different for different tissue types.

In each cohort, the hippocampi were also analyzed separately in order to demonstrate the utility of a 3-tissue CSD approach in a specific region of interest. Bilateral hippocampus was selected for this demonstration as a commonly studied brain ROI with representation from each of the three tissue compartments examined. Comparison of average CSF-like (free water) signal fraction in this ROI between baseline and retest resulted in an ICC value above 0.90 in both left and right hippocampus, as well as a significant Pearson's correlation (Figure 8A). In the short timescale cohort both left and right hippocampus similarly had an ICC value above 0.90 and a

significant Pearson's correlation (Figure 8B). In the long timescale cohort both hippocampus had an ICC value above 0.80 and a significant Pearson's correlation (Figure 8C).

There was a consistent asymmetrical effect observed between the CSF-like signal fraction in right and left hippocampus across all cohorts. The CSF-like signal fraction in each subject's right and left hippocampus were averaged between baseline and rescan and a paired t-test performed for each cohort. This showed that there was a significantly greater CSF-like signal fraction in the right versus the left hippocampus (T_{58} = -10.022, p<0.001; T_{19} = -6.002, p<0.001; and T_{51} = -23.486, p<0.001; for the immediate rescan, short timescale, and long timescale cohorts, respectively).

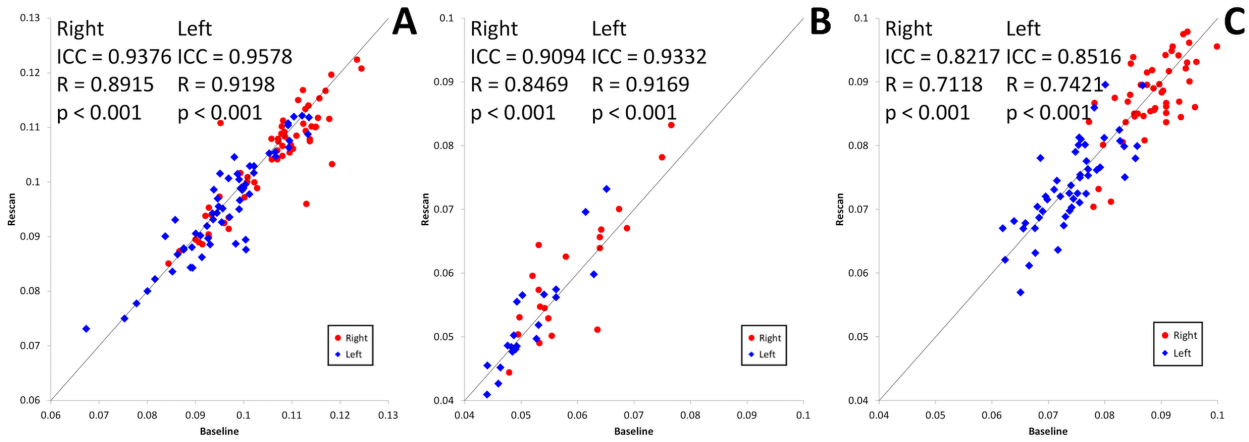

Figure 8: (A) CSF-like signal fraction for the left and right hippocampus in the 59 pairs of baseline-retest scans in the immediate rescan cohort. Values for the right hippocampus of each individual are shown in red and values for the left hippocampus are shown in blue. (B) CSF-like signal fraction for the left and right hippocampus in the 20 pairs of baseline-retest scans in the short timescale cohort. Values for the right hippocampus of each individual are shown in red and values for the left hippocampus are shown in blue. (C) CSF-like signal fraction for the left and right hippocampus in the 52 pairs of baseline-retest scans in the long timescale cohort. Values for the right hippocampus of each individual are shown in red and values for the left hippocampus are shown in blue.

Discussion

Each of the 3-tissue signal fractions demonstrated good reliability across all of the measured timescales we assessed in this work. ICC values were above 0.95 for each of the tissue compartments included in the immediate rescan and short timescale cohorts. This occurred

despite the short timescale cohort being single-shell data, a b-value of 1500, and a lower voxel size compared to the other two cohorts (both of which were multi-shell and had highest b-value of b=3000s/mm^2 and b=2000 s/mm^2 for the immediate timescale and long timescale cohorts, respectively). This result suggests that 3-tissue CSD techniques can reliably obtain quantitative measurements across a range of diffusion imaging protocols, including from openly available datasets. This performance, however, declined slightly in the long timescale cohort: the CSF-like (free water) signal fraction within tissue still had an ICC value above 0.95 while the WM-like and GM-like signal fractions had a slightly lower ICC value, which bootstrapping indicated did not overlap with the 95% confidence intervals from the immediate or short-timescale cohorts. Regardless, all Pearson's correlations were highly significant, indicating that 3-tissue CSD techniques are still able to obtain reliable measurements of brain tissue microstructure, stable up to 3 months from baseline.

In our study it was observed that the reliability of the WM-like signal fraction maps declined in the long timescale cohort compared to the immediate and short-term rescan cohorts as measured by both bootstrapping of ICCs and by analysis of the mean squared difference. It is also possible that the lower number of gradient directions at each non-zero b-value in the long timescale cohort, compared to the other cohorts, caused the estimation of WM FODs to be more variable between rescans. Given the methodology employed for generating response functions and FODs, it would be expected that the ability to distinguish between WM and GM would be more dependent on angular resolution and contrast, while CSF would be more dependent on contrast between b-value shells. This may be supported by the observation that the CSF-like signal fraction map still had a high ICC which bootstrapping indicated was within the 95% confidence interval of both other cohorts. Given the nature of our datasets and the differences in site, acquisition, and subject cohorts, it is not possible to precisely disentangle each of these contributing factors.

The free water signal fraction additionally demonstrated good reliability in both hippocampi at each of the examined timescales. ICC values were above 0.80 and a significant effect of laterality was observed consistently across each cohort, with the right hippocampus having a significantly higher free water signal fraction than the left hippocampus. Though this

study does not suggest any hypothesis for why this laterality was observed, it is consistent with volumetric MRI findings that demonstrate hippocampal asymmetry[163], as well as a recent study that reported asymmetry in hippocampal free water content[164]. That study reported a 1% higher free water content in the right hippocampus compared to the left hippocampus of healthy controls, remarkably similar to the significantly different average observed in this study (0.9% in the immediate timescale cohort, 0.7% in the short timescale cohort, and 1.5% in the long timescale cohort, with higher free water signal fraction in the right hippocampus in each cohort). This suggests that free water signal fraction is both a reliable quantitative measurement for subcortical ROIs, and that it may be able to detect meaningful microstructural properties of such regions.

Given the nature of the datasets and cohorts used in our study, we did not address the topic of reproducibility of tissue signal fractions between different diffusion acquisition methods, subject cohorts, especially cohorts of different age ranges and demographic compositions, and analysis protocols. Three different acquisition protocols were used in this study, each with different angular resolutions, b-value shells, and sequences. Also, two different 3-tissue CSD analysis methods were employed. Given the nature of our datasets and the intrinsic differences in site, acquisition, timescale, and subject cohorts, it is not possible to precisely disentangle each of these contributing factors retrospectively using the data available for this study nor do we believe that attempting to do so would provide robust estimates of variation. Prospectively designing a study to control for these factors would allow for these dimensions to be properly disentangled and the contributions to data variability from each to be determined.

More traditional neuroimaging techniques do not provide quantifiable data on tissue microstructure, however this study has demonstrated a reproducible and reliable method for obtaining whole brain maps with quantifiable estimates of tissue microstructure. We observed these measures to be stable enough to be used in longitudinal studies lasting at least up to three months. They provide information on a voxel- or region-wise basis for analysis of subcortical structures, lesions, or developing brains[91,92,102,157]. Related microstructural analysis of free water signal fractions has been performed in the context of Parkinson's disease[7,165], Schizophrenia[73,75],

and concussion[79]. 3-tissue CSD techniques may thus have the potential to be applied to a variety of these and other neurological conditions.

3-tissue CSD derived tissue fractions provide a flexible framework for analyzing diffusion images in ways not addressed in this paper. While we examined the reliability of WM/GM/CSF-like tissue signal fractions here, other researchers have used response functions representing different tissue compartments when contextually appropriate. Pietsch et al.[101], applied two different WM response functions representing mature and immature WM in a developing adolescent cohort to observe WM maturation. Mito et al.[91], proposed to apply a statistical framework of compositional data analysis to analyze the full 3-tissue composition of WM-, GM- and CSF-like signal fractions directly to study microstructure in white matter lesions, following the initial suggestion of moving towards such WM/GM/CSF-like diffusion signal fraction interpretation by Dhollander et al.[92]. In Aerts et al.[123], this idea was furthermore used for the purpose of disentangling WM FODs representing infiltrated WM tracts, in the presence of gliomas, so as to enable more reliable within-tumor tractography. Similar work has also recently been done by Chamberland et al.[166], who illustrated the use of 3-tissue signal fractions in the presence of cerebral metastases, both to assess their microstructure as well as to enable tractography through nearby edematous regions.

The relatively recent use of CSD to describe the diffusion signal[11] has led to some measure of controversy when compared to other established analysis techniques such as those based in multi-tensor models. One particular area of concern has been noted as the generation of 'false-fibers' on tracking algorithms due to spurious fODF peaks[96,97]. Some studies using recent methodological improvements have suggested that the prevalence of false-fibers in CSD is oversold compared to other methods[98,99]. In this study 3-tissue CSD demonstrated good reliability across all compartments. However as recent work has shown, false-fibers have been found to be reproducible between acquisitions[167,168]. As this study has not explored the presence of false-fibers, it is unknown to what degree they contributed to the WM-like signal fraction.

An additional benefit provided by 3-tissue CSD methods is in the potential for tissue type specific masking. The CSF-like compartment presented in this paper is calculated as CSF-like

diffusion in tissue by relying on the other compartments to identify which voxels were 'tissue'. Unlike a binary tissue segmentation based on T1 intensity, calculations of WM- and GM-like signal fraction compartments together were used to define voxels where 'tissue' composed a majority of signal from each voxel. This process relied exclusively on the single, native space diffusion image instead of reslicing and warping a separate structural image or atlas. Future studies might be able to take advantage of this approach by examining tissue compartment magnitudes inside voxels defined by the behavior of other tissue compartments. For example, tracking CSF-like (free water) tissue infiltration into voxels defined by the high proportion of WM-like tissue during aging or in certain pathological contexts.

Conclusion

In this study, we performed a test-retest reliability and longer term stability analysis of the 3-tissue signal fractions as obtained from 3-tissue CSD techniques. We found that 3-tissue CSD technique provide reliable and stable estimates of tissue microstructure composition, up to 3 months longitudinally in a control population. This forms an important basis for further investigations utilizing 3-tissue CSD techniques to track changes in microstructure across a variety of conditions.

Acknowledgements

NITRC, NITRC-IR, and NITRC-CE have been funded in whole or in part with Federal funds from the Department of Health and Human Services, National Institute of Biomedical Imaging and Bioengineering, the National Institute of Neurological Disorders and Stroke, under the following NIH grants: 1R43NS074540, 2R44NS074540, and 1U24EB023398 and previously GSA Contract No. GS-00F-0034P, Order Number HHSN268200100090U

Study 1d

Title: Inter-site reliability of diffusion microstructure measurements: A 3-tissue constrained spherical deconvolution study

Abstract

As large multi-site neuroimaging and diffusion MRI (dMRI) microstructure studies become more common, it is necessary to understand factors affecting reliability of outcome measurements collected across different sites. In this study, we analyze dMRI collected from 3 subjects traveling to 10 different sites with identical MRI scanners, sequence protocols, and software. We perform a detailed microstructural analysis is in 212 grey matter and white matter brain regions and find that measurements are generally reliable across sites. However, there remains variation in specific locations that may suggest caution when interpreting small effects in small or hard to measure brain regions.

Introduction

Large multi-site neuroimaging studies are becoming more common (e.g. ABCD[128,133], UK Biobank[169], HCP[170], and ADNI[171]) and come with the challenge of harmonizing dMRI across sites. Many factors are known to affect dMRI results, including a variety of MRI scanner, sequence protocol, and data analysis differences. However, the measurement variation effects of different sites having otherwise identical hardware, software, and data analysis is relatively understudied. In this study, we apply 3-tissue constrained spherical deconvolution (3T-CSD) to a publicly available dataset collected on 3 traveling subjects in 10 centers with 2 additional repeated scans in one center. We have previously demonstrated that 3T-CSD has high intrasite reliability when measured from scans at the same site[100]. Here we aim here to demonstrate that 3T-CSD has similar intersite variability when controlling for technical factors of MRI scanner model, software, and data analysis technique.

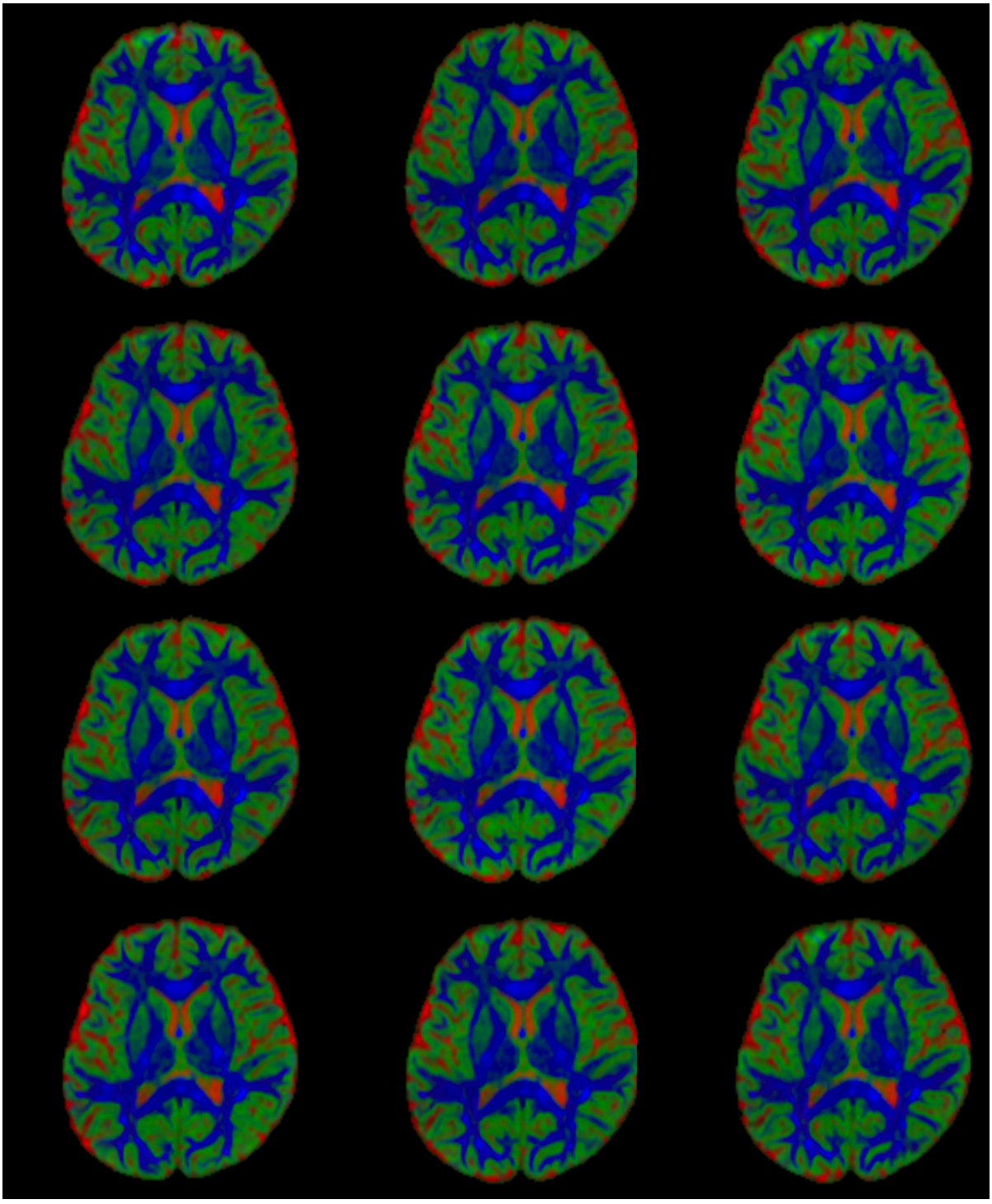

Figure 1: Illustration of the 12 3T-CSD maps obtained from a single subject. The first three rows were obtained from different sites/scanners while the bottom row of 3 images was obtained from a single scanner. All images were rigidly registered to a subject-specific template and are presented from an identical plane in that template (z=55).

Methods

In data collected and publicly released by Tong et al.[134], three healthy traveling subjects (23 y.o. male, 26 y.o. female, and 23 y.o. female) were scanned at 10 different sites to measure intersite variation. At one of the sites, all three subjects were scanned 2 additional times to measure intrasite variation. All 10 scanners were 3T MR MAGNETOM Prisma (Siemens, Erlangen, Germany), equipped with max gradient strength of 80 mT/m and slew rate of 200 T/m/s. Harmonized diffusion weight images were obtained on a 64-channel head coil using the following imaging parameters: TR/TE = 5.4 s/71 ms, FOV = 220 × 220 mm^2, slice number = 93, voxel size = 1.5×1.5×1.5mm^3. The diffusion scheme contained 30 directions each at b=1000, 2000, and 3000 s/mm^2 and 6 b=0 images. Scanner software was identical across sites.

Each subject was analyzed using SS3T-CSD[172,173] implemented on the b=3000 s/mm^2 shell as available in MRtrix3Tissue (https://3tissue.github.io/), a fork of Mrtrix3[174]. Several preprocessing steps utilized FSL[175]. Diffusion images were denoised[176], corrected for Gibbs ringing[177], susceptibility distortions[178], motion[179], and eddy currents[180] then voxels were upsampled to 1.3 mm isotropic[181]. Average response functions were generated for WM-, GM-, and CSF-like tissues from the images[182] and the fiber orientation distribution (FOD) calculated for each voxel[173]. 3-tissue signal fractions were calculated from the FODs[172], the ranges of each is between 0-1 in each voxel of the brain.

A cohort specific template was constructed from a random selection of 3 subjects' WM-FODs using symmetric diffeomorphic registration of the FODs themselves. Each subject was then individually rigidly registered to the template (Fig. 1), alongside a affine non-linearly registered, b-value matched version of the NTU-DSI-122 template to allow the 48 ROIs from the ICBM-DTI-81 template (JHU-DTI atlas[183,184,185]) and 164 ROIs from the Destrieux cortical atlas[186] to be moved into the cohort template[187]. The average signal fraction from each of the 3 tissue compartments (extracellular isotropic/freely diffusing water, ECI; intracellular isotropic, ICI; and intracellular anisotropic, ICA) was measured within each of these 212 ROIs and compared between the 9 intersite measurements and the 3 intrasite measurements. Measurements

were pooled across participants and a t-test was performed for each signal fraction measurement from each ROI to compare intersite to intrasite variability.

Results

In each of the 3 signal fractions the majority of ROIs were not significantly different between intersite and intrasite measurements, suggesting that 3T-CSD measurements are generally as reliable between sites as they are when measured at the same site. The ECI signal fraction had the largest number of significantly different measurements with 46 ROIs significantly different between intersite and intrasite while 173 ROIs were not significantly different (Fig. 2). This improved in the ICI signal fraction measurements to 38 ROIs significantly different between intersite and intrasite while 181 ROIs were not significantly different (Fig. 3), and improved further in the ICA signal fraction measurement to 25 ROIs significantly different between intersite and intrasite while 194 were not significantly different (Fig. 4). However, in each signal fraction compartment no ROIs had more than 0.055 mean difference between inter- and intrasite scans, very few had more than 0.03 mean difference, and the vast majority had less than 0.01 mean difference.

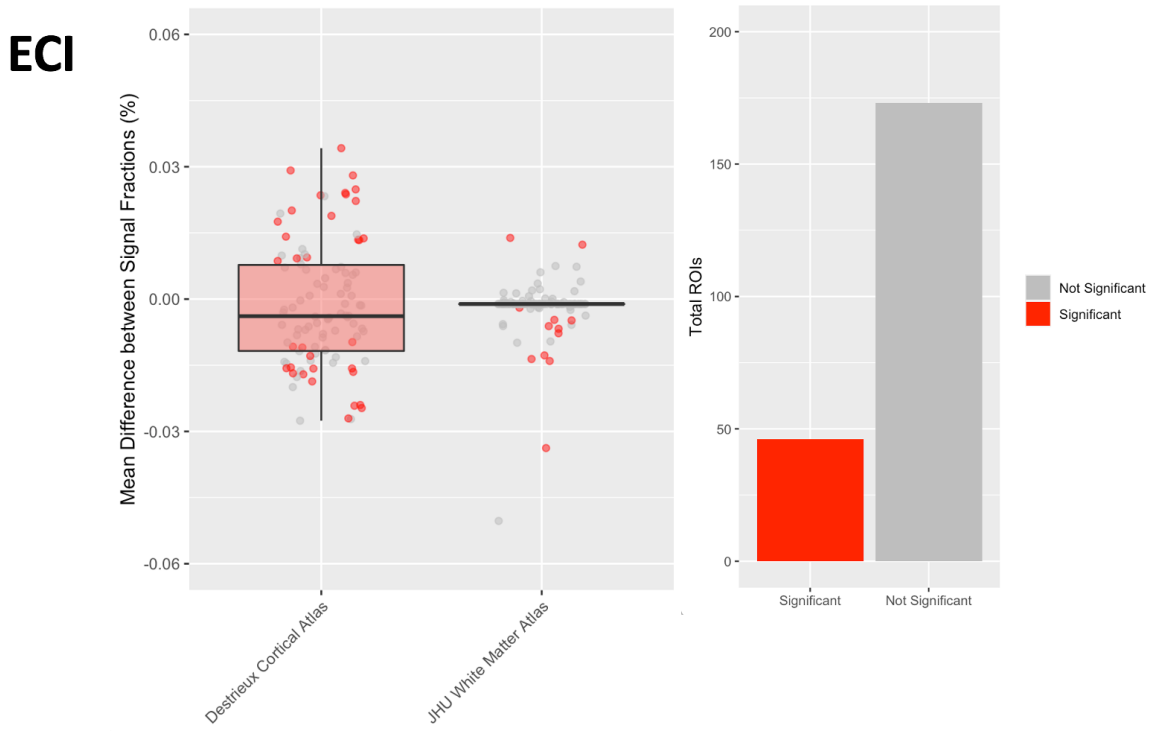

Figure 2: Boxplot in Panel 1 displaying the mean difference between inter- and intrasite measurements of the ECI signal fraction within each ROI, across participants, separated by atlas ROIs are sourced from with the Destrieux cortical atlas (red) and JHU white matter atlas (blue). Each dot represents an ROI. The vast majority of JHU white matter atlas measurements are so clustered around zero that the boxplot appears flat. Bar chart in Panel 2 sums the color coding for individual ROIs where the difference between inter- and intrasite measurements is statistically significant.

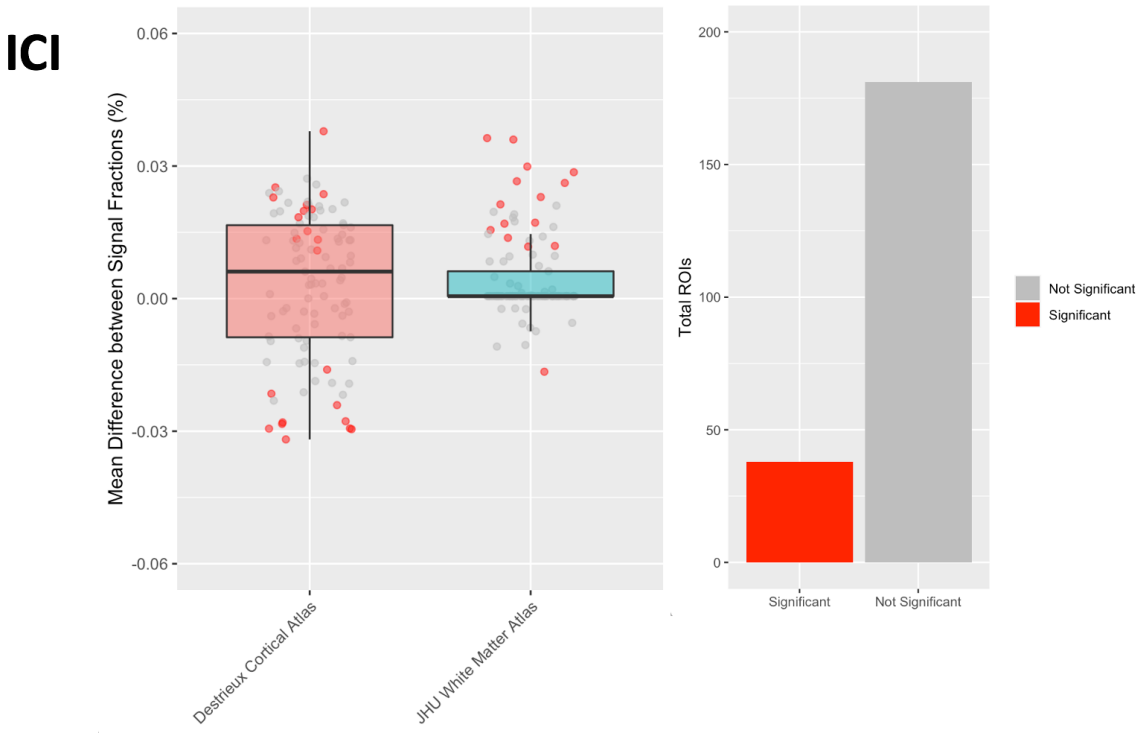

Figure 3: Boxplot in Panel 1 displaying the mean difference between inter- and intrasite measurements of the ICI signal fraction within each ROI, across participants, separated by atlas ROIs are sourced from with the Destrieux cortical atlas (red) and JHU white matter atlas (blue). Each dot represents an ROI. Bar chart in Panel 2 sums the color coding for individual ROIs where the difference between inter- and intrasite measurements is statistically significant.

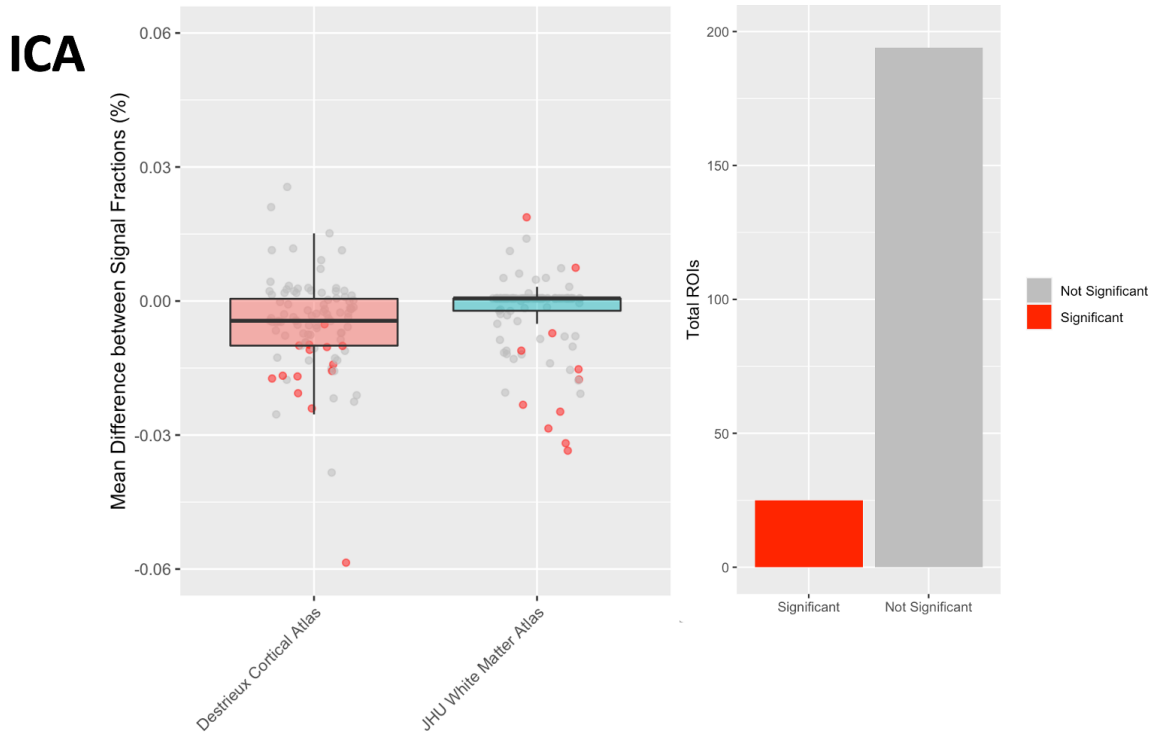

Figure 4: Boxplot in Panel 1 displaying the mean difference between inter- and intrasite measurements of the ICA signal fraction within each ROI, across participants, separated by atlas ROIs are sourced from with the Destrieux cortical atlas (red) and JHU white matter atlas (blue). Each dot represents an ROI. Bar chart in Panel 2 sums the color coding for individual ROIs where the difference between inter- and intrasite measurements is statistically significant.

Discussion

For multi-site studies this study provides evidence that measurements of diffusion microstructure from 3T-CSD are reliable and dependable. This study suggests a consistent pattern in each signal fraction where the mean difference within ROIs of the JHU-WM atlas were substantially closer to 0 and fewer were significantly different between intrer- and intrasite than ROIs taken from the Destrieux cortical atlas, suggesting that deep WM cellular microstructure may be more reliably determined than cortical cellular microstructure. We aimed here to provide the most straightforward comparison possible between scanning sites but do not have the data to account for what contributed to the small differences we did detect. It is possible this measurement was affected by differing effects of location and scanner setup, or by intrinsic subject factors such as hydration on brain macrostructure[188], cardiac[189], or breathing activity. Variation was more common in the cortex than in the deep white matter.

Conclusion

This study provides evidence for 3T-CSD measurements of brain tissue microstructure being a reliable metric for multi-site studies. Variation tends to be less than 0.01 for most ROIs across the brain, and is observed to be especially reliable within the white matter skeleton.

Summary

This study investigates the reliability of diffusion microstructure measurements acquired from 10 different scanning sites. We compare measurements from across the brain for inter- and intrasite reliability, finding that 3T-CSD is reliable, especially in white matter.

Study 1e

Title: The NTU-DSI-122 template as a flexible platform for fiber orientation distribution registration of diffusion microstructure into stereotaxic space.

Abstract

The registration of neuroimaging subjects to a common stereotaxic space allows for comparisons between timepoints, subjects, or with reference atlases of regions of interest. Typically, this has been performed by computing a similarity metric between the voxel-wise intensity values in the subject image and a reference image. Diffusion MRI is a method that provides far more detailed voxel-wise information than a simple scalar intensity value. This allows for the potential to use this additional information to perform registration with added within-tissue contrast. In this study, we present a novel use of the NTU-DSI-122 template as a fiber orientation distribution (FOD) template, for the purpose of registering subject dMRI images to stereotaxic space. The reliability and accuracy of this FOD-based registration method are compared to the intensity-based registration method ANTs by registering cellular microstructure maps from two separate cohorts to the NTU-DSI-122 template. The stochastic FOD-based method significantly outperformed the stochastic intensity-based metric on reliability and was able to more consistently register the same subject multiple times independently. The FOD-based method also significantly outperformed the intensity-based metric on registration accuracy by more completely aligning the microstructure maps to the template as measured by the Sorenson-Dice coefficient at multiple percentile thresholds. The NTU-DSI-122 template has the additional benefit of including multiple b-value shells between a wide range of feasible acquisition schemes, making the platform a flexible option for registering acquisitions of varying quality, including clinically acquired data.

Introduction

Registering subjects to a common template space is a necessary step in almost any neuroimaging study performing group-level comparisons. A straightforward process for doing so aligns the brains of each acquisition in a study cohort from the acquired ‘native’ space to a

'common' template space. This common space is intended to achieve voxel-voxel correspondence between images and allow for comparison between subjects without interference from factors such as head orientation in the scanner or naturally occurring anatomical variation. The idea of a stereotaxic common space that could allow for images, atlases, and ROIs from different studies to be applied in a standardized manner gained attention with the definition of Talairach space-registered atlases[190], and the release of stereotaxic templates such as the Colin 27 Average Brain[191], and the MNI 152 linear template[192].

While manual segmentation by multiple experienced raters was once viewed as the gold standard in anatomical parcellation[193], this procedure is not always available or practical for large volume multi-site cohorts. The Adolescent Brain Cognitive Development (ABCD) cohort, for example, contains imaging across multiple modalities and multiple timepoints for over 11,000 subjects, far too many to reasonably manually segment ROIs in a timely and cost efficient manner[128,133]. Automated methods are thus necessary to align subject brain scans collected in their native space with a suitable reference template in order to apply an atlas in an unbiased manner.

As the brain differs in size and proportion between subjects[194,195] registration algorithms must be able to warp the brain along multiple axes in order to achieve an accurate alignment. This is typically performed using an algorithm with 12 degrees of freedom: rotation, translation, scale, and shear in a non-linear affine transform based on mutual information[196]. This process is most straightforward when dealing with T1-weighted structural images of subjects because the voxel intensity values create a consistent contrast between cortex, white matter (WM), and CSF [197]. One of the most widely applied registration algorithms in neuroimaging, the 'SyN' model implemented in the program ANTs[119,120], utilizes a diffeomorphic regularization to minimize the intensity difference between images (by maximizing a cross-correlation metric), combined with assistance from anatomical priors[119]. This registration approach is highly reproducible[119], and has performed well against other methods in open competition[198,199].

Diffusion MRI (dMRI) images can present a particular challenge for this process, as each individual gradient direction may have different voxels with high and low intensity based on

gradient angle and subject positioning. The use of multiple b-value shell acquisitions provides an additional complication, as each individual voxel may have different intensity at each shell in addition to global intensity shifts dependent on the cellular tissue contents within each voxel[10]. One solution to this problem has been to register the b=0 s/mm^2 volumes collected with the diffusion images to a T2-weighted image due to the similar anatomical contrast present in both images[200–202]. However this method neglects the strength of dMRI's ability to provide detailed information *within* tissue compartments, especially WM and areas where myelinated axons extend into the cortex.

The voxel-wise image intensity between two WM fiber bundles may not be greatly different at b=0 (i.e., they *lack* within tissue contrast), thus intensity-based algorithms may have lower sensitivity toward within tissue location. However the *orientation* of those WM fiber bundles can vary, potentially including multiple directions within a single voxel depending on analysis method[53]. The presence of these crossing fibers complicates many common DTI derived metrics used in registration, such as fractional anisotropy based-registration[203,204]. Accounting for this orientation information during registration is important for tractography and reconstructing accurate connectomes. Additionally, some measures of cellular microstructure, such as free water signal fractions, have a small value range (between 0-1 in this case), making the measure sensitive to even small changes in value or introduction of noise. Symmetric diffeomorphic registration via cross-correlation of the spherical harmonic coefficients has previously been demonstrated as a means of accurately co-registering WM fiber orientation distributions (FODs) within a cohort[160]. This method allows for crossing fiber tracts to be registered between subjects, and can create group average templates composed of information from each subject in a particular study cohort. However, many neuroimaging methods such as connectome building or automated atlas fitting require registration to an existing template specifically in stereotaxic space. An additional requirement for any FOD template to achieve effective widespread use is for the FODs to be available for calculation from multiple b-values. Different b-values have greatly different FOD amplitudes[205] and WM fiber bundle signal varies between b-value shells[206], and constrained spherical deconvolution algorithms[207].

These two requirements: 1) that a diffusion FOD template be located in stereotaxic space, and 2) that the template be adaptable to a variety of b-values in order to match collected data, are both met by the NTU-DSI-122 template[135]. This template was developed by combining diffusion spectrum images obtained from 122 individual subjects through a multi-step registration procedure. The result is a template fit to ICBM space with multiple b-values up to b=4000 s/mm^2. Though designed as a diffusion spectrum template the number of b-values at each shell are suitable for extraction and FOD calculation. It is then possible to register subject FOD images or group level template images with the NTU-DSI-122 at an appropriate b-value for parcellation and analysis. This study introduces the NTU-DSI-122 as a candidate FOD template in stereotaxic space for the registration of dMRI images. The utility of this method is compared in two experiments to a commonly used standard registration method for both reliability (Experiment 1) and accuracy (Experiment 2) with a specific focus on the registration of dMRI derived measures of cellular microstructure.

Methods:

Template:

The NTU-DSI-122 was developed by combining 122 individual subjects (61 male, age 27.97 ± 5.25 years, ranging from 19-40 years-old) diffusion images through a two-step registration procedure incorporating structural and diffusion weighted registration[135]. This process involved 1) creating a mean tissue probability map from all input subjects, and aligning that mean image to stereotaxic space. 2) Aligning each subject's diffusion spectrum image and q-space information before averaging each subject to construct the final template [208].

Experiment 1: Assessment of Reliability

To assess the reliability of each transform method the same identical registration was performed repeatedly for a number of images and the results were compared for consistency. We collected 5 diffusion MRIs from healthy controls (all male) using a Siemens Prisma 3T scanner with an isotropic voxel size of 1.7×1.7×1.7 mm, TE=70 ms and TR=2900 ms; 10 b=0 images

and 64 gradient directions at both b=1500 s/mm^2 and b=3000 s/mm^2. Each image set was analyzed using MSMT-CSD[10] implemented in the open source software MRtrix[12]. Several preprocessing steps utilized FSL[104,105]. Diffusion images were denoised[107], corrected for Gibbs ringing[109], susceptibility distortions[104], subject motion[116], and eddy currents[110]. All images were upsampled to of 1.3×1.3×1.3 mm, and skull-stripping was performed using the Brain Extraction Tool[105]. Response functions were generated[88] from both experimental data and the NTU-DSI-122 template at b=1538 s/mm^2 and b=3077 s/mm^2 and used to generate FODs[10]. The number of directions was sufficient to generate FODs with a harmonic order of $l_{max} = 4$, which has been suggested to be optimal for registration[160]. Extracellular isotropic CSF-like free water signal fractions were calculated directly from the FODs using 3-tissue constrained spherical deconvolution (3T-CSD), a method that measures cellular microstructure within each voxel fitting into intracellular anisotropic (ICA, WM-like), intracellular isotropic (ICI, GM-like), and extracellular isotropic (ECI, CSF-like/Free Water) compartments[100].

Each of the 5 diffusion MRIs were then registered from native space to MNI space using both ANTs SyN algorithm[120] to register the processed b=0 s/mm^2 images with the Colin 27 T2 template[191] and using MRtrix[12] to register the WM FODs with the NTI-DSI-122 template WM FODs[160,209]. Each registration was used to generate a transform that was applied to the CSF-like free water signal fraction from that subject. Because these registrations are not deterministic processes, and can produce slightly different transforms each time it is performed on the same images, this procedure was repeated independently 5 times for each subject, via each method (Figure 1).

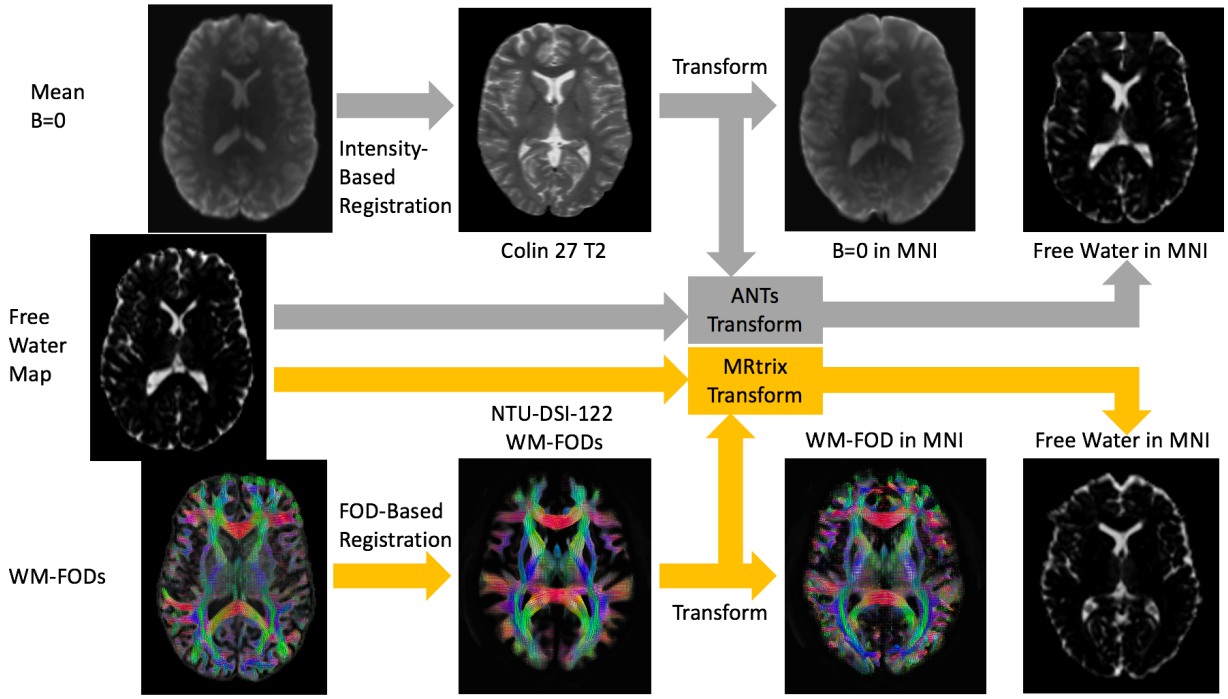

Figure 1: Study workflow illustrating the process of moving from native space images (three images on left), registering with the respective template for each method, applying the transform generated from that registration to the free water signal fraction map, and obtaining the free water signal fraction maps in stereotaxic MNI space (two images on right). This process was repeated 5 independent times for each of the 5 subjects for Experiment 1. In Experiment 2 this process was performed only once for each subject, and the resulting transform was used to move intracellular anisotropic (WM-like), intracellular isotropic (GM-like), and extracellular isotropic (CSF-like/Free Water) signal fraction maps to MNI space.

Experiment 2: Assessment of Accuracy

To assess the accuracy of each transform method we devised a new method for comparing signal fraction maps in stereotaxic space. A typical approach for registering structural MRIs using b=0 or T1-weighted images has less information for discriminating between voxels within the same tissue type (WM/GM/CSF). FODs however contain a great deal more information in both directional components and axonal fiber density[160]. We hypothesized that this additional information would lead to superior within-tissue registration of cellular microstructure signal fraction maps (as these are derived from FOD coefficients) and thus more accurate whole-brain registration. To test this hypothesis, we generated cellular microstructure signal fraction maps from a 'ground-truth' in stereotaxic space by applying the 3T-CSD analysis

to the NTU-DSI-122 template itself. Each subject image and the 'ground-truth' image could then be thresholded at different signal fraction values and in different directions (the threshold representing either an upper or lower based voxel-wise value limit, illustrated in Figures 2-4). The transformed and thresholded signal fraction image from each subject and from the appropriate tissue type could then be compared for accuracy at multiple levels of detail using the Sorensen-Dice coefficient, a metric of image overlap[210,211]. By thresholding the subject images after transformation the experiment is also able to account for the impact of interpolation on signal fraction maps. Both MRtrix and ANTs implement a nearest neighbor algorithm, however the greater local deformation that occurs can cause more severe distortions in values. So, while necessary to account for warped voxels, local interpolation changes can be severe for signal fraction maps with value ranges between 0-1. By creating threshold cutoffs between 0.10 or 0.25, large shifts from the ground truth values will cause regions to cross the cutoff threshold and the Dice coefficient value will be lower.

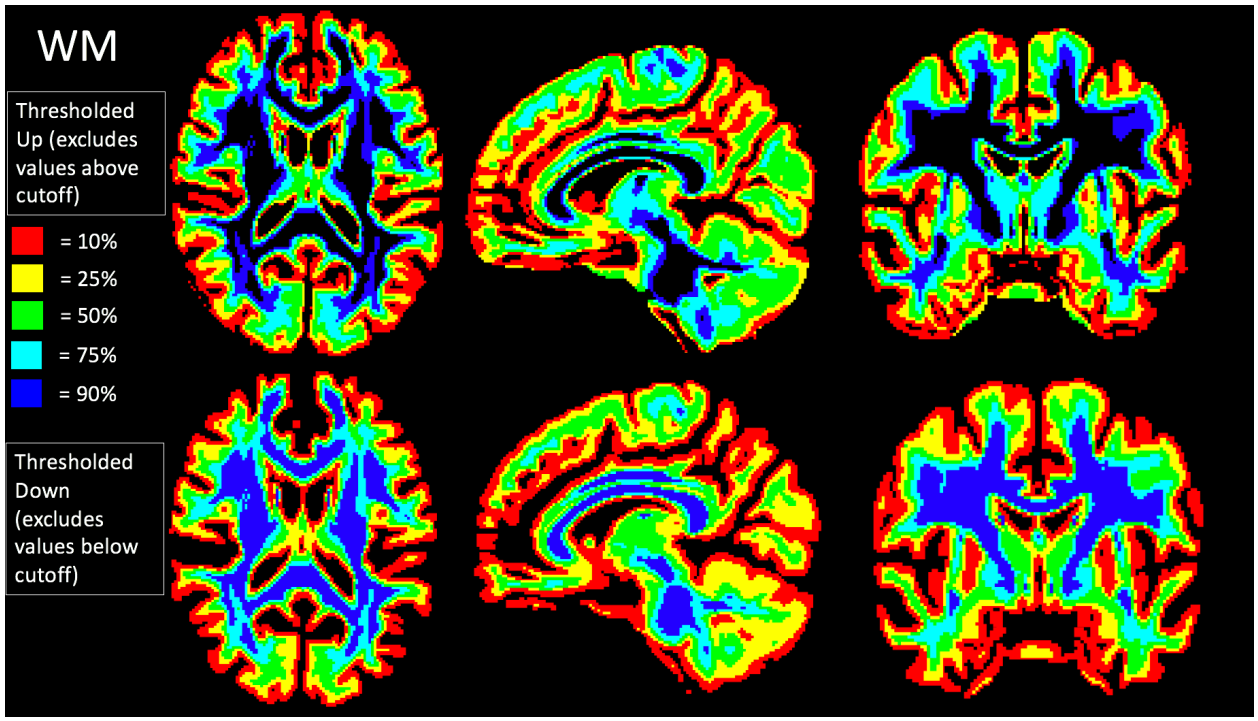

Figure 2: Map of the thresholding procedure for the intracellular, anisotropic (WM) signal fraction map. This is illustrated using the NTU-DSI-122 template which served as a ground-truth structural division in this study. The different direction of thresholding created 10 different ground truth maps for each tissue type, each covering different regions of the brain. For example, the region thresholded 'Up' at voxels where the WM signal fraction value was 25% includes both the red and yellow regions largely in the cortex where intracellular anisotropic signal is low, meanwhile the region thresholded 'Down' includes the yellow, green, cyan, and blue regions including deep WM but ecluding the outer cortex.

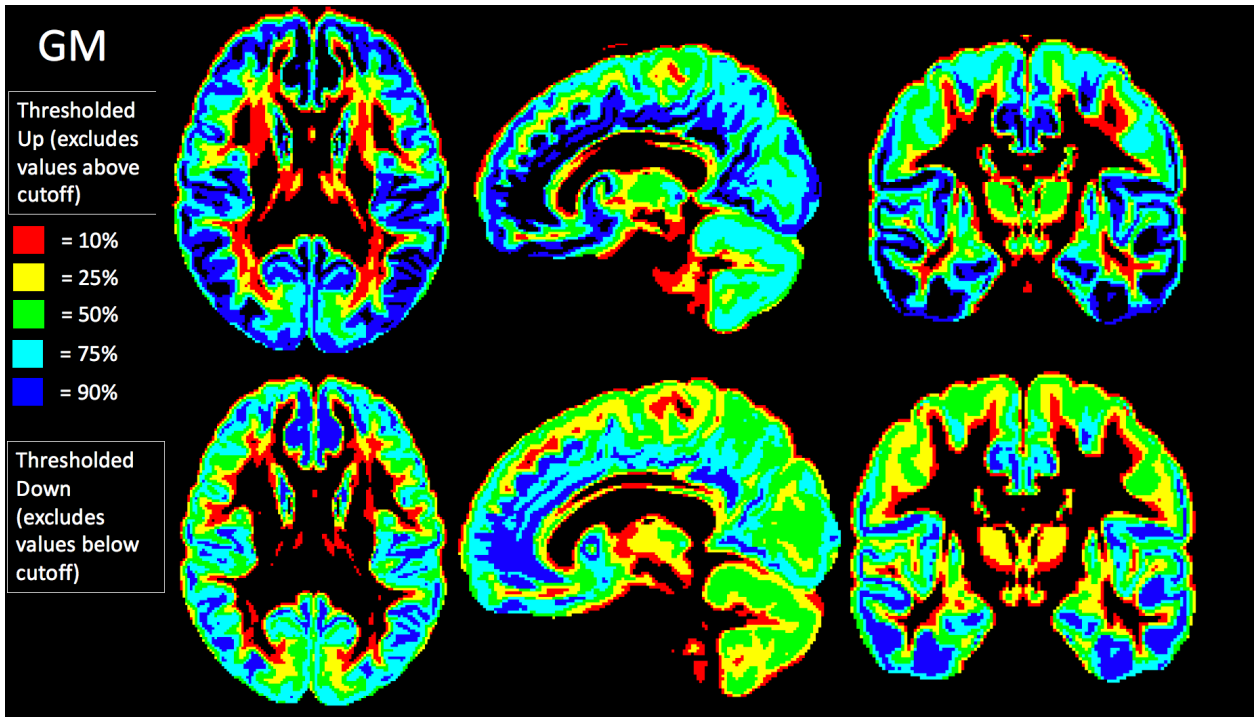

Figure 3: Map of the thresholding procedure for the intracellular, isotropic (GM) signal fraction map. This is illustrated using the NTU-DSI-122 template which served as a ground-truth structural division in this study. The different direction of thresholding created 10 different ground truth maps for each tissue type, each covering different regions of the brain. This patterning includes portions of central structures as well as detailed layering of the cortex without a large contribution from axonal WM areas.

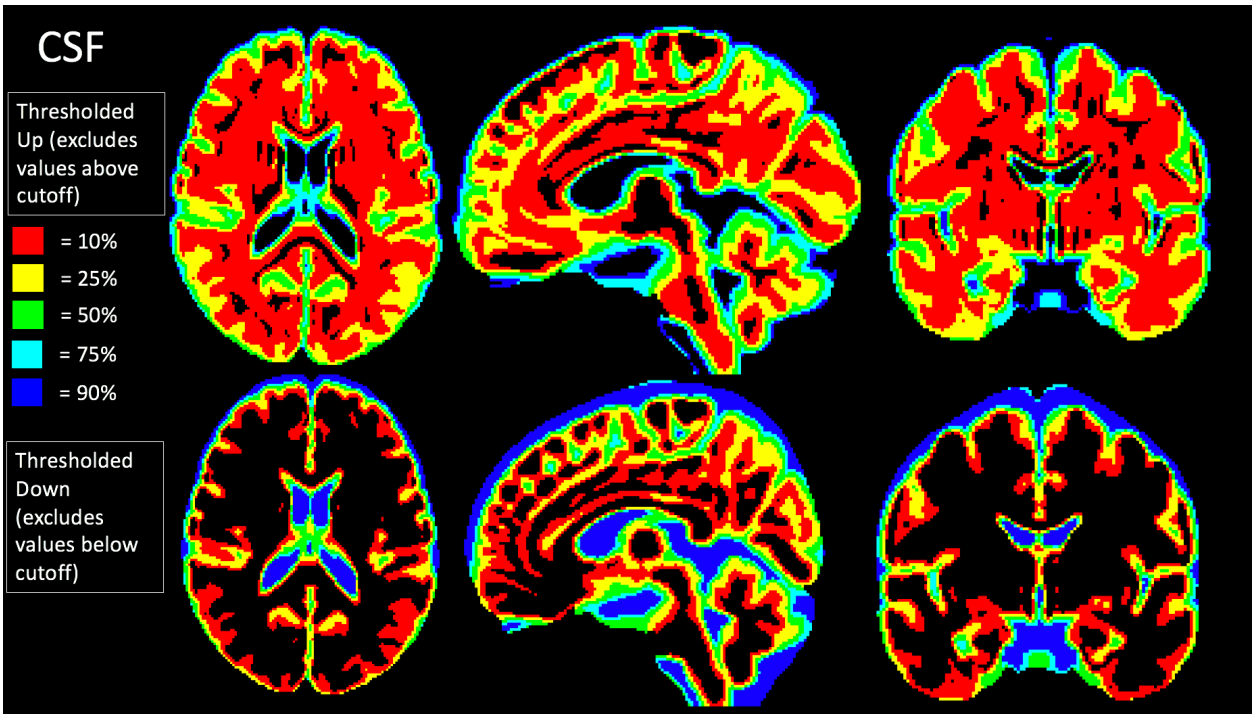

Figure 4: Map of the thresholding procedure for the extracellular, isotropic (CSF/free water) signal fraction map. This is illustrated using the NTU-DSI-122 template which served as a ground-truth structural division in this study. The different direction of thresholding created 10 different ground truth maps for each tissue type, each covering different regions of the brain. This patterning includes detailed ventricles as well as a highly detailed layering of the cortex displaying the gradient of fluid infiltration into cortex toward the outer edge of the brain parenchyma.

For subjects, diffusion MRI images were obtained from a random selection of 100 non-twin individuals in the Human Connectome Project (HCP)[131]. Subjects were scanned using a specially modified Siemens Skyra 3T scanner with acquisition parameters of 1.25x1.25x1.25mm^3 isotropic voxels, TE=89ms and TR=5520ms; 36 b=0 images were acquired interleaved with 180 gradient directions each at b=1000s/mm^2, b=2000s/mm^2, and b=3000s/mm^2[131,212]. Processing of dMRI data was performed identically to Experiment 1 with the exception of single-shell constrained spherical deconvolution following preprocessing[90]. Quality control was performed via manual visual inspection of each subject's signal fraction maps to remove subjects who experienced registration failure (largely blank final images or the presence of extreme distortions) and 4 subjects were removed from the study (three for failure of the FOD-based method and one for failure of the ANTs method).

The closest matching non-b=0 shell was extracted and FODs were calculated as before. Using the NTU-DSI-122 allowed for the creation of a 'ground-truth' signal fraction map for each of the tissue types derived from 3T-CSD (ICA, ICI, and ECI). For the Colin-27 template used as an example comparison tissue segmentation was performed using FSL[105]. No additional preprocessing was necessary and response functions were derived from the dMRI image itself following the protocol established in Experiment 1.

Statistical Approach

In Experiment 1 once the free water signal fraction maps had been moved into stereotaxic space the mean squared difference was then calculated for each whole-brain image between every same-method same-subject combination to analyze which method more consistently transformed the free water signal fraction map into MNI space. This approach allowed for transform reliability to be assessed using traditional statistical approaches.

In Experiment 2 Sorensen-Dice coefficients were calculated for each of the subjects' signal fraction maps that passed quality control. Each subject had 5 cutoff maps per direction of thresholding (upper thresholding above the cutoff value and lower thresholding below the cutoff value) for each of the three tissue types derived from 3T-CSD (ICA, ICI, and ECI) in addition to whole brain maps (compared against both NTU-DSI-122 and Colin27 ground truth signal fraction or determinative tissue divisions) for a total of 36 measurements per subject. Each direction of thresholding and each tissue type was compared between registration methods to determine if registration using intensity or FOD-based methods were consistently more successful at correctly aligning each level of the signal fraction maps.

Results

Experiment 1: Assessment of Reliability

Each of the subject's calculated mean squared difference was lower for the MRtrix FOD transform compared to the ANTs SyN tansform. This resulted in a significantly lower mean squared difference between repetitions compared to the ANTs SyN generated transform (pairwise T-test, $T_{49} = 8.02$, $p<0.001$) indicating that the FOD algorithm was able to more consistently register and transform the free water signal fraction maps (Figure 5).

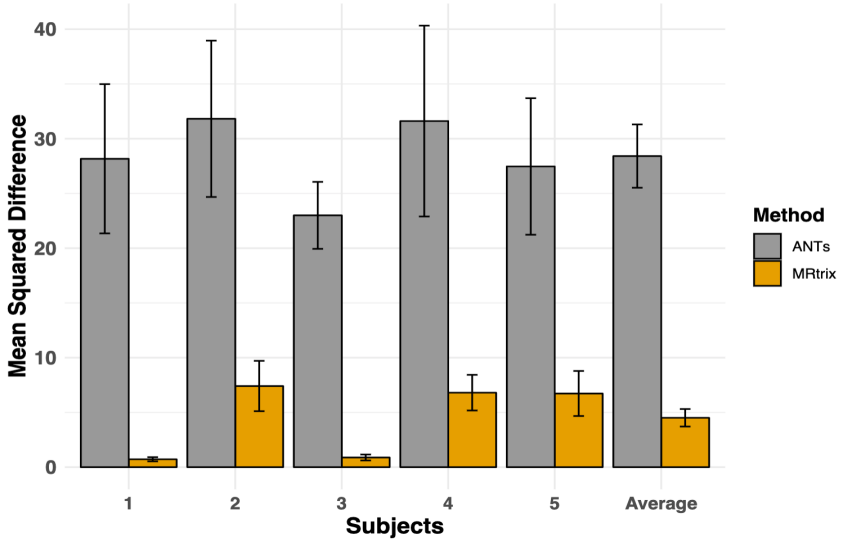

Figure 5: The mean squared difference results from Experiment 1 between each of the 5 independent registration attempts for each of the 5 subjects involved in analysis are presented, alongside the group mean (±SE). Grey bars represent the SyN intensity-based registration implemented in ANTs and yellow bars represent the WM-FOD based registration implemented in MRtrix. The reliability of the MRtrix implemented FOD-based registration method had a significantly lower mean squared difference between the transformed images of each subject (pairwise T-test, $T_{49} = 8.02$, $p<0.001$).

Experiment 2: Assessment of Accuracy

Registration using the FOD-based template resulted in signal fraction maps with a greater Sorenson-Dice coefficient in upper thresholded ICA (Repeated measures ANOVA, $F_{1,950}=28485.01$; $p<0.001$), upper thresholded ICI (Repeated measures ANOVA, $F_{1,950}=26033.74$; $p<0.001$), upper thresholded ECI (Repeated measures ANOVA, $F_{1,950}=11189.9$; $p<0.001$), lower thresholded ICA (Repeated measures ANOVA, $F_{1,950}=3600$; $p<0.001$), and lower thresholded ICI (Repeated measures ANOVA, $F_{1,950}=23.5$, $p<0.001$). Intensity-based registration implemented

using ANTs resulted in signal fraction maps with a greater Sorenson-Dice coefficient in lower thresholded ECI (Repeated measures ANOVA, $F_{1,950}$=892.8; p<0.001). When each directional threshold was combined FOD-based registration had a significantly higher Dice coefficient for each tissue type (ECI Repeated measures ANOVA, $F_{1,1910}$=25.78; p<0.001; ICI Repeated measures ANOVA, $F_{1,1910}$=35.36; p<0.001; ICA Repeated measures ANOVA, $F_{1,1910}$=40.26; p<0.001) These results are summarized in Figure 6. Whole brain registration results were compared by calculating Dice coefficients for both the 3T-CSD derived tissue signal fraction maps and the FSL intensity based determinative tissue segmentations. There was a significant effect of registration method on Dice coefficient (Fig. 6), with FOD-based registration performing better than intensity-based registration on each NTU-DSI-122 comparison while intensity-based registration had a higher dice coefficient when compared to the Colin-27 segmentations, however the NTU-DSI-122 comparison was far higher for both methods (Repeated measures ANOVA, $F_{1,1146}$=12.69; p<0.001). There was also a significant effect of tissue type (Repeated measures ANOVA, $F_{1,1146}$=21.77; p<0.001), with the ECI free water tissue compartment having the lowest Dice coefficient for both methods when compared to the Colin-27 segmentation and the highest Dice coefficient for both methods when compared to the NTU-DSI-122 template. There was no significant interaction between registration method and tissue type (Repeated measures ANOVA, $F_{1,1146}$=0.085; p=0.918 n.s.).

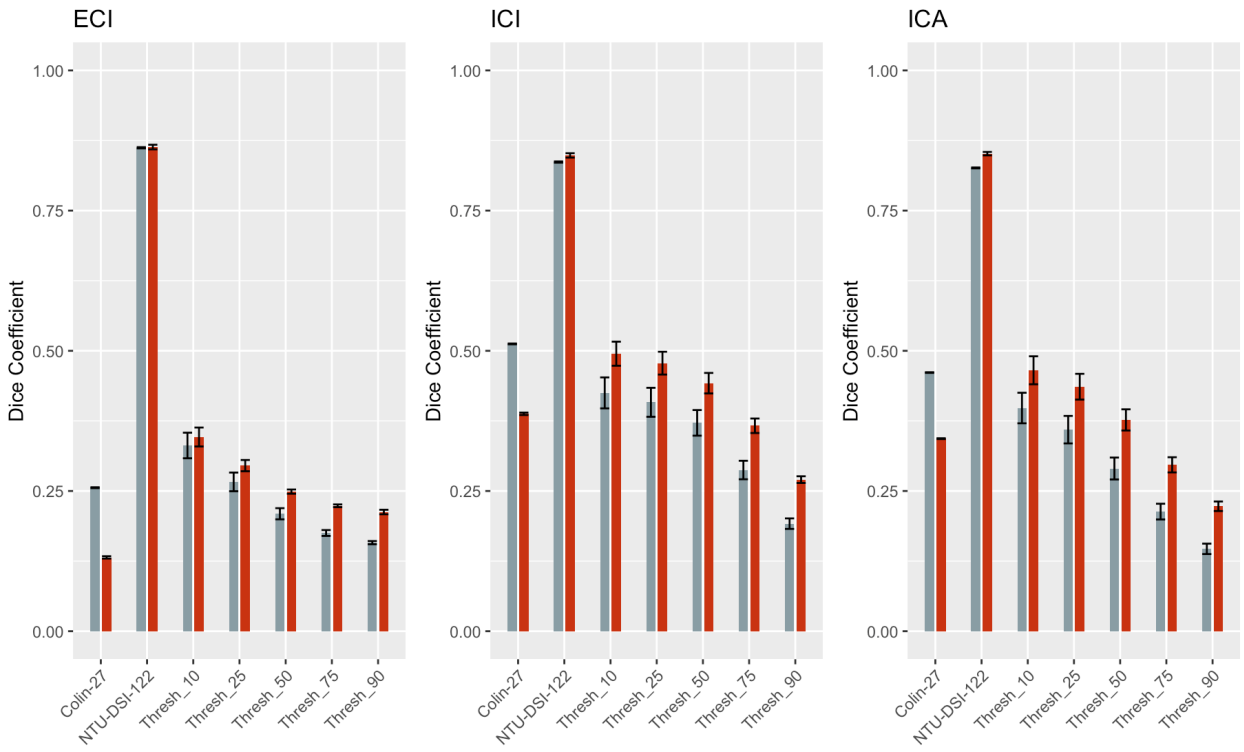

Figure 6: Chart displaying the Dice coefficient calculated for each tissue type and averaged across all subjects and threshold levels, and compared to the ground truth of either the Colin-27 binary tissue division (Gray; CSF/GM/WM) or the NTU-DSI-122 signal fractions (Red; ECI/ICI/ICA). Dice coefficient calculated from the intensity-based registration method is displayed in gray (±SE) and the FOD-based registration method is displayed in red (±SE).

Discussion

We have demonstrated the successful use of an FOD-based template for the reliable and accurate transformation of signal fraction maps into stereotaxic space. Using the NTU-DSI-122 we are able to create an FOD template suitable for individual or template-based registration. The NTU-DSI-122 is a flexible template with a variety of b-value shells to create suitable b-value matched templates to the majority of common acquisition schemes. The additional directional information inherent in the FOD map provides a powerful means to register axonal fibers and to generate within-tissue contrast that is not possible using regular structural imaging techniques.

We have compared this FOD-based template registration technique to the widely used intensity-based SyN transform implemented in ANTs[120,199]. Registering dMRI images using the NTU-DSI-122 template with an FOD-based apodized point spread function[209] was demonstrated

to be more reliable and, in a variety of contexts, more accurate at registering brain microstructure maps than the intensity-based method. The NTU-DSI-122 showed better whole brain registration and accuracy at various thresholds and in each of the tissue microstructure types examined. This is especially notable due to only information relating to the anisotropic tissue compartment (ICA/WM) being used in the registration process. Intensity-based registration uses information from each of the different tissue compartments, and so it would not have been unexpected to have performed better at the GM/CSF boundary at the edge of the cortex however each of the tissue compartments had a higher Dice coefficient when FOD-based registration was used. This finding supports the view that each tissue compartment contributes some signal to almost every voxel, in contrast to a binary view where voxels belong to a specific predominant tissue type. Perhaps unsurprisingly, the ECI compartment performed the worst in regards to accuracy at various thresholded levels between both FOD- and intensity-based registration methods. Interestingly however, the FOD-based registration outperformed the intensity-based registration method throughout the mid-range of thresholded values which suggests that the FOD-based method was more accurate at registering the sulci and gyri (the largest contributors to these thresholds as illustrated in Figs. 2-4).

The increased accuracy of the FOD-based registration method is complemented by the range of b-value shells present in the NTU-DSI-122 template, allowing for a template to be created that matches experimentally acquired acquisitions. In this study we have exclusively tested registering dMRI images from natively acquired subject space to stereotaxic space, while this is not necessarily the optimal method for every study, it allowed for an easy to analyze experimental design and presented a reasonably challenging task for a registration algorithm to align subject brains with individual variations to a normalized template. A common alternative to direct native space to stereotaxic space registration is to create a cohort specific template to first register all subjects to, then performing a single registration between that template and stereotaxic space[100,160]. To illustrate the utility of the NTU-DSI-122 and the suitability of this method to register cohort specific templates from a variety of acquisitions a number of templates from a wide variety of subject cohorts and acquisitions have been warped into stereotaxic space. The FODs from these templates in MNI space are illustrated in Figure 7, they display accurate anatomical registration from cohorts across the lifespan and including clinical quality data.

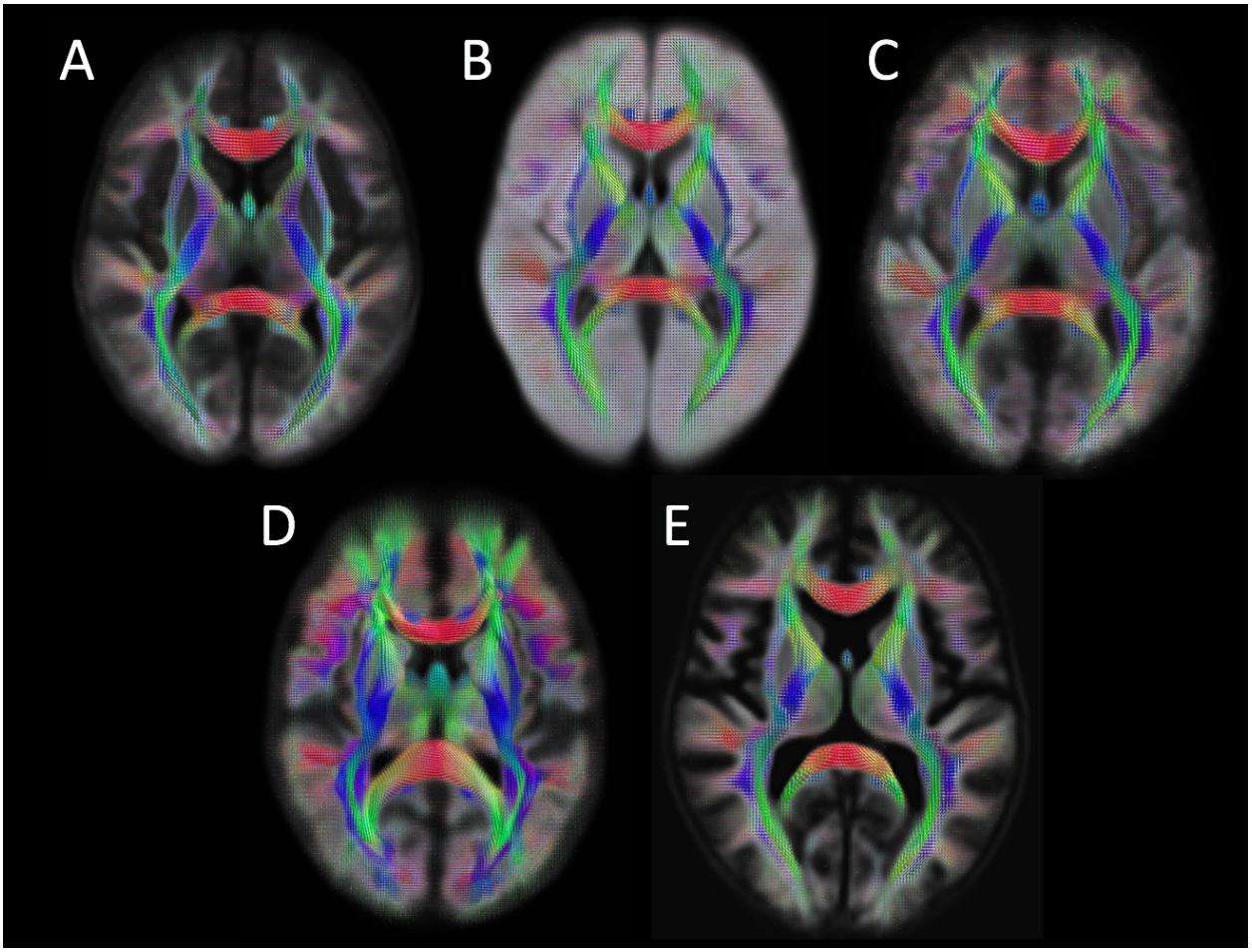

Figure 7: Illustration of 5 cohort-specific templates transformed into MNI space using b-value matched variants of the NTU-DSI-122. Each template was constructed from between 30-50 randomly selected individuals from their respective studies. Each cohort was collected with a different acquisition protocol (both single- and multi-shell acquisitions ranging from b=1000 s/mm^2 to b=3000 s/mm^2 maximum b-value) across different age groups and template B was constructed from a clinically acquired dataset. Cohort age ranged from 9-11 years old (A), 41-84 years old (B), 32-37 years old (C), 18-27 years old (D), and 56-82 years old (E).

The purpose of this study is to introduce a new template option for FOD-based registration of dMRI microstructure measurements to stereotaxic space. To that end, this study as much as possible strived to maintain a simple and straightforward registration pipeline that would mimic a typical user's 'out-of-the-box' experience using the neuroimaging software available with MRtrix and ANTs[12,120]. There are a number of ways to increase registration algorithm performance by altering the settings of these algorithms and optimizing the algorithm

to work with data from a particular pipeline or even from a specific subject. For example, the accuracy of both registration methods tested here can sometimes be improved if the number of iterations allowed before the algorithm terminates is increased, or if the hierarchical resolution steps are modified. While these are important considerations for implementing registration in any specific study, we aimed to demonstrate a simple comparison for validity, not to specify the total superiority of one method over another. Thus, optimizing the algorithms is beyond the scope of this paper.

Intensity-based registration has a number of advantages over an FOD-based method that were not evaluated. This study utilized two datasets with high-quality dMRI acquisitions intended for research applications, one collected locally and another from the HCP[131,212]. The high b-value shells and number of gradient directions are well-suited for generating FOD maps with sufficiently high ϑmax spherical harmonic degree to detect multiple directions of crossing WM fibers[10,206]. A clinically acquired dataset or dMRI with only a limited number of directions intended for diffusion tensor imaging (DTI) may not be suitable for FOD-based registration or may suffer decreased accuracy while intensity-based registration only requires a single b=0 image. This study also does not test the ability of intensity-based registration techniques to register single volume DTI derivative metrics, such as fractional anisotropy, to a template or stereotaxic space.

Given the rise in cellular microstructure models of dMRI data, it is imperative that well evaluated registration methods are used to ensure accurate and reliable transforms. This will only become more important as large cohort datasets require automated processing pipelines with minimal user intervention. The addition of multi-site data provides another imperative to have reliable registration that does not introduce a new source of variation into the study. This study describes a novel registration process that uses the NTU-DSI-122 as a FOD template located in stereotaxic space suitable for FOD-based registration. This template and the software used in this study are freely available and available for use by any dMRI researcher.

Conclusion

Using the NTU-DSI-122 as a template for FOD-based registration provides a means to register subject brain scans to stereotaxic space. This method is more reliable and more accurate than a leading intensity-based registration method at registering maps of brain cellular microstructure.

Chapter 2

Applying 3T-CSD to study the brain throughout the lifespan

With Chapter 1 focusing on the technical development of 3T-CSD as a reproducible technique for assessing and quantifying brain cellular microstructure Chapter 2 will focus on the application of 3T-CSD to assess major critical periods throughout the lifespan. While 3T-CSD has great potential for use in studying and quantifying nonstandard microstructure, or the brain in the context of gross pathology, it is important to demonstrate the utility and sensitivity of 3T-CSD in normal and healthy appearing individuals. The brain undergoes intense periods of change during development and during aging and 3T-CSD must be able to quantify these changes as well as show sensitivity to factors that are known to have an effect on the brain, such as puberty, chronological age, and cardiovascular health.

Aim 2a: To generate trajectories of 3T-CSD measurements of ICA, ICI, and ECI signal fractions across the lifespan and during a variety of developmental and degenerative processes similar to existing structural MRI modalities.

The basic cellular processes that occur in the brain during human development, aging, and decline, are still poorly understood. Volumetric MRI studies have established that the volumes of brain white matter and gray matter change dramatically across the lifespan[13,14]. However since 3T-CSD is potentially more sensitive to cellular changes at the sub-voxel level it may be able to detect changes in brain microstructure before they manifest as changes in brain volume[15]. It is also necessary to explore the cellular microstructure that underlies volumetric change with detailed analysis of specific regions of the brain at multiple scales and between hemispheres. The goal of this study is to analyze a large number of subjects from a publicly available population cohort in order to provide a lifespan trajectory for 3T-CSD measurements of cellular microstructure from multiple areas of the brain. Establishing the relationship between chronological age and microstructural metrics will establish normal reference ranges and trajectories that are essential before investigating abnormal populations.

Aim 2b: Determine if 3T-CSD microstructure measurements are altered by pubertal development during the critical period of early adolescence.

Adolescence is a time of rapid physiological and neurological change that is primarily driven by the surge in production of sex-specific hormones. Identifying microstructural changes that occur naturally during this time period will allow for further evaluation into life events that alter brain cellular microstructure. Understanding the relationship between the cells of the brain and maturation is an important component of adolescent health and well-being throughout the remainder of the lifespan.

Aim 2c: Determine if the epigeneticly derived risk score 'GrimAge' is an effective peripheral blood biomarker of small vessel disease driven damage to brain microstructure in a 'healthy' aging cohort.

Though macro-level changes in the aging brain are well described, the microstructural cellular alterations underlying these changes are relatively unknown. We would expect microstructural alterations to be more sensitive to physiological change or pathological development before they accumulated into macro-level changes in brain structure. The age-adjusted version of GrimAge presents a powerful means for studying the effects of cardiovascular health on the brain and has been shown to be predictive of the presence and size of white matter hyperintensities (WMH)[16]. A specific focus will be made on white matter hyperintensities, a visible neurological manifestation of small vessel disease, and the microstructural composition of the axonal pathways throughout each individual's brain affected by their unique white matter hyperintensity location and volume.

Study 2a

Aim 2a: To generate trajectories of 3T-CSD measurements of ICA, ICI, and ECI signal fractions across the lifespan and during a variety of developmental and degenerative processes similar to existing structural MRI modalities.

Rationale: The human brain undergoes a great deal of physical change throughout the lifespan, both in size and in arrangement. The brain changes both in response to chronological age (both developmentally in early age and decline in later age), and due to internal and external forces as varied as puberty, traumatic brain injury, socioeconomic status, exercise, and many others[6,213–215]. We hypothesize that 3T-CSD metrics of brain cellular microstructure will be highly sensitive to structural alterations of the brain and can provide deeper insight at the voxel-wise level regarding cellular processes underlying observed changes than traditional volumetric structural measurements[15].

As a novel metric, 3T-CSD measurements will benefit from proper contextualization within the lifespan. We expect significant changes to occur in 3T-CSD brain microstructure measurements as the brain develops and ages but the distribution of these changes within the brain and the direction of these changes is unknown. Establishing a baseline trajectory for brain microstructure will aid interpretation of future experiments and allow for comparisons between individual subjects and baseline or between a clinical population and baseline. Though this work could be extended using the concept of 'brain age' this aim is initially descriptive in nature, and will primarily be used to contextualize the results from models in later Study 2b and Study 2c.

Experimental Design: To achieve this aim, we will first analyze a harmonized whole lifespan cohort and parcellate each subject to obtain measurements from 212 ROIs across the brain. This will be performed using the Nathaniel Kline Institute (NKI) Rockland Cohort, a well-established cohort of several hundred subjects ranging in age from 5-85 years-old[158]. The cross-sectional trajectory of cellular microstructure from ICA, ICI, and ECI tissue compartments will be plotted for each of the 212 ROIs for the entire age range present in the NKI-Rockland dataset. Results from this experiment will inform interpretation of results from subsequent experiments.

Direction of observed effects in particular, will give valuable insight into which factors accelerate/slow maturity in development and which accelerate/slow decline in aging. The ROI-based approach will allow for compatibility with subsequent studies by covering a comprehensive series of distinct brain areas such as both cortical and subcortical GM, axonal skeleton, cerebellum, and including both left and right components of lateralized structures where appropriate.

Study 2a

Title**:** Diffusion MRI microstructure markers of changes in the human brain across the lifespan

Abstract

Understanding how the brain develops, matures, ages, and declines is one of the fundamental questions facing neuroscience. Recent advances in diffusion MRI microstructure analysis have allowed for detailed descriptions of neuronal change in humans. However, it is essential that findings from these studies are appropriately contextualized to general age-related changes in the brain. This study uses 3-tissue constrained spherical deconvolution (3T-CSD) to examine the relationship between brain diffusion microstructure and chronological age. 3T-CSD is able to quantify signal fraction measurements at the voxel-wise level from three different tissue microenvironments found in the brain: extracellular free water, intracellular isotropic, and intracellular anisotropic. This study applies 3T-CSD analysis to the Nathanial Kline Institute's Rockland cohort, a large-scale community sample of brain MRI data across the lifespan. Microstructural measurements were taken in a number of structures throughout the white matter, subcortical gray matter, and lobar cortical regions while additionally evaluating lateral differences in microstructural measurements. The general trajectory of signal fraction measurements was a positive relationship with age and extracellular signal fraction, a negative relationship between age and intracellular isotropic signal fraction, and an inverted U-shaped trajectory for the intracellular anisotropic signal fraction. In individual sub-areas these trends tended to still be present, with some notable exceptions. However there were large differences in 3T-CSD microstructure measurements between individual structures, including significant lateral differences between hemispheres for each of the subcortical gray matter structures and for each of the cortical regions. These results demonstrate that 3T-CSD is able to describe age-related change across the brain and lifespan. By using a healthy population cohort this study can be used as a point of comparison for 3T-CSD analysis of microstructure changes in the presence of pathology. Finally, the detailed analysis of lateralized ROI results can inform diffusion microstructure studies examining cortical and subcortical regions.

Introduction

Throughout the human lifespan the structure of the brain changes dynamically in response to internal and external factors. A wealth of volumetric MRI studies have shown that early in life the brain dramatically increases in size while in older individuals the brain shows a remarkable decrease in volume[216–221]. Two recent studies using extremely large numbers of subjects have firmly established a general trajectory for changes in brain volume, with peaks in volume occurring around 12 years of age (for subcortical GM, surface area, and cerebrum volume)[14]. However these trajectories show comparatively little movement following development (especially after puberty, but with the greatest rates of change occurring before 2 years of age)[13]. This leads to a long and slightly downward plateau before decline begins in earnest in advanced age, with especially noticeable increases in ventricular volume and declines in cortical GM volume[13,14]. This lifespan trajectory is interwoven with complex processes during development and decline, such as hormone levels following the onset of puberty in early adolescence[222] and changes in vascular health during aging[223]. Concurrent with changes in gross anatomy are changes occurring at the cellular level, such as extensive synaptic pruning in development[224,225] and excessive atrophy and cellular death in mild cognitive impairment and progressive decline[226]. Understanding the trajectory of these changes in the brain, as well as understanding what processes drive these changes, are important for research into neurological disease.

Recently, measures of cellular brain microstructure derived from diffusion MRI (dMRI) have proliferated in number and become more commonly applied in the analysis of development and pathology[24,58]. Each model has particularly defined functions applied to the raw diffusion signal, such as the separation of freely diffusing water from tissue in the bi-tensor free water elimination model[24] the 'ball and stick' model of isotropic and anisotropic diffusion[21], or the detailed delineation of cellular somas from neurites (dendrites, axons, etc.) and extracellular water available with NODDI[58]. While these models have seen widespread application in recent years, most are still reliant on tensor-based diffusion models or require sufficiently detailed acquisitions to accurately quantify all of their output metrics. Our lab has recently developed a model of diffusion microstructure known as 3-tissue constrained spherical deconvolution (3T-

CSD)[100]. 3T-CSD relies on more complex models of diffusion signal calculated using spherical harmonics[11] and is able to measure both isotropic and anisotropic intracellular microstructure and extracellular water compartments derived from single-shell clinical quality acquisitions with a high level of reliability and stability[90,100]. The ability of 3T-CSD and other quantitative diffusion models to measure multiple microstructure compartments provides a far greater level of detail at the voxel-wise level compared to well-established volumetric MRI and voxel-based morphometry measurements. These advantages mean that 3T-CSD is well-positioned to investigate changes in brain cellular microstructure across the lifespan. Within a specific age cohort, deviations from established age-related trajectories might indicate accelerated or slowed aging or development, depending on the context being studied. Microstructural measurements may have increased sensitivity by detecting changes in cellular architecture before they become apparent as changes in volume or density, particularly the signal from extracellular freely diffusing cerebrospinal fluid (CSF) infiltrating into brain tissue[15].

3T-CSD has several other advantages in examining changes in the brain across the lifespan. Importantly the intracellular isotropic component is flexible and nonspecific, and is intentionally not restricted to any specific cellular type or location within the brain. Changes in this signal fraction compartment are thought to arise from either neuronal soma or glial cell population changes. Voxels with the highest intracellular isotropic signal fraction occur in the typically defined gray matter areas (GM) in the cortex and subcortical structures. However nearly all voxels have a non-trivial contribution from each signal fraction compartment, including in axonal areas (so called 'deep' white matter (WM)) where neuronal somas are unlikely to be found[91,227]. This makes the intra- and extracellular isotropic signal fraction compartments excellent markers for changes in axonal white matter areas. 3T-CSD can detect meaningful shifts from very high (~90% or more) intracellular anisotropic signal fraction in healthy axonal areas toward increasing intra- and extracellular isotropic signal fraction measurements in early development[101] or in the presence of pathology[227]. But this specific pathological context is not always available and as 3T-CSD begins to be applied to the study of broader conditions and developmental situations additional context is necessary to formulate hypotheses regarding the physiological change to the cellular microstructure that is observed in human studies. This context is especially necessary to interpret results from studies observing the

relationship between cellular microstructure and variables with undetermined effects on neuronal physiology, such as pubertal hormones.

With the trajectory of volumetric MRI well established it is necessary to explore the cellular microstructure that underlies volumetric change with much greater detail, both with advanced dMRI models such as 3T-CSD and with detailed analysis of specific regions of the brain at multiple scales and between hemispheres. The goal of this study is to analyze a large number of subjects from a publicly available population cohort in order to provide a lifespan trajectory for 3T-CSD measurements of cellular microstructure from multiple areas of the brain. Establishing the relationship between chronological age and microstructural metrics will establish normal reference ranges and trajectories that are essential before investigating abnormal populations. This study will additionally investigate differences in cortical and subcortical areas and lateralized effects to inform future studies of significant regional and laterality differences that must be accounted for.

Methods

NKI/Rockland Cohort Data Acquisition

Data for this study was obtained from the Nathaniel Kline Institute's Rockland Study (NKI/Rockland) cohort[158]. NKI/Rockland is a large-scale community sample of participants with ages across the lifespan gathered in Rockland County, New York. Rockland County was selected in part because its diverse ethnic and economic demographics resemble those of the United States as a whole, which aids generalizability to the broader population. A wide array of physiological, cognitive, genetic and neuroimaging assessments are collected and publicly released (available at: http://fcon_1000.projects.nitrc.org/indi/enhanced/index.html)[158].

In this study the 409 subjects from the NKI/Rockland study that passed quality control and were publicly available at the time proceeded to analysis. These subjects ranged in age from 6-85 years-old (mean 42.67 ± 20.79 S.D.). There were 144 male and 265 female participants with average ages of 36.09 ± 21.22 S.D. and 46.25 ± 19.68 S.D., respectively. These ages were

not equivalently distributed between sexes (Kolmogorov-Smirnov; D=0.276, p<0.001) which precluded performing analysis to compare trajectories between sexes.

Diffusion image processing and analysis

dMRI data from 521 subjects was acquired using a Siemens MAGNETOM TrioTim 3T scanner with an isotropic voxel size of 2.0×2.0×2.0mm^3, TE=85ms and TR=2400ms; 9 b=0s/mm^2 images and 127 gradient directions at b=1500 s/mm^2. These images were processed through an automated pipeline with several manual quality control steps as follows. Each diffusion image set was analyzed using SS3T-CSD[10,90] implemented in the open source software MRtrix and Mrtrix3Tissue[12,90]. Several preprocessing steps utilized FSL[104,105]. Diffusion images were denoised [107], corrected for Gibbs ringing[109], susceptibility distortions[104], subject motion[116], and eddy currents[110]. All images were upsampled to of 1.3×1.3×1.3mm, and skull-stripping was performed using the Brain Extraction Tool [105]. Response functions were generated[88] from each tissue type and used to generate fiber orientation distributions (FODs)[10]. Signal fractions were calculated directly from the FODs using 3-tissue constrained spherical deconvolution (3T-CSD), a method that measures cellular microstructure within each voxel fitting into intracellular anisotropic (ICA, white matter-like), intracellular isotropic (ICI, gray matter-like), and extracellular isotropic (ECI, cerebrospinal fluid-like/Free Water) compartments[100]. Whole brain measurements were calculated from native space signal fraction compartments. These metrics used a smaller whole brain mask that excluded the ventricles and subarachnoid space via a ECI threshold that restricted the voxels to only those containing a majority signal fraction from brain tissue compartments and not extracellular fluid.

White matter FODs were used to generate a cohort-specific FOD template image from 50 individuals between ages 32-38 years-old and each subject's individual WM FOD image was registered to this template. Manual quality control of registration to the cohort-specific FOD template was performed by visual inspection, excluding any subjects with obvious distortions or extreme shears. Following this procedure 409 subjects remained in the study for analysis. An FOD template in stereotaxic space was created using the NTU-DSI-122 template (https://www.nitrc.org/projects/ntu-dsi-122/), extracting the equivalent single b-value shell and

was registered to the cohort-specific template generated from this study[135]. This allowed for two separate atlases to be warped into the cohort template space to measure signal fraction averages within specific regions of interest.

Regions of Interest

In order to cover a wide range of brain regions including cortex and deep white matter both the JHU-DTI based ICBM-DTI-81 white matter atlas (available as part of FSL, hereafter referred to as the JHU WM atlas) including 48 ROIs[105,228–230], and the Destrieux atlas including 164 ROIs[186] were warped into the study space. The cortical ROIs from the Destrieux atlas were summarized in a whole cortical ribbon ROI, as well as a cerebellum GM, and a total subcortical GM ROI. The 48 ROIs from the JHU WM atlas were also combined to provide a summary of the WM skeleton.

Subcortical GM ROIs were utilized from the Destrieux atlas, the nucleus accumbens, amygdala, caudate, hippocampus, putamen, and thalamus were included without alteration. The Destrieux atlas cortical ROIs were also separately combined into one of 8 lobar cortical regions per hemisphere as specified by the atlas and packaged in Freesurfer[186,231]. The cortical ROIs separately encompassed frontal, insular, limbic, motor, occipital, parietal, sensory, and temporal cortices.

Statistical Approach

Signal fraction values from each of the three tissue compartments (ICA, ICI, and ECI) were averaged within each of the ROIs for use in analysis. The average values for the three tissue compartments were plotted against age for each of the 409 subjects. Total age-related change was examined both across these age groups and within each phase by the plotting of locally weighted scatterplot smoothing lines (loess) lines of best fit. This was performed in R using the default settings of a 2nd order polynomial and span of 0.75 (meaning the localized slope reflects the closest 75% of data points). As a model-free way of displaying general trends loess lines were selected for descriptive purposes to show overall change in each signal fraction and

facilitate between ROI comparisons. To provide more precise information on rates of change simple linear models were calculated predicting signal fraction from subject age and the slope of that relationship displayed for each ROI. For ease of comprehension as well as to delineate periods of particular interest across the lifespan (i.e. development, late age-related decline) we have divided the subject cohort into 4 different life phases: 1) developmental phase before 20 years of age, 2) early adulthood phase between 20-40 years of age, 3) late adulthood phase between 40-60 years of age, and 4) senescence phase greater than 60 years of age. This division allows for an overview of the entire lifespan as well as comparisons to studies which only feature cohorts within a particular age range (for example, development or advanced age).

The lateralized approach taken in this study for each of the subcortical and cortical ROIs allows for the comparison for each signal fraction between the left and right hemispheres. Measurements were taken from the left and right ROIs and compared across the lifespan using pairwise t-tests to compare each lateralized region within subjects. P-values were subsequently adjusted using a Benjamini & Hochberg correction for multiple comparisons.

Results

Whole brain shows developmental shift from ICI to ICA, followed by increasing ECI in aging

As each whole brain signal fraction was individually collected in an equivalent native space they are displayed, colored by age, as a ternary plot to illustrate change across the brain, across the lifespan (Fig. 1). It was observed that whole brain metrics begin with a higher percentage of signal from the ICI compartment early in development, then progressing toward a greater signal fraction contribution from ICA in adulthood. Signal fraction contribution from ECI does not appear to change greatly during this time. During aging however, ECI increases at the expense of both ICA and ICI as the brain declines and atrophy occurs.

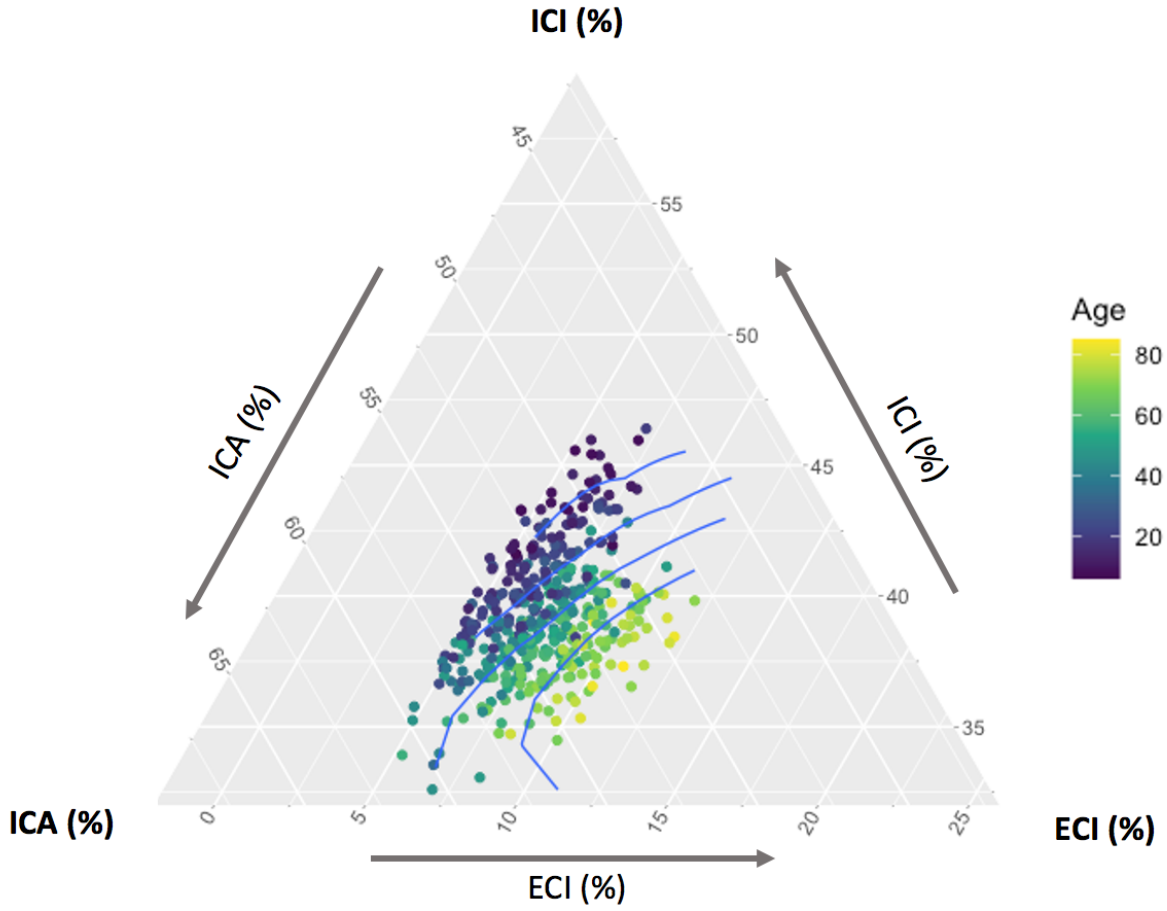

Figure 1: Ternary plot showing whole brain relationship between each of the 3T-CSD tissue compartments and subject age. Blue lines divide subjects into five 20%-tile groups based on age to illustrate change in signal fraction values across the lifespan. Whole brain tissue has the highest proportion of ICI signal fraction early in the lifespan, as development occurs the ICA signal fraction reaches its highest peak, and in later life the ECI signal fraction increases as the brain tissue declines.

Large anatomical subregions show increasing ECI, decreasing ICI, and an inverted U-shaped ICA signal fraction across the lifespan

Loess lines of best fit (A) and the linear slope of change per year within each age group (B) are presented for the initial 4 generalized regions in Fig. 2. While the specific proportion of ICA, ICI, and ECI is different in each region, which is to be expected given that each region is largely defined by the predominance of a specific cell type, there is largely a consistent pattern of change in each across the lifespan. Matching the whole brain results, ECI showed low levels in

development before 20 years of age, ECI even decreased in white matter areas covered by the JHU WM atlas and in subcortical GM structures. ECI remained largely flat in the early adulthood phase, between 20-40 years of age, but began to rise sharply during late adulthood between 40-60 years of age, with the sharpest increase occurring in the subcortical structures and cortical ribbon. In senescence greater than 60 years of age all major regions showed increasing levels of ECI reflecting widespread brain atrophy, loss of cellular integrity, and decline. The ICI signal fraction largely declined in all regions of the brain across the lifespan, though with important exceptions. The WM skeleton in the senescence phase showed a surprising *increase* in ICI signal fraction, especially considering that this is an area with very little ICI signal fraction. The cerebellum also remained relatively static in ICI signal fraction measurements until the senescence phase. The ICA signal fraction however, displays an inverted U shape across the lifespan, first rising greatly during development, slowing during the early adulthood phase, then increasing in decline during the early and senescence phases. The cerebellum is relatively consistent in ICA signal fraction in the development and late adulthood phases but otherwise each region is consistent in the trajectory of ICA measurements.

Subcortical GM ROIs typically follow whole brain trajectory but differ greatly from each other

Proceeding to a greater level of detail in different components of the subcortical GM, were independently measured in each hemisphere and plotted similarly to the larger anatomical areas (Fig. 3). A majority of the ROIs in this sample followed the general pattern observed for the area as a whole, but several important deviations can be observed, both in absolute differences in tissue composition as well as different trajectories across the lifespan. For example, the caudate nucleus early in life has a relatively low ECI signal fraction closer to the more internally located nucleus accumbens, but by middle age this structure contains a higher ECI signal fraction than the hippocampus, and the rate of increase then continues to accelerate until the structure has the highest average signal fraction of any subcortical structure late in life. Other structures demonstrate substantial deviations from the trajectory of the subcortex as a whole, most notably the putamen, which appears largely resistant to large age-related increases in ECI signal fraction, but in early development also the amygdala and hippocampus which decrease in ECI signal fraction more akin to the WM skeletal trajectory than the cortical

trajectory. The basal ganglia appear to have the least ECI signal fraction and have matching trajectories, but the ventral striatum nucleus accumbens and the dorsal striatum putamen show different trajectories in the other signal fraction compartments indicating different responses to age-related change.

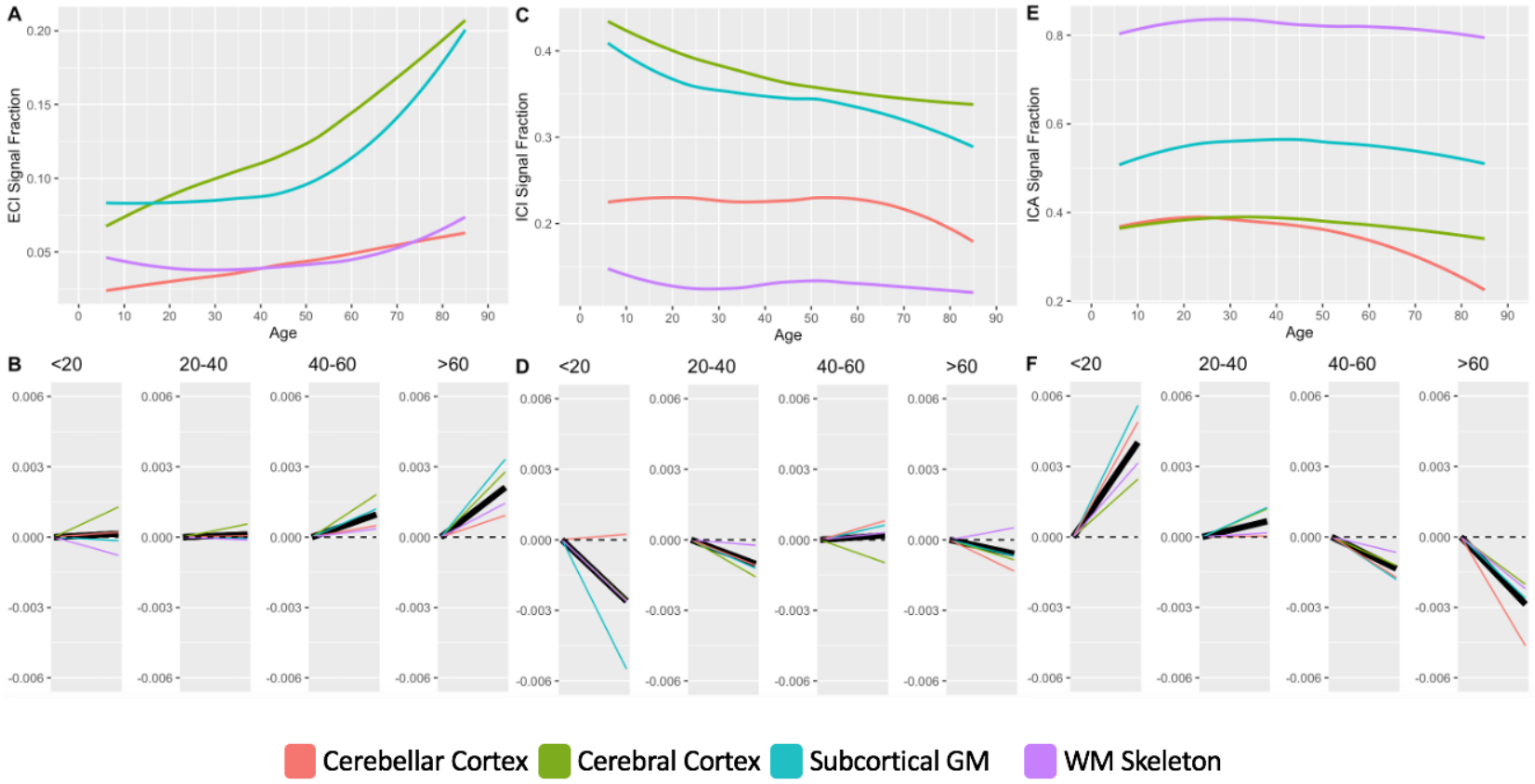

Figure 2: Charts displaying the lifespan trajectories of each 3T-CSD metric in 4 large anatomical brain subareas. The relationship between age and signal fraction is displayed either across the whole lifespan (A, C, & E for ECI, ICI, & ICA respectively) or as the slope of the linear relationship during a limited age range (B, D, & F for ECI, ICI, & ICA respectively). Overall, signal fraction compartment trajectories were relatively consistent between brain subareas, with a positive relationship between ECI and age, a negative relationship between ICI and age, and a positive relationship between ICA and age in the first two life phases, followed by a negative relationship between ICA and age in the later two life phases. There were however several interesting exceptions to this general trend. Within the WM skeleton there was a negative relationship between age and ECI signal fraction in the developmental

phase, likely due to increased myelination reducing the extracellular space available for freely diffusing water. On the opposite end of the lifespan, in the senescence phase the WM skeleton displays an increase in ICI signal fraction.

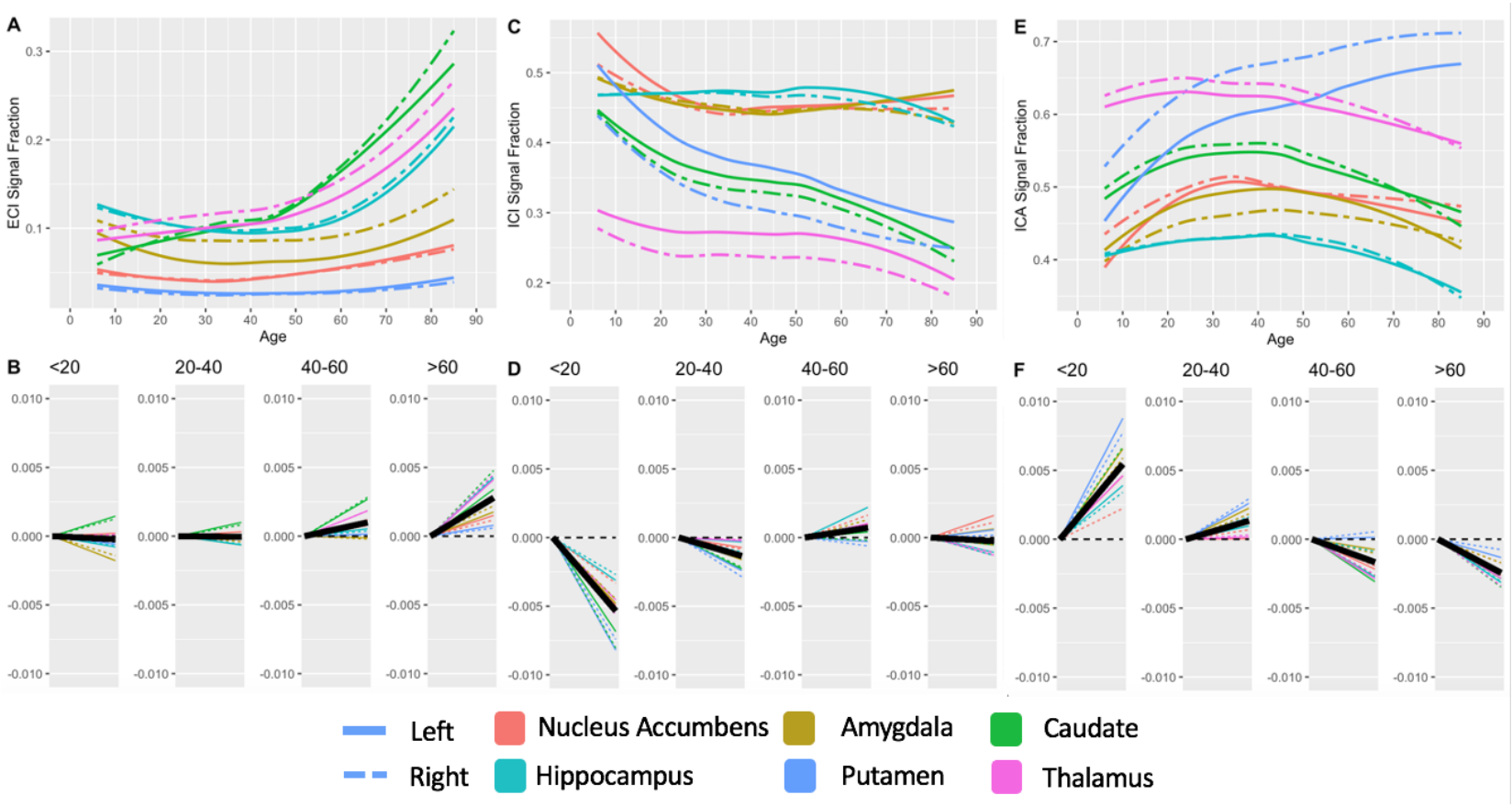

Figure 3: Charts displaying the lifespan trajectories of each 3T-CSD metric in 6 subcortical gray matter structures, including both left and right structures. The relationship between age and signal fraction is displayed either across the whole lifespan (A, C, & E for ECI, ICI, & ICA respectively) or as the slope of the linear relationship during a limited age range (B, D, & F for ECI, ICI, & ICA respectively). Trajectories largely follow the pattern established for the whole subcortical GM structure in Fig. 2, however some notable deviations: for the ECI signal fraction both amygdala, hippocampal, and amygdala drive the slight decrease in ECI signal fraction before 20 years of age, while caudate and thalamus surprisingly show steep increases during this time period and the hippocampus continues decreasing until reaching the late adulthood phase. In the ICI tissue compartment the thalamus, caudate, and

putamen follow the whole subcortical trajectory, but the amygdala, nucleus accumbens, and to a near degree the hippocampus, are more resistant to age-related decline. In the ICA tissue compartment the putamen is likewise resilient to age-related decline.

While the trajectory of each subarea largely appears more or less extreme in the ECI signal fraction, in the ICI and ICA signal fraction compartments some of the subareas deviate entirely from the established trajectory. The amygdala, nucleus accumbens, and to a near degree the hippocampus, are more resistant to age-related decline and do not display substantial ICI signal fraction decrease in the early adulthood and late adulthood phases. These three regions approach the highest age included in this study with approximately 15% points higher (a greater than 50% increase over) ICI signal fraction than the putamen and caudate which begin development at a reasonably similar ICI signal fraction. The hippocampus follows a trajectory more akin to the cerebral cortex, but this is not relevant for the deep internal structure of the amygdala and nucleus accumbens. While each of the subcortical GM structures shows a wide range of ICA signal fraction compositions, the largest outlier is the putamen, which shows an increase in ICA signal fraction throughout the lifespan even as every other region begins to decline in the early and senescence phases. Toward the end of the lifespan the putamen even approaches within 10% points of the ICA signal fraction within the WM skeleton.

Subcortical GM show significant and consistent lateralized differences

Results from lateralized comparisons are presented in Table 1. There was a high degree of lateralization in nearly all signal fractions with 15 out of 18 possible signal fraction/ROI combinations showing a significant difference between right and left hemispheres after correction for multiple comparisons. The ECI signal fraction was significantly higher in the right hemisphere in 4 of the 6 ROIs, as was the ICA signal fraction. The ICI signal fraction was higher in each left hemisphere ROI and was significantly so in all but the amygdala. The putamen, thalamus, and amygdala were observed to have the greatest laterality (at least one signal fraction compartment with a mean difference greater than 2%). The Hippocampus displayed the smallest average difference between left and right hemispheres, but was still significantly different for 2 of the 3 signal fractions, displaying how prevalent lateralized differences in structure are in the brain.

ROI	Tissue Type	Higher Signal Fraction	Mean Difference	t-value	Adjusted p-value	
N. Accumbens	ECI	*Left*	0.0005	0.359	0.720	n.s.
	ICI	*Left*	0.0106	2.634	0.012	*
	ICA	*Right*	0.0100	2.139	0.040	*
Amygdala	ECI	*Right*	0.0232	19.596	<0.001	***
	ICI	*Left*	0.0010	0.554	0.614	n.s.
	ICA	*Left*	0.0226	11.264	<0.001	***
Caudate	ECI	*Right*	0.0049	3.073	0.003	**
	ICI	*Left*	0.0156	10.608	<0.001	***
	ICA	*Right*	0.0106	7.158	<0.001	***
Hippocampus	ECI	*Right*	0.0029	2.517	0.016	*
	ICI	*Left*	0.0066	3.995	<0.001	***
	ICA	*Right*	0.0031	1.768	0.088	n.s.
Thalamus	ECI	*Right*	0.0169	21.483	<0.001	***
	ICI	*Left*	0.0324	32.87	<0.001	***
	ICA	*Right*	0.0155	12.574	<0.001	***
Putamen	ECI	*Left*	0.0021	5.632	<0.001	***
	ICI	*Left*	0.0578	22.783	<0.001	***
	ICA	*Right*	0.0598	22.542	<0.001	***

Table 1: Lateral differences between subcortical GM structures across the lifespan. Pairwise t-tests were used to compare each lateralized region within subjects and p-values were adjusted using a Benjamini & Hochberg correction for multiple comparisons. The ICI signal fraction was higher in each left hemisphere ROI and was significantly so in all but the amygdala. The putamen, thalamus, and amygdala were observed to have the greatest laterality (at least one signal fraction compartment with a mean difference greater than 2%).

Lobar cortical regions show similar trajectories across the lifespan but different absolute measurements and inconsistent but significant lateral differences

The cerebral cortex was then subdivided into 8 regions of cortex separated by left and right hemisphere as defined by the Destrieux atlas and measurements were made as before (Fig. 4). The signal fraction measurements in these regions generally followed the overall region trajectory displayed in Figure 3 but as with the subcortical GM there were some exceptions. The

ECI signal fraction increased in every ROI in both the early and senescence phases. In the ICI and ICA signal fractions the insular and limbic cortices displayed markedly higher solid tissue values than other cortical regions while still following relatively similar trajectories. There was a significant degree of hemispheric laterality between the left and right sides of the brain (Table 2), with little consistent differences between the signal fraction compartments.

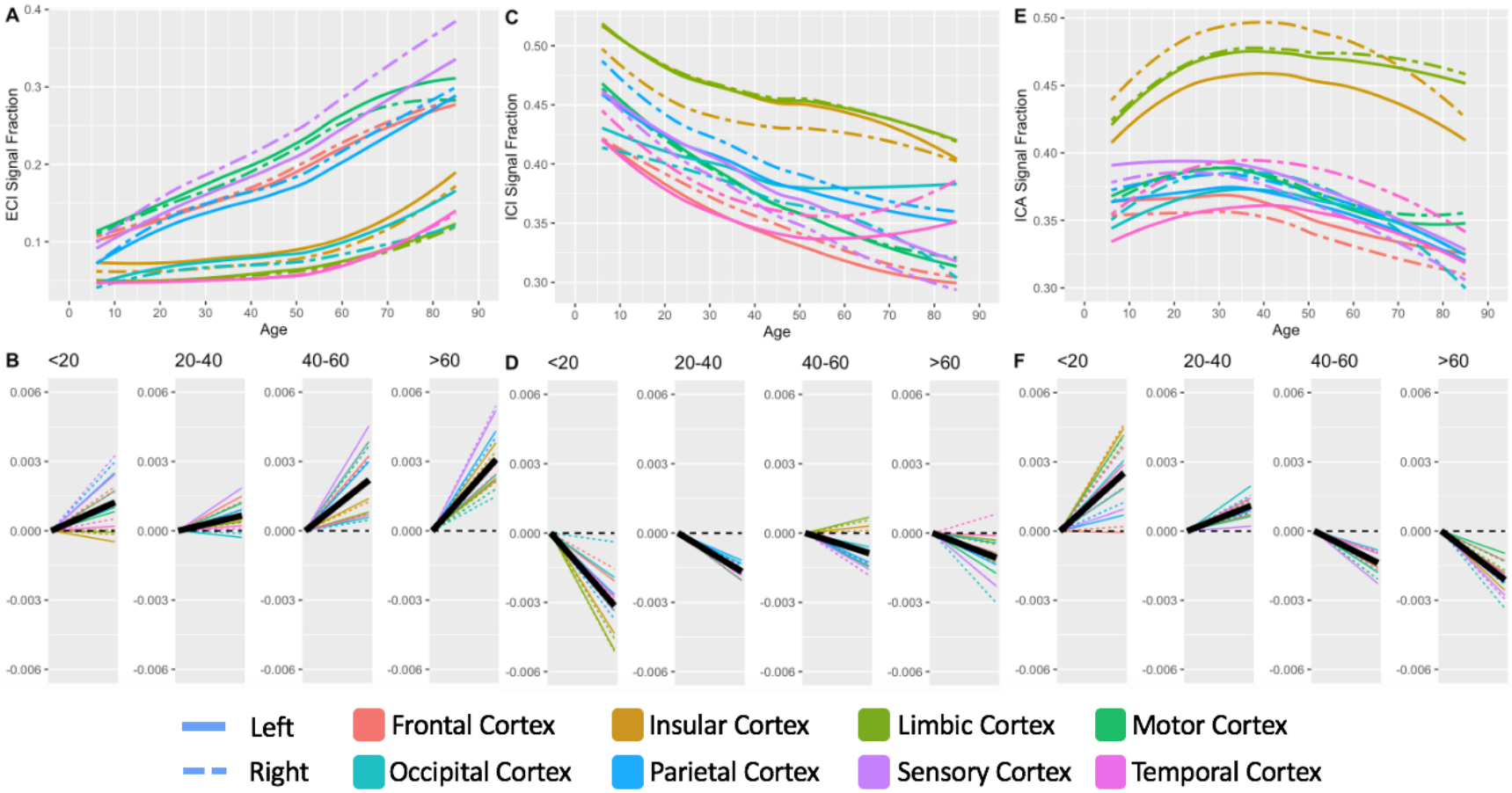

Figure 4: Charts displaying the lifespan trajectories of each 3T-CSD metric in 8 cortical ROIs. The relationship between age and signal fraction is displayed either across the whole lifespan (A, C, & E for ECI, ICI, & ICA respectively) or as the slope of the linear relationship during a limited age range (B, D, & F for ECI, ICI, & ICA respectively). Several deviations from the average trajectory occur in the middle age phases in the cortex in the insular and limbic cortices in the ICI signal fraction but otherwise declines across the lifespan. The frontal cortex in the developmental age phase shows little to slightly positive change in the ICA signal fraction but otherwise follows a consistent upward trajectory during the initial two life phases followed by decreases in the next two life phases.

ROI	Tissue Type	Higher Signal Fraction	Mean Difference	t-value	Adjusted p-value	
Frontal Cortex	ECI	*Right*	0.0052	6.861	<0.001	***
	ICI	*Right*	0.0088	9.783	<0.001	***
	ICA	*Left*	0.0111	12.376	<0.001	***
Insular Cortex	ECI	*Left*	0.0121	16.632	<0.001	***
	ICI	*Left*	0.0207	15.656	<0.001	***
	ICA	*Right*	0.0339	30.966	<0.001	***
Limbic Cortex	ECI	*Left*	0.0021	4.365	<0.001	***
	ICI	*Right*	0.0012	1.896	0.067	n.s.
	ICA	*Right*	0.0036	4.665	<0.001	***
Motor Cortex	ECI	*Left*	0.0088	5.579	<0.001	***
	ICI	*Left*	0.0009	0.742	0.4583	n.s.
	ICA	*Right*	0.0021	1.425	0.1692	n.s.
Occipital Cortex	ECI	*Left*	0.0124	14.573	<0.001	***
	ICI	*Left*	0.0196	7.591	<0.001	***
	ICA	*Right*	0.0078	4.227	<0.001	***
Parietal Cortex	ECI	*Right*	0.0116	10.953	<0.001	***
	ICI	*Right*	0.0137	15.809	<0.001	***
	ICA	*Right*	0.0089	12.574	<0.001	***
Sensory Cortex	ECI	*Right*	0.0312	16.461	<0.001	***
	ICI	*Left*	0.0186	13.752	<0.001	***
	ICA	*Left*	0.0124	8.283	<0.001	***
Temporal Cortex	ECI	*Right*	0.0008	1.232	0.2282	n.s.
	ICI	*Right*	0.0209	14.775	<0.001	***
	ICA	*Right*	0.0308	19.764	<0.001	***

Table 2: Lateral differences between cortical GM regions across the lifespan. Pairwise t-tests were used to compare each lateralized region within subjects and p-values were adjusted using a Benjamini & Hochberg correction for multiple comparisons. All cortical regions showed some significant degree of lateralization with the insular and temporal cortices each having a mean difference of greater than 2% ICA and ICI signal fraction measurements between left and right hemispheres. Conversely the limbic and motor cortices each had a mean difference of less than 0.5% excepting the ECI signal fraction in the motor cortex. Interestingly, as opposed to the subcortical areas which demonstrated relatively consistent right/left biases for the signal fraction compartments, there was a more balanced distribution of right/left biases for each of the signal fractions.

Discussion

This study examined a large population cohort using an advanced diffusion microstructure analysis technique to describe the relationship between chronological age and changes in brain cellular structure. The slope of these changes was steeper during the developmental phase before 20 years of age and in the senescence phase after 60 years of age with more gradual changes occurring between 20 and 60 years of age in the middle of the adult phases of the lifespan. The pattern established at the whole brain level, a shift toward increasing ICA signal fraction in the first half of the lifespan largely coupled with decreasing ICI signal fraction (as they sum to 1, any increase/decrease in one signal fraction compartment must be coupled with equivalent increases/decreases in the others); subsequently gives way to a decline pattern later in life characterized by increasing ECI signal fraction coupled with decreasing ICA signal fraction.

When the WM skeleton, cerebral cortex, cerebellular cortex, and subcortical GM were parcellated from the cohort it was observed that the ECI signal fraction increased precipitously with increasing age after 40 in all 4 ROIs but during development was stable in the subcortical GM and cerebellum, declined in the WM skeleton, and increased in the cortex. Despite three of the ROIs being thought of as predominantly GM areas there was observed a widespread negative correlation with age throughout the lifespan. During the developmental phase the ICA signal fraction increased dramatically in each of the 4 ROIs, matching the well-established trajectories observed in volumetric data from this time period[232,233]. Interestingly, the increased axonal innervation of the cortex during development can be observed in this trajectory as well as in the subcortical GM structures. This axonal innervation has been suggested to shift the WM/GM boundary line in volumetric studies[234] and this study certainly supports the cortex and subcortical GM structures becoming more similar to the WM skeleton in microstructural profile as development progresses. An interesting exception to this trend is in the frontal cortex, which has a flat slope for the relationship between ICA signal fraction and age during the developmental phase. This study also showed far more dramatic changes throughout the lifespan compared to large-scale volumetric MRI studies[13,14]. Change in brain metrics in this study was not solely confined to early development and late senescence, and there was very large and distinct

trajectories for each tissue compartment across different ROIs, suggesting that age-related change is a highly complex process with different, distributed effects in different brain structures.

Laterality was examined and was found to have a highly significant effect across multiple regions but this was typically without a consistent direction. The putamen, thalamus, amygdala, insular cortex, and temporal cortex were observed to have the greatest laterality (at least one signal fraction compartment with a mean difference greater than 2%). The Hippocampus displayed the smallest average difference between left and right hemispheres, but the ECI and ICI signal fraction compartments were still significantly different, recapitulating previous work that found a significantly increased ECI signal fraction in the right hippocampus[100].

Other advanced dMRI models have examined the relationship between their quantitative measurements and age across the lifespan. In a recent study NODDI outputs of isotropic volume fraction, roughly comparable to 3T-CSD's ECI signal fraction, increased throughout the lifespan across the whole brain. Meanwhile intracellular volume fraction displayed an inverted U shaped pattern similar to 3T-CSD's companion ICA signal fraction[235]. Another NODDI study however found conflicting results using orientation dispersion index, which does not have a direct 3T-CSD parallel, with results from Nazeri et al., finding orientation dispersion decreased across the lifespan in 4 cortical lobe ROIs, and Beck et al., finding that orientation dispersion increased across the whole brain[235,236]. The current study found much more complicated relationships between many of the cortical lobes and age across the lifespan, and while this study did not directly compare results from different quantitative dMRI models, it is notable that NODDI and other advanced models did not perform better than traditional DTI metrics at predicting brain age[235].

There may be an expressed relationship in this study between signal fraction (particularly the relative proportion of ICA and ICI signal fractions) and neuronal cellular density as determined by histology. In particular the limbic cortex is known as having a particularly low neuronal density in humans[237] and in this study was surprisingly found to have the highest level of ICI signal fraction (along with the insular cortex) throughout the lifespan. This suggests that a

relatively low density of neurons may not cause a high ECI signal fraction but will instead be represented as an overly high ICI signal fraction, perhaps due to increased glial cell population or larger levels of intracellular space in comparison to areas of high neuronal and dendritic density, such as the cerebellum. This ROI did subsequently follow similar trajectories to other ROIs with differing levels of neuronal density and arrangement, but it regardless may hold promise as an effect replicable in pathological conditions affecting neuronal density. Decreased neuronal density in the prefrontal cortex has been implicated in major depressive and bipolar disorders, suggesting 3T-CSD may be a potential mechanism for tracking alterations in these patients[238,239].

Other disorders may result from increased neuronal density including schizophrenia which may present a different signal fraction profile that is able to be detected using 3T-CSD[240,241]. The developmental component of schizophrenia may allow for early detection if adolescents begin deviating from age-related trajectories similar to those established in this study. Another dMRI microstructural analysis technique, termed free water elimination, has suggested that increased extracellular water may also contribute to the development of schizophrenia[75], however this method does not measure both extracellular and isotropic intracellular tissue compartments and thus makes an imperfect point of comparison to the 3T-CSD technique used here.

A known feature of the aging brain that was not accounted for in this study is the development of white matter hyperintensities (WMH). Previous work has demonstrated that developed and developing WMH are detectable using 3T-CSD and have increased ECI and ICI signal fraction with correspondingly reduced ICA signal fraction compared to normal appearing areas of the WM skeleton[91]. The presence of WMH not accounted for in this study for several reasons, including that the location of the WMH in the brain was largely determinative of its microstructural properties, with WMH located proximal to the ventricles having a greater amount of ECI signal fraction than WMH located within the deep WM[91]. Additionally, there is evidence that 3T-CSD is sensitive to developing WMH that subsequently appear after cerebral infarction[227]. This created a situation where removing tissue identified via independent means as a WMH might contribute noise to estimates of subjects in the senescence phase and would be difficult to account for in the whole lifespan trajectories. Another feature not accounted for was

subject sex due to the imbalance of women to men especially in the late adulthood and senescence phases, but this is undoubtably a subject worth investigating for differences between sexes in future lifespan work.

In conclusion these results describe the relationship between brain microstructure and age and illustrate how dMRI correlates of cellular microstructure changes throughout the lifespan. These results provide a powerful illustration of the dramatic shifts in microstructure metrics during development and aging and highlight the potential of 3T-CSD as a tool to study development and aging. Establishing patterns of microstructure change across the lifespan will aid in studying and interpreting microstructure change in the presence of pathology. Studies analyzing dMRI microstructure in developing or aging cohorts should address shifts in anisotropic and isotropic signal in development and dramatically increased levels of extracellular water in aging.

Study 2b

Aim 2b: Determine if 3T-CSD microstructure measurements are altered by pubertal development during the critical period of early adolescence.

Rationale: Adolescent development is a time of great structural and functional change. 3T-CSD measurements of brain microstructure may be more sensitive to factors affecting development than traditional structural metrics. This sensitivity can be augmented by the recent release of the massive Adolescent Brain Cognitive Development (ABCD) Study, an exceptionally high quality longitudinal dataset tracking over 11,000 children[128]. Understanding neuronal development during the critical period of puberty will support understanding of lifelong brain and mental health. During puberty the developing brain undergoes substantial neuroanatomical reorganization at both global and cellular scales[222]. This critical period can leave the brain particularly vulnerable, and puberty marks the peak emergence of a majority of neuropsychiatric disorders[242,243]. Understanding the relationship between the cells of the brain and pubertal maturation is an important component of adolescent health and well-being throughout the remainder of the lifespan.

Experimental Design: The ABCD Study will be analyzed using the previously established 3T-CSD pipeline and microstructure measurements will be analyzed from the same 212 ROIs examined in the NKI-Rockland dataset in Study 2a. Pubertal development has been assessed by the ABCD Study and the pubertal development score (PDS) is available for each subject[244]. The PDS measures physical manifestations of pubertal development on a scale from 1 (no development) to 4 (development seems complete) across 3 measures common to both sexes and 2 measures each for adrenarche and gonadarche features. A total PDS score (PDSS) was calculated for each individual by summing the combined common, adrenarche, and gonadarche features of the questionnaire[245]. Microstructure measurements from ICA, ICI, and ECI tissue compartments will be taken in each of the 212 ROIs across the axonal areas and cortex in each subject. Once the microstructural results from the ABCD study are controlled for chronological age, sex, brain volume, and handedness, this will allow for identification of how puberty affects brain development trajectory and if this effect is localized to particular regions of the brain.

Study 2b

Title: More than just axons: A positive relationship between an intracellular isotropic diffusion signal and pubertal development in white matter regions in a massive adolescent cohort

Abstract

Puberty is a key event in adolescent development that involves significant, hormone-driven changes to many aspects of physiology including the brain. Understanding how the brain responds during this time period is important for evaluating neuronal developments that affect mental health throughout adolescence and the adult lifespan. This study examines diffusion MRI scans from the cross-sectional ABCD Study baseline cohort, a large multi-site study containing thousands of participants, to describe the relationship between pubertal development and brain microstructure. Using advanced, 3-tissue constrained spherical deconvolution methods, this study is able to describe multiple tissue compartments beyond only white matter (WM) axonal qualities. After controlling for age, sex, brain volume, and subject handedness, we observe a positive relationship between an isotropic, intracellular diffusion signal fraction and pubertal development, and a negative relationship between an anisotropic, intracellular tissue compartment and pubertal development throughout the WM regions. We also observe a small, regional effect from an extracellular isotropic free water-like compartment in several ROIs. This work suggests that changes during pubertal development elicit a complex response from brain tissue that cannot be completely described by traditional methods focusing only on WM axonal properties. This work brings in vivo human neuroimaging studies more into line with work performed on animal models, which describe an interaction between increased myelination, neurogenesis, angiogenesis, and glial cell proliferation in response to pubertal hormones.

Introduction

In adolescent development, puberty is a critical period that marks the hormonally driven transition into reproductive maturity[246]. Extensive physical, behavioral, and neurological changes occur rapidly and can have lifelong consequences for health and well-being. The developing brain undergoes substantial neuroanatomical reorganization at both global and cellular scales[222].

This critical period can leave the brain particularly vulnerable, and puberty marks the peak emergence of a majority of neuropsychiatric disorders[242,243]. Understanding the relationship between the cells of the brain and pubertal maturation is an important component of adolescent health and well-being throughout the remainder of the lifespan[222,247]. Previous neuroimaging studies have largely focused on axonal changes, however the white matter regions of the brain contain numerous glial cell varieties and extracellular space that contributes to a diverse diffusion profile[248]. In this study we present evidence for a widespread positive relationship between pubertal stage and an isotropic, intracellular, gray matter-like diffusion signal within the white matter skeleton. This signal may be indicative of the beginning of pubertal neuronal reorganization, with implications for understanding the neurobiology of maturing brain tissue.

Evidence from studies in animal models, where the levels of pubertal hormones can be directly manipulated, has demonstrated the effect of these hormones on the organization of brain tissue[249]. Pre-pubertal gonadectomy was shown to reduce the number of new, BrdU-positive cells in the brains of male and female rats, localized in a sex-dependent manner to regions that show post-pubertal sex-dependent differences in volume[250]. In female songbirds, axonal organization in song motor pathways have been reversibly manipulated via a testosterone injecting implant[251]. It has been suggested that pubertal hormones can influence the proliferation and survival of neurons mediated by local production of vascular endothelial growth factor and brain-derived neurotrophic factor[252]. Though it is unknown to what degree this process is analogous to human development, and in vivo human studies must largely rely on neuroimaging techniques for insight.

Structural neuroimaging studies have consistently described a pattern of brain changes following the onset of puberty: an increase in the global volume of white matter (WM) and a decrease in the volume of gray matter (GM) both cortically, sub-cortically, and at the WM-GM boundary[232,233,253]. It was long thought that this 'thinning' of the GM cortical areas was the result of synaptic pruning of unnecessary or inefficient synapses[254]. However, treating brain tissue as homogenous, binary, compartments to be examined individually may have obscured the process underlying the observed effect. The microstructural mechanism for this decrease in GM and increase in WM has been suggested to rely on increased myelination into the cortical GM areas

which then appear to shift the location of the GM/WM boundary on T_1-weighted images[234]. This highlights the necessity for neuroimaging methods that can examine within-tissue cellular characteristics.

Diffusion MRI (dMRI) has provided more detailed measurements of in vivo brain development and allows for characterization of cellular microstructure within WM areas. Early dMRI studies using diffusion tensor imaging (DTI) found an increase in fractional anisotropy (FA), a measurement of axon coherence and myelination, and a decrease in mean diffusivity (MD) and radial diffusivity, indicative of reduced cellular permeability, as adolescents matured[232,255–257]. DTI is limited however, by a lack of specificity and from interference from heterogenous tissue composition or from multiple WM orientations (the 'crossing fibers' problem) in a single voxel[53,150]. By collapsing the diffusion signal into a single tensor, standard DTI metrics may be obscuring subtle but important cellular and sub-cellular changes in tissue composition.

More advanced diffusion analysis techniques such as multi-compartment models and constrained spherical deconvolution methods have improved on DTI by characterizing signals from multiple tissue types, multiple WM fiber orientations, or both. Two studies have examined the early adolescent period using multi-compartment neurite orientation dispersion and density imaging (NODDI) which can provide more detailed measurements of brain microstructure than DTI[58]. Both studies found a widespread positive association with age in neurite density index, a model of intra-neurite space thought to describe myelination and axonal growth, but no relationship between age and orientation dispersion index, a model of inter-neurite space[258,259].

Fixel-based analysis (FBA) is a promising dMRI model that builds off of spherical harmonic representations of WM that can overcome the pitfalls of DTI by being both sensitive and specific to WM fiber bundles without interference from isotropic signal from cell bodies/somas or from extra-cellular CSF[94,260]. A pair of studies have used FBA to examine a cross-sectional[258] and longitudinal sample[261] of developing subjects from the Children's Attention Project study[262]. These studies explored the relationship between pubertal development, as measured by the pubertal development scale[244,245], and WM measurements derived from FBA in

ROIs defined by the JHU-ICBM atlas[183,228,230]. The cross-sectional study only found a significant relationship between fiber density and pubertal development in the splenium of the corpus callosum, while the longitudinal study found a broader range of significant areas throughout the WM skeleton.

In this study, we aim to move away from the WM axon focused metrics toward a more holistic measurement of brain microstructure accounting for multiple cellular environments encountered in the brain: axonal, anisotropic, WM-like diffusion; intracellular, isotropic, GM-like diffusion; and extracellular, isotropic, CSF-like diffusion[91,100]. Each of these compartments allow for the evaluation of different and distinct cellular environments within the same voxel. This study examines the relationship between pubertal development and cellular microstructure at the beginning of adolescence within 'WM' areas but measuring the whole microstructural environment, not exclusively axonal characteristics, as previous literature has done.

Methods

Participants

This study utilized baseline data obtained from the Adolescent Brain Cognitive Development (ABCD) Study, a publicly available neuroimaging and demographic study examining child development and factors leading to substance abuse. The ABCD study is the largest adolescent neuroimaging dataset ever acquired in the United States with an enrollment of 11,874 subjects at baseline. From this we selected a subset of 7,219 subjects enrolled at sites equipped with Siemens manufacturer scanners for processing and analysis. Following an automated quality control process including removing subjects without completed diffusion scans, excessive motion, or other imaging artifacts, we were able to successfully analyze 5,245 subjects in native, scanner space. Following template construction successful registration and warp into the template space was assessed by visual inspection aided by a semi-automated process and 4752 subjects remained for final analysis.

Imaging data

Unprocessed dMRI images were obtained from the ABCD study and were acquired with a multiband accelerated sequence that had an isotropic voxel size 1.7 x 1.7 x 1.7 mm^3 with TE = 88 ms and TR = 4100 ms. Using a multi-shell protocol 7 images were acquired at b= 0, 6 directions were acquired at b=500 s/mm^2, 15 directions were acquired at both b=1000 s/mm^2 and at b=2000 s/mm^2, and 60 directions were acquired at b=3000 s/mm^2 [133]. Only images acquired using the Siemens Prisma 3T platform were analyzed to avoid manufacturer and sequence differences, including field gradient strength, TE, and TR, that have previously been demonstrated to affect outcome 3T-CSD signal fraction results[100].

Total brain volume was obtained from the ABCD study which released processed data as part of the baseline data release. Study organizers obtained this volumetric data from T1 weighted images with an isotropic voxel size 1.0 x 1.0 x 1.0 mm^3 with TE = 2.88 and TR = 2500 with a flip angle of 8 degrees and an FOV of 256 x 256 mm[133]. Volumetric data was calculated using an automated processing pipeline in Freesurfer and released as part of the ABCD data release 2.0.1. For further ABCD image processing details see[263].

Image Preprocessing and Analysis

Image preprocessing was performed consistent with prior protocols that have been shown to result in consistent and reliable signal fraction measurements[100]. All dMRI images were corrected for thermal noise using the "dwidenoise" command implemented in MRtrix3[107]. Gibbs rings were then removed with the "dwidegibbs" MRtrix3 function[109]. The FSL package ("topup" and "eddy") was subsequently applied to correct for susceptibility-induced (EPI) distortions, eddy currents, and subject motion, including the Gaussian replacement of outliers[104,110,115,116]. Finally the preprocessed images were upsampled using MRtrix3 to 1.3 x 1.3 x 1.3 mm^3 isotropic voxel size, similar to the high-resolution of images in the Human Connectome Project[117,212]. The b=0 and b=3000 s/mm^2 shells were then extracted to form a single-shell image set suitable for SS3T-CSD. This step was performed because prior investigations have suggested SS3T-CSD is superior at differentiating between brain regions compared to MSMT-CSD at b=3000 s/mm^2 [100].

Brain masks were obtained for all subjects by performing a recursive application of the Brain Extraction Tool[264]. Response functions from each of the three tissue types were estimated from a randomly selected subset of nearly 500 subjects and averaged to produce a single set of tissue response functions[88]. SS3T-CSD was then performed using the average response functions with MRtrix3Tissue, a fork of MRtrix3, to estimate an anisotropic WM-like (represented by a complete WM FOD); an isotropic, intracellular GM-like; and an isotropic, extracellular CSF-like compartments[90]. An example of this general pipeline, including preprocessing steps, is available at https://3tissue.github.io/doc/single-subject.html. Each subject's three tissue compartments were then normalized to sum to 1 on a voxel-wise basis, resulting in the final three-tissue signal fraction maps[91,100]. Summing the spherical harmonic coefficients on a rotational-invariant voxel-wise basis provides the added benefit of harmonizing inter-scanner and inter-subject signal intensity differences while preserving between-subject biological variation[265].

A cohort specific template was constructed from a random selection of 50 subjects' WM-FODs (Fig. 1a) using symmetric diffeomorphic registration of the FOD themselves and implemented in MRtrix3 with the "population_template" function[160]. Each subject was then individually registered to the cohort template using an affine, followed by a nonlinear registration guided by the WM FODs themselves in an unbiased manner. The resulting warp was used to move each of the subjects' three-tissue signal fraction maps into template space. Quality control was performed on the transformed signal fraction maps via visual confirmation of a semi-automated method that flagged images with abnormal values.

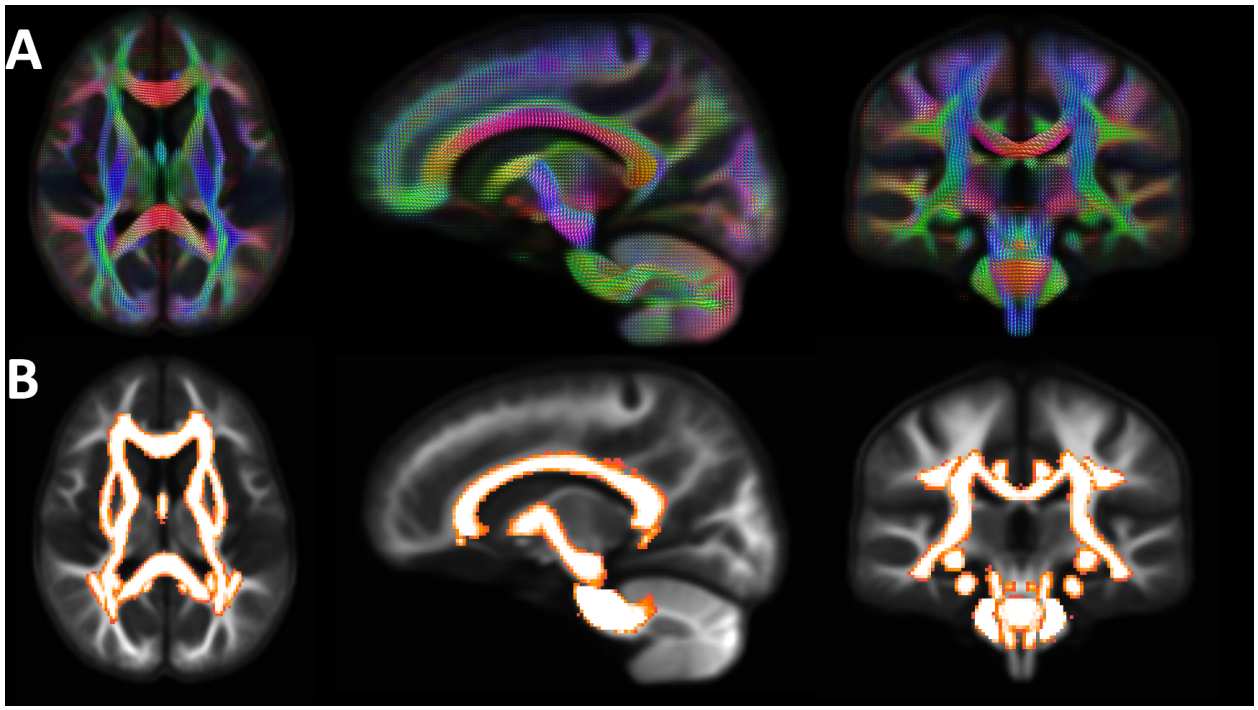

Figure 1: Graphic displaying the WM FODs of the cohort specific group template constructed from the average of 50 randomly selected ABCD subjects. The top row (A) displays the FODs themselves while the bottom row (B) shows the positioning of the 48 ROIs in the JHU-ICBM atlas after being warped into the template.

The cohort template was then registered to stereotaxic space with a similar FOD-based diffeomorphic registration procedure to a b-value matched version of the NTU-DSI-122 template[187]. The resulting warp from stereotaxis space was used to move the 48 ROIs included in the JHU-DTI based ICBM-DTI-81 white matter atlas (available as part of FSL, hereafter referred to as the JHU WM atlas; Fig. 1b) into the cohort specific template space[105,183,228,230]. The average value of each signal fraction map within each of the 48 ROIs was calculated using the "mrstats" function from MRtrix3.

Pubertal Development Scale

Measures of pubertal development were assessed via parental completion of the Pubertal Development Scale (PDS) questionnaire during the baseline subject visit[244,266]. The PDS measures physical manifestations of pubertal development on a scale from 1 (no development) to

4 (development seems complete) across 3 measures common to both sexes and 2 measures each for adrenarche and gonadarche features. A total PDS score (PDSS) was calculated for each individual by summing the combined common, adrenarche, and gonadarche features of the questionnaire[245]. PDSS has been demonstrated to significantly correlate with saliva testosterone, DHEA, and estradiol levels[245], was recorded for nearly every ABCD subject, and allows for more simplified direct comparison between sexes compared to saliva or serum hormone levels.

Statistical Analyses

Data summarization: Categorical data are summarized by frequencies (n) and percentages (%). Continuous scaled data are summarized by the mean, standard deviation, and range of the empirical distribution.

Patient demographic and patient characteristic analyses: A one-sample binomial exact test was performed to compare gender cross-sectional frequencies. A two-sample t-test was performed to compare the age distributions of the female and male cross-sectional samples. A two-sample t-test was also performed to compare the subject-specific average puberty score between female and male children.

Tissue signal fraction regression analyses: Ordinary least-square (OLS) regression was performed to predict the mean ROI tissue signal fraction (i.e. extracellular isotropic CSF-like; or intracellular isotropic GM-like; or intracellular anisotropic WM-like) in a given JHU atlas ROI as a function of the sum of the child's PDS scores (PDSS-sum), the child's age (years) and sex (female, male), the child's handedness (left, right, and ambidextrous) and the child's total brain volume (cm^3). The OLS regression model also included sex by age interaction, sex by PDSS-sum interaction, age by PDSS-sum interaction, and sex by age by PDSS-sum interaction. All of the OLS regression model predictor variables and interactions that were selected a priori based on scientific merit.

With regards to hypothesis testing, ANOVA type III F-tests were conducted to identify among the entire set of predictor variables and the entire set of predictor variable interactions

those predictor variables and those predictor interactions that explained unique information about tissue signal fraction variability that would not be expected to be explained purely by chance. Since a total of 48 OLS regression analyses were conducted per tissue signal fraction type (e.g. CSF), the Benjamini and Hochberg false discovery procedure[267] was used to identify pre JHU atlas ROI the predictor variables and the predictor interactions that were important predictors of tissue signal fraction. Predictor variables that produced an ANOVA type III F-test p-value for the null hypothesis test that the complete set of the OLS regression model coefficients associated with predictor variable (main effects and interactions combined) are equal to 0, less than the Benjamini and Hochberg 0.05 false discovery error rate threshold were deemed unique predictors of tissue signal fraction. Similarly, predictor variables that produced an ANOVA type III F-test p-value for the null hypothesis test that the complete set of OLS regression model coefficients associated with the interaction terms of the predictor variable are equal to 0, less than the Benjamini and Hochberg 0.05 false discovery error rate threshold were deem significant interaction terms with respect to predicting tissue signal fraction. Finally, per JHU atlas ROI, an ANOVA type III F-test was conducted to test the null hypothesis that the complete set of OLS regression model coefficients associated with the OLS regression model interaction terms are equal to 0. Benjamini and Hochberg 0.05 false discovery error rate procedure was applied to the entire set of 48 p-values. If the p-value was less than the Benjamini and Hochberg 0.05 false discovery error rate threshold value, the null hypothesis the complete set of OLS regression model coefficients associated with the OLS regression model interaction terms are equal to 0 was rejected.

Concomitant variable adjusted associations between tissue signal fraction and PDSS-sum. OLS regression was performed to examine concomitant variable adjusted associations between tissue signal fraction and PDSS-sum. The concomitant variables of the OLS regression model were child age and sex, child handedness, and child total brain volume. For each JHU atlas ROI, the concomitant variable adjusted association between tissue signal fraction (extracellular isotropic CSF-like, or intracellular isotropic GM-like, or intracellular anisotropic WM-like) and PDSS-sum was quantified by the regression slope coefficient estimate associated with PDSS-sum. For each JHU atlas ROI, a null hypothesis test was performed to test the null hypothesis that the slope of the association between the tissue signal fraction and PDSS-sum is equal to 0,

versus the alternative that the slope of the association between the tissue signal fraction and PDSS-sum is not equal to 0. The complete set of p-values from the 48 different JHU atlas ROI were then subjected to the Benjamini and Hochberg false discovery procedure to identify those ROI, in which the ANOVA type II F-test p-value of the null hypothesis test was less than the Benjamini and Hochberg 0.05 false discovery threshold.

Note that with respect to predictor variable interaction, only 7 null hypothesis out of 192 null hypotheses produced a p-value that meet the Benjamini and Hochberg false discovery error rate rejection threshold (summarized in Table 1), and no p-value meet the Benjamini and Hochberg false discovery error rate rejection threshold for the null hypothesis test that the complete set of the OLS regression model interactions provide no unique information about tissue signal fraction. Due to the sparsity of ROIs in which predictor variable interactions were identified, the entire set of interaction terms of the OLS regression model were removed for the OLS regression model so that partial associations between tissue signal fraction and PDSS-sum could be estimated by way of a more parsimonious OLS regression model in which child age and sex, child handedness, and child total volume served as the concomitant variables.

Tissue Signal Fraction	PDSS-sum # ROI (%)	Sex # ROI (%)	Age # ROI (%)	Total Volume # ROI (%)	Handedness # ROI (%)
CSF-like	18 (37.5)	22 (45.8)	40 (83.3)	35 (72.9)	6 (1.25)
GM-like	39 (81.3%)	45 (93.8)	48 (100)	43 (89.6)	0 (0)
WM-like	34 (70.8)	42 (87.5)	46 (95.8)	43 (89.6)	0 (0)

Table 1: Number of JHU ROI, in which the global hypothesis test for testing for no adjusted association between the tissue signal fraction and the predictor variable was be rejected after implementation of the Benjamini and Hochberg false discovery error rate procedure with an overall false discovery error rate of 0.05 for the entire set of 48 null hypothesis tests.

Results

Participant Demographics

There were significantly more males than females in the cross-sectional sample (2496 males (52.5%) versus 2256 females (47.5%), $p<0.001$) and significantly more right-handed

subjects (right = 3806 (80.2%) versus left = 628 (13.2) versus ambidextrous = 315, p<0.001 for all). The age range was the same for the female cohort and the male cohort (107.0 to 132 months), and there was no significant difference between the average age of females (119.5 months ± 7.4 SD) and the average age of males (119.9 months ± 7.5 SD) (p=0.086). As predicted by the early age range of participants, the distribution of the pubertal development scale score (PDSS) was not uniformly distributed across the range of PDSS values (i.e. 1 to 4). The mean of the distribution for average PDSS was 1.62 units (95% CI: [1.60, 1.63]). There was a highly significant relationship between average PDSS and age (slope = 0.118 PDSS/month; 95% CI: [0.096, 0.141], p<0001); which remained true for both females (slope = 0.212 PDSS/year; 95% CI: [0.181, 0.244], p<0.001) and males (slope = 0.049; 95% CI: [0.02, 0.078], p=0.001), but the slope for rate in change in average PDSS/month was greater for females than for males (p<0.001). Females also had a significantly higher average PDSS score compared to males (1.77; 95% CI: [1.76, 1.80] versus 1.47; 95% CI: [1.45,1.49], respectively, p<0.001) (Fig. 2).

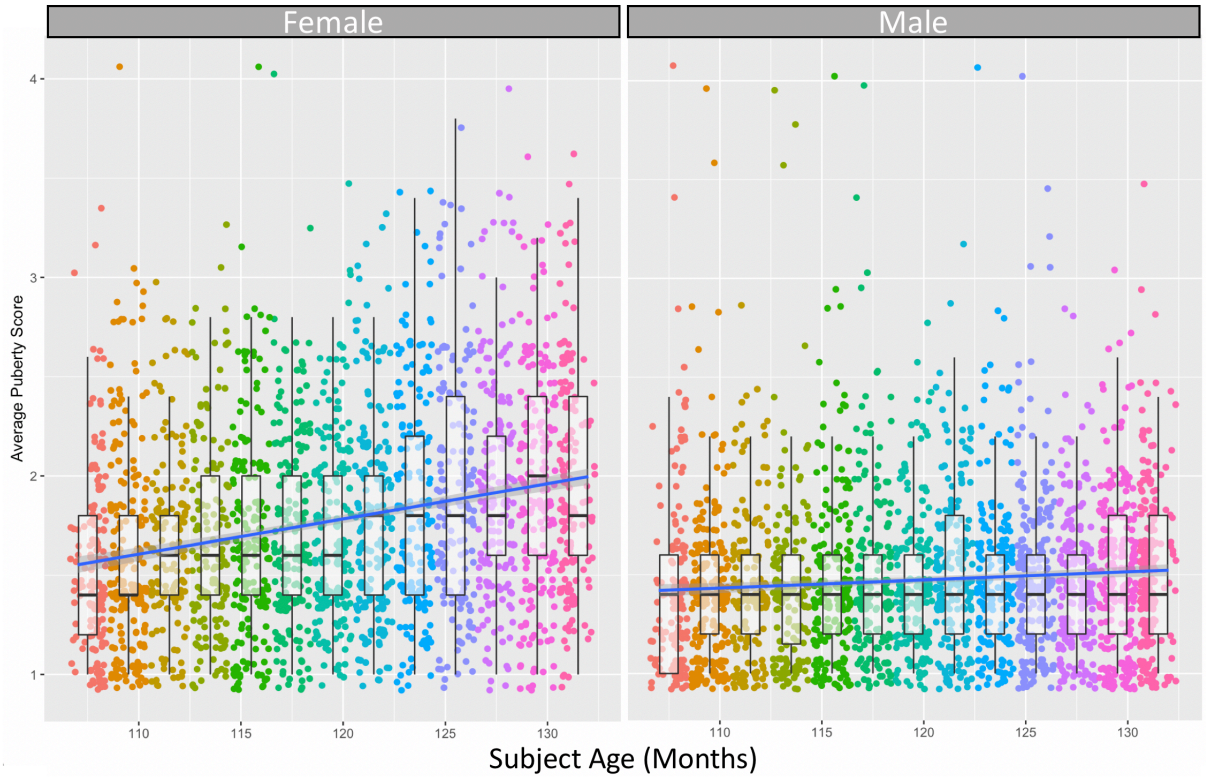

Figure 2: The relationship between subject age and average PDSS score with each boxplot and corresponding color representing a 2-month bin of participants. A linear model is displayed (shading is SE) to illustrate the relationship between age and average PDSS score. Both male and female members of the participant cohort tended to have a higher mean PDSS score as age increased, with this positive relationship being significantly more pronounced for female participants compared to males.

Regression Analyses

Tissue signal fraction regression analyses: The ANOVA summaries for the OLS regression models that were utilized to predict tissue signal fraction (i.e. extracellular isotropic CSF-like; or intracellular isotropic GM-like or intracellular anisotropic WM-like) as a function of the sum of the child's PDS scores (PDSS-sum), the child's age and sex, the child's handedness, child's total brain volume, PDSS-sum by sex interaction, PDSS-sum by age interaction, PDSS-sum by sex by age interaction, and sex by age interaction are presented in supplemental Tables S1-S3. These results are summarized in Table 2 displaying the number of JHU ROI that had a significant association with each of the predictor variables. Of note is the widespread reliability of PDSS-score, age, sex, and total brain volume as significant predictors across multiple tissue types, particularly of intracellular signal fraction compartments (GM-like and WM-like). Also of note is the complete lack of handedness as a predictor of intracellular signal fraction compartments. Table 1 lists the number of JHU ROI in which the global hypothesis test for testing for no partial-association between the tissue signal fraction and the predictor variable was rejected after implementation of the Benjamini and Hochberg 0.05 false discovery error rate procedure for the complete set of 48 null hypothesis tests. Table 2 lists the number of JHU ROI in which the global null hypothesis test for testing for no predictor variable interaction, with respect to predicting tissue signal fraction, was rejected after implementation of the Benjamini and Hochberg 0.05 false discovery error rate procedure for the entire set of 48 null hypothesis tests.

Tissue Signal Fraction	All PDSS-sum Interactions # ROI (%)	All Sex Related Interactions # ROI (%)	All Age Related Interactions # ROI (%)	All Model Interactions Combined

CSF-like	0 (0)	0 (0)	0 (0)	0 (0)
GM-like	2 (4.2)	0 (0)	0 (0)	0 (0)
WM-like	4 (8.3)	0 (0)	1 (2.1)	0 (0)

Table 2: Number of JHU ROI, in which the global null hypothesis test for testing for no predictor variable associated interaction, with respect to the adjusted association between the tissue signal fraction and the predictor variable, was be rejected after implementation of the Benjamini and Hochberg false discovery error rate procedure with an overall false discovery error rate of 0.05 for the entire set of 48 null hypothesis tests. Note that in the final column it lists the number of ROI in which the null hypothesis that all of the OLS regression model coefficients related to the model interaction terms are equal to 0, was rejected after implementation of the Benjamini and Hochberg false discovery error rate procedure with an overall false discovery error rate of 0.05 for the entire set of 48 null hypothesis tests

Concomitant variable adjusted associations between tissue signal fraction and PDSS-sum:

Listed in Tables S4 and S5 are the OLS regression model adjusted slopes, 95% confidence intervals, and p-values for predicting tissue signal fraction as a function of PDSS sum when the OLS regression model input values for child age and sex, the child handedness and child total brain volume are held constant. The intracellular anisotropic WM-like, intracellular isotropic GM-like, and extracellular isotropic CSF-like tissue signal fraction related adjusted slopes, and 95% confidence intervals atlas are graphically displayed for the 48 different JHU atlas ROIs in Figure 3, Figure 4, and Figure 5, respectively.

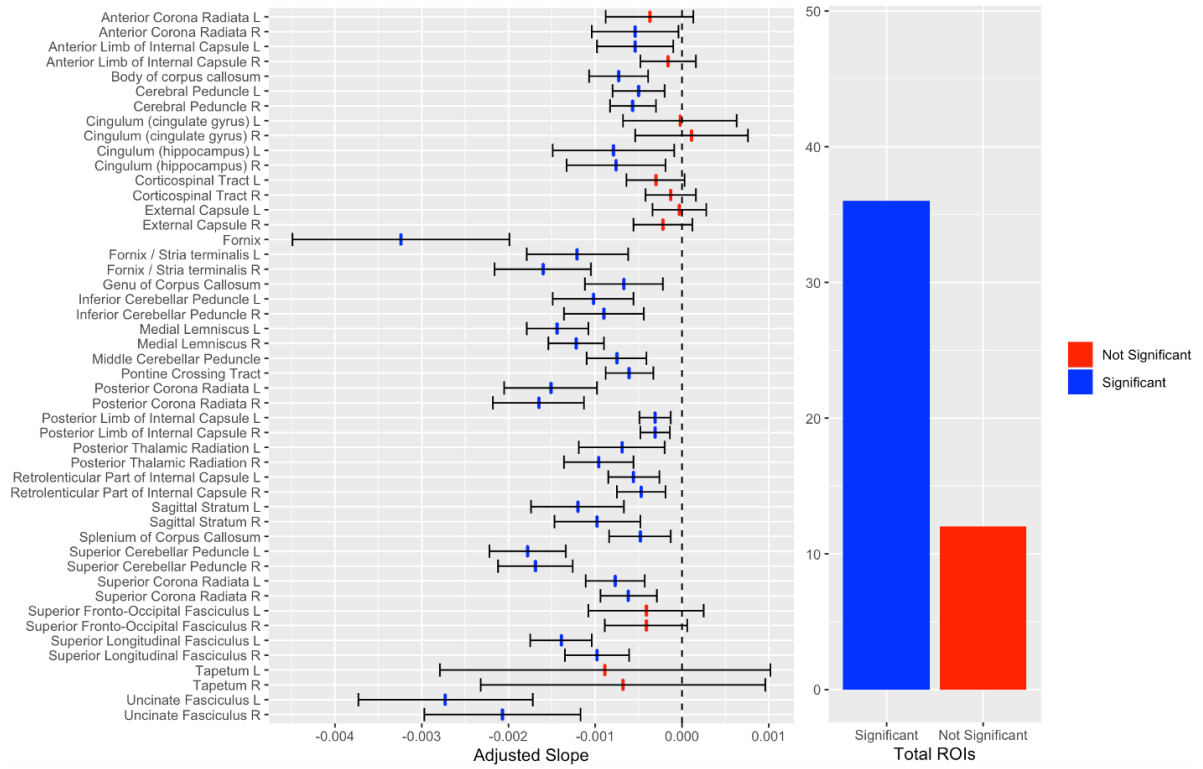

Figure 3: Chart displaying the adjusted slope with 95% confidence interval for the relationship between WM-like signal fraction and average PDSS score in each of the 48 JHU atlas ROIs. Blue bars indicate the model calculated a significant relationship ($p<0.05$) after Benjamini and Hochberg (1995) adjustment.

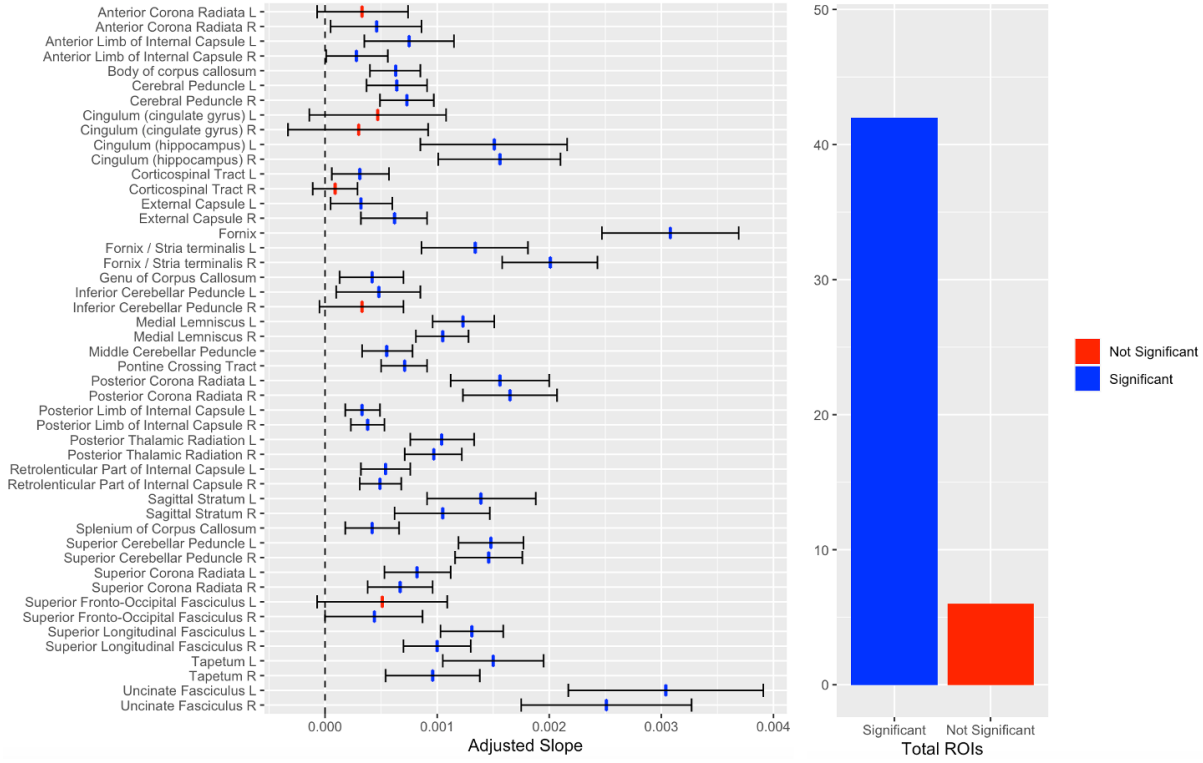

Figure 4: Chart displaying the adjusted slope with 95% confidence interval for the relationship between GM-like signal fraction and average PDSS score in each of the 48 JHU atlas ROIs. Blue bars indicate the model calculated a significant relationship (p<0.05) after Benjamini and Hochberg (1995) adjustment.

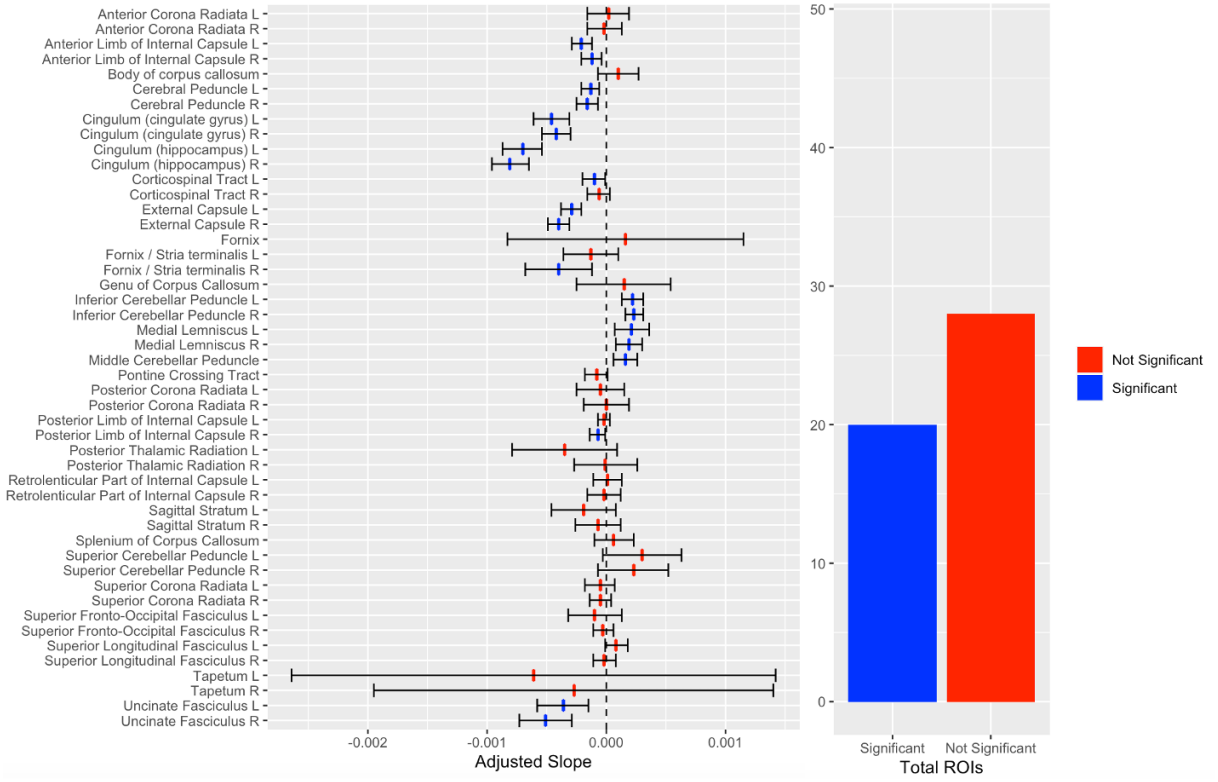

Figure 5: Chart displaying the adjusted slope with 95% confidence interval for the relationship between CSF-like signal fraction and average PDSS score in each of the 48 JHU atlas ROIs. Blue bars indicate the model calculated a significant relationship (p<0.05) after Benjamini and Hochberg (1995) adjustment.

For each significant ROI from the intracellular tissue compartments the direction of the association is consistent, with intracellular isotropic GM-like signal fraction increasing with PDSS and intracellular anisotropic WM-like signal fraction decreasing. The direction of association for extracellular signal fraction was not consistent. The location of significant intracellular anisotropic WM-like, intracellular isotropic GM-like, and extracellular isotropic CSF-like tissue signal fraction adjusted model slopes are displayed in position on the cohort specific template in Figure 6, Figure 7, and Figure 8, respectively. Significant regions for both the intracellular tissue types tended to localize to the posterior portions of the brain, while significant extracellular regions had a located below the brainstem had a positive association with PDSS, while those above had a negative association with PDSS score.

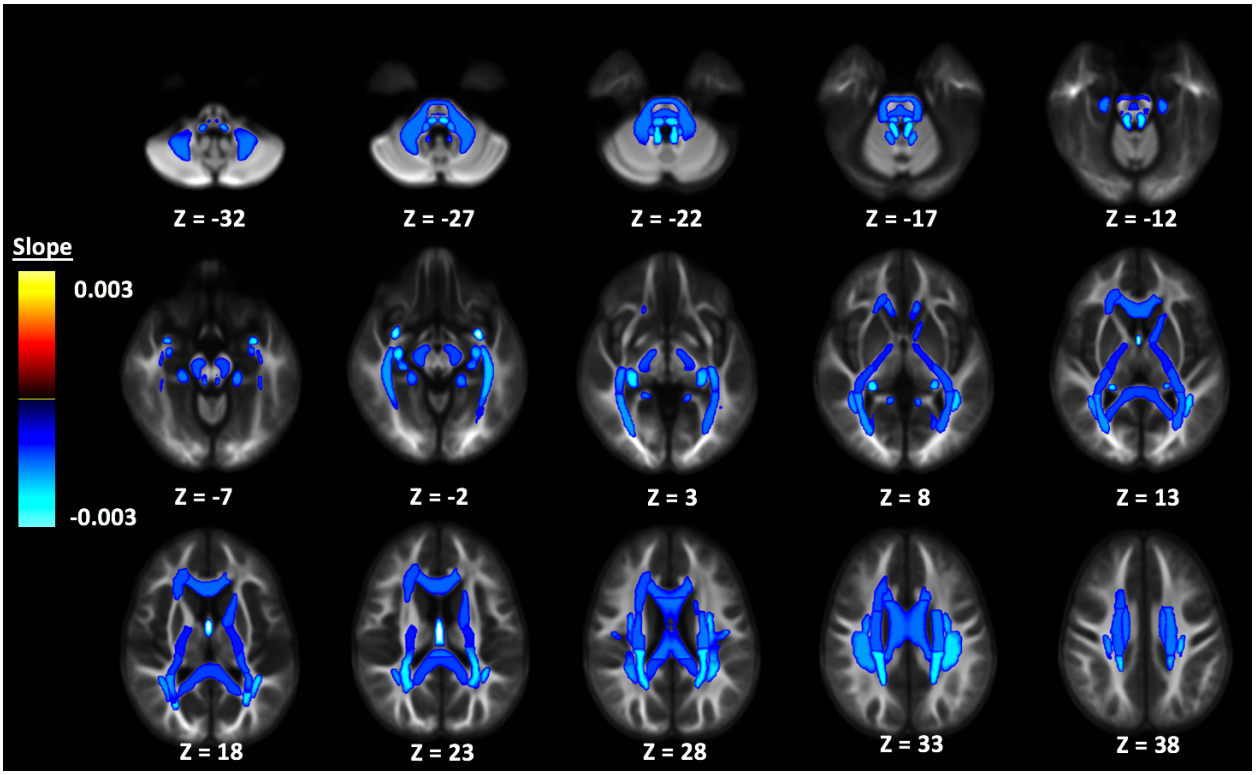

Figure 6: Display of significant adjusted anisotropic intracellular WM-like signal fraction model slopes from ROIs in the JHU WM atlas colored by slope and displayed on the cohort specific template. ROIs located in the posterior parts of the brain appear to be more strongly negatively associated with PDSS score than regions elsewhere.

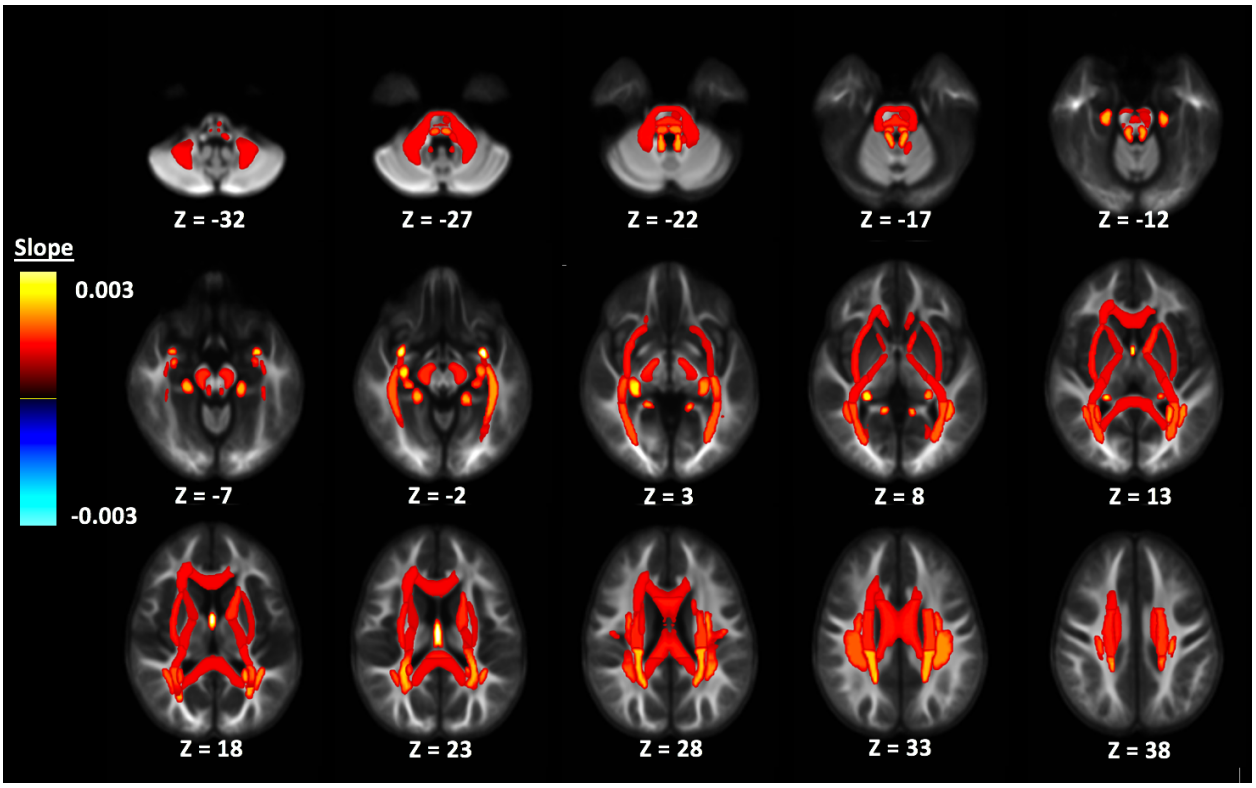

Figure 7: Display of significant adjusted isotropic intracellular GM-like signal fraction model slopes from ROIs in the JHU WM atlas colored by slope and displayed on the cohort specific template. ROIs located in the posterior parts of the brain appear to be more strongly positively associated with PDSS score than regions elsewhere.

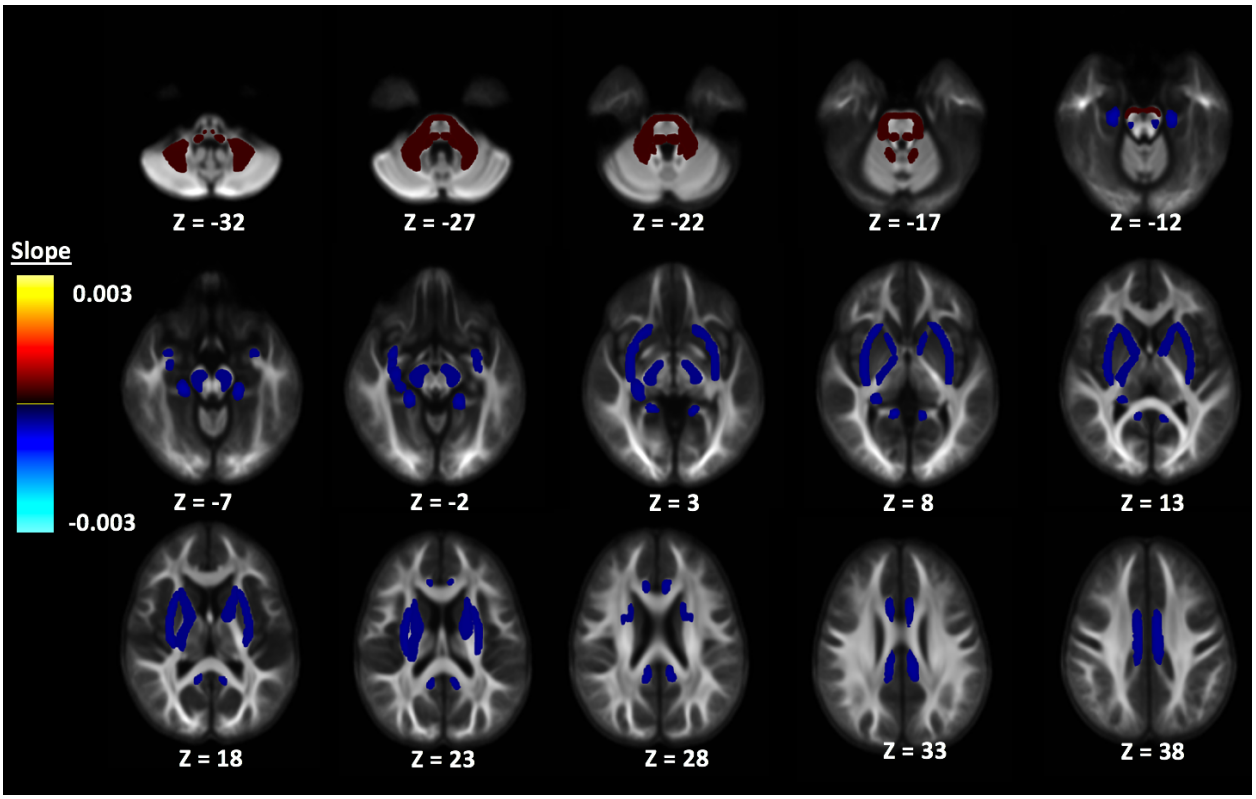

Figure 8: Display of significant adjusted isotropic extracellular CSF-like signal fraction model slopes from ROIs in the JHU WM atlas colored by slope and displayed on the cohort specific template. The CSF-like signal fraction was the only tissue compartment to have ROIs with significant adjusted model slopes both positive and negatively associated with PDSS score. Significant ROIs located below the brainstem had a positive association with PDSS, while those above had a negative association with PDSS score.

Discussion

In this cross-sectional diffusion MRI study of 4752 adolescents from the baseline collection of the ABCD study we have identified a relationship between physical manifestations of pubertal status and several measurements of brain tissue microstructure across a widespread number of WM brain regions. In ROIs for which the relationship was significant, 3T-CSD measures of intracellular anisotropic WM-like signal fraction were found to have a negative relationship with PDSS, while 3T-CSD measures of intracellular isotropic GM-like signal fraction were found to have a positive relationship with PDSS. The extracellular isotropic CSF-like signal fraction, in contrast, did not have a consistent direction across all significant ROIs.

There are several plausible mechanisms occurring at the cellular level of the brain that might underly the effect observed in this study. Studies in animal models have previously described neurogenesis and the development of new astrocytes occurring during puberty which could be a plausible reason for the observed GM-like signal fraction increase[249,250,268,269]. Neurogenesis and astrocytic growth would add to the intra-cellular space within a voxel without necessarily contributing immediately to the axonal volume and would thus appear as an increase in intracellular isotropic GM-like signal fraction at the expense of intracellular anisotropic WM-like signal fraction instead of extracellular isotropic CSF-like signal fraction (already relatively low in the predominantly WM JHU-ICBM atlas ROIs). Work performed using a songbird model observed angiogenesis and altered neuronal processes such as dendrite outgrowth, cell spacing, and an increased number of synaptic vesicles in response to increased levels of androgenic and estrogenic exposure[252]. These changes could underly the changes observed in this study, especially as recent work has found relationships between CSD- and DTI-based measures of microstructure in song-specific brain areas and plasma testosterone levels[251].

It is also possible that our results largely reflect a critical period early in pubertal development due to the early age and pubertal status of our cross-sectional sample. Some studies have suggested that GM volume peaks around the age of our cohort. One DTI study found that for males in an early stage of pubertal development, as determined by hormone measures, there was a positive relationship between MD and age[270]. While they are not equivalent, increasing MD and increasing isotropic GM-like signal fraction could both occur from the same underlying cause in predominantly axonal areas, such as neurogenesis or increased cellularity. Given the ages of males in our study and the low average PDSS score for individually in the group it is possible that this effect contributed to the observed results in this study.

This study also observed significant effects of age, sex, and total brain volume on the signal fraction measurements across the vast majority of ROIs. Several neuroimaging studies have not reported sex differences or have reported a limited effect of sex despite an earlier onset of puberty in girls. Genc et al.,[261] for example reported a significant effect of sex on fiber density in only one ROI. Similarly, a longitudinal study focusing on cortical thickness found changes associated with pubertal development and a significant effect of sex in only two ROIs[271]. Despite

being cross-sectional in design, this study has included a great deal more participants (over 4,700, compared to 74 in Genc et al.,[258] 130 in Genc et al.,[261] and 126 in Herting et al.,[271]) which may have provided the necessary statistical power while performing a conservative family-wise error correction across 48 ROIs. Our study also benefitted from the design of the ABCD study, which recruited an extremely diverse sample of participants that may have insulated our results from biases due to variables outside of our model design, such as socioeconomic status or racial group. Larger studies across longer timescales have reported findings that appear more similar to the present study. One longitudinal study examining DTI metrics across a 5 year longitudinal sample of 8-28 year-olds' found broad changes across a number of ROIs, suggesting that WM maturation is a gradual process that requires either large cohorts of subjects or long longitudinal data to fully detect[257].

The findings from this study detailing an intracellular isotropic signal positively associated with puberty appear counterintuitive compared to prior studies examining the relationship between puberty and dMRI measures of brain microstructure, which have generally found that measures related to WM integrity (such as FA) increase while measures of permeability (such as MD) decrease (for review see[272]). This review includes studies using other similar CSD-based metrics such as fixels, which have found significantly increased axonal fiber development related to the same PDSS measurement employed in our study[258,261] and to testosterone[273]. Our results however, surprisingly diverge from these studies in that the intracellular anisotropic WM-like tissue compartment was negatively associated with pubertal development, and the intracellular isotropic GM-like tissue compartment was positively associated with pubertal development in the same atlas and with the same pubertal measurements used previously[258,261]. It is important to note that the 3T-CSD technique measures relative levels of each tissue compartment and does not exclude the possibility WM fibers also mature in response to pubertal development. Possible physiological interpretations of this effect include changes in the number or activity of glial cells, such as oligodendrocytes responsible for increased myelin[274], or apoptotic events that are thought to occur during neuronal pruning, which may contribute to an increased intracellular isotropic signal via the breakup of axons and their consumption by glial cells[275].

Another study focusing on fixel-based metrics found a significant relationship between pubertal hormone levels and fiber density and fiber cross section across much of the posterior voxels in the JHU-ICBM atlas in a longitudinal cohort of children aged 8.5-10 years old[273]. While the pattern of significant voxels largely matches expectations from earlier structural studies[249] and ROIs found to be significant in this study, there are several methodological reasons why this result may be similar to volumetric studies without shedding light on brain microstructure. The authors used a CSD method previously shown to systematically *overestimate* the contribution of WM fibers to the diffusion signal[90] and the analyses did not control for longitudinal effects of change in brain volume. The combination of these two methodologic choices may be enough to cause some of the reported effects. These same methodologic factors could also plausibly explain the lack of sex effects, as well as the largely testosterone-based hormone relationship as testosterone has been reported as having a large effect on brain volume[276].

Perhaps the most straightforward reconciliation between the fixel results and the present study is that fixel-based metrics are - at the voxel level - freely-varying descriptions of WM signal characteristics whereas 3T-CSD signal fractions are relative measurements of each tissue compartment's contribution to total signal[94,100]. Fixel-based analysis discards the isotropic signal from CSF and GM in order to better characterize the WM signal while 3T-CSD examines how each tissue exists to some degree in every voxel. It is thus entirely possible that axonal microstructure matures in response to pubertal development, and that this process is accompanied by a local increase in cellularity with a GM-like intracellular diffusion profile. 3T-CSD is not specific enough to determine if this is caused by increased glial cell activity, neurogenesis, developing myelination, or a gross change in cellular architecture as axons reorganize, but it does suggest that a focus exclusively on WM is insufficient to understand the whole brain response to pubertal development.

While it is difficult to attribute the origin of the effects observed in this study to a specific cellular process, it is apparent that there is a broad and significant change within axonal regions of the brain in response to adolescent pubertal development. Using advanced dMRI measurements we have found a positive relationship between an isotropic, intracellular GM-like

signal fraction and pubertal development a corresponding negative relationship between anisotropic WM-like signal fraction and pubertal development in a cross-sectional cohort. This finding has implications for the study of the cellular basis of human brain development, suggesting microstructure beyond axons or processes such as neurogenesis or phagocytosis contribute to adolescent brain WM development and are measurable by dMRI. This work also suggests that future adolescent neuroimaging studies should account for changes in non-axonal tissue compartments and pubertal development.

Conclusion

In this cross-sectional dMRI study of 4752 adolescents from the baseline collection of the ABCD study we have identified a relationship between physical manifestations of pubertal status and several measurements of brain tissue microstructure across a widespread number of primarily axonal brain regions. Our multicompartment 3T-CSD model agrees with evidence from animal models that cellular processes other than axonal signal are involved in white matter development and that future neuroimaging studies of WM in pubertal cohorts might benefit from a focus on cellular signal beyond axons.

Supplementary Tables

Table S1. Regression model term p-values for predicting CSF tissue signal fraction as a function of sex, PDSS-sum, age, brain volume, and handedness with PDSS-sum by sex, PDSS-sum by age, sex by age, and PDSS-sum by sex by age interaction. Note that the "Global" p-values involve a test that includes all regression terms related to the predictor and "All Interactions" p-values involve a test that includes all interaction terms related to the predictor. Note that when the false discovery error rate is set at 0.05, applying the Benjamini and Hochberg false discovery procedure results in none of the "All Model Interactions" p-values meeting the threshold required to declare the model interactions -as a whole- statistically relevant. Bold and italicized p-values had magnitude less than the Benjamini and Hochberg false discovery procedure threshold for a p-value in its sequential position among 48 p-values ranked from smallest to largest.

Region	Global Puberty	All PDSS-sum Interaction	Global Sex	All Sex Interaction	Global Age	All Age Interaction	Global Volume	Global Handedness	All Model Interactions
1 Anterior Corona Radiata L	0.93662	0.849329	***0.02030***	0.73656	***0.00044***	0.72002	***<0.00001***	0.05322	0.60109
2Anterior Corona Radiata R	0.93910	0.864853	***0.00130***	0.84778	***0.00001***	0.91588	***<0.00001***	***0.00326***	0.57641
3Anterior Limb of Internal Capsule L	***<0.00001***	0.135924	0.19261	0.21485	***<0.00001***	0.14659	0.22897	0.01240	0.69693
4Anterior Limb of Internal Capsule R	***0.00015***	0.005177	***0.00018***	0.01948	***<0.00001***	0.00917	0.06628	0.08904	0.24618
5Body of corpus callosum	0.48352	0.538036	***0.00001***	0.54356	***0.00003***	0.57684	***<0.00001***	0.03645	0.23552
6Cerebral Peduncle L	***0.00119***	0.14668	0.07790	0.19418	***<0.00001***	0.56695	***<0.00001***	0.34577	0.63547
7Cerebral Peduncle R	***0.00498***	0.507962	0.72201	0.64378	***<0.00001***	0.56832	***<0.00001***	0.50597	0.72626
8Cingulum (cingulate gyrus) L	***<0.00001***	0.671039	0.12357	0.54280	***<0.00001***	0.55196	0.08730	0.24857	0.18308
9Cingulum (cingulate gyrus) R	***<0.00001***	0.383244	0.15430	0.36532	***<0.00001***	0.75832	***0.00196***	0.03612	0.45678
10Cingulum (hippocampus) L	***<0.00001***	0.250556	***0.00530***	0.10025	***<0.00001***	0.11478	0.79651	0.40314	0.89911
11Cingulum (hippocampus) R	***<0.00001***	0.016918	***0.00412***	0.02042	***<0.00001***	0.02970	***0.02409***	0.45980	0.89575
12Corticospinal Tract L	0.16595	0.677999	0.35598	0.80132	***0.00002***	0.63792	***<0.00001***	0.29415	0.46999
13Corticospinal Tract R	0.48471	0.67344	0.17649	0.89641	***<0.00001***	0.67077	***<0.00001***	0.88190	0.73602
14External Capsule L	***<0.00001***	0.597848	0.50940	0.66001	***<0.00001***	0.77845	0.16128	0.17565	0.53136
15External Capsule R	***<0.00001***	0.056367	***0.02076***	0.10551	***<0.00001***	0.53960	***0.00443***	0.02148	0.30087

16Fornix	0.58538	0.445362	0.94166	0.98749	0.12213	0.33620	***<0.00001***	0.02988	0.85583
17Fornix / Stria terminalis L	0.51997	0.515241	0.62392	0.46112	***0.00003***	0.39572	***<0.00001***	0.74936	0.29872
18Fornix / Stria terminalis R	0.04468	0.46358	0.86158	0.82767	***0.00001***	0.27370	***<0.00001***	0.39297	0.73560
19Genu of Corpus Callosum	0.40570	0.309191	0.21586	0.41418	0.39229	0.25389	***0.00510***	0.00856	0.29043
20Inferior Cerebellar Peduncle L	***0.00002***	0.270426	0.35013	0.25757	0.35698	0.57456	0.10354	0.35990	0.41232
21Inferior Cerebellar Peduncle R	***<0.00001***	0.797835	0.23749	0.69652	0.54458	0.73466	0.10715	0.79259	0.39074
22Medial Lemniscus L	***0.00318***	0.054527	***0.01274***	0.24522	***0.00105***	0.11815	***<0.00001***	0.24841	0.28056
23Medial Lemniscus R	***0.00008***	0.003906	***0.00041***	0.14636	***<0.00001***	0.00366	***<0.00001***	0.80595	0.15621
24Middle Cerebellar Peduncle	0.00306	0.207496	0.08195	0.11139	0.06122	0.08445	***<0.00001***	0.55330	0.22139
25Pontine Crossing Tract	0.17649	0.281217	0.10217	0.57666	***<0.00001***	0.21731	***<0.00001***	0.98901	0.18863
26Posterior Corona Radiata L	0.92323	0.903635	0.73863	0.83221	***<0.00001***	0.63422	***<0.00001***	**0.00198**	0.67968
27Posterior Corona Radiata R	0.72323	0.55855	0.00825	0.70638	***<0.00001***	0.77455	***<0.00001***	**0.00128**	0.71632
28Posterior Limb of Internal Capsule L	0.07262	0.050345	0.17006	0.11637	***<0.00001***	0.37589	0.42784	0.64424	0.46010
29Posterior Limb of Internal Capsule R	***0.00123***	0.007621	0.02570	0.01163	***<0.00001***	0.01387	0.11401	0.34294	0.40040
30Posterior Thalamic Radiation L	0.22113	0.375666	***<0.00001***	0.54057	***0.04008***	0.52795	***<0.00001***	**0.00562**	0.31367
31Posterior Thalamic Radiation R	0.80239	0.653204	***<0.00001***	0.67426	***<0.00001***	0.61635	***<0.00001***	0.03019	0.23318
32Retrolenticular Part of Internal Capsule L	0.28847	0.173284	***0.00499***	0.11042	***<0.00001***	0.20200	0.19494	0.09564	0.49619
33Retrolenticular Part of Internal Capsule R	0.06008	0.030695	***0.00004***	0.03954	***<0.00001***	0.20302	***<0.00001***	0.01858	0.67164
34Sagittal Stratum L	0.40017	0.620267	***<0.00001***	0.79045	***0.00171***	0.38494	0.69341	0.02080	0.67939
35Sagittal Stratum R	0.09774	0.061917	***<0.00001***	0.06465	***<0.00001***	0.79601	***0.00180***	**0.00051**	0.43600
36Splenium of Corpus Callosum	0.88576	0.861585	***<0.00001***	0.94395	***<0.00001***	0.67149	***0.00459***	0.01011	0.92750
37Superior Cerebellar Peduncle L	0.09031	0.208828	***<0.00001***	0.44203	***0.00232***	0.12155	***<0.00001***	0.10821	0.12257
38Superior Cerebellar Peduncle R	0.12439	0.187882	***<0.00001***	0.60604	***0.00016***	0.15958	***<0.00001***	0.30149	0.23913
39Superior Corona Radiata L	0.66693	0.708189	0.29168	0.55098	***<0.00001***	0.57942	***<0.00001***	0.02669	0.28606

40Superior Corona Radiata R	0.57196	0.670039	0.80983	0.76840	***<0.00001***	0.73230	***<0.00001***	**0.00033**	0.76607
41Superior Fronto-Occipital Fasciculus L	0.56424	0.562506	0.62013	0.47769	***0.13179***	0.58595	***0.00002***	0.35868	0.26277
42Superior Fronto-Occipital Fasciculus R	0.98043	0.996925	0.91706	0.98676	***0.00129***	0.98383	***0.00006***	0.44055	0.85958
43Superior Longitudinal Fasciculus L	0.16779	0.325761	***<0.00001***	0.31810	***<0.00001***	0.93228	***<0.00001***	0.05585	0.73797
44Superior Longitudinal Fasciculus R	0.32292	0.207055	***0.00001***	0.25789	***<0.00001***	0.47125	***<0.00001***	0.02031	0.23204
45Tapetum L	0.85370	0.845863	***0.02261***	0.72549	0.59841	0.47297	***<0.00001***	0.02894	0.74992
46Tapetum R	0.70834	0.564513	0.71426	0.88420	0.71447	0.60810	***<0.00001***	0.18518	0.56302
47Uncinate Fasciculus L	***0.01540***	0.529203	0.41446	0.32958	***<0.00001***	0.43781	0.13364	0.56290	0.64013
48Uncinate Fasciculus R	***0.00009***	0.226723	0.21624	0.32912	***<0.00001***	0.11787	0.24092	0.18315	0.17688

Table S2. Regression model term p-values for predicting GM tissue signal fraction as a function of sex, PDSS-sum, age, brain volume, and handedness with PDSS-sum by sex, PDSS-sum by age, sex by age, and PDSS-sum by sex by age interaction. Note that the "Global" p-values involve a test that includes all regression terms related to the predictor and "All Interactions" p-values involve a test that includes all interaction terms related to the predictor. Note that when the false discovery error rate is set at 0.05, applying the Benjamini and Hochberg false discovery procedure results in none of the "All Model Interactions" p-values meeting the threshold required to declare the model interactions -as a whole- statistically relevant. Bold and italicized p-values had magnitude less than the Benjamini and Hochberg false discovery procedure threshold for a p-value in its sequential position among 48 p-values ranked from smallest to largest.

Region	Global Puberty	All PDSS-sum Interaction	Global Sex	All Sex Interaction	Global Age	All Age Interaction	Global Volume	Global Handedness	All Model Interaction
1 Anterior Corona Radiata L	0.25483	0.41450	***0.00947***	0.56437	***<0.00001***	0.65814	***0.01272***	0.12566	0.75630
2Anterior Corona Radiata R	0.13300	0.46759	***0.00009***	0.45119	***<0.00001***	0.46538	0.06737	0.23338	0.35873
3Anterior Limb of Internal Capsule L	***0.00121***	0.28514	***<0.00001***	0.34300	***<0.00001***	0.45780	***<0.00001***	0.97192	0.41885
4Anterior Limb of Internal Capsule R	***0.01368***	0.04544	***<0.00001***	0.67932	***<0.00001***	0.07103	***<0.00001***	0.98907	0.52816
5Body of corpus callosum	***<0.00001***	0.03834	***0.00002***	0.05654	***<0.00001***	0.08326	***<0.00001***	0.37242	0.01654
6Cerebral Peduncle L	***0.00001***	0.19043	***<0.00001***	0.26534	***<0.00001***	0.15239	***<0.00001***	0.76919	0.79286
7Cerebral Peduncle R	***<0.00001***	0.13598	***<0.00001***	0.15355	***<0.00001***	0.00272	***<0.00001***	0.93541	0.66947
8Cingulum (cingulate gyrus) L	0.32684	0.72331	***0.01025***	0.05551	***<0.00001***	0.04573	***<0.00001***	0.79098	0.28589
9Cingulum (cingulate gyrus) R	0.75129	0.91315	0.07913	0.13858	***<0.00001***	0.12971	***<0.00001***	0.98008	0.38813
10Cingulum (hippocampus) L	***0.00002***	0.16172	***<0.00001***	0.19557	***<0.00001***	0.01833	***<0.00001***	0.06574	0.16243
11Cingulum (hippocampus) R	***<0.00001***	0.55629	***<0.00001***	0.91529	***<0.00001***	0.56528	***<0.00001***	0.30128	0.55044
12Corticospinal Tract L	0.11219	0.57697	***<0.00001***	0.78110	***<0.00001***	0.61961	***<0.00001***	0.83269	0.48417
13Corticospinal Tract R	0.16243	0.13338	***0.00001***	0.67120	***<0.00001***	0.18679	***<0.00001***	0.69977	0.78573
14External Capsule L	0.05867	0.35904	***<0.00001***	0.29793	***<0.00001***	0.62507	***<0.00001***	0.54772	0.50413
15External Capsule R	***0.00032***	0.39296	***<0.00001***	0.27945	***<0.00001***	0.27045	***<0.00001***	0.82279	0.17824

16Fornix	***<0.00001***	0.03478	***0.00031***	0.43505	***0.00009***	0.03193	***<0.00001***	0.23655	0.80298
17Fornix / Stria terminalis L	***<0.00001***	0.78995	***<0.00001***	0.40194	***<0.00001***	0.33739	***<0.00001***	0.14261	0.40175
18Fornix / Stria terminalis R	***<0.00001***	0.67292	***<0.00001***	0.33587	***<0.00001***	0.38230	***<0.00001***	0.15939	0.75087
19Genu of Corpus Callosum	0.09261	0.98140	0.46704	0.98233	***0.00001***	0.97627	***<0.00001***	0.43879	0.78849
20Inferior Cerebellar Peduncle L	***0.00231***	0.02436	***<0.00001***	0.16921	***<0.00001***	0.03205	***<0.00001***	0.96756	0.17297
21Inferior Cerebellar Peduncle R	***0.01835***	0.03455	***<0.00001***	0.27337	***<0.00001***	0.05778	***<0.00001***	0.77478	0.12044
22Medial Lemniscus L	***<0.00001***	0.02740	***0.00082***	0.70872	***<0.00001***	0.02651	***<0.00001***	0.41507	0.34446
23Medial Lemniscus R	***<0.00001***	0.00178	***0.00152***	0.42506	***<0.00001***	0.00315	***<0.00001***	0.13489	0.29231
24Middle Cerebellar Peduncle	***<0.00001***	0.14107	***0.00001***	0.05182	***<0.00001***	0.01421	***<0.00001***	0.26207	0.04134
25Pontine Crossing Tract	***<0.00001***	0.86492	***<0.00001***	0.87215	***0.00014***	0.95836	***<0.00001***	0.43930	0.61587
26Posterior Corona Radiata L	***<0.00001***	0.90379	***<0.00001***	0.61927	***<0.00001***	0.65427	***0.00088***	0.39649	0.93162
27Posterior Corona Radiata R	***<0.00001***	0.34523	***<0.00001***	0.40551	***<0.00001***	0.63376	***<0.00001***	0.77820	0.25102
28Posterior Limb of Internal Capsule L	***<0.00001***	0.01403	***0.00964***	0.06433	***<0.00001***	0.05326	***<0.00001***	0.18548	0.21778
29Posterior Limb of Internal Capsule R	***<0.00001***	0.00873	***0.00972***	0.16176	***<0.00001***	0.00474	***<0.00001***	0.38158	0.23746
30Posterior Thalamic Radiation L	***<0.00001***	0.00960	***<0.00001***	0.18867	***<0.00001***	0.07231	***0.04205***	0.32346	0.73935
31Posterior Thalamic Radiation R	***<0.00001***	0.07907	***<0.00001***	0.16473	***<0.00001***	0.40456	***0.03129***	0.05289	0.32682
32Retrolenticular Part of Internal Capsule L	***<0.00001***	0.00168	***<0.00001***	0.05311	***<0.00001***	0.01434	***<0.00001***	0.11980	0.12787
33Retrolenticular Part of Internal Capsule R	***<0.00001***	0.00249	***<0.00001***	0.05937	***<0.00001***	0.01740	***<0.00001***	0.21434	0.14948
34Sagittal Stratum L	***<0.00001***	0.04593	***0.00015***	0.18455	***<0.00001***	0.21020	***<0.00001***	0.64347	0.25363
35Sagittal Stratum R	***0.00001***	0.34925	***<0.00001***	0.67107	***<0.00001***	0.25782	***<0.00001***	0.74194	0.53659
36Splenium of Corpus Callosum	***0.00106***	0.13459	***<0.00001***	0.09610	***<0.00001***	0.68492	***0.00877***	0.18289	0.39694
37Superior Cerebellar Peduncle L	***<0.00001***	0.13785	***<0.00001***	0.77816	***<0.00001***	0.07801	***<0.00001***	0.12794	0.59814

38Superior Cerebellar Peduncle R	***<0.00001***	0.14454	***<0.00001***	0.56910	***<0.00001***	0.18173	***<0.00001***	0.04602	0.87308
39Superior Corona Radiata L	***<0.00001***	0.19517	***<0.00001***	0.20304	***<0.00001***	0.59684	0.99266	0.92974	0.71058
40Superior Corona Radiata R	***0.00010***	0.19574	***<0.00001***	0.21697	***<0.00001***	0.22346	0.19751	0.98761	0.75054
41Superior Fronto-Occipital Fasciculus L	0.12006	0.21964	***<0.00001***	0.31084	***0.04541***	0.67971	***<0.00001***	0.77676	0.42915
42Superior Fronto-Occipital Fasciculus R	***0.01808***	0.04694	***<0.00001***	0.25944	***0.00004***	0.18878	0.48439	0.61417	0.31686
43Superior Longitudinal Fasciculus L	***<0.00001***	0.12904	***<0.00001***	0.44421	***<0.00001***	0.13629	0.00019	0.24746	0.31445
44Superior Longitudinal Fasciculus R	***<0.00001***	0.00873	***<0.00001***	0.31422	***<0.00001***	0.00762	0.23089	0.17740	0.10326
45Tapetum L	***<0.00001***	0.39571	***0.00007***	0.20044	***0.00122***	0.40647	***<0.00001***	0.21590	0.46062
46Tapetum R	***0.00023***	0.78503	0.76323	0.63161	***0.00013***	0.62218	***<0.00001***	0.35138	0.37593
47Uncinate Fasciculus L	***<0.00001***	0.51743	***<0.00001***	0.03230	***<0.00001***	0.03283	***<0.00001***	0.03175	0.43171
48Uncinate Fasciculus R	***<0.00001***	0.25691	***0.01279***	0.20263	***<0.00001***	0.28224	***<0.00001***	0.00491	0.65538

Table S3. Regression model term p-values for predicting WM tissue signal fraction as a function of sex, PDSS-sum, age, brain volume, and handedness with PDSS-sum by sex, PDSS-sum by age, sex by age, and PDSS-sum by sex by age interaction. Note that the "Global" p-values involve a test that includes all regression terms related to the predictor and "All Interactions" p-values involve a test that includes all interaction terms related to the predictor. Note that when the false discovery error rate is set at 0.05, applying the Benjamini and Hochberg false discovery procedure results in none of the "All Model Interactions" p-values meeting the threshold required to declare the model interactions -as a whole- statistically relevant. Bold and italicized p-values had magnitude less than the Benjamini and Hochberg false discovery procedure threshold for a p-value in its sequential position among 48 p-values ranked from smallest to largest.

Region	Global Puberty	All PDSS-sum Interaction	Global Sex	All Sex Interaction	Global Age	All Age Interaction	Global Volume	Global Handedness	All Model Interactions
1 Anterior Corona Radiata L	0.35475	0.47705	0.25662	0.52556	***<0.00001***	0.71657	***0.01347***	0.07070	0.69970
2Anterior Corona Radiata R	0.06932	0.21301	***0.03246***	0.25113	***<0.00001***	0.31646	***0.00489***	0.15097	0.23631
3Anterior Limb of Internal Capsule L	***0.02553***	0.18516	***0.00010***	0.36325	***<0.00001***	0.44143	***<0.00001***	0.83166	0.41805
4Anterior Limb of Internal Capsule R	***0.01804***	0.01238	***<0.00001***	0.38805	***<0.00001***	0.03430	***<0.00001***	0.86741	0.40431
5Body of corpus callosum	***0.00007***	0.07467	***<0.00001***	0.09943	***<0.00001***	0.13251	***<0.00001***	0.34851	0.03086
6Cerebral Peduncle L	***0.00114***	0.10070	***<0.00001***	0.24371	***<0.00001***	0.21153	***<0.00001***	0.87047	0.89939
7Cerebral Peduncle R	***0.00002***	0.07799	***<0.00001***	0.31886	***<0.00001***	0.00646	***<0.00001***	0.87708	0.61869
8Cingulum (cingulate gyrus) L	0.73843	0.60540	***0.00432***	0.04830	***<0.00001***	0.04175	***<0.00001***	0.78942	0.17916
9Cingulum (cingulate gyrus) R	0.96510	0.90356	0.07931	0.20052	***<0.00001***	0.19139	***<0.00001***	0.95872	0.31551
10Cingulum (hippocampus) L	***0.01288***	0.07767	***<0.00001***	0.30199	***<0.00001***	0.02463	***<0.00001***	0.05558	0.16279
11Cingulum (hippocampus) R	***0.03511***	0.30218	***<0.00001***	0.86283	***<0.00001***	0.30239	***<0.00001***	0.24839	0.58807
12Corticospinal Tract L	0.23172	0.46572	***<0.00001***	0.78774	***<0.00001***	0.50900	***<0.00001***	0.64898	0.64855
13Corticospinal Tract R	0.21588	0.18661	***0.00013***	0.94938	***<0.00001***	0.12191	***<0.00001***	0.81014	0.79640
14External Capsule L	0.39690	0.26489	***<0.00001***	0.28810	***<0.00001***	0.63153	***<0.00001***	0.33100	0.43672
15External Capsule R	0.13472	0.17771	***<0.00001***	0.16304	***<0.00001***	0.24428	***<0.00001***	0.49998	0.14661

16Fornix	***<0.00001***	0.07638	0.56925	0.84568	***0.00045***	0.03922	***<0.00001***	0.02446	0.98211
17Fornix / Stria terminalis L	***0.00073***	0.74681	***<0.00001***	0.35042	***<0.00001***	0.20690	***<0.00001***	0.16720	0.27665
18Fornix / Stria terminalis R	***<0.00001***	0.48617	***<0.00001***	0.31893	***<0.00001***	0.18358	***<0.00001***	0.28719	0.68035
19Genu of Corpus Callosum	***0.00362***	0.04772	0.12384	0.06489	***0.00006***	0.03799	***<0.00001***	0.02535	0.08547
20Inferior Cerebellar Peduncle L	***0.00001***	0.02719	***<0.00001***	0.56162	***<0.00001***	0.00971	***<0.00001***	0.99580	0.26662
21Inferior Cerebellar Peduncle R	***0.00010***	0.04116	***<0.00001***	0.45024	***<0.00001***	0.02559	***<0.00001***	0.77822	0.21854
22Medial Lemniscus L	***<0.00001***	0.01313	***0.00012***	0.58989	***<0.00001***	0.00751	***<0.00001***	0.40524	0.20964
23Medial Lemniscus R	***<0.00001***	***0.00060***	***0.00011***	0.35861	***<0.00001***	0.00065	***<0.00001***	0.51412	0.15492
24Middle Cerebellar Peduncle	***0.00005***	0.22201	***0.00030***	0.05088	***0.00004***	0.02072	***<0.00001***	0.77233	0.06776
25Pontine Crossing Tract	***0.00036***	0.66004	***<0.00001***	0.62236	***0.00001***	0.61600	***<0.00001***	0.76013	0.32451
26Posterior Corona Radiata L	***<0.00001***	0.91821	***<0.00001***	0.82181	***<0.00001***	0.92835	0.67899	0.05092	0.82130
27Posterior Corona Radiata R	***<0.00001***	0.45882	***<0.00001***	0.46645	***<0.00001***	0.87559	0.09631	0.19648	0.43094
28Posterior Limb of Internal Capsule L	***0.00007***	0.00620	***0.01108***	0.04912	***<0.00001***	0.07118	***<0.00001***	0.39141	0.21360
29Posterior Limb of Internal Capsule R	***<0.00001***	***0.00063***	***0.01366***	0.10770	***<0.00001***	0.00406	***<0.00001***	0.70757	0.18806
30Posterior Thalamic Radiation L	0.08059	0.82675	***<0.00001***	0.90065	***<0.00001***	0.85487	***<0.00001***	0.00181	0.47971
31Posterior Thalamic Radiation R	***0.00006***	0.48484	***<0.00001***	0.55305	***<0.00001***	0.95455	***<0.00001***	0.01437	0.85973
32Retrolenticular Part of Internal Capsule L	***0.00002***	***0.00328***	***<0.00001***	0.03437	***<0.00001***	0.02404	***<0.00001***	0.10965	0.16728
33Retrolenticular Part of Internal Capsule R	***0.00003***	***0.00142***	***<0.00001***	0.01705	***<0.00001***	0.02321	0.70421	0.05173	0.24015
34Sagittal Stratum L	***0.00004***	0.09167	***<0.00001***	0.15077	***<0.00001***	0.48312	***<0.00001***	0.15769	0.21720
35Sagittal Stratum R	***0.00028***	0.13570	***<0.00001***	0.30035	***<0.00001***	0.36443	***<0.00001***	0.15594	0.40575
36Splenium of Corpus Callosum	0.04092	0.44831	***<0.00001***	0.41808	***<0.00001***	0.95375	***0.00191***	0.05356	0.53997
37Superior Cerebellar Peduncle L	***<0.00001***	0.03098	***<0.00001***	0.37626	***<0.00001***	0.00897	***<0.00001***	0.08070	0.13314

38Superior Cerebellar Peduncle R	***<0.00001***	0.03036	***<0.00001***	0.41412	***<0.00001***	0.02878	***<0.00001***	0.04327	0.36389
39Superior Corona Radiata L	***0.00036***	0.48180	***<0.00001***	0.35746	***<0.00001***	0.62442	***0.00407***	0.47473	0.95126
40Superior Corona Radiata R	***0.00114***	0.15523	***<0.00001***	0.18856	***<0.00001***	0.18807	***0.00002***	0.46801	0.71341
41Superior Fronto-Occipital Fasciculus L	0.50050	0.57640	***<0.00001***	0.61459	***0.02062***	0.84726	***0.00001***	0.94343	0.75284
42Superior Fronto-Occipital Fasciculus R	0.04502	0.07887	***<0.00001***	0.31787	***0.00001***	0.25073	0.92024	0.52645	0.33957
43Superior Longitudinal Fasciculus L	***<0.00001***	0.24025	***<0.00001***	0.43232	***<0.00001***	0.38752	***<0.00001***	0.15567	0.47677
44Superior Longitudinal Fasciculus R	***<0.00001***	0.01335	***<0.00001***	0.25609	***<0.00001***	0.01972	0.15310	0.11765	0.09799
45Tapetum L	0.81406	0.81712	0.16435	0.78495	0.75321	0.62465	***<0.00001***	0.04272	0.86837
46Tapetum R	0.63371	0.59681	0.75742	0.90197	0.71885	0.63983	***<0.00001***	0.22186	0.71639
47Uncinate Fasciculus L	***<0.00001***	0.65696	***0.00023***	0.03661	***<0.00001***	0.03816	***<0.00001***	0.08411	0.69938
48Uncinate Fasciculus R	***0.00002***	0.16741	***0.04306***	0.13390	***<0.00001***	0.20714	***<0.00001***	0.02553	0.53629

Table S4: Adjusted slopes, 95% confidence levels, and p-values for the relationship between tissue signal fraction and PDSS sum in each of the JHU atlas ROIs.

Region	CSF				GM				WM			
	ADJ Slope	Lower 95% CL	Upper 95% CL	ADJ P-value	ADJ Slope	Lower 95% CL	Upper 95% CL	ADJ P-value	ADJ Slope	Lower 95% CL	Upper 95% CL	ADJ P-value
Anterior Corona Radiata L	0.00002	-0.00016	0.00019	0.83487	0.00033	-0.00007	0.00074	0.10461	-0.00037	-0.00088	0.00013	0.14916
Anterior Corona Radiata R	-0.00002	-0.00016	0.00013	0.82952	0.00046	0.00005	0.00086	0.02676	-0.00054	-0.00104	-0.00004	0.03325
Anterior Limb of Internal Capsule L	-0.00021	-0.00029	-0.00012	<0.00001	0.00075	0.00035	0.00115	0.00026	-0.00054	-0.00098	-0.00010	0.01588
Anterior Limb of Internal Capsule R	-0.00012	-0.00021	-0.00004	0.00265	0.00028	0.00001	0.00056	0.04024	-0.00016	-0.00048	0.00016	0.32691
Body of corpus callosum	0.00010	-0.00007	0.00027	0.23804	0.00063	0.00040	0.00085	<0.00001	-0.00073	-0.00107	-0.00039	0.00003
Cerebral Peduncle L	-0.00013	-0.00021	-0.00006	0.00042	0.00064	0.00037	0.00091	<0.00001	-0.00050	-0.00080	-0.00020	0.00099
Cerebral Peduncle R	-0.00016	-0.00025	-0.00007	0.00046	0.00073	0.00049	0.00097	<0.00001	-0.00057	-0.00083	-0.00030	0.00003
Cingulum (cingulate gyrus) L	-0.00046	-0.00061	-0.00031	<0.00001	0.00047	-0.00014	0.00108	0.12982	-0.00002	-0.00068	0.00063	0.94533
Cingulum (cingulate gyrus) R	-0.00042	-0.00054	-0.00030	<0.00001	0.00030	-0.00033	0.00092	0.34923	0.00011	-0.00054	0.00076	0.73299
Cingulum (hippocampus) L	-0.00070	-0.00087	-0.00054	<0.00001	0.00151	0.00085	0.00216	0.00001	-0.00079	-0.00149	-0.00009	0.02655
Cingulum (hippocampus) R	-0.00081	-0.00096	-0.00065	<0.00001	0.00156	0.00101	0.00210	<0.00001	-0.00076	-0.00133	-0.00019	0.00872
Corticospinal Tract L	-0.00010	-0.00020	-0.00001	0.02853	0.00031	0.00006	0.00057	0.01727	-0.00030	-0.00064	0.00003	0.07609
Corticospinal Tract R	-0.00006	-0.00016	0.00003	0.17431	0.00009	-0.00011	0.00029	0.39239	-0.00013	-0.00042	0.00016	0.37658

External Capsule L	-0.00029	-0.00038	-0.00021	<0.00001	0.00032	0.00005	0.00060	0.02166	-0.00003	-0.00034	0.00028	0.84498
External Capsule R	-0.00040	-0.00049	-0.00031	<0.00001	0.00062	0.00032	0.00091	0.00004	-0.00022	-0.00056	0.00012	0.19666
Fornix	0.00016	-0.00083	0.00115	0.75136	0.00308	0.00247	0.00369	<0.00001	-0.00324	-0.00449	-0.00199	<0.00001
Fornix / Stria terminalis L	-0.00013	-0.00036	0.00010	0.25898	0.00134	0.00086	0.00181	<0.00001	-0.00121	-0.00179	-0.00062	0.00005
Fornix / Stria terminalis R	-0.00040	-0.00068	-0.00012	0.00466	0.00201	0.00158	0.00243	<0.00001	-0.00160	-0.00216	-0.00105	<0.00001
Genu of Corpus Callosum	0.00015	-0.00025	0.00054	0.46972	0.00042	0.00013	0.00070	0.00454	-0.00067	-0.00112	-0.00022	0.00368
Inferior Cerebellar Peduncle L	0.00022	0.00013	0.00031	<0.00001	0.00048	0.00010	0.00085	0.01245	-0.00102	-0.00149	-0.00056	0.00002
Inferior Cerebellar Peduncle R	0.00023	0.00016	0.00031	<0.00001	0.00033	-0.00005	0.00070	0.08832	-0.00090	-0.00136	-0.00044	0.00015
Medial Lemniscus L	0.00021	0.00007	0.00036	0.00459	0.00123	0.00096	0.00151	<0.00001	-0.00144	-0.00179	-0.00108	<0.00001
Medial Lemniscus R	0.00019	0.00008	0.00030	0.00089	0.00105	0.00081	0.00128	<0.00001	-0.00122	-0.00154	-0.00090	<0.00001
Middle Cerebellar Peduncle	0.00016	0.00006	0.00026	0.00142	0.00055	0.00033	0.00078	<0.00001	-0.00075	-0.00110	-0.00041	0.00002
Pontine Crossing Tract	-0.00008	-0.00018	0.00001	0.09343	0.00071	0.00050	0.00091	<0.00001	-0.00061	-0.00088	-0.00033	0.00002
Posterior Corona Radiata L	-0.00005	-0.00025	0.00015	0.63892	0.00156	0.00112	0.00200	<0.00001	-0.00151	-0.00205	-0.00098	<0.00001
Posterior Corona Radiata R	<0.00001	-0.00019	0.00019	0.96158	0.00165	0.00123	0.00207	<0.00001	-0.00165	-0.00218	-0.00113	<0.00001
Posterior Limb of Internal Capsule L	-0.00002	-0.00007	0.00003	0.39065	0.00033	0.00018	0.00049	0.00002	-0.00031	-0.00049	-0.00013	0.00098
Posterior Limb of Internal Capsule R	-0.00007	-0.00014	-0.00001	0.02125	0.00038	0.00023	0.00053	<0.00001	-0.00031	-0.00048	-0.00014	0.00047
Posterior Thalamic Radiation L	-0.00035	-0.00079	0.00009	0.12239	0.00104	0.00076	0.00133	<0.00001	-0.00069	-0.00119	-0.00020	0.00625

Posterior Thalamic Radiation R	-0.00001	-0.00027	0.00026	0.96603	0.00097	0.00071	0.00122	<0.00001	-0.00096	-0.00136	-0.00056	<0.00001
Retrolenticular Part of Internal Capsule L	0.00001	-0.00011	0.00013	0.81451	0.00054	0.00032	0.00076	<0.00001	-0.00056	-0.00085	-0.00026	0.00025
Retrolenticular Part of Internal Capsule R	-0.00002	-0.00016	0.00012	0.78742	0.00049	0.00031	0.00068	<0.00001	-0.00047	-0.00075	-0.00019	0.00090
Sagittal Stratum L	-0.00019	-0.00046	0.00008	0.16518	0.00139	0.00091	0.00188	<0.00001	-0.00120	-0.00174	-0.00067	0.00001
Sagittal Stratum R	-0.00007	-0.00026	0.00012	0.48845	0.00105	0.00062	0.00147	<0.00001	-0.00098	-0.00147	-0.00048	0.00011
Splenium of Corpus Callosum	0.00006	-0.00010	0.00023	0.46048	0.00042	0.00018	0.00066	0.00055	-0.00048	-0.00084	-0.00013	0.00750
Superior Cerebellar Peduncle L	0.00030	-0.00003	0.00063	0.07932	0.00148	0.00119	0.00177	<0.00001	-0.00178	-0.00222	-0.00134	<0.00001
Superior Cerebellar Peduncle R	0.00023	-0.00007	0.00052	0.13525	0.00146	0.00116	0.00176	<0.00001	-0.00169	-0.00212	-0.00126	<0.00001
Superior Corona Radiata L	-0.00005	-0.00018	0.00007	0.37910	0.00082	0.00053	0.00112	<0.00001	-0.00077	-0.00111	-0.00043	0.00001
Superior Corona Radiata R	-0.00005	-0.00014	0.00004	0.25934	0.00067	0.00038	0.00096	0.00001	-0.00062	-0.00094	-0.00029	0.00018
Superior Fronto-Occipital Fasciculus L	-0.00010	-0.00032	0.00013	0.39533	0.00051	-0.00007	0.00109	0.08671	-0.00041	-0.00108	0.00025	0.22367
Superior Fronto-Occipital Fasciculus R	-0.00003	-0.00011	0.00006	0.56369	0.00044	<0.00001	0.00087	0.04975	-0.00041	-0.00089	0.00006	0.08897
Superior Longitudinal Fasciculus L	0.00008	-0.00001	0.00018	0.08868	0.00131	0.00103	0.00159	<0.00001	-0.00139	-0.00175	-0.00104	<0.00001
Superior Longitudinal Fasciculus R	-0.00002	-0.00011	0.00008	0.76045	0.00100	0.00070	0.00130	<0.00001	-0.00098	-0.00135	-0.00061	<0.00001

Tapetum L	-0.00061	-0.00264	0.00142	0.55616	0.00150	0.00105	0.00195	<0.00001	-0.00089	-0.00279	0.00102	0.36058
Tapetum R	-0.00027	-0.00195	0.00140	0.74742	0.00096	0.00054	0.00138	0.00001	-0.00068	-0.00232	0.00096	0.41375
Uncinate Fasciculus L	-0.00036	-0.00058	-0.00015	0.00088	0.00304	0.00217	0.00391	<0.00001	-0.00273	-0.00373	-0.00172	<0.00001
Uncinate Fasciculus R	-0.00051	-0.00073	-0.00029	<0.00001	0.00251	0.00175	0.00327	<0.00001	-0.00207	-0.00297	-0.00117	0.00001

Table S5: Adjusted p-values for the concomitant covariates in the models for predicting tissue signal fraction in each JHU atlas ROI.

Region	CSF				GM				WM			
	Sex P-value	Age P-value	Volume P-value	Handed P-value	Sex P-value	Age P-value	Volume P-value	Handed P-value	Sex P-value	Age P-value	Volume P-value	Handed P-value
Anterior Corona Radiata L	0.00109	0.00001	<0.00001	0.05521	0.00056	<0.00001	0.01199	0.12333	0.07018	<0.00001	0.01400	0.06808
Anterior Corona Radiata R	0.00003	<0.00001	<0.00001	0.00320	<0.00001	<0.00001	0.06571	0.23568	0.00916	<0.00001	0.00514	0.14919
Anterior Limb of Internal Capsule L	0.24312	<0.00001	0.23981	0.01286	<0.00001	<0.00001	<0.00001	0.95631	<0.00001	<0.00001	<0.00001	0.81093
Anterior Limb of Internal Capsule R	0.00024	<0.00001	0.06087	0.09307	<0.00001	<0.00001	<0.00001	0.96253	<0.00001	<0.00001	<0.00001	0.85507
Body of corpus callosum	<0.00001	<0.00001	<0.00001	0.03482	0.00001	<0.00001	<0.00001	0.36045	<0.00001	<0.00001	<0.00001	0.32468
Cerebral Peduncle L	0.06353	<0.00001	<0.00001	0.35750	<0.00001	<0.00001	<0.00001	0.71694	<0.00001	<0.00001	<0.00001	0.84090
Cerebral Peduncle R	0.47829	<0.00001	<0.00001	0.48226	<0.00001	<0.00001	<0.00001	0.89922	<0.00001	<0.00001	<0.00001	0.79853
Cingulum (cingulate gyrus) L	0.02414	<0.00001	0.08660	0.24730	0.02256	<0.00001	<0.00001	0.83054	0.00903	<0.00001	<0.00001	0.82001
Cingulum (cingulate gyrus) R	0.06326	<0.00001	0.00191	0.03439	0.09527	<0.00001	<0.00001	0.98048	0.05720	<0.00001	<0.00001	0.95173
Cingulum (hippocampus) L	0.00283	<0.00001	0.78459	0.40757	<0.00001	<0.00001	<0.00001	0.04981	<0.00001	<0.00001	<0.00001	0.04295
Cingulum (hippocampus) R	0.01321	<0.00001	0.02640	0.46442	<0.00001	<0.00001	<0.00001	0.28032	<0.00001	<0.00001	<0.00001	0.23151
Corticospinal Tract L	0.05632	<0.00001	<0.00001	0.30682	<0.00001	<0.00001	<0.00001	0.84891	<0.00001	<0.00001	<0.00001	0.67659
Corticospinal Tract R	0.01343	<0.00001	<0.00001	0.89858	<0.00001	<0.00001	<0.00001	0.72854	<0.00001	<0.00001	<0.00001	0.86712
External Capsule L	0.17682	<0.00001	0.16481	0.17088	<0.00001	<0.00001	<0.00001	0.51942	<0.00001	<0.00001	<0.00001	0.30812
External Capsule R	0.01498	<0.00001	0.00488	0.01920	<0.00001	<0.00001	<0.00001	0.78767	<0.00001	<0.00001	<0.00001	0.46200
Fornix	0.50172	0.04693	<0.00001	0.02243	0.00001	0.00007	<0.00001	0.21363	0.09499	0.00043	<0.00001	0.01670
Fornix / Stria terminalis L	0.91964	<0.00001	<0.00001	0.73122	<0.00001	<0.00001	<0.00001	0.13193	<0.00001	<0.00001	<0.00001	0.15470
Fornix / Stria terminalis R	0.44237	<0.00001	<0.00001	0.33636	<0.00001	<0.00001	<0.00001	0.15256	<0.00001	<0.00001	<0.00001	0.25370

Genu of Corpus Callosum	0.10207	0.85320	0.00536	0.00790	0.06717	<0.00001	<0.00001	0.44472	0.98475	0.00004	<0.00001	0.02204
Inferior Cerebellar Peduncle L	0.50004	0.14696	0.10390	0.40448	<0.00001	<0.00001	<0.00001	0.93516	<0.00001	<0.00001	<0.00001	0.96103
Inferior Cerebellar Peduncle R	0.04051	0.18890	0.10612	0.80323	<0.00001	<0.00001	<0.00001	0.72336	<0.00001	<0.00001	<0.00001	0.67692
Medial Lemniscus L	0.00211	0.00056	<0.00001	0.20219	0.00001	<0.00001	<0.00001	0.33328	<0.00001	<0.00001	<0.00001	0.30668
Medial Lemniscus R	0.00004	<0.00001	<0.00001	0.85550	0.00004	<0.00001	<0.00001	0.09310	<0.00001	<0.00001	<0.00001	0.39968
Middle Cerebellar Peduncle	0.10583	0.14422	<0.00001	0.53584	<0.00001	<0.00001	<0.00001	0.21290	0.00016	0.00009	<0.00001	0.72365
Pontine Crossing Tract	0.01181	<0.00001	<0.00001	0.99034	<0.00001	<0.00001	<0.00001	0.42934	<0.00001	<0.00001	<0.00001	0.72325
Posterior Corona Radiata L	0.32180	<0.00001	<0.00001	0.00228	<0.00001	<0.00001	0.00082	0.37851	<0.00001	<0.00001	0.68574	0.04921
Posterior Corona Radiata R	0.00054	<0.00001	<0.00001	0.00140	<0.00001	<0.00001	<0.00001	0.76430	<0.00001	<0.00001	0.09477	0.19389
Posterior Limb of Internal Capsule L	0.41231	<0.00001	0.41014	0.63718	0.00759	<0.00001	<0.00001	0.15858	0.01340	<0.00001	<0.00001	0.34616
Posterior Limb of Internal Capsule R	0.70601	<0.00001	0.12257	0.34484	0.00181	<0.00001	<0.00001	0.33262	0.00492	<0.00001	<0.00001	0.62221
Posterior Thalamic Radiation L	<0.00001	0.00649	<0.00001	0.00660	<0.00001	<0.00001	0.04900	0.28959	<0.00001	<0.00001	<0.00001	0.00168
Posterior Thalamic Radiation R	<0.00001	<0.00001	<0.00001	0.03317	<0.00001	<0.00001	0.03447	0.04858	<0.00001	<0.00001	<0.00001	0.01402
Retrolenticular Part of Internal Capsule L	0.00237	<0.00001	0.20023	0.09256	<0.00001	<0.00001	<0.00001	0.09254	<0.00001	<0.00001	<0.00001	0.08913
Retrolenticular Part of Internal Capsule R	0.00002	<0.00001	<0.00001	0.01712	<0.00001	<0.00001	<0.00001	0.17294	<0.00001	<0.00001	0.66893	0.04190
Sagittal Stratum L	<0.00001	0.00015	0.71456	0.02359	0.00001	<0.00001	<0.00001	0.59764	<0.00001	<0.00001	<0.00001	0.14539
Sagittal Stratum R	<0.00001	<0.00001	0.00189	0.00046	<0.00001	<0.00001	<0.00001	0.68678	<0.00001	<0.00001	<0.00001	0.13714

Splenium of Corpus Callosum	<0.00001	<0.00001	0.00490	0.01178	<0.00001	<0.00001	0.00811	0.18685	<0.00001	<0.00001	0.00186	0.05595
Superior Cerebellar Peduncle L	<0.00001	0.00094	<0.00001	0.09427	<0.00001	<0.00001	<0.00001	0.09449	<0.00001	<0.00001	<0.00001	0.05325
Superior Cerebellar Peduncle R	<0.00001	0.00003	<0.00001	0.25593	<0.00001	<0.00001	<0.00001	0.03181	<0.00001	<0.00001	<0.00001	0.02625
Superior Corona Radiata L	0.10024	<0.00001	<0.00001	0.02920	<0.00001	<0.00001	0.99379	0.92809	<0.00001	<0.00001	0.00418	0.47513
Superior Corona Radiata R	0.46237	<0.00001	<0.00001	0.00031	<0.00001	<0.00001	0.20551	0.98379	<0.00001	<0.00001	0.00003	0.45916
Superior Fronto-Occipital Fasciculus L	0.73865	0.02753	0.00002	0.37400	<0.00001	0.00287	<0.00001	0.77818	<0.00001	0.00077	0.00001	0.93950
Superior Fronto-Occipital Fasciculus R	0.37220	0.00002	0.00006	0.44312	<0.00001	<0.00001	0.45874	0.60888	<0.00001	<0.00001	0.95028	0.51875
Superior Longitudinal Fasciculus L	<0.00001	<0.00001	<0.00001	0.05893	<0.00001	<0.00001	0.00023	0.20487	<0.00001	<0.00001	<0.00001	0.13420
Superior Longitudinal Fasciculus R	<0.00001	<0.00001	<0.00001	0.01901	<0.00001	<0.00001	0.20825	0.12781	<0.00001	<0.00001	0.16969	0.08849
Tapetum L	0.00111	0.62013	<0.00001	0.03344	0.00001	0.00006	<0.00001	0.22543	0.01606	0.67690	<0.00001	0.04930
Tapetum R	0.25963	0.61429	<0.00001	0.20912	0.73395	<0.00001	<0.00001	0.35546	0.28792	0.50474	<0.00001	0.24829
Uncinate Fasciculus L	0.45396	<0.00001	0.13618	0.56028	<0.00001	<0.00001	<0.00001	0.03143	0.00026	<0.00001	<0.00001	0.08060
Uncinate Fasciculus R	0.15691	<0.00001	0.22783	0.17529	0.00329	<0.00001	<0.00001	0.00347	0.03042	<0.00001	<0.00001	0.01883

Study 2c

Aim 2c: Determine if the epigeneticly derived risk score 'GrimAge' is an effective peripheral blood biomarker of small vessel disease driven damage to brain microstructure in a 'healthy' aging cohort.

Rationale: All humans experience age-related decline toward the end of the lifespan. This can affect the brain in a number of ways, including atrophy, loss of volume particularly in cortex, and the appearance and enlargement of white matter hyperintensities. These structural changes can occur in otherwise seemingly 'healthy' aged individuals, without any diagnosed neurological issue. Using 3T-CSD measurements of brain microstructure we will be able to examine how the brain declines due to age at a cellular level. This will give insight into factors affecting age-related decline, as well as highlight areas of the brain that may be more closely associated with behavioral and cognitive outcomes.

Experimental Design: dMRI images from the Virginia Cognitive Aging Project (VCAP) will be leveraged to explore age-related decline. VCAP is a longitudinal study currently featuring 100 healthy elderly subjects at baseline and 42 scanned 2 years later. Rates of change will be measured longitudinally to investigate how factors might influence the acceleration or slowing of decline.

Additionally, there is a growing understanding within the dMRI microstructure community that not all brain injuries or instances of decline are generalizable across subjects in a fashion amenable to traditional parametric mean testing. To address this deficiency there is a need to move toward subject-specific analysis techniques that can incorporate differences in anatomical structure and lesion burden or location. Age-related changes later in life include the appearance of areas within the deep WM termed white matter hyperintensities. White matter hyperintensities are a manifestation of small vessel disease and can indicate damage to extracellular matrix, demyelination, or even axonal loss[277]. White matter hyperintensities are common features of the aging brain but appear differently in location or size across subjects and presumably have subsequently different effects on cognitive functioning or indicate different

susceptibility to brain damage. Using VCAP, we will analyze white matter hyperintensities as subject-specific, independent ROIs both for analyzing the composition of the hyperintensities and the relationship of the longitudinal change between scanning sessions to behavioral outputs. A lesionometric framework will be applied to examine areas of the brain affected by white matter hyperintensities[278,279]. This method uses tractography to select axonal fiber bundles traversing 'lesioned' areas of the brain and assesses microstructure in areas traversed by affected tracts. This has the practical application of expanding the regions of the brain affected by the lesion but also generates a subject-specific area that may be more sensitive to detecting the full extent of neuronal damage inflicted by factors such as lesion size and location.

Finally, VCAP includes epigenetic clock data which seeks to determine if aging is accelerating or slowing compared to chronological age. Termed GrimAge, the epigenetic clock is based off of 12 DNA methylation sites that correlate with blood plasma proteins and smoking pack years and represents a mortality risk estimator when compared to chronological age[280,281]. The approach using VCAP will be twofold: first, microstructural correlates of epigenetic clocks will be explored to discover microstructural markers of aging and decline, especially subject-specific markers of existing neuroradiological decline due to the presence and lesionometric burden of white matter hyperintensities. Second, the longitudinal component of VCAP will inform the relationship between GrimAge and differing rates of decline across participants.

Study 2c

Title: Epigenetic age acceleration predicts subject-specific white matter degeneration in the human brain.

Abstract

Epigenetic clocks provide powerful tools for estimating health and lifespan but their ability to predict brain degeneration and neuronal damage during the aging process is unknown. In this study, we use GrimAge, an epigenetic clock correlated to several blood plasma proteins, to longitudinally investigate brain cellular microstructure in axonal white matter from a cohort of healthy aging individuals. Given the blood plasma correlations used to develop GrimAge, a specific focus was made on white matter hyperintensities, a visible neurological manifestation of small vessel disease, and the axonal pathways throughout each individual's brain affected by their unique white matter hyperintensity location and volume. 98 subjects over 55 years of age were scanned at baseline with 41 returning for a follow-up scan 2 years later. Using diffusion MRI lesionometry, we reconstructed subject-specific networks of affected axonal tracts and examined the diffusion cellular microstructure composition of these areas, both at baseline and longitudinally, for evidence of cellular degeneration. A chronological age-adjusted version of GrimAge was significantly correlated with baseline WMH volume and markers of neuronal decline, indicated by increased extracellular free water, increased intracellular signal, and decreased axonal signal within WMH. By isolating subject-specific axonal regions 'lesioned' by crossing through a WMH, age-adjusted GrimAge was also able to predict longitudinal development of similar patterns of neuronal decline throughout the brain. This study is the first to establish a relationship between accelerated epigenetic GrimAge and brain cellular microstructure in humans.

Introduction

Recent advances in epigenetic sequencing and analysis have led to the development of a number of epigenetic clocks that act as biomarkers for chronological age[282,283]. GrimAge is an epigenetic clock that calculates expected time-to-death due to all-cause mortality based on a number of surrogate DNA methylation based biomarkers of stress and physiological risk[280]. AgeAccelGrim is an age-adjusted version of GrimAge shown to be highly predictive of time-to-coronary heart disease, congestive heart failure, hypertension, type 2 diabetes, and physical functioning[280]. It is well established that cardiovascular health affects brain integrity and cognitive functioning[223,284,285] and has been implicated in the formation of white matter hyperintensities (WMH) on T2-weighted brain MRI. WHM are thought to be the consequence of small vessel disease (SVD) which can cause microinfarcts, edema, and cortical thinning[286–288]. WMH are associated with declining cognitive and perceptual functioning and are thus an important marker for age-related brain health[289,290]. In this study, we pair AgeAccelGrim with an advanced diffusion microstructure analysis technique, 3-Tissue Constrained Spherical Deconvolution (3T-CSD), in a subject-specific manner to test associations between AgeAccelGrim estimates of mortality risk and brain cellular microstructure. Analyses will be focused on WMH due to their connection to SVD, as well as on the ability of AgeAccelGrim to predict future neuronal decline in an aging cohort.

The GrimAge model was generated from the Framingham Heart Study Offspring Cohort[291] and is specifically composed of 12 DNA methylation (DNAm) based biomarkers for plasma proteins, plus age, gender, and smoking pack-years, regressed to time-to-death. The age-adjusted version of GrimAge presents a powerful means for studying the effects of cardiovascular health on the brain. Not only is the clock optimized to estimate plasma proteins sensitive to aging and general heart health, but by finding DNAm correlates for factors such as smoking pack-years GrimAge allows for the assessment of levels of methylation present on the relevant site even in the absence of self-report metrics or any history of smoking at all. Age-adjusted GrimAge is not only reported to be more closely correlated with time-to-death than self-reported smoking pack-years alone, but it allows for risk evaluation and stratification of all non-smokers, providing a more powerful and accurate statistical sample[280].

At the population level, cardiovascular risk factors in humans have been strongly linked to degenerative changes in brain structure using brain diffusion MRI (dMRI). Greater arterial stiffness has been associated with reduced white matter (WM) fractional anisotropy in the corpus callosum and corona radiata as well as lower grey matter (GM) density in the thalamus[292]. In a recent study using dMRI and positron emission tomography (PET), MRI-based markers of SVD (measured by WMH volume) were more correlated with dMRI extracellular free water than PET measures of Tau or Aβ, and SVD contributed more to diffusion alterations than did biomarkers of Alzheimer's disease[286]. Another dMRI study suggested that diffusion differences between patients with SVD and healthy controls were primarily driven by increased extracellular free water rather than neuronal tissue alterations, and that this finding predicted clinical status[62]. These dMRI-based degenerative changes follow similar trajectories across the 'healthy' population (those explicitly without a diagnosed neurodegenerative disease), but there is wide individual variation in the chronological age at which degenerative brain changes begin and how they progress.

GrimAge metrics may be a useful biomarker for decline related to WMH and SVD as WMH volume is one of the few neuroimaging markers of SVD to be positively associated with AgeAccelGrim[16]. Though previous studies have examined this relationship no conclusive link between AgeAccelGrim and WMH has been established[293–295]. The difficulty in establishing this link highlights the shortcomings of whole brain or one-size-fits-all approaches to studying features such as WMH that vary greatly in presentation between individuals. Individual differences in age-related neuronal decline are evident in whole-brain metrics and particularly in the presentation of WMH. Analyzing the composition of WMH presents a challenge for typical neuroimaging analysis pipelines but particularly using 3T-CSD. Each subject has a different spatial location of WMH volume and a distinct spatial progression longitudinally. The location of WMH has been implicated in cognitive deficits in patients with SVD[296] so it is crucial to account for subject-specific WMH features. Being located in the predominantly axonal WM, WMH can induce damage and Wallerian degeneration on axonal pathways traversing the lesioned area[288] presenting a challenge to investigate distant regions of the brain that may show signs of damage that form unique subject-specific spatial patterns.

To address this problem, our study will apply 3T-CSD microstructural metrics within a lesionometry framework[278,279]. 3T-CSD analysis of cellular microstructure has previously been used to successfully characterize WMH and is also able to detect areas of 'normal appearing' WM that develop into WMH following cerebrovascular injury[91,227]. Lesionometry is a fusion of voxel-wise diffusion metrics and subject specific lesion analysis to isolates axonal networks that traverse lesioned voxels with diffusion tractography and analyze the cellular microstructure within that network (Figure 1). This technique has previously been applied to the study of multiple sclerosis, and was able to correlate a number of diffusion metrics and network measures, such as the proportion of lesioned volume to whole affected network volume referred to as 'lesion load', to cognitive, learning, and memory symptoms[279].

Using this subject-specific method to focus highly sensitive 3T-CSD microstructural methods may be the key to finding a relationship between GrimAge clock measurements and changes in brain microstructure. Due to its connection to cardiovascular risk factors, GrimAge may be well-suited to determining where an individual falls on the age-related decline trajectory. This study aims to evaluate GrimAge as an effective peripheral blood biomarker of SVD driven damage to the brain.

Methods

Subjects

Participants were recruited from the ongoing Virginia Cognitive Aging Project (VCAP), a multi-year cross-sectional and longitudinal study of cognition in over 5,000 participants[297,298]. VCAP subjects have been recruited from the local community and have agreed to participate in multiple study visits over several years. A subset of aged subjects was selected from VCAP and an equal number of subjects from each quantile of performance based on cognitive tasks during prior visits was recruited for additional MR imaging.

98 subjects were recruited for baseline neuroimaging with an age range between 58-81 (mean = 68 ± 5.67 S.D.) years old. There were 30 male and 68 female participants with average ages of 67.53 ± 5.44 S.D. and 68.84 ± 5.75 S.D., respectively. Follow-up neuroimaging planned for 1 year was delayed by the COVID-19 pandemic and ended up occurring approximately 2 years later. Many of the elderly subjects declined the follow-up neuroimaging study due to ongoing COVID-related concerns. A total of 41 subjects were successfully recruited for follow-up scans with an age range of 61-81 (mean = 69 ± 5.00 S.D.) years old. This follow up group was composed of 16 male and 25 female participants with average ages of 68.19 ± 4.96 S.D. and 69.86 ± 5.02 S.D., respectively.

Image Acquisition

All subjects were scanned at the University of Virginia using a Siemens Prisma 3T MRI with a 32-channel head coil. T1-weighted images were acquired using the ADNI3 designed MP-RAGE sequence[299] with an isotropic voxel size 1.0×1.0×1.0mm^3, TE=2980ms and TR=2300ms with full dimensions of a 208×240×256 viewing window. Diffusion-weighted images were acquired with an isotropic voxel size of 1.7×1.7×1.7mm^3, TE=70ms and TR=2900ms; using a multi-shell protocol, 10 b=0 images and 64 gradient directions were collected at both b=1500s/mm^2 and b=3000s/mm^2. An identical imaging protocol was used at both baseline and follow-up.

Preprocessing

Each diffusion image set was analyzed using SS3T-CSD[10,90] implemented in the open source software MRtrix and MRtrix3Tissue[12,90]. Several preprocessing steps utilized FSL[104,105]. Diffusion images were denoised[107], corrected for Gibbs ringing[109], susceptibility distortions[104], subject motion[116], and eddy currents[110]. Skull-stripping was performed and volumetric data was gathered by analyzing each subject's T1 image from each visit using the 'recon-all' pipeline in Freesurfer version 6.0.1[231]. All images were upsampled to 1.3×1.3×1.3mm and a whole brain mask was derived by rigidly registering each subject's skull-stripped T1 image from the appropriate scanning session to the average b=0 s/mm^2 dMRI acquisition using ANTs[120].

Response functions were generated[88] from each tissue type (WM, GM, and CSF) and the white matter fiber orientation distribution (FOD) was then resolved at the voxel-wise level by processing the outermost b-value shell (b=3000s/mm^2) using single-shell constrained spherical deconvolution, a technique to separate directional axonal signal from intracellular and extracellular isotropic diffusion[90]. Primarily for the purposes of visualization, a cohort-specific FOD template was generated from 20 subject's WM FODs acquired from both baseline and follow-up for a total of 40 FOD images being used in template construction. Each subject was subsequently registered to this template using the individual WM FODs from each timepoint to warp tractography and signal fraction maps into a common space[300]. However, all calculations used in the analysis were derived from native, acquisition space images.

Tractography

Probabilistic tractography was performed on each subject's diffusion images by applying the iFOD2 algorithm which propagates streamlines between voxels based on the direction and amplitude of the underlying WM FOD[301]. Seeding of streamlines was performed by randomly selecting voxels within the whole brain mask. Streamlines were seeded and generated until 10,000,000 tracts were created that were each longer than 2.6mm without terminating. These streamlines were then pruned to 2,000,000 total tracts using spherical-deconvolution informed filtering of tractograms (SIFT), which ties the number of streamlines in each voxel to the magnitude of the underlying FOD[302]. This process matches the randomly generated streamlines to the underlying anatomically derived signal and prevents a biologically implausible number of tracts from traversing the same voxel. As all subjects provide the same number of total streamlines, the number of tracts inferences can be made in a between-subject or longitudinal manner.

Diffusion Microstructure

3T-CSD measurements of brain cellular microstructure were calculated directly from each subject's FODs at each timepoint. 3T-CSD is a voxel-wise quantitative method that measures cellular microstructure within each voxel fitting into intracellular anisotropic (ICA,

WM-like), intracellular isotropic (ICI, GM-like), and extracellular isotropic (ECI, CSF-like/Free Water) compartments[100]. This approach allows for contributions from each cellular microstructure compartment to be calculated for each image in any defined ROI. The quantitative measurement of 3 different tissue compartments, the improvements to tractography by separating isotropic signal from anisotropic WM for tractography, and the specific ability to measure extracellular freely diffusing water (a potentially highly sensitive marker for neuronal degeneration during aging[15]).

Identification of WMH

Voxels composing WMH were identified through application of the 'recon-all' pipeline to each subject's T1 images at each timepoint collected. Freesurfer identifies WMH via segmentation of WM voxels followed by a voxel-wise probabilistic local and intensity-related analysis informed by a library of manually segmented images[231]. While Freesurfer has been shown to systematically underestimate WMH volume when applied to T1 images, volume estimations were closely correlated with Fazekas score, a measure of WMH severity[303]. No FLAIR acquisition was collected during this study. Masks highlighting voxels containing WMH were rigidly transformed into the space of the respective diffusion image acquired during the same session using the previously generated ANTs rigid transform from the T1 to average b=0 registration described previously[120].

Lesionometry

Lesionometry was used to examine the relationship between WMH volume, cellular microstructure composition, and spatial positioning to whole brain structure. This recently developed technique was applied to generate subject- and timepoint-specific measures of 'lesion-load'[278,279]. This method examines microstructural metrics within voxels traversed by WM fiber bundles, and theoretically the axons they model, that also traverse WMH (Fig. 1). WMH masks generated by Freesurfer and registered to the diffusion space were used to filter tracts from the final whole brain tractogram after the processing pipeline described earlier. To reduce spurious individual tracts from being overrepresented in analysis a threshold was applied so that voxels

were only included in the final ROI if at least 10 separate tracts traversed both the voxel and a WMH. Volumetric and 3T-CSD measurements were then measured within each ROI from all subjects at both timepoints excluding voxels that were part of the original WMH mask so that no voxels were in both the lesionometric ROI and a WMH (for individual examples see Fig. 2).

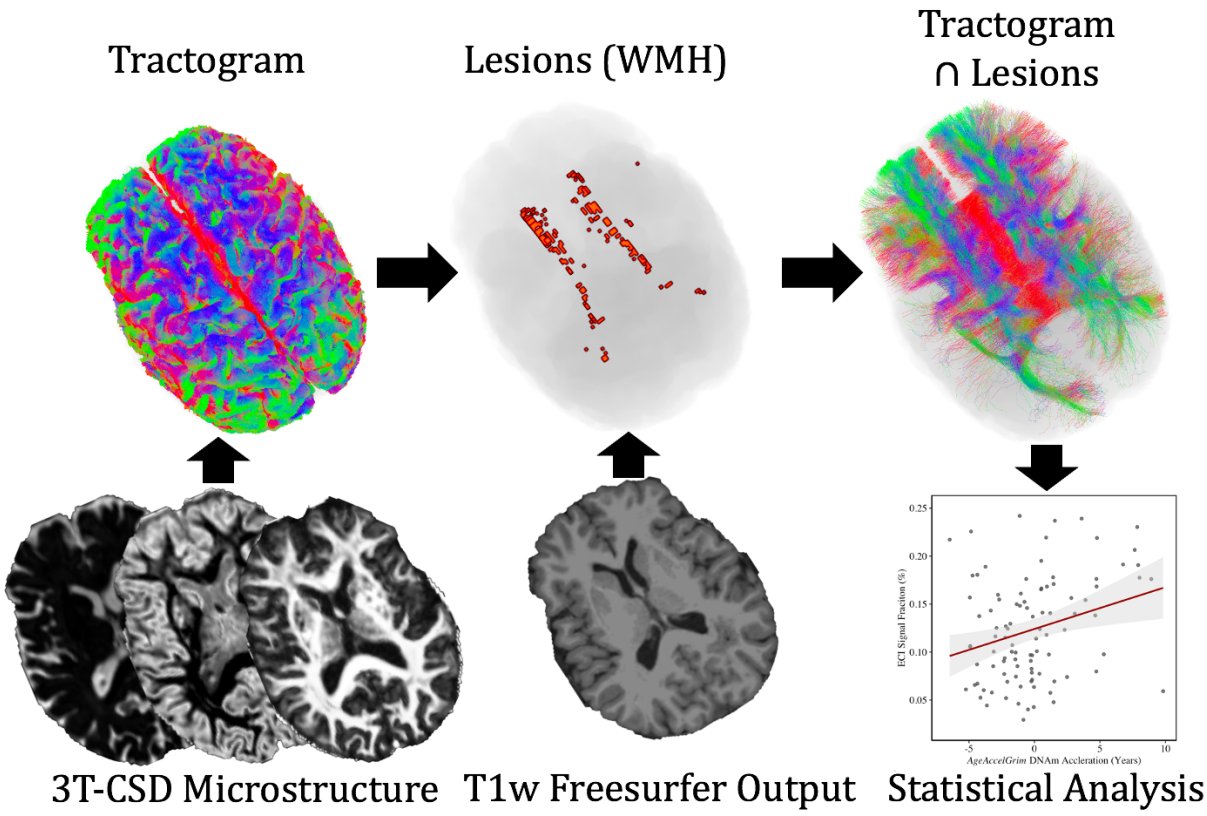

Figure 1: Flowchart demonstrating Lesionometry analysis pipeline, first described in Chamberland et al. (2020) and Winter et al. (2021). Subjects dMRI data is processed thorough the 3T-CSD microstructure pipeline and FODs are used to generate a whole brain tractogram. 'Lesions' representing WMH are derived from T1-weighted images taken from the 'recon-all' processing pipeline in freesurfer. Voxels traversed by tracts that also traverse WMH lesions are included for final microstructure statistical analysis.

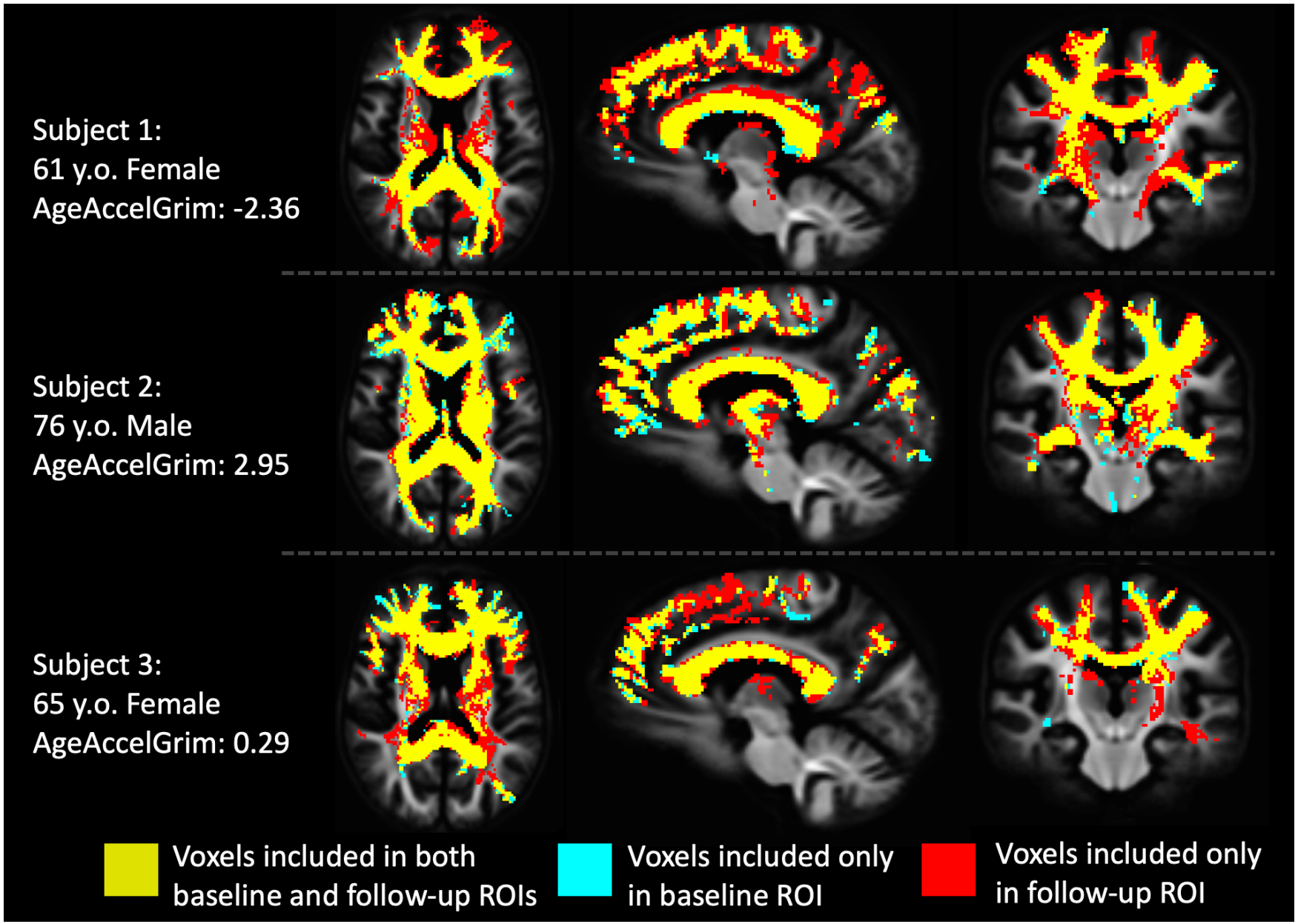
Subject 1:
61 y.o. Female
AgeAccelGrim: -2.36
Subject 2:
76 y.o. Male
AgeAccelGrim: 2.95
Subject 3:
65 y.o. Female
AgeAccelGrim: 0.29
Voxels included in both baseline and follow-up ROIs
Voxels included only in baseline ROI
Voxels included only in follow-up ROI

Figure 2: Illustration of subject-specific lesionometry ROIs in the whole-group template space from 3 example participants. Each subject in the study at each timepoint contributed a unique scan- and subject-specific ROI for analysis. ROIs were generated by filtering any 'lesioned' axonal tracts from the whole brain tractogram that passed through a voxel identified as being part of a WMH. This WMH-derived tractogram was then converted to a typical binary voxel ROI with the use of a low pass filter to only include voxels containing 10 or more tracts to ensure consistency. The volume of the ROI once the WMH volume was corrected for was not significantly different between baseline and follow-up ($F_{1,36}$=0.0272, p=0.870 n.s.).

Epigenetic Analysis

For full description of the epigenetic protocol see supplementary methods. Briefly, 8.5 ml blood were drawn from each participant at the baseline visit and DNA was extracted and amplified with PCR before being assayed using the Illumina Infinium MethylationEPIC BeadChip according to manufacturer instruction. The R packages *minfi* and *shinyMethyl* were used for background subtraction, dye-bias normalization, removal of missing values, quality control, and to check for batch effects[304–308]. All samples passed Illumina quality controls as assessed using the *ewastools* R package[309]. Unnormalized betas were filtered to include CpGs specified by Horvath as necessary for calculation of various clocks[282]. The betas were uploaded to Horvath's online DNA methylation age calculator (htpps://dnamage.genetics.ucla.edu), which provides measures of DNA methylation GrimAge[280]. AgeAccelGrim was calculated by regression of GrimAge onto subject age, providing a chronological age normed value of accelerated or decelerated mortality risk relative to the subject's age at baseline.

Statistical Analysis

After AgeAccelGrim was calculated for each subject at baseline a general linear model was constructed using a planned set of covariates to test their association with GrimAge. Subject chronological age at baseline, sex, and total brain volume at baseline were initially tested for relationship with AgeAccelGrim. Following this analysis for all imaging results unless otherwise noted, chronological age at scan acquisition, sex, and a volumetric component of either the whole brain or the subject- and scan-specific ROI were used as covariates.

For longitudinal results, a within-subjects ANOVA approach was used to specifically examine the 41 subjects scanned longitudinally, with controls for subject sex, age at baseline, and total brain volume at both timepoints when appropriate.

Results

AgeAccelGrim is associated with sex and brain volume

As expected, there was no significant relationship between AgeAccelGrim and chronological age in the baseline sample ($T_{4,94}$=-0.431, p=0.667 n.s.), interestingly however there was a highly significant relationship between AgeAccelGrim and sex ($T_{4,94}$=-5.200, p<0.001) with female subjects typically having a lower AgeAccelGrim, particularly after 65 years of age which is to be expected given that sex is included in GrimAge calculation[280]. There was also a significant relationship between AgeAccelGrim and total brain volume ($T_{4,94}$=-2.782, p<0.01).

AgeAccelGrim is not associated with whole brain dMRI microstructure metrics

Significance values that follow are for AgeAccelGrim as a predictor of the respective microstructural signal fraction. Whole brain microstructural composition was first assessed at baseline for relationships to AgeAccelGrim. There was no significant relationship between global ICI signal fraction ($T_{5,93}$=1.353, p=0.179 n.s.), nor global ICA signal fraction ($T_{5,93}$=-0.298, p=0.766 n.s.), but there was a trend toward significance with global ECI signal fraction ($T_{5,93}$=1.797, p=0.0755 n.s.) indicating that AgeAccelGrim may be indicating the presence of extracellular water in the aging brain (Fig. 3a).

AgeAccelGrim predicts WMH size and microstructural composition at baseline

Moving into subject specific analysis of WMH, 3T-CSD microstructure and volume were measured within each subjects' WMH at baseline. Greater WMH volume was significantly predicted by increased AgeAccelGrim ($T_{5,93}$=2.931, p<0.01) and was added as an additional volumetric control variable for the WMH microstructure model to account for variances in

WMH volume between subjects. All three microstructural tissue compartments averaged across the WMH had a significant relationship with AgeAccelGrim (ECI: $T_{6,92}$=2.844, p<0.01; ICI: $T_{6,92}$=2.741, p<0.01; ICA: $T_{6,92}$=-3.140, p<0.01). For these models ECI and ICA had additional significant relationships with WMH volume (ECI: $T_{6,92}$=5.537, p<0.001; ICA: $T_{6,92}$=-2.494, p<0.05) while ICI did not have a significant relationship with WMH volume (ICI: $T_{6,92}$=0.348, p=0.728 n.s.) suggesting that spatial location of the WMH plays a role in tissue composition but that AgeAccelGrim is able to predict ICI signal fraction, a potential marker for neuroinflammation, and increased ECI, a marker for neuronal degeneration and atrophy, occurring at the expense of ICA, or healthy axonal signal (Fig. 3b).

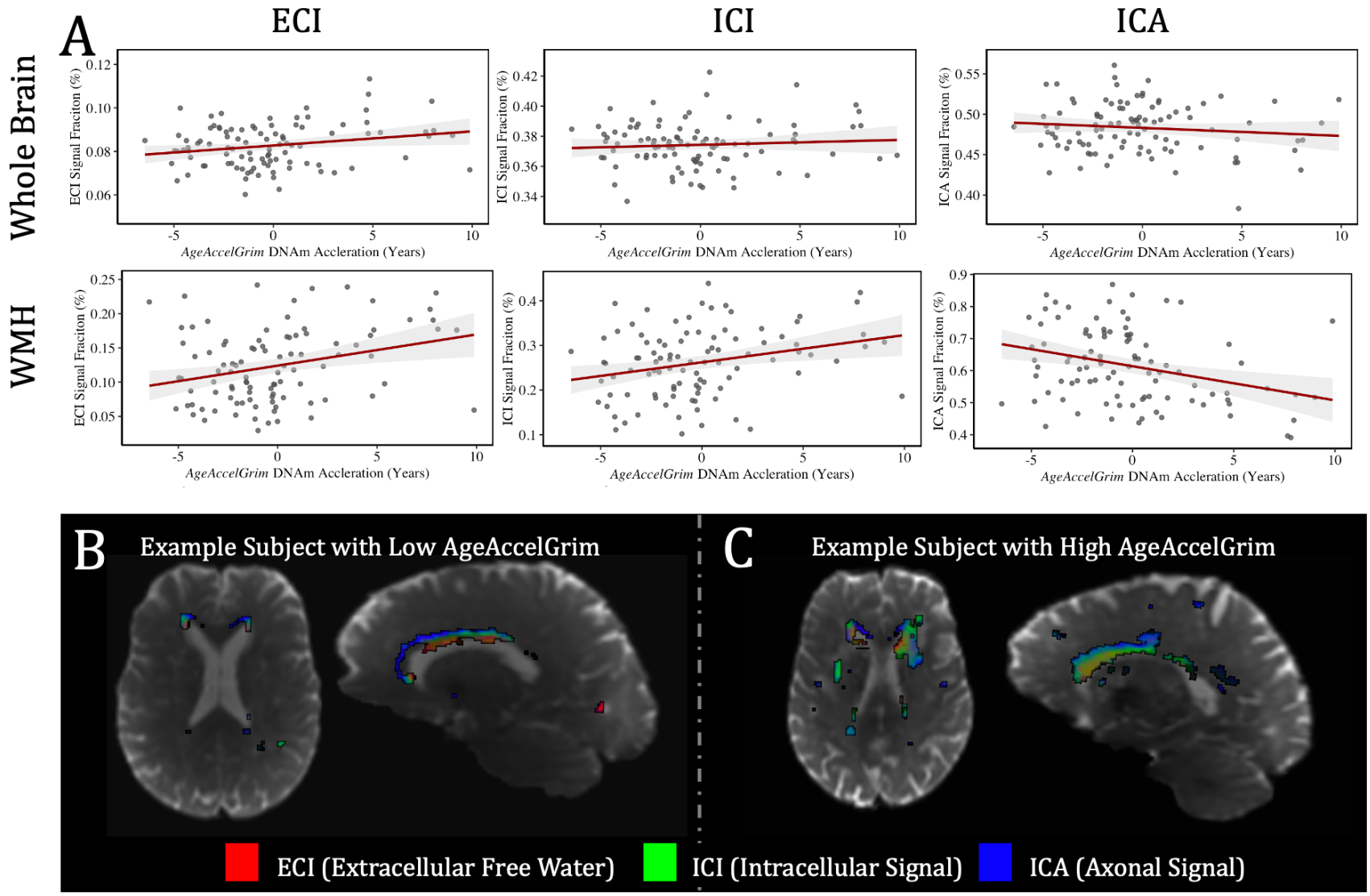
A
ECI
ICI
ICA
Whole Brain
WMH
ECI Signal Fraciton (%)
ICI Signal Fraciton (%)
ICA Signal Fraciton (%)
AgeAccelGrim DNAm Accleration (Years)
B
Example Subject with Low AgeAccelGrim
C
Example Subject with High AgeAccelGrim
ECI (Extracellular Free Water)
ICI (Intracellular Signal)
ICA (Axonal Signal)

Figure 3: (A) Charts showing the relationship between whole brain (top row) and WMH (bottom row) 3T-CSD microstructure measurements (from left to right: ECI, ICI, and ICA signal fractions) and AgeAccelGrim at baseline. All three microstructural tissue compartments averaged across the whole brain did not have a significant relationship with AgeAccelGrim ECI: $T_{6,93}$=1.797, p=0.076 n.s.; ICI: $T_{6,93}$=1.353, p=0.179 n.s.; ICA: $T_{6,93}$=-0.298, p=.767 n.s.). But when measured exclusively within the WMH all microstructure compartments had a significant relationship with AgeAccelGrim (ECI: $T_{6,92}$=2.844, p<0.01; ICI: $T_{6,92}$=2.741, p<0.01; ICA: $T_{6,92}$=-3.140, p<0.01). (B) Image of an example subject with low AgeAccelGrim with voxels composing the WMH RGB color-coded based on the respective proportion of signal fraction composition (ECI in red, ICI in green, and ICA in blue). (C) Image of an example subject with high AgeAccelGrim with voxels composing the WMH colored using the same approach. The subject with high AgeAccelGrim shows characteristically elevated levels of ECI and ICI signal fraction throughout the area identified as belonging to a WMH while in the low AgeAccelGrim subject the WMH is still largely composed of ICA signal fraction, indicating that it's composition is still similar to healthy nearby WM.

AgeAccelGrim does not predict WMH size and microstructural composition longitudinally

Looking longitudinally however AgeAccelGrim collected at baseline was less predictive of rates of changes in these metrics. As expected in an aging cohort total brain volume significantly declined between baseline and follow-up scans ($F_{1,40}$=9.163, p<0.01), while WMH volume significantly increased ($F_{1,40}$=7.688, p<0.01). For the microstructural metrics between baseline and follow-up whole brain ECI signal fraction significantly increased ($F_{1,36}$=5.395, p<0.05), while significant decreases were observed in whole brain ICI signal fraction ($F_{1,36}$=4.075, p<0.05) and no significant change was observed in ICA signal fraction ($F_{1,36}$=1.776, p=0.189 n.s.). AgeAccelGrim was not significantly predictive of changes in total brain volume ($F_{1,37}$=3.172, p=0.083 n.s.) (Fig. 4) nor was it predictive of any changes in whole brain cellular microstructure measurements (ECI: $F_{1,36}$= 0.412, p=0.525 n.s.; ICI: $F_{1,36}$=0.173, p=0.680 n.s.; ICA: $F_{1,36}$=1.292, p=0.263 n.s.). Despite strong correlations in the baseline data AgeAccelGrim was also not predictive of changes in WMH volume ($F_{1,36}$=2.377, p=0.131 n.s.) nor any microstructural composition measures (ECI: $F_{1,36}$=1.738, p=0.195 n.s.; ICI: $F_{1,36}$=0.141, p=0.709 n.s.; ICA: $F_{1,36}$=0.861, p=0.359 n.s.) (Fig. 5).

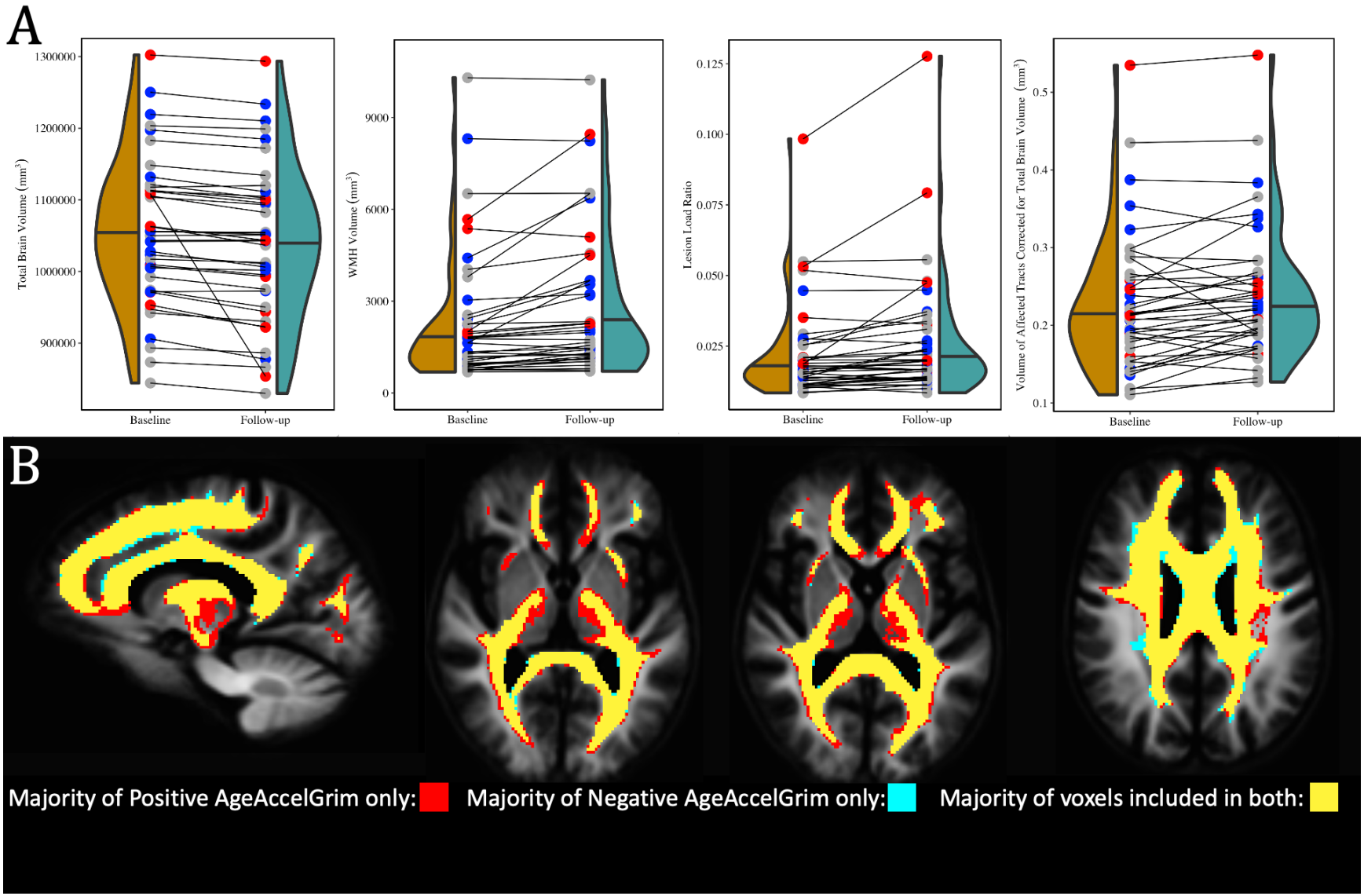
A
Total Brain Volume (mm³)
1300000
1200000
1100000
1000000
900000
Baseline
Follow-up
WMH Volume (mm³)
9000
6000
3000
0
Baseline
Follow-up
Lesion Load Ratio
0.125
0.100
0.075
0.050
0.025
Baseline
Follow-up
Volume of Affected Tracts Corrected for Total Brain Volume (mm³)
0.5
0.4
0.3
0.2
0.1
Baseline
Follow-up
B
Majority of Positive AgeAccelGrim only:
Majority of Negative AgeAccelGrim only:
Majority of voxels included in both:

Figure 4: (A) Charts displaying the observed longitudinal change in total brain volume, WMH volume, lesion load ratio (WMH volume to lesionometry ROI volume), and the volume of the lesionometry ROI volume corrected for total brain volume, from left to right. Individual subjects are represented in each chart by points at both baseline and follow-up, and are colored according to AgeAccelGrim measured at baseline (Blue = low AgeAccelGrim (less than -2), Red = high AgeAccelGrim (greater than 2), Gray = AgeAccelGrim close to chronological age (between -2 and 2)). Longitudinally, AgeAccelGrim was not significantly predictive of changes in total brain volume ($F_{1,37}$=3.172, p=0.083 n.s.) and was also not predictive of changes in WMH volume ($F_{1,36}$=2.377, p=0.131 n.s.). AgeAccelGrim was also did not significantly predict the longitudinal change in size of the network passing through the WMH ($F_{1,36}$=3.476, p=0.070 n.s.) but had a significant relationship with lesion load ($F_{1,36}$=5.397, p<0.05). (B) Images displaying the overlapping locations included in the lesionometry ROIs. The baseline lesionometry ROIs in template space from each subject were divided into two groups depending on AgeAccelGrim, with the positive group having a value greater than 0 indicating accelerated aging and the negative group having a value lower than 0 indicating slowed aging. A voxel was included in that group's mask if it was present in a majority (>50%) of subject's lesionometry ROIs. Both groups masks are presented above with voxels unique to each colored respectively (red for positive and blue for negative) and voxels common to both colored in yellow. Positive AgeAccelGrim subjects were more likely to have affected tracts that extended into the thalamus and frontal lobe, while negative AgeAccelGrim subjects were more likely to have affected periventricular and cingulate tracts.

AgeAccelGrim predicts baseline and longitudinal changes in microstructural composition in lesionometry ROIs

The microstructure measurements taken from the lesionometry ROIs however, were able to be predicted by AgeAccelGrim both cross-sectionally at baseline and longitudinally. At baseline AgeAccelGrim was trending toward a significant positive relationship with the size of the network passing through the WMH (volume of lesionometry ROI; $T_{5,93}$=1.976, p=0.0512) and was not significantly predictive of longitudinal change ($F_{1,36}$=3.476, p=0.070 n.s.) (Fig. 4). The subsequent microstructural models are corrected for subject age at baseline, sex, and volume of the lesionometry ROI. At baseline AgeAccelGrim had a significantly positive relationship with ECI signal fraction in the lesionometric ROI ($T_{5,93}$=2.586, p<0.05), a significantly positive relationship with ICI signal fraction ($T_{5,93}$=2.073, p<0.05), and a significantly negative relationship with ICA signal fraction ($T_{5,93}$=-2.299, p<0.05). Longitudinally AgeAccelGrim was able to significantly predict the change in microstructural measurements in the lesionometry ROI between baseline and follow-up for each signal fraction compartment (Fig. 5), with a positive

relationship between AgeAccelGrim and ECI signal fraction ($F_{1,36}$=11.11, p<0.01), a positive relationship between AgeAccelGrim and ICI signal fraction ($F_{1,36}$=4.352, p<0.05), and a negative relationship between AgeAccelGrim and ICA signal fraction ($F_{1,36}$=6.243, p<0.05). This is particularly interesting because when AgeAccelGrim is removed and the lesionometry ROIs are exclusively tested for longitudinal change between scanning sessions (including sex, age at baseline, and ROI volume as controls identical to before) there was only a significant difference between baseline and follow-up for the ECI signal fraction ($F_{1,37}$=8.846, p<0.01) and there was no significant difference between baseline and follow-up for the ICI signal fraction ($F_{1,37}$=1.143, p=0.291 n.s.) nor for the ICA signal fraction ($F_{1,37}$=4.051, p=0.051 n.s.). Finally, AgeAccelGrim had a significantly positive relationship with lesion load, a ratio between the volume of each subject's WMH and the volume of the lesionometry ROI (which does not include the WMH) at baseline ($T_{5,93}$=4.245, p<0.001) and longitudinally ($F_{1,36}$=5.397, p<0.05) (Fig. 4).

WMH Composition
ECI Signal Fraction (%)
0.25
0.20
0.15
0.10
0.05
Baseline
Follow-up
ICI Signal Fraction (%)
0.4
0.3
0.2
0.1
Baseline
Follow-up
ICA Signal Fraction (%)
0.8
0.7
0.6
0.5
Baseline
Follow-up
Lesionometry ROI
ECI Signal Fraction (%)
0.08
0.06
0.04
Baseline
Follow-up
ICI Signal Fraction (%)
0.25
0.20
0.15
0.10
Baseline
Follow-up
ICA Signal Fraction (%)
0.85
0.80
0.75
0.70
0.65
Baseline
Follow-up

Figure 5: Charts displaying longitudinal 3T-CSD microstructural results from both WMH and lesionometry ROIs from each of the 3 signal fraction compartments (ECI, ICI, and ICA, arranged left to right). Individual subjects are colored according to AgeAccelGrim measured at baseline (Blue = low AgeAccelGrim (less than -2), Red = high AgeAccelGrim (greater than 2), Gray = AgeAccelGrim close to chronological age (between -2 and 2)). Despite strong correlations in the baseline data AgeAccelGrim was not predictive of longitudinal changes in any WMH microstructural composition measures (ECI: $F_{1,36}=1.738$, $p=0.195$ n.s.; ICI: $F_{1,36}=0.141$, $p=0.709$ n.s.; ICA: $F_{1,36}=0.861$, $p=0.359$ n.s.). However AgeAccelGrim in the lesionometry ROI was able to significantly predict longitudinal change in each signal fraction compartment, with a positive relationship between AgeAccelGrim and ECI signal fraction ($F_{1,36}=11.11$, $p<0.01$), a positive relationship between AgeAccelGrim and ICI signal fraction ($F_{1,36}=4.353$, $p<0.05$), and a negative relationship between AgeAccelGrim and ICA signal fraction ($F_{1,36}=6.243$, $p<0.05$).

Discussion

By examining markers of SVD using advanced measures of diffusion microstructure in a subject-specific lesionometry approach this study has established a connection between a blood-based measure of mortality risk and neuronal damage. AgeAccelGrim was significantly correlated with WMH volume, supporting previous findings from other groups[16] and was significantly correlated with WMH microstructural composition. To date, this study is the first to demonstrate an association between accelerated epigenetic age derived from peripheral blood and brain cellular microstructure[293–295]. Specifically, AgeAccelGrim was associated with higher WMH ECI or extracellular free water signal fraction, higher ICI signal fraction, and lower ICA or axonal signal fraction (which in healthy WM areas can be typically observed at values exceeding 90-95% signal fraction). This either indicates that cellular microstructure in WMH areas was more heavily damaged in individuals with accelerated epigenetic age, or that that WMH in these subjects was located in a specific spatial pariventricular arrangement[91] or a combination of both (Fig. 3b&c, Fig. 4b).

Analyzing the axonal bundles that passed through the WMH showed that AgeAccelGrim was able to predict the size of the lesionometric ROI, an increased lesion burden, and increased degeneration within the lesionometric ROI. Many of these differences were not observable from a straightforward longitudinal perspective, highlighting the utility in using epigenetic clocks to measure age acceleration. The subject-specific lesionometric approach combined with 3T-CSD

analysis of cellular microstructure was able to isolate areas of the brain vulnerable to SVD-related damage. This further reinforced by the lack of longitudinal association between accelerated DNAm and whole brain microstructural measurements. It is necessary to narrowly define localized regions of the brain where vascular damage is likely occurring at an individual level. Related to this idea is the observed significant relationship between AgeAccelGrim and increased ICI signal fraction. When 3T-CSD is applied to the brain the ICI signal fraction (also referred to as the GM-like signal fraction) predominates in the cortex. Observing increased ICI signal fraction, especially within the WM skeleton where the WMH and lesionometry ROIs are located, is likely indicative of increased neuroinflammation or activated glial cells in response to injury[310]. The increased ECI signal fraction however, is straightforwardly interpretable as either edema or the absence of cellular tissue as a result of axonal degeneration. Together these longitudinal microstructure results indicate that AgeAccelGrim can predict subsequent neuronal deterioration over multiple years. This suggests that GrimAge may be a useful marker for positioning an individual on the trajectory of age-related neuronal decline, mediated via cardiovascular factors and SVD.

This study did not address the potential change in GrimAge calculation between baseline and follow-up, which is a missed opportunity to evaluate how changes in the metric relate to outcomes. It is possible that participants could have undertaken a major lifestyle change that would have altered their AgeAccelGrim, such as beginning a prolific smoking habit, between the baseline and follow-up recruitment. However, the relatively short period of time would likely not be long enough to impart significant change. Follow-up work to this study will aim to tie performance on cognitive tasks performed during assessment to epigenetic, cardiovascular, and diffusion microstructure metrics to evaluate the behavioral output of changed observed here. Further refinement of the GrimAge clock could include different combinations of plasma-proteins in order to discern which proteins are primarily driving observed changed in brain microstructure instead of general mortality.

The degree to which these results are based in WMH suggests a cardiovascular connection via SVD between the epigenetic clock estimates provided by AgeAccelGrim and brain cellular microstructure. While GrimAge has generally been shown to be highly predictive

of the development of several cardiovascular health related pathologies such as time-to-coronary heart disease, congestive heart failure, hypertension, type 2 diabetes, and physical functioning[280], it is still unknown exactly which features of the cardiovascular system drive this change and contribute to the results seen in this study. Several other studies have found that GrimAge is related to heart failure[311] and composite measures of whole cardiovascular health including diet, smoking, physical activity body mass index, blood pressure, total cholesterol, and blood glucose [312] but physiological measures of brain cardiovascular health have not been clearly associated with GrimAge[313]. WMH volume has previously been used as a biomarker for SVD severity[286] and ECI signal fraction analogues such as free water have been established as a marker for cerebral SVD[314]. These studies suggest that the results presented in this study indicate that AgeAccelGrim may be a biomarker for SVD-related brain injury and degeneration.

This study has provided evidence that a blood-based epigenetic marker of age acceleration can predict the degenerative effects of SVD in the brain. AgeAccelGrim was able to predict the volume and composition of WMH as well as widespread diffusion microstructure signatures of neuronal decline in a subject-specific manner.

Supplementary Methods

Epigenetic Age

Eight and a half milliliters of whole blood were drawn into a PAXgene Blood DNA Tube (PreAnalytiX, Hombrechtikon, Switzerland). Samples were stored at 20°C for short-term storage (up to 3 months) then transferred to -80°C for long-term storage. DNA was extracted using the PAXgene Blood DNA kit (PreAnalytiX, Hombrechtikon, Switzerland) according to manufacturer instructions. DNA concentration was determined by Quant-iT™ PicoGreen® dsDNA reagent (Thermofisher Scientific, Waltham, MA, USA) per manufacturers instruction. Florescence was detected using a Tecan Infinite M200 Pro microplate reader (Tecan, Switzerland). 500 ng of DNA was bisulfite treated using a Zymo EZ DNA Methylation kit (Zymo Research, Irvine, CA) using PCR conditions for Illumina's Infinium Methylation assay (95°C for 30 seconds, 50°C for 60 minutes×16 cycles). DNA methylation was assayed using the Illumina Infinium MethylationEPIC BeadChips. Briefly, a total of 4μL of bisulfite converted DNA was hybridized to Illumina BeadChips using the manufacturer's protocols. Samples were denatured and amplified overnight for 20 to 24 hours. Fragmentation, precipitation, and resuspension of the samples followed overnight incubation, before hybridization to EPIC BeadChips for 16 to 24 hours. BeadChips were then washed to remove any unhybridized DNA and labeled with nucleotides to extend the primers to the DNA sample. Following the Infinium HD Methylation protocol, the BeadChips were imaged using the Illumina iScan system (Illumina).

Raw .idat files were read and preprocessed using the minfi R package[304,306]. The data set was preprocessed using noob for background subtraction and dye-bias normalization. All methylation values with detection P>0.01 were set to missing (median sample: 765 probes, range: 319 to 4453), and probes with >1% missing values (n=6,663) were removed from further analysis. All samples were checked and confirmed to ensure that predicted sex matched reported sex. Additionally, samples were checked for excessive missing data (>5%) and unusual cell mixture estimates, which was estimated using the Houseman method as implemented in minfi[307,308]. All samples passed these quality controls. Principal components analysis, as

implemented in the shinyMethyl R package, was used to examine batch effects [305]. The first seven principal components were examined using plots and potential batch effects were tested using linear models. Principal components 3 and 6, which account for 2.38% and 1.65% of total variance respectively, were associated with position on the array (PC3: $F_{(7, 100)} = 6.668$, p = 1.77e-6, adjusted $R^2 = 0.271$; PC6: $F_{(7, 100)} = 2.328$, p = 0.030, adjusted $R^2 = 0.080$). Principal components 1, 4, and 5, which account for 3.63%, 1.89%, and 1.77% of the total variance were associated with bisulfite conversion plate (PC1: $F_{(1, 106)} = 9.918$, p = 0.002, adjusted $R^2 = 0.077$; PC4: $F_{(1, 100)} = 34.04$, p = 5.932e-8, adjusted $R^2 = 0.236$; PC5: $F_{(1, 100)} = 31.07$, p = 1.91e-7, adjusted $R^2 = 0.219$). Principal components 4 and 5, were associated with array (PC4: $F_{(13, 94)} = 4.332$, p = 1.14e-5, adjusted $R^2 = 0.288$; PC5: $F_{(13, 94)} = 4.229$, p = 1.06e-5, adjusted $R^2 = 0.282$). Bisulfite conversion plate and array number were associated with each other, as samples on the same array originated from the same bisulfite conversion plate. Because samples were randomized across plates and arrays, and proportions of variance explained by associated principle components were low, no batch correction method was used. The ewastools R package was used to assess Illumina quality control metrics and call genotypes and donor IDs to ensure the identity of repeated samples from the same individual[309]. All samples passed Illumina quality controls.

To determine assay variability, we included one set of five technical replicates and an additional three sets of two technical replicates. After quality control filters and normalization procedures were applied, the 5,000 CpGs with the most variable M values were used as input for calculating Pearson's correlation coefficients among all pairwise combinations of samples. Pearson's correlation of unrelated samples (different individuals) were below 0.8. Pearson's while correlations of technical replicates ranged from 0.988-0.994, indicating high agreement between technical replicates.

Unnormalized betas were filtered to include CpGs specified by Horvath as necessary for calculation of various clocks. The betas were uploaded to Horvath's online DNA methylation age calculator (htpps://dnamage.genetics.ucla.edu), which provides measures of Horvath's multi-tissue age estimator[282], DNA methylation GrimAge[280], and cell type abundance. A sample annotation file was included. The options to normalize data and apply advanced analysis were

selected. Technical replicates were used to determine measurement error of DNAmAge, the output of Horvath's multi-tissue age estimator. The absolute difference of DNAmAge between technical replicate pairs was taken, as was the highest absolute difference in the set of five technical replicates. The median of the absolute difference was 2.02 years (range: 0.44-5.73 years).

Conclusion

This completed dissertation expands the field of neuroimaging by creating a novel, reproducible, and reliable, quantitative technique for the estimation of brain cellular microstructure from diffusion MRI. Termed 3T-CSD, this dissertation has extensively tested 3T-CSD metrics under a variety of research and clinical conditions and MR acquisition parameters in order to confidently present a ready to use method applicable in traditional research studies. In the second chapter of this dissertation 3T-CSD was applied to the study of the human lifespan, deploying the method both in large 'big data' cohorts of thousands of individuals and in a subject-specific manner. Studies covered the range of the lifespan and characterized neuronal development and decline at the microstructural level. By relating observed changes in neuronal microstructure to biological outputs in developing and aging cohorts this dissertation connects observable phenotypes to neurology and advances scientific understanding of the brain.

To summarize, the various components of this project have addressed the following:

Aim 1

Study 1a: Evaluated a number of acquisition factors and their effect on output extracellular free water signal fraction measurements. This highlighted components of the acquisition that biased output measurements as well as suggested that smaller ROIs were more vulnerable to these effects. Deploying SS3T-CSD reduced the relationship between smaller ROIs and acquisition factors so that it was no longer significant.

Study 1b: Further explored the differences between single- and multi-shell CSD algorithms, and found that SS3T-CSD was more able to differentiate between subregions of the hippocampus based on 3T-CSD microstructure profiles.

Study 1c: Established the reliability and stability of 3T-CSD microstructure profiles in both immediate scan-rescan conditions, with 2 weeks between scan rescan, and with 3-4 months

between scan and rescan. All tissue signal fraction compartments showed excellent reliability across a number of assessment metrics though there was a slight decline in the 3-4 month group especially in ICI (GM-like) and ICA (WM-like) signal fraction measurements.

Study 1d: Investigated reliability of 3T-CSD measurements when taken at multiple scanning sites. Measurements were taken from 212 ROIs across the cortex and WM the large majority of ROIs were not significantly different when measured at different sites vs when measured repeatedly at a single site. This supports the use of 3T-CSD in cohorts collected across multiple scanning sites such as ABCD.

Study 1e: Described a novel means to register 3T-CSD signal fraction maps to stereotaxic space for subsequent measurement or parcellation. Using underlying FOD information from WM axon bundle orientation alongside an FOD template derived from the NTU-DSI-122 template provided superior registration to intensity-based methods.

Aim 2

Study 2a: Described 3T-CSD measurements across the brain and lifespan in a number of ROIs. Demonstrated a general trend where ECI increased throughout the lifespan, ICI decreased, and ICA had an initial increase until middle age then a steady decrease into advanced age. Some degree of hemispheric laterality was also generally present in most ROIs examined.

Study 2b: Examined the relationship between 3T-CSD measurements in deep white matter ROIs and pubertal development in a cross-sectional group of 4752 adolescents. An anisotropic diffusion signal fraction was found to have a negative correlation, while an intracellular isotropic diffusion signal fraction had a positive correlation with pubertal development across the majority of axonal ROIs. These results provide evidence for complex microstructural changes in brain development within the white matter skeleton.

Study 2c: Used a subject-specific approach applying lesionometry to the study of WMH for the first time to compare 3T-CSD microstructure output with GrimAge, an epigenetic marker

for mortality risk. GrimAge is correlates with 12 plasma-proteins and may be sensitive to cardiovascular health. Using WMH as a symptom of SVD, we found a relationship between an age-adjusted version of GrimAge and 3T-CSD measurements both within WMH and in areas across the brain where axonal tracts also traversed WMH areas. GrimAge was associated with increased ECI signal fraction, increased ICI signal fraction, and decreased ICA signal fraction. This is the first study to demonstrate a connection between GrimAge and brain cellular microstructure, as well as suggesting GrimAge as a proxy for the degenerative effects of SVD on the brain.

The studies performed in Chapter 1 of this dissertation describe the technical development and testing of the novel 3T-CSD model for quantitatively assessing brain microstructure. The ability of 3T-CSD to measure brain microstructure in both clinical and experimental situations was examined, as was the ability of different CSD algorithms to discriminate between anatomical structures. Reliability of ICA, ICI, and ECI tissue compartment signal fractions were assessed both cross-sectionally between scanning locations and longitudinally in the same scanning location. Finally, a novel method of registering the signal fraction maps to a common space was developed and demonstrated with comparisons to previous best practices. This technical development was followed by 3 novel applications: First to study 3T-CSD metrics across the lifespan similar to volumetric MRI lifespan studies, showing that there was significant variation across the lifespan and between hemispheres. Secondly during development, to demonstrate that 3T-CSD signal fractions are sensitive to pubertal development. Lastly during aging, to establish a relationship between cardiovascular health and accelerated epigenetic aging that drives subject-specific patterns of neuronal degeneration and decline. Together the studies in this dissertation establish 3T-CSD as an effective tool to measure brain cellular microstructure throughout development and aging. These studies provide an analysis pipeline and strategy for continued application of 3T-CSD signal fractions in lifespan studies, as well as the possibility to expand use into the study of pathology.

Acknowledgements

I would like to acknowledge the support of my family and particularly my partner Nat, I genuinely could not have done it without you and I'll be there every step of the way for you, like you were for me, as you finish your PhD and beyond on every adventure. My broader family has been instrumental in supporting and helping me pursue this degree, they've supported my sacrifices of time and their interest in my work has carried me through many a discouraging moment. To Jan, Kim, Ben, Jake, Austin, Elliot, Mike, and Lee thank you all so much. A very heartfelt thanks to Jason Druzgal for the years of mentorship and guidance. You not only took a chance on me at the beginning but kept me focused and let me explore this work and this entire field more than I ever dreamed when I started my career. At the outset of this project, you gave me a paper and a program and asked if I could bring that technique to UVA. Turns out I didn't bring that technique to UVA, and I didn't use it to model Parkinson's like we planned, but I hope 3T-CSD is a good consolation prize. I'm excited to see what we can do together over the coming years.

I would also like to acknowledge the tremendous effort of all our collaborators and the people who recruited, collected, and made available the thousands of scans used in this dissertation. This project would never have happened without their generous effort and the gracious time of all the participants who took part in these studies. I would like to specifically thank the efforts of the Morris and Connelly Labs from the Psychology Department at the University of Virginia for the immense amount of work they performed to make the Virginia Cognitive Aging Project dataset a reality. Morgan Lynch, now at USC, deserves credit and thanks for being the primary point of contact and guide for all participants at their baseline visit. Amalia McDonald Skyberg has been an invaluable collaborator and friend through several projects both in this dissertation and outside it. Josh Danoff has done an incredible job with the epigenetic work that appears in the final paper in this dissertation.

Matt Panzer and his team have been phenomenal collaborators as well, Kristen Reynier both helped me through statistical coursework and handled subject recruitment and transport for the Head Bop project. Jake Resch has been a great early mentor from when I first arrived at

UVA and through many PET/TBI planning meetings. Tom Fletcher and his lab have been wonderful collaborators and Tom has been a fantastic mentor through my fellowship project and working with ABCD. Jim Patrie has provided excellent statistical support through the years and on several projects included here, I hope he's having a wonderful time in Iowa where he now lives. Any acknowledgement of my time at UVA would be incomplete without highlighting the work done by Nadia Cempre as the Neuroscience Graduate Program administrator, she helped keep me in line to graduate many times and has been a great friend over the years at UVA. All of my friends in the NGP and BIMS Core who are too numerous to mention and who helped me survive this program (and especially core course) and who I will count as lifelong friends. In the Druzgal lab I benefitted greatly from data collected by Bryson Reynolds and work done by Christina Gancayco. Jamie Blair provided endless help and support navigating my early years at UVA, as well as recruiting me in the first place. I wouldn't be here without him and he made it worth journeying into the lab each day in those early years.

I would also like to acknowledge the various funding bodies that supported me through this degree. The University, School of Medicine, BIMS, and especially the Brain Institute made my continued work possible. A special thanks to all the members of my committee Alev Erisir for agreeing to Chair and to Jack Van Horn for helping me take the next steps in my career.

A final, special acknowledgement goes to Jose Reyes, who has been in the position of MRI Technologist throughout the entirety of this degree, and who has personally collected and catalogued nearly all the images from my own projects.

On December 1, 2017 at 8:58am, Jose responded to my request for a phantom scan using our diffusion sequence which, later that day, became the first image ever analyzed using the technique we now call 3-Tissue Constrained Spherical Deconvolution. That image led directly to everything presented in this dissertation, and is reprinted below:

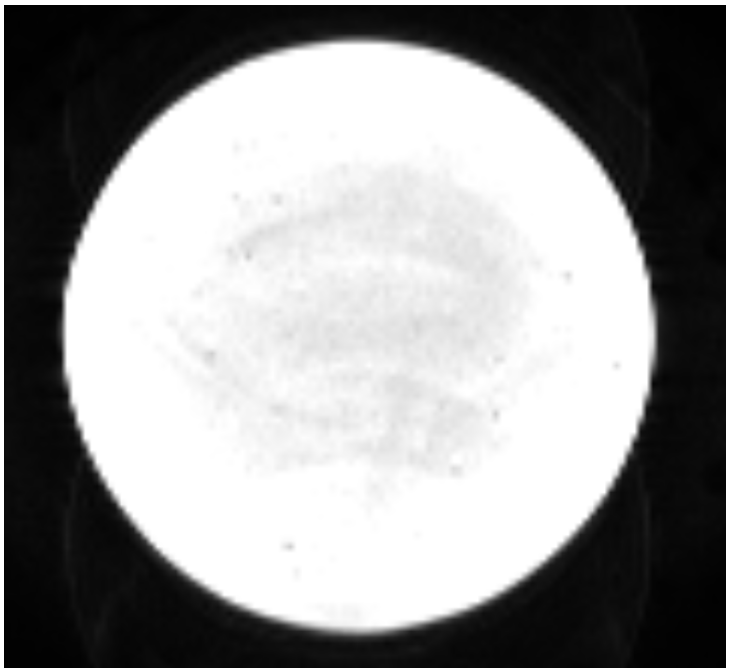

Works Cited

1. Brown R. XXVII. A brief account of microscopical observations made in the months of June, July and August 1827, on the particles contained in the pollen of plants; and on the general existence of active molecules in organic and inorganic bodies. *The philosophical magazine*. 1828;4(21):161-173.

2. Basser PJ. Inferring microstructural features and the physiological state of tissues from diffusion-weighted images. *NMR in Biomedicine*. 1995;8(7):333-344.

3. Pierpaoli C, Basser PJ. Toward a quantitative assessment of diffusion anisotropy. *Magnetic resonance in Medicine*. 1996;36(6):893-906.

4. Conturo TE, Lori NF, Cull TS, et al. Tracking neuronal fiber pathways in the living human brain. *Proceedings of the National Academy of Sciences*. 1999;96(18):10422-10427.

5. Mori S, Crain BJ, Chacko VP, Van Zijl PC. Three-dimensional tracking of axonal projections in the brain by magnetic resonance imaging. *Annals of Neurology: Official Journal of the American Neurological Association and the Child Neurology Society*. 1999;45(2):265-269.

6. Lee JK, Koppelmans V, Riascos RF, et al. Spaceflight-associated brain white matter microstructural changes and intracranial fluid redistribution. *JAMA neurology*. 2019;76(4):412-419.

7. Ofori E, Pasternak O, Planetta PJ, et al. Longitudinal changes in free-water within the substantia nigra of Parkinson's disease. *Brain*. 2015;138(8):2322-2331.

8. Pasternak O, Kelly S, Sydnor VJ, Shenton ME. Advances in microstructural diffusion neuroimaging for psychiatric disorders. *Neuroimage*. 2018;182:259-282.

9. Healy Jr DM, Hendriks H, Kim PT. Spherical deconvolution. *Journal of Multivariate Analysis*. 1998;67(1):1-22.

10. Jeurissen B, Tournier JD, Dhollander T, Connelly A, Sijbers J. Multi-tissue constrained spherical deconvolution for improved analysis of multi-shell diffusion MRI data. *NeuroImage*. 2014;103:411-426. doi:10.1016/j.neuroimage.2014.07.061

11. Tournier JD, Calamante F, Connelly A. Robust determination of the fibre orientation distribution in diffusion MRI: non-negativity constrained super-resolved spherical deconvolution. *Neuroimage*. 2007;35(4):1459-1472.

12. Tournier JD, Smith R, Raffelt D, et al. MRtrix3: A fast, flexible and open software framework for medical image processing and visualisation. *NeuroImage*. 2019;202:116137.

13. Dima D, Modabbernia A, Papachristou E, et al. Subcortical volumes across the lifespan: Data from 18,605 healthy individuals aged 3–90 years. *Human brain mapping*. 2022;43(1):452-469.

14. Bethlehem RA, Seidlitz J, White SR, et al. Brain charts for the human lifespan. *Nature*. Published online 2022. doi:https://doi.org/10.1038/s41586-022-04554-y

15. Blair J C, Newman BT, Druzgal TJ. Evaluating Lifespan Tissue Structure: Comparing CSD Signal Fraction and VBM Grey Matter Density. *Proceedings of the ISMRM 27th General Meeting*. Published online 2019.

16. Hillary RF, Stevenson AJ, Cox SR, et al. An epigenetic predictor of death captures multi-modal measures of brain health. *Molecular psychiatry*. Published online 2019:1-11.

17. Stejskal EO, Tanner JE. Spin diffusion measurements: spin echoes in the presence of a time-dependent field gradient. *The journal of chemical physics*. 1965;42(1):288-292.

18. Einstein A. On the motion of small particles suspended in liquids at rest required by the molecular-kinetic theory of heat. *Annalen der physik*. 1905;17(549-560):208.

19. Basser PJ, Mattiello J, LeBihan D. MR diffusion tensor spectroscopy and imaging. *Biophysical journal*. 1994;66(1):259-267.

20. Assaf Y, Freidlin RZ, Rohde GK, Basser PJ. New modeling and experimental framework to characterize hindered and restricted water diffusion in brain white matter. *Magnetic Resonance in Medicine: An Official Journal of the International Society for Magnetic Resonance in Medicine*. 2004;52(5):965-978.

21. Assaf Y, Basser PJ. Composite hindered and restricted model of diffusion (CHARMED) MR imaging of the human brain. *Neuroimage*. 2005;27(1):48-58.

22. Assaf Y, Pasternak O. Diffusion tensor imaging (DTI)-based white matter mapping in brain research: a review. *Journal of molecular neuroscience*. 2008;34(1):51-61.

23. Behrens TE, Woolrich MW, Jenkinson M, et al. Characterization and propagation of uncertainty in diffusion-weighted MR imaging. *Magnetic Resonance in Medicine: An Official Journal of the International Society for Magnetic Resonance in Medicine*. 2003;50(5):1077-1088.

24. Pasternak O, Sochen N, Gur Y, Intrator N, Assaf Y. Free water elimination and mapping from diffusion MRI. *Magnetic Resonance in Medicine: An Official Journal of the International Society for Magnetic Resonance in Medicine*. 2009;62(3):717-730.

25. Ofori E, Pasternak O, Planetta PJ, et al. Increased free water in the substantia nigra of Parkinson's disease: a single-site and multi-site study. *Neurobiology of aging*. 2015;36(2):1097-1104.

26. Wheeler-Kingshott CA, Cercignani M. About “axial” and “radial” diffusivities. *Magnetic Resonance in Medicine: An Official Journal of the International Society for Magnetic Resonance in Medicine*. 2009;61(5):1255-1260.

27. Tournier JD, Mori S, Leemans A. Diffusion tensor imaging and beyond. *Magnetic resonance in medicine*. 2011;65(6):1532.

28. Kamagata K, Zalesky A, Hatano T, et al. Connectome analysis with diffusion MRI in idiopathic Parkinson’s disease: Evaluation using multi-shell, multi-tissue, constrained spherical deconvolution. *NeuroImage: Clinical*. 2018;17:518-529.

29. Hahn EL. Spin echoes. *Physical review*. 1950;80(4):580.

30. Boss BD, Stejskal EO, Ferry JD. Self-diffusion in high molecular weight polyisobutylene-benzene mixtures determined by the pulsed-gradient, spin-echo method. *The Journal of Physical Chemistry*. 1967;71(5):1501-1506.

31. Murday JS, Cotts RM. Self-diffusion coefficient of liquid lithium. *The Journal of Chemical Physics*. 1968;48(11):4938-4945.

32. Harmon JF. Low frequency spin lattice relaxation in glycerol. *Chemical Physics Letters*. 1970;7(2):207-208.

33. James TL, McDonald GG. Measurement of the self-diffusion coefficient of each component in a complex system using pulsed-gradient Fourier transform NMR. *Journal of Magnetic Resonance (1969)*. 1973;11(1):58-61.

34. Le Bihan D, Breton E, Lallemand D, Grenier P, Cabanis E, Laval-Jeantet M. MR imaging of intravoxel incoherent motions: application to diffusion and perfusion in neurologic disorders. *Radiology*. 1986;161(2):401-407.

35. Turner R, Le Bihan D, Maier J, Vavrek R, Hedges LK, Pekar J. Echo-planar imaging of intravoxel incoherent motion. *Radiology*. 1990;177(2):407-414.

36. Boss BD, Stejskal EO. Restricted, anisotropic diffusion and anisotropic nuclear spin relaxation of protons in hydrated vermiculite crystals. *Journal of Colloid and Interface Science*. 1968;26(3):271-278.

37. Tanner JE. Self diffusion of water in frog muscle. *Biophysical journal*. 1979;28(1):107-116.

38. Chenevert TL, Brunberg JA, Pipe JG. Anisotropic diffusion in human white matter: demonstration with MR techniques in vivo. *Radiology*. 1990;177(2):401-405.

39. Moseley ME, Cohen Y, Kucharczyk J, et al. Diffusion-weighted MR imaging of anisotropic water diffusion in cat central nervous system. *Radiology*. 1990;176(2):439-445.

40. O'Donnell LJ, Westin CF. An introduction to diffusion tensor image analysis. *Neurosurgery Clinics*. 2011;22(2):185-196.

41. Mattiello J, Basser PJ, LeBihan D. Analytical expressions for the b matrix in NMR diffusion imaging and spectroscopy. *Journal of magnetic resonance, Series A*. 1994;108(2):131-141.

42. De Stefano N, Narayanan S, Francis GS, et al. Evidence of axonal damage in the early stages of multiple sclerosis and its relevance to disability. *Archives of neurology*. 2001;58(1):65-70.

43. Song SK, Sun SW, Ramsbottom MJ, Chang C, Russell J, Cross AH. Dysmyelination revealed through MRI as increased radial (but unchanged axial) diffusion of water. *Neuroimage*. 2002;17(3):1429-1436.

44. Song SK, Yoshino J, Le TQ, et al. Demyelination increases radial diffusivity in corpus callosum of mouse brain. *Neuroimage*. 2005;26(1):132-140.

45. van Gelderen P, de Vleeschouwer MH, DesPres D, Pekar J, van Zijl PC, Moonen CT. Water diffusion and acute stroke. *Magnetic resonance in medicine*. 1994;31(2):154-163.

46. Soares JM, Marques P, Alves V, Sousa N. A hitchhiker's guide to diffusion tensor imaging. *Frontiers in neuroscience*. 2013;7:31.

47. Bihan DL. Molecular diffusion, tissue microdynamics and microstructure. *NMR in Biomedicine*. 1995;8(7):375-386.

48. Nakada T, Matsuzawa H, Kwee IL. Magnetic resonance axonography of the rat spinal cord. *Neuroreport*. 1994;5(16):2053-2056.

49. Pajevic S, Pierpaoli C. Color schemes to represent the orientation of anisotropic tissues from diffusion tensor data: application to white matter fiber tract mapping in the human brain. *Magnetic Resonance in Medicine: An Official Journal of the International Society for Magnetic Resonance in Medicine*. 1999;42(3):526-540.

50. Basser PJ, Pajevic S, Pierpaoli C, Duda J, Aldroubi A. In vivo fiber tractography using DT-MRI data. *Magnetic resonance in medicine*. 2000;44(4):625-632.

51. Pierpaoli C, Barnett A, Pajevic S, et al. Water diffusion changes in Wallerian degeneration and their dependence on white matter architecture. *Neuroimage*. 2001;13(6):1174-1185.

52. Tournier JD, Calamante F, King MD, Gadian DG, Connelly A. Limitations and requirements of diffusion tensor fiber tracking: an assessment using simulations. *Magnetic Resonance in Medicine: An Official Journal of the International Society for Magnetic Resonance in Medicine*. 2002;47(4):701-708.

53. Jeurissen B, Leemans A, Tournier JD, Jones DK, Sijbers J. Investigating the prevalence of complex fiber configurations in white matter tissue with diffusion magnetic resonance imaging. *Human brain mapping*. 2013;34(11):2747-2766.

54. Tuch DS. High angular resolution diffusion imaging of the human brain. In: *Proceedings of the 7th Annual Meeting of ISMRM, Philadelphia, 1999*. Vol 321. ; 1999.

55. Tuch DS, Reese TG, Wiegell MR, Makris N, Belliveau JW, Wedeen VJ. High angular resolution diffusion imaging reveals intravoxel white matter fiber heterogeneity. *Magnetic Resonance in Medicine: An Official Journal of the International Society for Magnetic Resonance in Medicine*. 2002;48(4):577-582.

56. Dell'Acqua F, Rizzo G, Scifo P, et al. A deconvolution approach based on multi-tensor model to solve fiber crossing in diffusion-MRI. In: *2005 IEEE Engineering in Medicine and Biology 27th Annual Conference*. IEEE; 2006:1415-1418.

57. Pasternak O, Sochen N, Assaf Y. PDE based estimation and regularization of multiple diffusion tensor fields. *Visualization and Image Processing of Tensor Fields Springer-Verlag Berlin/New York*. Published online 2005.

58. Zhang H, Schneider T, Wheeler-Kingshott CA, Alexander DC. NODDI: practical in vivo neurite orientation dispersion and density imaging of the human brain. *Neuroimage*. 2012;61(4):1000-1016.

59. Behrens TE, Berg HJ, Jbabdi S, Rushworth MF, Woolrich MW. Probabilistic diffusion tractography with multiple fibre orientations: What can we gain? *neuroimage*. 2007;34(1):144-155.

60. Seunarine KK, Alexander DC. Multiple fibers: beyond the diffusion tensor. In: *Diffusion Mri*. Elsevier; 2014:105-123.

61. Metzler-Baddeley C, O'Sullivan MJ, Bells S, Pasternak O, Jones DK. How and how not to correct for CSF-contamination in diffusion MRI. *Neuroimage*. 2012;59(2):1394-1403.

62. Duering M, Finsterwalder S, Baykara E, et al. Free water determines diffusion alterations and clinical status in cerebral small vessel disease. *Alzheimer's & Dementia*. 2018;14(6):764-774.

63. Burciu RG, Ofori E, Archer DB, et al. Progression marker of Parkinson's disease: a 4-year multi-site imaging study. *Brain*. 2017;140(8):2183-2192.

64. Planetta PJ, Ofori E, Pasternak O, et al. Free-water imaging in Parkinson's disease and atypical parkinsonism. *Brain*. 2016;139(2):495-508.

65. Braak H, Del Tredici K, Rüb U, De Vos RA, Steur ENJ, Braak E. Staging of brain pathology related to sporadic Parkinson's disease. *Neurobiology of aging*. 2003;24(2):197-211.

66. Venkateshappa C, Harish G, Mythri RB, Mahadevan A, Srinivas Bharath MM, Shankar SK. Increased oxidative damage and decreased antioxidant function in aging human substantia nigra compared to striatum: implications for Parkinson's disease. *Neurochemical research*. 2012;37(2):358-369.

67. Marek K, Jennings D, Lasch S, et al. The Parkinson progression marker initiative (PPMI). *Progress in neurobiology*. 2011;95(4):629-635.

68. Nasreddine ZS, Phillips NA, Bédirian V, et al. The Montreal Cognitive Assessment, MoCA: a brief screening tool for mild cognitive impairment. *Journal of the American Geriatrics Society*. 2005;53(4):695-699.

69. Hoehn MM, Yahr MD. Parkinsonism: onset, progression, and mortality. *Neurology*. 1998;50(2):318-318.

70. Schuff N, Wu IW, Buckley S, et al. Diffusion imaging of nigral alterations in early Parkinson's disease with dopaminergic deficits. *Movement Disorders*. 2015;30(14):1885-1892.

71. Gurholt TP, Haukvik UK, Lonning V, Jönsson EG, Pasternak O, Agartz I. Microstructural white matter and links with subcortical structures in chronic schizophrenia: a free-water imaging approach. *Frontiers in psychiatry*. 2020;11:56.

72. Lyall AE, Pasternak O, Robinson DG, et al. Greater extracellular free-water in first-episode psychosis predicts better neurocognitive functioning. *Molecular psychiatry*. 2018;23(3):701-707.

73. Mandl RC, Pasternak O, Cahn W, et al. Comparing free water imaging and magnetization transfer measurements in schizophrenia. *Schizophrenia research*. 2015;161(1):126-132.

74. Oestreich LK, Pasternak O, Shenton ME, et al. Abnormal white matter microstructure and increased extracellular free-water in the cingulum bundle associated with delusions in chronic schizophrenia. *NeuroImage: Clinical*. 2016;12:405-414.

75. Pasternak O, Westin CF, Bouix S, et al. Excessive extracellular volume reveals a neurodegenerative pattern in schizophrenia onset. *Journal of Neuroscience*. 2012;32(48):17365-17372.

76. Pasternak O, Westin CF, Dahlben B, Bouix S, Kubicki M. The extent of diffusion MRI markers of neuroinflammation and white matter deterioration in chronic schizophrenia. *Schizophrenia research*. 2015;161(1):113-118.

77. Bergamino M, Pasternak O, Farmer M, Shenton ME, Hamilton JP. Applying a free-water correction to diffusion imaging data uncovers stress-related neural pathology in depression. *NeuroImage: Clinical*. 2016;10:336-342.

78. Tuozzo C, Lyall AE, Pasternak O, James AC, Crow TJ, Kubicki M. Patients with chronic bipolar disorder exhibit widespread increases in extracellular free water. *Bipolar disorders*. 2018;20(6):523-530.

79. Pasternak O, Koerte IK, Bouix S, et al. Hockey Concussion Education Project, Part 2. Microstructural white matter alterations in acutely concussed ice hockey players: a longitudinal free-water MRI study. *Journal of neurosurgery*. 2014;120(4):873-881.

80. Albi A, Pasternak O, Minati L, et al. *Free Water Elimination Improves Test–Retest Reproducibility of Diffusion Tensor Imaging Indices in the Brain: A Longitudinal Multisite Study of Healthy Elderly Subjects*. Wiley Online Library; 2017.

81. Catani M, Howard RJ, Pajevic S, Jones DK. Virtual in vivo interactive dissection of white matter fasciculi in the human brain. *Neuroimage*. 2002;17(1):77-94.

82. Pierpaoli C, Jones DK. Removing CSF contamination in brain DT-MRIs by using a two-compartment tensor model. In: *International Society for Magnetic Resonance in Medicine Meeting*. ; 2004:1215.

83. Bett KE, Cappi JB. Effect of pressure on the viscosity of water. *Nature*. 1965;207(4997):620-621.

84. Bradley KC. Cerebrospinal fluid pressure. *Journal of Neurology, Neurosurgery & Psychiatry*. 1970;33(3):387-397.

85. Childs C, Hiltunen Y, Vidyasagar R, Kauppinen RA. Determination of regional brain temperature using proton magnetic resonance spectroscopy to assess brain–body temperature differences in healthy human subjects. *Magnetic Resonance in Medicine: An Official Journal of the International Society for Magnetic Resonance in Medicine*. 2007;57(1):59-66.

86. Thomsen C, Henriksen O, Ring P. In vivo measurement of water self diffusion in the human brain by magnetic resonance imaging. *Acta radiologica*. 1987;28(3):353-361.

87. Dell'Acqua F, Tournier JD. Modelling white matter with spherical deconvolution: How and why? *NMR in Biomedicine*. 2019;32(4):e3945.

88. Dhollander T, Raffelt D, Connelly A. Unsupervised 3-tissue response function estimation from single-shell or multi-shell diffusion MR data without a co-registered T1 image. In: *ISMRM Workshop on Breaking the Barriers of Diffusion MRI*. Vol 5. ISMRM; 2016.

89. Ridgway GR, Omar R, Ourselin S, Hill DL, Warren JD, Fox NC. Issues with threshold masking in voxel-based morphometry of atrophied brains. *Neuroimage*. 2009;44(1):99-111.

90. Dhollander T, Connelly A. A novel iterative approach to reap the benefits of multi-tissue CSD from just single-shell (+ b= 0) diffusion MRI data. In: *Proc ISMRM*. Vol 24. ; 2016:3010.

91. Mito R, Dhollander T, Xia Y, et al. In vivo microstructural heterogeneity of white matter lesions in healthy elderly and Alzheimer's disease participants using tissue compositional analysis of diffusion MRI data. *NeuroImage: Clinical*. 2020;28:102479.

92. Dhollander T, Raffelt D, Connelly A. Towards interpretation of 3-tissue constrained spherical deconvolution results in pathology. In: *Proc. Intl. Soc. Mag. Reson. Med*. Vol 25. ; 2017:1815.

93. Wells WM, Grimson WEL, Kikinis R, Jolesz FA. Adaptive segmentation of MRI data. *IEEE transactions on medical imaging*. 1996;15(4):429-442.

94. Raffelt D, Dhollander T, Tournier JD, et al. Bias field correction and intensity normalisation for quantitative analysis of apparent fibre density. In: *Proc. Intl. Soc. Mag. Reson. Med*. Vol 25. ; 2017:3541.

95. Lim JC, Phal PM, Desmond PM, et al. Probabilistic MRI tractography of the optic radiation using constrained spherical deconvolution: a feasibility study. *PloS one*. 2015;10(3):e0118948.

96. Ning L, Laun F, Gur Y, et al. Sparse Reconstruction Challenge for diffusion MRI: Validation on a physical phantom to determine which acquisition scheme and analysis method to use? *Medical image analysis*. 2015;26(1):316-331.

97. Parker GD, Marshall D, Rosin PL, Drage N, Richmond S, Jones DK. A pitfall in the reconstruction of fibre ODFs using spherical deconvolution of diffusion MRI data. *Neuroimage*. 2013;65:433-448.

98. Schilling KG, Janve V, Gao Y, Stepniewska I, Landman BA, Anderson AW. Histological validation of diffusion MRI fiber orientation distributions and dispersion. *Neuroimage*. 2018;165:200-221.

99. Wilkins B, Lee N, Gajawelli N, Law M, Leporé N. Fiber estimation and tractography in diffusion MRI: development of simulated brain images and comparison of multi-fiber analysis methods at clinical b-values. *Neuroimage*. 2015;109:341-356.

100. Newman BT, Dhollander T, Reynier KA, Panzer MB, Druzgal TJ. Test–retest reliability and long-term stability of three-tissue constrained spherical deconvolution methods for analyzing diffusion MRI data. *Magn Reson Med*. 2020;84(4):2161-2173. doi:10.1002/mrm.28242

101. Pietsch M, Christiaens D, Hutter J, et al. A framework for multi-component analysis of diffusion MRI data over the neonatal period. *NeuroImage*. 2019;186:321-337.

102. Bastiani M, Andersson JL, Cordero-Grande L, et al. Automated processing pipeline for neonatal diffusion MRI in the developing Human Connectome Project. *Neuroimage*. 2019;185:750-763.

103. Tournier JD, Calamante F, Connelly A. MRtrix: diffusion tractography in crossing fiber regions. *International journal of imaging systems and technology*. 2012;22(1):53-66.

104. Smith SM, Jenkinson M, Woolrich MW, et al. Advances in functional and structural MR image analysis and implementation as FSL. *Neuroimage*. 2004;23:S208-S219.

105. Jenkinson M, Beckmann CF, Behrens TE, Woolrich MW, Smith SM. Fsl. *Neuroimage*. 2012;62(2):782-790.

106. Jones DK. Precision and accuracy in diffusion tensor magnetic resonance imaging. *Topics in Magnetic Resonance Imaging*. 2010;21(2):87-99.

107. Veraart J, Fieremans E, Novikov DS. Diffusion MRI noise mapping using random matrix theory. *Magnetic resonance in medicine*. 2016;76(5):1582-1593.

108. Bracewell RN, Bracewell RN. *The Fourier Transform and Its Applications*. Vol 31999. McGraw-hill New York; 1986.

109. Kellner E, Dhital B, Kiselev VG, Reisert M. Gibbs-ringing artifact removal based on local subvoxel-shifts. *Magnetic resonance in medicine*. 2016;76(5):1574-1581.

110. Andersson JL, Sotiropoulos SN. An integrated approach to correction for off-resonance effects and subject movement in diffusion MR imaging. *Neuroimage*. 2016;125:1063-1078.

111. Schenck JF. The role of magnetic susceptibility in magnetic resonance imaging: MRI magnetic compatibility of the first and second kinds. *Medical physics*. 1996;23(6):815-850.

112. Irfanoglu MO, Walker L, Sarlls J, Marenco S, Pierpaoli C. Effects of image distortions originating from susceptibility variations and concomitant fields on diffusion MRI tractography results. *Neuroimage*. 2012;61(1):275-288.

113. Reese TG, Heid O, Weisskoff RM, Wedeen VJ. Reduction of eddy-current-induced distortion in diffusion MRI using a twice-refocused spin echo. *Magnetic Resonance in Medicine: An Official Journal of the International Society for Magnetic Resonance in Medicine*. 2003;49(1):177-182.

114. Holdsworth SJ, Skare S, Newbould RD, Guzmann R, Blevins NH, Bammer R. Readout-segmented EPI for rapid high resolution diffusion imaging at 3T. *European journal of radiology*. 2008;65(1):36-46.

115. Andersson JL, Skare S, Ashburner J. How to correct susceptibility distortions in spin-echo echo-planar images: application to diffusion tensor imaging. *Neuroimage*. 2003;20(2):870-888.

116. Andersson JL, Graham MS, Zsoldos E, Sotiropoulos SN. Incorporating outlier detection and replacement into a non-parametric framework for movement and distortion correction of diffusion MR images. *Neuroimage*. 2016;141:556-572.

117. Greenspan H. Super-resolution in medical imaging. *The computer journal*. 2009;52(1):43-63.

118. Kuklisova-Murgasova M, Quaghebeur G, Rutherford MA, Hajnal JV, Schnabel JA. Reconstruction of fetal brain MRI with intensity matching and complete outlier removal. *Medical image analysis*. 2012;16(8):1550-1564.

119. Avants BB, Tustison NJ, Song G, Cook PA, Klein A, Gee JC. A reproducible evaluation of ANTs similarity metric performance in brain image registration. *NeuroImage*. 2011;54(3):2033-2044. doi:10.1016/j.neuroimage.2010.09.025

120. Avants BB, Tustison NJ, Stauffer M, Song G, Wu B, Gee JC. The Insight ToolKit image registration framework. *Front Neuroinform*. 2014;8. doi:10.3389/fninf.2014.00044

121. Mito R, Raffelt D, Dhollander T, et al. Fibre-specific white matter reductions in Alzheimer's disease and mild cognitive impairment. *Brain*. 2018;141(3):888-902.

122. Dhollander T, Zanin J, Nayagam BA, Rance G, Connelly A. Feasibility and benefits of 3-tissue constrained spherical deconvolution for studying the brains of babies. In: *Proceedings of the 26th Annual Meeting of the International Society of Magnetic Resonance in Medicine*. ; 2018:3077.

123. Aerts H, Dhollander T, Marinazzo D. Evaluating the performance of 3-tissue constrained spherical deconvolution pipelines for within-tumor tractography. *BioRxiv*. Published online 2019:629873.

124. Biswal BB, Mennes M, Zuo XN, et al. Toward discovery science of human brain function. *Proceedings of the National Academy of Sciences*. 2010;107(10):4734-4739.

125. Oscar-Berman M, Marinković K. Alcohol: effects on neurobehavioral functions and the brain. *Neuropsychology review*. 2007;17(3):239-257.

126. Jiang J, Zhao YJ, Hu XY, et al. Microstructural brain abnormalities in medication-free patients with major depressive disorder: a systematic review and meta-analysis of diffusion tensor imaging. *Journal of Psychiatry and Neuroscience*. 2017;42(3):150-163.

127. Reitan RM. Validity of the Trail Making Test as an indicator of organic brain damage. *Perceptual and motor skills*. 1958;8(3):271-276.

128. Volkow ND, Koob GF, Croyle RT, et al. The conception of the ABCD study: From substance use to a broad NIH collaboration. *Developmental cognitive neuroscience*. 2018;32:4-7.

129. Elias WJ, Huss D, Voss T, et al. A pilot study of focused ultrasound thalamotomy for essential tremor. *New England Journal of Medicine*. 2013;369(7):640-648.

130. Wintermark M, Huss DS, Shah BB, et al. Thalamic connectivity in patients with essential tremor treated with MR imaging–guided focused ultrasound: in vivo fiber tracking by using diffusion-tensor MR imaging. *Radiology*. 2014;272(1):202-209.

131. Van Essen DC, Smith SM, Barch DM, et al. The WU-Minn human connectome project: an overview. *Neuroimage*. 2013;80:62-79.

132. Bycroft C, Freeman C, Petkova D, et al. The UK Biobank resource with deep phenotyping and genomic data. *Nature*. 2018;562(7726):203-209.

133. Casey BJ, Cannonier T, Conley MI, et al. The adolescent brain cognitive development (ABCD) study: imaging acquisition across 21 sites. *Developmental cognitive neuroscience*. 2018;32:43-54.

134. Tong Q, He H, Gong T, et al. Multicenter dataset of multi-shell diffusion MRI in healthy traveling adults with identical settings. *Scientific Data*. 2020;7(1):1-7.

135. Hsu YC, Lo YC, Chen YJ, Wedeen VJ, Isaac Tseng WY. NTU-DSI-122: A diffusion spectrum imaging template with high anatomical matching to the ICBM-152 space. *Human brain mapping*. 2015;36(9):3528-3541.

136. Karayumak SC, Bouix S, Ning L, et al. Retrospective harmonization of multi-site diffusion MRI data acquired with different acquisition parameters. *Neuroimage*. 2019;184:180-200.

137. Mirzaalian H, Ning L, Savadjiev P, et al. Multi-site harmonization of diffusion MRI data in a registration framework. *Brain imaging and behavior*. 2018;12(1):284-295.

138. Ning L, Bonet-Carne E, Grussu F, et al. Muti-shell diffusion MRI harmonisation and enhancement challenge (MUSHAC): progress and results. In: *International Conference on Medical Image Computing and Computer-Assisted Intervention*. Springer; 2019:217-224.

139. Zhu AH, Moyer DC, Nir TM, Thompson PM, Jahanshad N. Challenges and opportunities in dMRI data harmonization. In: *International Conference on Medical Image Computing and Computer-Assisted Intervention*. Springer; 2019:157-172.

140. Amunts K, Kedo O, Kindler M, et al. Cytoarchitectonic mapping of the human amygdala, hippocampal region and entorhinal cortex: intersubject variability and probability maps. *Anatomy and embryology*. 2005;210(5):343-352.

141. Lorio S, Fresard S, Adaszewski S, et al. New tissue priors for improved automated classification of subcortical brain structures on MRI. *Neuroimage*. 2016;130:157-166.

142. Zaborszky L, Hoemke L, Mohlberg H, Schleicher A, Amunts K, Zilles K. Stereotaxic probabilistic maps of the magnocellular cell groups in human basal forebrain. *Neuroimage*. 2008;42(3):1127-1141.

143. Venables WN, Ripley BD. *Modern Applied Statistics with S-PLUS*. Springer Science & Business Media; 2013.

144. Boullerne AI. The history of myelin. *Experimental neurology*. 2016;283:431-445.

145. Alexander AL, Lee JE, Lazar M, Field AS. Diffusion tensor imaging of the brain. *Neurotherapeutics*. 2007;4(3):316-329.

146. Johansen-Berg H, Behrens TE. *Diffusion MRI: From Quantitative Measurement to in Vivo Neuroanatomy*. Academic Press; 2013.

147. Le Bihan D, Mangin JF, Poupon C, et al. Diffusion tensor imaging: concepts and applications. *Journal of Magnetic Resonance Imaging: An Official Journal of the International Society for Magnetic Resonance in Medicine*. 2001;13(4):534-546.

148. Nimsky C, Ganslandt O, Hastreiter P, et al. Preoperative and intraoperative diffusion tensor imaging-based fiber tracking in glioma surgery. *Neurosurgery*. 2005;56(1):130-138.

149. Tuch DS, Reese TG, Wiegell MR, Wedeen VJ. Diffusion MRI of complex neural architecture. *Neuron*. 2003;40(5):885-895.

150. Wiegell MR, Larsson HB, Wedeen VJ. Fiber crossing in human brain depicted with diffusion tensor MR imaging. *Radiology*. 2000;217(3):897-903.

151. Jones DK, Cercignani M. Twenty-five pitfalls in the analysis of diffusion MRI data. *NMR in Biomedicine*. 2010;23(7):803-820.

152. Roine T, Jeurissen B, Perrone D, et al. Isotropic non-white matter partial volume effects in constrained spherical deconvolution. *Frontiers in neuroinformatics*. 2014;8:28.

153. Roine T, Jeurissen B, Perrone D, et al. Informed constrained spherical deconvolution (iCSD). *Medical Image Analysis*. 2015;24(1):269-281.

154. Rydhög AS, Szczepankiewicz F, Wirestam R, et al. Separating blood and water: Perfusion and free water elimination from diffusion MRI in the human brain. *Neuroimage*. 2017;156:423-434.

155. Alexander AL, Hasan KM, Lazar M, Tsuruda JS, Parker DL. Analysis of partial volume effects in diffusion-tensor MRI. *Magnetic Resonance in Medicine: An Official Journal of the International Society for Magnetic Resonance in Medicine*. 2001;45(5):770-780.

156. Raffelt D, Tournier JD, Rose S, et al. Apparent fibre density: a novel measure for the analysis of diffusion-weighted magnetic resonance images. *Neuroimage*. 2012;59(4):3976-3994.

157. Mito R, Dhollander T, Raffelt D, et al. Investigating microstructural heterogeneity of white matter hyperintensities in Alzheimer's disease using single-shell 3-tissue constrained spherical deconvolution. In: *Proc. Intl. Soc. Mag. Reson. Med*. ; 2018:135.

158. Nooner KB, Colcombe SJ, Tobe RH, et al. The NKI-Rockland sample: a model for accelerating the pace of discovery science in psychiatry. *Frontiers in neuroscience*. 2012;6:152.

159. Reynolds BB, Stanton AN, Soldozy S, Goodkin HP, Wintermark M, Druzgal TJ. Investigating the effects of subconcussion on functional connectivity using mass-univariate and multivariate approaches. *Brain imaging and behavior*. 2018;12(5):1332-1345.

160. Raffelt D, Tournier JD, Fripp J, Crozier S, Connelly A, Salvado O. Symmetric diffeomorphic registration of fibre orientation distributions. *NeuroImage*. 2011;56(3):1171-1180.

161. Shattuck DW, Mirza M, Adisetiyo V, et al. Construction of a 3D probabilistic atlas of human cortical structures. *Neuroimage*. 2008;39(3):1064-1080.

162. Avants BB, Tustison N, Song G. Advanced normalization tools (ANTS). *Insight j*. 2009;2(365):1-35.

163. Pedraza O, Bowers D, Gilmore R. Asymmetry of the hippocampus and amygdala in MRI volumetric measurements of normal adults. *Journal of the International Neuropsychological Society*. 2004;10(5):664-678.

164. Ofori E, DeKosky ST, Febo M, et al. Free-water imaging of the hippocampus is a sensitive marker of Alzheimer's disease. *NeuroImage: Clinical*. 2019;24:101985.

165. Burciu RG, Ofori E, Shukla P, et al. Free-water and BOLD imaging changes in Parkinson's disease patients chronically treated with a MAO-B inhibitor. *Human brain mapping*. 2016;37(8):2894-2903.

166. Chamberland M, Iqbal NS, Rudrapatna SU, et al. Characterising tissue heterogeneity in cerebral metastases using multi-shell multi-tissue constrained spherical deconvolution. *International Society for Magnetic Resonance in Medicine (ISMRM) Montreal*. Published online 2019.

167. Maier-Hein KH, Neher PF, Houde JC, et al. The challenge of mapping the human connectome based on diffusion tractography. *Nature communications*. 2017;8(1):1-13.

168. Roine T, Jeurissen B, Perrone D, et al. Reproducibility and intercorrelation of graph theoretical measures in structural brain connectivity networks. *Medical image analysis*. 2019;52:56-67.

169. Bycroft C, Freeman C, Petkova D, et al. The UK Biobank resource with deep phenotyping and genomic data. *Nature*. 2018;562(7726):203-209. doi:10.1038/s41586-018-0579-z

170. Van Essen DC, Ugurbil K, Auerbach E, et al. The Human Connectome Project: A data acquisition perspective. *NeuroImage*. 2012;62(4):2222-2231. doi:10.1016/j.neuroimage.2012.02.018

171. Weiner MW, Veitch DP, Aisen PS, et al. The Alzheimer's Disease Neuroimaging Initiative 3: Continued innovation for clinical trial improvement. *Alzheimer's & Dementia*. 2017;13(5):561-571. doi:10.1016/j.jalz.2016.10.006

172. Newman B, Dhollander T, Druzgal T. *Single-Shell Derived Tissue Signal Fraction Maps Show Increased Contrast between Hippocampal Subfields Compared to Multi-Shell Analysis*.; 2020.

173. Dhollander T, Connelly A. *A Novel Iterative Approach to Reap the Benefits of Multi-Tissue CSD from Just Single-Shell (+b=0) Diffusion MRI Data*.; 2016.

174. Tournier JD, Smith R, Raffelt D, et al. MRtrix3: A fast, flexible and open software framework for medical image processing and visualisation. *NeuroImage*. 2019;202:116137. doi:10.1016/j.neuroimage.2019.116137

175. Sm S, M J, Mw W, et al. Advances in functional and structural MR image analysis and implementation as FSL. *Neuroimage*. 2004;23 Suppl 1:S208-S219. Accessed November 8, 2021. https://www.win.ox.ac.uk/publications/116895

176. Veraart J, Novikov DS, Christiaens D, Ades-aron B, Sijbers J, Fieremans E. Denoising of diffusion MRI using random matrix theory. *NeuroImage*. 2016;142:394-406. doi:10.1016/j.neuroimage.2016.08.016

177. Gibbs-ringing artifact removal based on local subvoxel-shifts - Kellner - 2016 - Magnetic Resonance in Medicine - Wiley Online Library. Accessed September 20, 2021. https://onlinelibrary.wiley.com/doi/abs/10.1002/mrm.26054

178. Andersson JLR, Skare S, Ashburner J. How to correct susceptibility distortions in spin-echo echo-planar images: application to diffusion tensor imaging. *NeuroImage*. 2003;20(2):870-888. doi:10.1016/S1053-8119(03)00336-7

179. Andersson JLR, Graham MS, Zsoldos E, Sotiropoulos SN. Incorporating outlier detection and replacement into a non-parametric framework for movement and distortion correction of diffusion MR images. *Neuroimage*. 2016;141:556-572. doi:10.1016/j.neuroimage.2016.06.058

180. Andersson JLR, Sotiropoulos SN. An integrated approach to correction for off-resonance effects and subject movement in diffusion MR imaging. *NeuroImage*. 2016;125:1063-1078. doi:10.1016/j.neuroimage.2015.10.019

181. Greenspan H. Super-Resolution in Medical Imaging. *Comput J*. 2009;52:43-63. doi:10.1093/comjnl/bxm075

182. (ISMRM 2019) Improved white matter response function estimation for 3-tissue constrained spherical deconvolution. Accessed November 8, 2021. https://archive.ismrm.org/2019/0555.html

183. Mori S, Wakana S, Zijl PCM van, Nagae-Poetscher LM. *MRI Atlas of Human White Matter*. Elsevier; 2005.

184. Hua K, Zhang J, Wakana S, et al. Tract probability maps in stereotaxic spaces: analyses of white matter anatomy and tract-specific quantification. *Neuroimage*. 2008;39(1):336-347. doi:10.1016/j.neuroimage.2007.07.053

185. Wakana S, Caprihan A, Panzenboeck MM, et al. Reproducibility of quantitative tractography methods applied to cerebral white matter. *Neuroimage*. 2007;36(3):630-644. doi:10.1016/j.neuroimage.2007.02.049

186. Destrieux C, Fischl B, Dale A, Halgren E. Automatic parcellation of human cortical gyri and sulci using standard anatomical nomenclature. *Neuroimage*. 2010;53(1):1-15.

187. Newman B, Untaroiu A, Druzgal T. *A Novel Diffusion Registration Method with the NTU-DSI-122 Template to Transform Free Water Signal Fraction Maps to Stereotaxic Space*.; 2020.

188. Franceschini G, Bigoni D, Regitnig P, Holzapfel GA. Brain tissue deforms similarly to filled elastomers and follows consolidation theory. *Journal of the Mechanics and Physics of Solids*. 2006;54(12):2592-2620.

189. Nunes RG, Jezzard P, Clare S. Investigations on the efficiency of cardiac-gated methods for the acquisition of diffusion-weighted images. *Journal of magnetic resonance*. 2005;177(1):102-110.

190. Collins DL, Neelin P, Peters TM, Evans AC. Automatic 3D intersubject registration of MR volumetric data in standardized Talairach space. *J Comput Assist Tomogr*. 1994;18(2):192-205.

191. Fonov V, Evans AC, Botteron K, Almli CR, McKinstry RC, Collins DL. Unbiased average age-appropriate atlases for pediatric studies. *NeuroImage*. 2011;54(1):313-327. doi:10.1016/j.neuroimage.2010.07.033

192. Holmes CJ, Hoge R, Collins L, Woods R, Toga AW, Evans AC. Enhancement of MR images using registration for signal averaging. *Journal of computer assisted tomography*. 1998;22(2):324-333.

193. Desikan RS, Ségonne F, Fischl B, et al. An automated labeling system for subdividing the human cerebral cortex on MRI scans into gyral based regions of interest. *Neuroimage*. 2006;31(3):968-980.

194. Allen JS, Damasio H, Grabowski TJ. Normal neuroanatomical variation in the human brain: An MRI-volumetric study. *American Journal of Physical Anthropology: The Official Publication of the American Association of Physical Anthropologists*. 2002;118(4):341-358.

195. Reardon PK, Seidlitz J, Vandekar S, et al. Normative brain size variation and brain shape diversity in humans. *Science*. 2018;360(6394):1222-1227.

196. Maes F, Collignon A, Vandermeulen D, Marchal G, Suetens P. Multimodality image registration by maximization of mutual information. *IEEE transactions on Medical Imaging*. 1997;16(2):187-198.

197. Mugler III JP, Brookeman JR. Three-dimensional magnetization-prepared rapid gradient-echo imaging (3D MP RAGE). *Magnetic resonance in medicine*. 1990;15(1):152-157.

198. Fu Z, Lin L, Tian M, et al. Evaluation of five diffeomorphic image registration algorithms for mouse brain magnetic resonance microscopy: EVALUATION OF FIVE DIFFEOMORPHIC IMAGE REGISTRATION ALGORITHMS. *Journal of Microscopy*. 2017;268(2):141-154. doi:10.1111/jmi.12594

199. Klein A, Andersson J, Ardekani BA, et al. Evaluation of 14 nonlinear deformation algorithms applied to human brain MRI registration. *NeuroImage*. 2009;46(3):786-802. doi:10.1016/j.neuroimage.2008.12.037

200. Huang H, Ceritoglu C, Li X, et al. Correction of B0 susceptibility induced distortion in diffusion-weighted images using large-deformation diffeomorphic metric mapping. *Magnetic Resonance Imaging*. 2008;26(9):1294-1302. doi:10.1016/j.mri.2008.03.005

201. McLaughlin NCR, Paul RH, Grieve SM, et al. Diffusion tensor imaging of the corpus callosum: a cross-sectional study across the lifespan. *Int j dev neurosci*. 2007;25(4):215-221. doi:10.1016/j.ijdevneu.2007.03.008

202. Pierpaoli C, Walker L, Irfanoglu MO, et al. TORTOISE: an integrated software package for processing of diffusion MRI data. In: *ISMRM 18th Annual Meeting*. Vol 1597. ; 2010.

203. Farquharson S, Tournier JD, Calamante F, et al. White matter fiber tractography: why we need to move beyond DTI. *Journal of neurosurgery*. 2013;118(6):1367-1377.

204. Oouchi H, Yamada K, Sakai K, et al. Diffusion anisotropy measurement of brain white matter is affected by voxel size: underestimation occurs in areas with crossing fibers. *American Journal of Neuroradiology*. 2007;28(6):1102-1106.

205. Tournier JD, Calamante F, Connelly A. Determination of the appropriate b value and number of gradient directions for high-angular-resolution diffusion-weighted imaging. *NMR in Biomedicine*. 2013;26(12):1775-1786.

206. Genc S, Tax CM, Raven EP, Chamberland M, Parker GD, Jones DK. Impact of b-value on estimates of apparent fibre density. *Human brain mapping*. 2020;41(10):2583-2595.

207. Newman BT, Dhollander T, Druzgal TJ. Single-shell derived tissue signal fraction maps show increased contrast between hippocampal subfields compared to multi-shell analysis. *Proceedings of the ISMRM 28th General Meeting*. Published online 2020.

208. Hsu YC, Hsu CH, Tseng WYI. A large deformation diffeomorphic metric mapping solution for diffusion spectrum imaging datasets. *NeuroImage*. 2012;63(2):818-834.

209. Raffelt D, Tournier JD, Crozier S, Connelly A, Salvado O. Reorientation of fiber orientation distributions using apodized point spread functions. *Magnetic resonance in medicine*. 2012;67(3):844-855.

210. Dice LR. Measures of the amount of ecologic association between species. *Ecology*. 1945;26(3):297-302.

211. Sorensen TA. A method of establishing groups of equal amplitude in plant sociology based on similarity of species content and its application to analyses of the vegetation on Danish commons. *Biol Skar*. 1948;5:1-34.

212. Sotiropoulos SN, Jbabdi S, Xu J, et al. Advances in diffusion MRI acquisition and processing in the Human Connectome Project. *Neuroimage*. 2013;80:125-143.

213. Kaufman J, Plotsky PM, Nemeroff CB, Charney DS. Effects of early adverse experiences on brain structure and function: clinical implications. *Biological psychiatry*. 2000;48(8):778-790.

214. Raz N. Aging of the brain and its impact on cognitive performance: Integration of structural and functional findings. Published online 2000.

215. Valkenborghs SR, Noetel M, Hillman CH, et al. The impact of physical activity on brain structure and function in youth: a systematic review. *Pediatrics*. 2019;144(4).

216. Driscoll I, Davatzikos C, An Y, et al. Longitudinal pattern of regional brain volume change differentiates normal aging from MCI. *Neurology*. 2009;72(22):1906-1913.

217. Fotenos AF, Snyder AZ, Girton LE, Morris JC, Buckner RL. Normative estimates of cross-sectional and longitudinal brain volume decline in aging and AD. *Neurology*. 2005;64(6):1032-1039.

218. Good CD, Johnsrude IS, Ashburner J, Henson RN, Friston KJ, Frackowiak RS. A voxel-based morphometric study of ageing in 465 normal adult human brains. *Neuroimage*. 2001;14(1):21-36.

219. Group BDC. Total and regional brain volumes in a population-based normative sample from 4 to 18 years: the NIH MRI Study of Normal Brain Development. *Cerebral Cortex*. 2012;22(1):1-12.

220. Pomponio R, Erus G, Habes M, et al. Harmonization of large MRI datasets for the analysis of brain imaging patterns throughout the lifespan. *NeuroImage*. 2020;208:116450.

221. Raz N, Lindenberger U, Rodrigue KM, et al. Regional brain changes in aging healthy adults: general trends, individual differences and modifiers. *Cerebral cortex*. 2005;15(11):1676-1689.

222. Juraska JM, Willing J. Pubertal onset as a critical transition for neural development and cognition. *Brain Research*. 2017;1654:87-94.

223. Jefferson AL, Himali JJ, Beiser AS, et al. Cardiac index is associated with brain aging: the Framingham Heart Study. *Circulation*. 2010;122(7):690-697.

224. Feinberg I. Schizophrenia: caused by a fault in programmed synaptic elimination during adolescence? *Journal of psychiatric research*. 1982;17(4):319-334.

225. Selemon LD. A role for synaptic plasticity in the adolescent development of executive function. *Translational psychiatry*. 2013;3(3):e238-e238.

226. Stephan BCM, Hunter S, Harris D, et al. The neuropathological profile of mild cognitive impairment (MCI): a systematic review. *Molecular psychiatry*. 2012;17(11):1056-1076.

227. Khan W, Khlif MS, Mito R, Dhollander T, Brodtmann A. Investigating the microstructural properties of normal-appearing white matter (NAWM) preceding conversion to white matter hyperintensities (WMHs) in stroke survivors. *NeuroImage*. 2021;232:117839.

228. Hua K, Zhang J, Wakana S, et al. Tract probability maps in stereotaxic spaces: analyses of white matter anatomy and tract-specific quantification. *Neuroimage*. 2008;39(1):336-347.

229. Mori S, Wakana S, Van Zijl PC, Nagae-Poetscher LM. *MRI Atlas of Human White Matter*. Elsevier; 2005.

230. Wakana S, Caprihan A, Panzenboeck MM, et al. Reproducibility of quantitative tractography methods applied to cerebral white matter. *Neuroimage*. 2007;36(3):630-644.

231. Fischl B. FreeSurfer. *Neuroimage*. 2012;62(2):774-781.

232. Lebel C, Beaulieu C. Longitudinal development of human brain wiring continues from childhood into adulthood. *Journal of Neuroscience*. 2011;31(30):10937-10947.

233. Lebel C, Deoni S. The development of brain white matter microstructure. *Neuroimage*. 2018;182:207-218.

234. Natu VS, Gomez J, Barnett M, et al. Apparent thinning of human visual cortex during childhood is associated with myelination. *Proceedings of the National Academy of Sciences*. 2019;116(41):20750-20759.

235. Beck D, de Lange AMG, Maximov II, et al. White matter microstructure across the adult lifespan: A mixed longitudinal and cross-sectional study using advanced diffusion models and brain-age prediction. *Neuroimage*. 2021;224:117441.

236. Nazeri A, Chakravarty MM, Rotenberg DJ, et al. Functional consequences of neurite orientation dispersion and density in humans across the adult lifespan. *Journal of Neuroscience*. 2015;35(4):1753-1762.

237. Semendeferi K, Armstrong E, Schleicher A, Zilles K, Van Hoesen GW. Limbic frontal cortex in hominoids: a comparative study of area 13. *American Journal of Physical Anthropology: The Official Publication of the American Association of Physical Anthropologists*. 1998;106(2):129-155.

238. Cotter D, Mackay D, Landau S, Kerwin R, Everall I. Reduced glial cell density and neuronal size in the anterior cingulate cortex in major depressive disorder. *Archives of general psychiatry*. 2001;58(6):545-553.

239. Rajkowska G, Halaris A, Selemon LD. Reductions in neuronal and glial density characterize the dorsolateral prefrontal cortex in bipolar disorder. *Biological psychiatry*. 2001;49(9):741-752.

240. Benes FM, Davidson J, Bird ED. Quantitative cytoarchitectural studies of the cerebral cortex of schizophrenics. *Archives of general psychiatry*. 1986;43(1):31-35.

241. Selemon LD, Rajkowska G, Goldman-Rakic PS. Abnormally high neuronal density in the schizophrenic cortex: a morphometric analysis of prefrontal area 9 and occipital area 17. *Archives of general psychiatry*. 1995;52(10):805-818.

242. Kessler RC, Berglund P, Demler O, Jin R, Merikangas KR, Walters EE. Lifetime prevalence and age-of-onset distributions of DSM-IV disorders in the National Comorbidity Survey Replication. *Archives of general psychiatry*. 2005;62(6):593-602.

243. Paus T, Keshavan M, Giedd JN. Why do many psychiatric disorders emerge during adolescence? *Nature reviews neuroscience*. 2008;9(12):947-957.

244. Petersen AC, Crockett L, Richards M, Boxer A. A self-report measure of pubertal status: Reliability, validity, and initial norms. *Journal of youth and adolescence*. 1988;17(2):117-133.

245. Shirtcliff EA, Dahl RE, Pollak SD. Pubertal development: correspondence between hormonal and physical development. *Child development*. 2009;80(2):327-337.

246. Lerner RM, Steinberg L. *Handbook of Adolescent Psychology, Volume 1: Individual Bases of Adolescent Development*. Vol 1. John Wiley & Sons; 2009.

247. Cahill L. Why sex matters for neuroscience. *Nature reviews neuroscience*. 2006;7(6):477-484.

248. Nave KA. Myelination and support of axonal integrity by glia. *Nature*. 2010;468(7321):244-252.

249. Sisk CL, Zehr JL. Pubertal hormones organize the adolescent brain and behavior. *Frontiers in neuroendocrinology*. 2005;26(3-4):163-174.

250. Ahmed EI, Zehr JL, Schulz KM, Lorenz BH, DonCarlos LL, Sisk CL. Pubertal hormones modulate the addition of new cells to sexually dimorphic brain regions. *Nature neuroscience*. 2008;11(9):995-997.

251. Orije J, Cardon E, De Groof G, et al. In vivo online monitoring of testosterone-induced neuroplasticity in a female songbird. *Hormones and behavior*. 2020;118:104639.

252. Chen Z, Ye R, Goldman SA. Testosterone modulation of angiogenesis and neurogenesis in the adult songbird brain. *Neuroscience*. 2013;239:139-148.

253. Peper JS, Pol HH, Crone EA, Van Honk J. Sex steroids and brain structure in pubertal boys and girls: a mini-review of neuroimaging studies. *Neuroscience*. 2011;191:28-37.

254. Huttenlocher PR. Synaptic density in human frontal cortex-developmental changes and effects of aging. *Brain Res*. 1979;163(2):195-205.

255. Asato MR, Terwilliger R, Woo J, Luna B. White matter development in adolescence: a DTI study. *Cerebral cortex*. 2010;20(9):2122-2131.

256. Lebel C, Walker L, Leemans A, Phillips L, Beaulieu C. Microstructural maturation of the human brain from childhood to adulthood. *Neuroimage*. 2008;40(3):1044-1055.

257. Simmonds DJ, Hallquist MN, Asato M, Luna B. Developmental stages and sex differences of white matter and behavioral development through adolescence: a longitudinal diffusion tensor imaging (DTI) study. *Neuroimage*. 2014;92:356-368.

258. Genc S, Malpas CB, Holland SK, Beare R, Silk TJ. Neurite density index is sensitive to age related differences in the developing brain. *Neuroimage*. 2017;148:373-380.

259. Mah A, Geeraert B, Lebel C. Detailing neuroanatomical development in late childhood and early adolescence using NODDI. *PLoS One*. 2017;12(8):e0182340.

260. Raffelt DA, Smith RE, Ridgway GR, et al. Connectivity-based fixel enhancement: Whole-brain statistical analysis of diffusion MRI measures in the presence of crossing fibres. *Neuroimage*. 2015;117:40-55.

261. Genc S, Malpas CB, Gulenc A, et al. Longitudinal patterns of white matter fibre density and morphology in children are associated with age and pubertal stage. *Developmental cognitive neuroscience*. 2020;45:100853.

262. Silk TJ, Genc S, Anderson V, et al. Developmental brain trajectories in children with ADHD and controls: a longitudinal neuroimaging study. *BMC psychiatry*. 2016;16(1):1-9.

263. Hagler Jr DJ, Hatton S, Cornejo MD, et al. Image processing and analysis methods for the Adolescent Brain Cognitive Development Study. *Neuroimage*. 2019;202:116091.

264. Smith SM. Fast robust automated brain extraction. *Human brain mapping*. 2002;17(3):143-155.

265. Pinto MS, Paolella R, Billiet T, et al. Harmonization of brain diffusion MRI: Concepts and methods. *Frontiers in Neuroscience*. Published online 2020:396.

266. Barch DM, Albaugh MD, Avenevoli S, et al. Demographic, physical and mental health assessments in the adolescent brain and cognitive development study: Rationale and description. *Developmental cognitive neuroscience*. 2018;32:55-66.

267. Benjamini Y, Hochberg Y. Controlling the false discovery rate: a practical and powerful approach to multiple testing. *Journal of the Royal statistical society: series B (Methodological)*. 1995;57(1):289-300.

268. De Lorme KC, Schulz KM, Salas-Ramirez KY, Sisk CL. Pubertal testosterone organizes regional volume and neuronal number within the medial amygdala of adult male Syrian hamsters. *Brain research*. 2012;1460:33-40.

269. Zhang Z, Cerghet M, Mullins C, Williamson M, Bessert D, Skoff R. Comparison of in vivo and in vitro subcellular localization of estrogen receptors α and β in oligodendrocytes. *Journal of neurochemistry*. 2004;89(3):674-684.

270. Menzies L, Goddings AL, Whitaker KJ, Blakemore SJ, Viner RM. The effects of puberty on white matter development in boys. *Developmental cognitive neuroscience*. 2015;11:116-128.

271. Herting MM, Gautam P, Spielberg JM, Dahl RE, Sowell ER. A longitudinal study: changes in cortical thickness and surface area during pubertal maturation. *PLoS One*. 2015;10(3):e0119774.

272. Tamnes CK, Roalf DR, Goddings AL, Lebel C. Diffusion MRI of white matter microstructure development in childhood and adolescence: Methods, challenges and progress. *Developmental cognitive neuroscience*. 2018;33:161-175.

273. Barendse ME, Simmons JG, Smith RE, Seal ML, Whittle S. Adrenarcheal hormone-related development of white matter during late childhood. *Neuroimage*. 2020;223:117320.

274. Paus T. Growth of white matter in the adolescent brain: myelin or axon? *Brain and cognition*. 2010;72(1):26-35.

275. Willing J, Juraska JM. The timing of neuronal loss across adolescence in the medial prefrontal cortex of male and female rats. *Neuroscience*. 2015;301:268-275.

276. Perrin JS, Hervé PY, Leonard G, et al. Growth of white matter in the adolescent brain: role of testosterone and androgen receptor. *Journal of Neuroscience*. 2008;28(38):9519-9524.

277. Prins ND, Scheltens P. White matter hyperintensities, cognitive impairment and dementia: an update. *Nature Reviews Neurology*. 2015;11(3):157-165.

278. Chamberland M, Winter M, Brice TA, Jones DK, Tallantyre EC. Beyond lesion-load: tractometry-based metrics for characterizing white matter lesions within fibre pathways. Published online 2020.

279. Winter M, Tallantyre EC, Brice TA, Robertson NP, Jones DK, Chamberland M. Tract-specific MRI measures explain learning and recall differences in multiple sclerosis. *Brain Communications*. 2021;3(2):fcab065.

280. Lu AT, Quach A, Wilson JG, et al. DNA methylation GrimAge strongly predicts lifespan and healthspan. *Aging (Albany NY)*. 2019;11(2):303.

281. McCrory C, Fiorito G, Hernandez B, et al. GrimAge outperforms other epigenetic clocks in the prediction of age-related clinical phenotypes and all-cause mortality. *The Journals of Gerontology: Series A*. 2021;76(5):741-749.

282. Horvath S. DNA methylation age of human tissues and cell types. *Genome biology*. 2013;14(10):1-20.

283. Lin Q, Weidner CI, Costa IG, et al. DNA methylation levels at individual age-associated CpG sites can be indicative for life expectancy. *Aging (Albany NY)*. 2016;8(2):394.

284. Felder RB, Francis J, Zhang ZH, Wei SG, Weiss RM, Johnson AK. Heart failure and the brain: new perspectives. *American Journal of Physiology-Regulatory, Integrative and Comparative Physiology*. 2003;284(2):R259-R276.

285. Hillman CH, Erickson KI, Kramer AF. Be smart, exercise your heart: exercise effects on brain and cognition. *Nature reviews neuroscience*. 2008;9(1):58-65.

286. Finsterwalder S, Vlegels N, Gesierich B, et al. Small vessel disease more than Alzheimer's disease determines diffusion MRI alterations in memory clinic patients. *Alzheimer's & Dementia*. 2020;16(11):1504-1514.

287. Tuladhar AM, van Norden AG, de Laat KF, et al. White matter integrity in small vessel disease is related to cognition. *NeuroImage: Clinical*. 2015;7:518-524.

288. Wardlaw JM, Smith C, Dichgans M. Small vessel disease: mechanisms and clinical implications. *The Lancet Neurology*. 2019;18(7):684-696.

289. Di Stadio A, Messineo D, Ralli M, et al. The impact of white matter hyperintensities on speech perception. *Neurological Sciences*. 2020;41(7):1891-1898.

290. Gunning-Dixon FM, Raz N. The cognitive correlates of white matter abnormalities in normal aging: a quantitative review. *Neuropsychology*. 2000;14(2):224.

291. Dawber TR, Meadors GF, Moore Jr FE. Epidemiological approaches to heart disease: the Framingham Study. *American Journal of Public Health and the Nations Health*. 1951;41(3):279-286.

292. Maillard P, Mitchell GF, Himali JJ, et al. Effects of arterial stiffness on brain integrity in young adults from the Framingham Heart Study. *Stroke*. 2016;47(4):1030-1036.

293. Fransquet PD, Lacaze P, Saffery R, et al. Accelerated Epigenetic Aging in Peripheral Blood does not Predict Dementia Risk. *Current Alzheimer Research*. 2021;18(5):443-451.

294. Russ TC. DNA methylation-based measures of accelerated biological ageing and the risk of dementia in the oldest-old: a study of the Lothian Birth Cohort 1921. Published online 2020.

295. Shadyab AH, McEvoy LK, Horvath S, et al. Association of Epigenetic Age Acceleration With Incident Mild Cognitive Impairment and Dementia Among Older Women. *The Journals of Gerontology: Series A*. Published online 2021.

296. Biesbroek JM, Weaver NA, Hilal S, et al. Impact of strategically located white matter hyperintensities on cognition in memory clinic patients with small vessel disease. *PLoS One*. 2016;11(11):e0166261.

297. Salthouse TA. Trajectories of normal cognitive aging. *Psychology and aging*. 2019;34(1):17.

298. Siedlecki K. Findings From the Virginia Cognitive Aging Project: Individual Differences, Well-Being, and Cognition. *Innovation in Aging*. 2020;4(Supplement_1):591-592.

299. Gunter J, Thostenson K, Borowski B, et al. ADNI-3 MRI Protocol. *Alzheimer's Dementia*. 2017;13(7):P104-P105.

300. Newman BT, Untaroiu A, Druzgal TJ. A novel diffusion registration method with the NTU-DSI-122 template to transform free water signal fraction maps to stereotaxic space. 2020;Proceedings of the ISMRM 28th General Meeting.

301. Tournier JD, Calamante F, Connelly A. Improved probabilistic streamlines tractography by 2nd order integration over fibre orientation distributions. In: *Proceedings of the International Society for Magnetic Resonance in Medicine*. Vol 1670. John Wiley & Sons, Inc. New Jersey, USA; 2010.

302. Smith RE, Tournier JD, Calamante F, Connelly A. SIFT: Spherical-deconvolution informed filtering of tractograms. *Neuroimage*. 2013;67:298-312.

303. Hotz I, Deschwanden PF, Liem F, et al. *Performance of Three Freely Available Methods for Extracting White Matter Hyperintensities: FreeSurfer, UBO Detector, and BIANCA*. Wiley Online Library; 2022.

304. Aryee MJ, Jaffe AE, Corrada-Bravo H, et al. Minfi: a flexible and comprehensive Bioconductor package for the analysis of Infinium DNA methylation microarrays. *Bioinformatics*. 2014;30(10):1363-1369.

305. Fortin JP, Fertig E, Hansen K. shinyMethyl: interactive quality control of Illumina 450k DNA methylation arrays in R. *F1000Research*. 2014;3.

306. Fortin JP, Triche Jr TJ, Hansen KD. Preprocessing, normalization and integration of the Illumina HumanMethylationEPIC array with minfi. *Bioinformatics*. 2017;33(4):558-560.

307. Houseman EA, Accomando WP, Koestler DC, et al. DNA methylation arrays as surrogate measures of cell mixture distribution. *BMC bioinformatics*. 2012;13(1):1-16.

308. Jaffe AE, Irizarry RA. Accounting for cellular heterogeneity is critical in epigenome-wide association studies. *Genome biology*. 2014;15(2):1-9.

309. Heiss JA, Just AC. Identifying mislabeled and contaminated DNA methylation microarray data: an extended quality control toolset with examples from GEO. *Clinical epigenetics*. 2018;10(1):1-9.

310. Newman BT, Untaroiu A, Druzgal TJ. A method for post-surgical evaluation of targeting accuracy in transcranial focused ultrasound thalamic ablation. *28th International Society of Magnetic Resonance in Medicine*. 2020;28:4111.

311. Nguyen S, Northuis CA, Guan W, et al. Epigenetic Clocks And Incident Heart Failure: The Atherosclerosis Risk In Communities (aric). *Circulation*. 2021;143(Suppl_1):A033-A033.

312. Joyce BT, Gao T, Zheng Y, et al. Epigenetic Age Acceleration Reflects Long-Term Cardiovascular Health. *Circulation research*. 2021;129(8):770-781.

313. Grodstein F, Lemos B, Yu L, et al. The association of epigenetic clocks in brain tissue with brain pathologies and common aging phenotypes. *Neurobiology of Disease*. Published online 2021:105428.

314. Huang P, Zhang R, Jiaerken Y, et al. White Matter Free Water is a Composite Marker of Cerebral Small Vessel Degeneration. *Translational Stroke Research*. Published online 2021:1-9.